Mapping the fundamental metabolic drivers of inflammation with molecular imaging

Alexia Kirby

A thesis submitted in partial fulfillment
of the requirements for the

Doctorate in Philosophy

degree in

Biology

Faculty of Science

University of Ottawa

Supervisor:	Adam Shuhendler, PhD
Examining Board:	Emily Standen, PhD, Biology Katey Rayner, PhD, Biochemistry, Microbiology and Immunology Michael Downey, PhD, Cellular and Molecular Medicine
External Examiner:	Peter Scott, PhD, Radiology, Pharmacology and Medicinal Chemistry, University of Michigan

Abstract

Inflammation and oxidative stress are tightly linked processes underlying the pathogenesis of a wide variety of diseases. Using molecular imaging, we can enhance our understanding of these mechanisms through non-invasive visualization of important mediators of disease at the molecular and cellular level. Aldehydes are toxic biproducts of inflammation and oxidative stress, formed by many metabolic pathways including lipid peroxidation, autoxidation, oxidative burst from inflammatory monocytes, polyamine catabolism, and drug metabolism. These aldehydes are highly reactive electrophiles, rapidly forming adducts with phospholipids, proteins, and DNA, regulating cell survival, autophagy, senescence, apoptosis, and necrosis. These endogenous aldehydes and their adducts have been implicated in many pathological conditions including neurodegenerative, metabolic, and cardiovascular diseases, cancer, drug toxicity, and traumatic brain injury. However, due to their transient and highly reactive nature, the direct investigation of aldehydes and their role in disease has been challenging. The contents of this thesis include the development and application of molecular imaging probes for fluorescence, positron emission tomography (PET), and magnetic resonance imaging (MRI) targeted toward the cellular and *in vivo* visualization of aldehydes in models of oxidative stress, inflammation, mild traumatic brain injury, and acetaminophen overdose. Using these probes, the direct mapping of endogenous production has been elucidated, and with this data I propose aldehydes are mediators and propagators of inflammatory and oxidative pathologies.

Another metabolic driver of disease is the cellular switch from glucose to fructose metabolism (fructolysis). Fructose can be generated endogenously from glucose *via* the polyol pathway or consumed from dietary sources. Fructolysis has been identified as the driver of end-stage diabetes complications including retinopathy, nephropathy, and neuropathy. Fructose is also effective at protein glycation, leading to the production of advanced glycation end products (AGEs), which have been suggested as promotors of metabolic syndrome and chronic inflammatory conditions. The metabolism of fructose disrupts the delicate balance between antioxidant and pro-oxidant systems, leading to oxidative stress. Some cancers have demonstrated preference for fructose over glucose metabolism, making them difficult to visualize using

standard PET imaging with [^{18}F]-2-fluoro-2-deoxy-D-glucose ([^{18}F]-FDG), a radiolabeled glucose analog for mapping of glycolysis. Herein, I describe a novel metabolic PET radiotracer, [^{18}F]4-fluoro-4-deoxyfructose ([^{18}F]4-FDF), for *in vivo* mapping of fructose metabolism. The utility of this radiotracer is demonstrated in mouse models of cancer and systemic inflammation and represents a powerful clinical tool for the non-invasive diagnosis of many diseases.

The final topic of this thesis involves molecular imaging of inactivated bacteria to determine its trafficking and biodistribution *in vivo*. Site Specific Immunomodulators (SSIs) are a novel class of immunotherapy derived from bacteria that usually infect specific organs (*Escherichia coli* for the gut, and *Klebsiella pneumoniae* for the lungs). While it is understood that in keeping the macromolecular components of these inactivated bacteria modulates the innate immune system, it was previously unknown whether their biodistribution matched that of the live bacteria, and how they were trafficked within the body. The biodistribution of the SSIs was mapped in healthy mice through radiolabeling, and the involvement of phagocytosing cells was elucidated by immunohistochemical evaluation of local innate immune cells. Thus, by using molecular imaging, the inflammatory response to immunomodulating therapies was mapped *in vivo* by PET.

In conclusion, this thesis highlights the pivotal role of molecular imaging in advancing our comprehension of inflammation and oxidative stress, shedding light on the intricate interplay of aldehydes in various diseases. Furthermore, the *in vivo* mapping of fructolysis with [^{18}F]4-FDF contributes valuable insights into the metabolic drivers of diseases, offering potential diagnostic avenues for neuro and cardio-inflammatory conditions. Finally, the application of molecular imaging to unravel the trafficking and biodistribution of inactivated bacteria underscores its significance in mapping the inflammatory response to immunomodulating therapies, providing a new perspective on the intricate dynamics of disease pathogenesis.

Acknowledgements

This endeavor would not have been possible without my supervisor and mentor, Dr. Adam Shuhendler. We have accomplished a lot together over these past few years (who's counting?), and your support has been instrumental every step of the way. You have taught me to persevere through all the curve balls life throws, and to always have a plan B, C, and D.

I am also grateful to my lab-mates, past and present, for all of your help and moral support throughout my time in the lab. I would like to specifically thank Dr. Mojmir Suchy for being my right-hand chemist. To my lab-mate and long-time friend Nick, thank you for your (at times unconventional) support. Even if that meant playing cribbage during long imaging days.

Thank you to my Thesis Advisory Committee Members, Drs. Katey Rayner, Emily Standen, and Mike Downey, for always providing excellent feedback with your wide breadth of knowledge and expertise.

Lastly, I would like to thank everyone in my personal life who has gotten me through all these years of being a professional student including my family, friends, and my wonderful supportive husband Anthony. I truly could not have done this without each and every one of you.

Table of Contents

List of Tables

List of Figures

List of Symbols, Nomenclature, and Abbreviations

$[^{18}F]$FDG	$[^{18}F]$-2-fluoro-2-deoxy-D-glucose
$[^{18}F]$FDF	$[^{18}F]$-4-fluoro-4-droxy-D-fructose
$[^{18}F]NA_3BF_3$	$[^{18}F]$ N-aminoanthranilic acid trifluoroborate
3D-OSEM	3 Dimensional Ordered-Subset Expectation Maximization
4HNE	4-Hydroxynonenal
ACHI	Awake Closed Head Impact
ADH	Alcohol Dehydrogenase
AGE	Advanced Glycation End Products
AIF	Apoptosis Inducing Factor
ALDH	Aldehyde Dehydrogenase
ALDMP	Aldehyde Bearing Microparticles
APAP	Acetaminophen
αTOH	Alpha Tocopherol
ATP	Adenosine Triphosphate
AUC	Area Under the Curve
BBB	Blood Brain Barrier
BDNF	Brain-Derived Neurotrophic Factor
BSA	Bovine Serum Albumin
CEST	Chemical Exchange Saturation Transfer
CLN	Cervical Lymph Node
CT	Computed Tomography
CYP450	Cytochrome P450
DAMPS	Damage Associated Molecular Patterns
DEM	Diethyl Maleate
DFO	Desferrioxamine
DHAP	Dihydroxyacetone Phosphate
DIC	Differential Interference Contrast
DMEM	Dulbecco's Modified Eagle Medium
ECM	Extra Cellular Matrix
EEM	Excitation Emission Matrices
EI	Electron Impact
END.G	Endonuclease G
ETHD-1	Ethidium Homodimer-1

FASTMAP	Fast Maximum *A Posterioiri*
FBS	Fetal Bovine Serum
FCC	Flash Column Chromatography
FOV	Field Of View
GC-MS	Gas Chromatography Mass Spectrometry
GFAP	Glial Fibrillary Acid Protein
GI	Gastro-Intestinal
GLUT	Glucose Transporter
GSH	Glutathione
GST	Glutathione-*S*-Transferase
H&E	Hematoxylin And Eosin
HDAC3	Histone Deacetylase 3
HEV	High Endothelial Venule
HIF	Hypoxia Inducible Factor
ILN	Inguinal Lymph Node
IPSC	Induced Pluripotent Stem Cell
KHK	Ketohexokinase
λ_{em}	Emission Wavelength
λ_{ex}	Excitation Wavelength
LOX	Lysyl Oxidase
LPS	Lipopolysaccharide
MBP	Multi-Bandpass Filter
MDA	Malondialdehyde
MI	Myocardial Infarction
MIP	Maximum Intensity Projection
MRI	Magnetic Resonance Imaging
MS	Mass Spectrometry
MTBI	Mild Traumatic Brain Injury
NAC	*N*-Acetylcysteine
NAD+/NADH	Nicotinamide Adenine Dinucleotide
NADPH	Nicotinamide Adenine Dinucleotide Phosphate
NAPQI	*N*-Acetyl-P-Benzoquinone
NASH	Non-Alcoholic Steatohepatitis
NFKB	Nuclear Factor Kappa B

NK	Natural Killer
NSS	Neurological Severity Score
PAMP	Pathogen Associated Molecular Pattern
PAOX	Polyamine Oxidase
PDXK	Pyridoxal Kinase
PET	Positron Emission Tomography
PFK	Phosphofructokinase
PL	Pyridoxine
PLO	Poly-L-Ornithine
PLP	Pyridoxal-5'-Phosphate
PN	Pyridoxal
PPE	Personal Protective Equipment
ProxyNA$_3$	5-propargyloxy-N-aminoanthranilic acid
PRR	Pattern Recognition Receptor
PSR	Picrosirius Red
RF	Radiofrequency
ROS	Reactive Oxygen Species
SEM	Scanning Electron Microscopy
SMOX	Spermine Oxidase
SOD	Superoxide Dismutase
SSI	Site Specific Immunomodulator
TAC	Time *vs.* Activity Curve
TBI	Traumatic Brain Injury
TLC	Thin Layer Chromatography
TLR4	Toll-Like Receptor 4
TNFA	Tumour Necrosis Factor alpha
UC	Ulcerative colitis
UTM	Universal Testing Machine
WT	Wild Type

Chapter 1: Introduction

1.1. Endogenous sources of aldehydes

Aldehydes are highly reactive intermediate or final products of many biochemical, physiological, and pharmacological mechanisms, including the metabolism of amino acids, lipids, carbohydrates, vitamins, steroids, and biogenic amines. Numerous environmental agents and drugs undergo biotransformations resulting in endogenous production of aldehydes[1]. The production and clearance of endogenous aldehydes are controlled through tightly regulated mechanisms, and dysregulation of these systems leads to the buildup of structurally diverse aldehydes in cells and tissues, which can have toxic effects leading to the propagation of many diseases, underlying the aldehydic load hypothesis[2,3]. As aldehydes are highly reactive electrophiles, they can interact with thiol and amino groups of phospholipids, proteins, and DNA, forming adducts and are therefore cytotoxic, mutagenic, or carcinogenic[4]. The detoxification of aldehydes proceeds through numerous enzymatic and non-enzymatic reactions. The major enzymatic pathways include oxidation by aldehyde dehydrogenases (ALDHs)[5], reduction by aldo-keto reductases, and conjugation with glutathione (GSH)[6]. Non-enzymatic conjugation with nucleophiles such as glutathione and carnosine also occur. Other means of aldehyde detoxification include alcohol dehydrogenase (ADH), present largely in the liver, as the enzymatic conversion of alcohol to aldehyde by ADH is reversible. However, this reaction proceeds strongly toward acetaldehyde *in vivo* due to the activity of ALDH2[7]. Bioconversion of aldehydes by glutathione S-transferase A4 (GST-A4) to form aldehyde-glutathione adducts is also possible[8]. This is the primary enzymatic method for lipid aldehyde detoxification[9]. The rate of detoxification of aldehydes depends on the local availability of these cellular detoxifying and conjugating systems (for example, cellular GSH and GST concentrations), and the ability of the cell to degrade the modified proteins/lipids[10].

1.1.1 Oxidative Stress

Oxidative stress occurs when there is an imbalance between the accumulation of reactive oxygen species (ROS) and the ability to eliminate them with antioxidant defense systems, resulting in excessive, damaging ROS concentrations[11]. ROS are derived from the O_2 molecule's ability to accept electrons, forming unstable

molecules including superoxide ($O_2^{-\bullet}$), hydrogen peroxide (H_2O_2), hydroxyl radical $OH^{\bullet}$, and singlet oxygen ($^1O_2$) [12]. ROS are primarily produced in the mitochondria, plasma membrane, endoplasmic reticulum, and peroxisomes[13] *via* enzymatic reactions and/or autooxidation. Physiological levels of ROS are generated as natural biproducts of metabolism, acting as cell signaling agents and maintaining homeostasis[14]. For example, mitochondrial respiration is a major source of $O_2^{-\bullet}$ and H_2O_2[15]. The folding of proteins and formation of disulfide bonds form ROS in the endoplasmic reticulum. Enzymes including nicotinamide adenine dinucleotide phosphate (NADPH) oxidases, xanthine oxidase, and nitric acid oxidase all form ROS[16]. However, when ROS are produced in excess and when antioxidant systems are overwhelmed, oxidative stress occurs, which leads to the formation of reactive aldehydes.

A major source of endogenous aldehydes is lipid peroxidation, which is implicated in the pathogenesis of many diseases[17] (Fig.1.1). Lipid peroxidation alone contributes to a wide range of various aldehydes including alkenals, hydroxyalkenals, and dialdehydes[18]. Lipid peroxidation is a three-step process where oxidants (free radicals or nonradical species) attack lipids containing carbon-carbon double bonds[19]. Free radical-mediated lipid peroxidation initiates with a single free radical, usually by a hydroxyl radical ($HO^{\bullet}$) or hydroperoxyl ($HO^{\bullet}_2$), that oxidizes a lipid (e.g., glycolipids, phospholipids, and cholesterol), initiating a chain reaction that oxidizes more lipids. The chain reaction starts with the abstraction of hydrogen from a polyunsaturated fatty acid, producing a carbon-centered lipid radical. Then, the addition of oxygen to the radical forms a lipid peroxyl radical. Lipid peroxyl radicals can abstract hydrogen from surrounding lipids, propagating the reaction. The final step is termination where an antioxidant donates a hydrogen atom to the lipid peroxyl radical forming a nonradical product, or the substrate is consumed. In response to membrane lipid peroxidation, cells may initiate repair mechanisms, or induce cell death, leading to molecular cell damage.

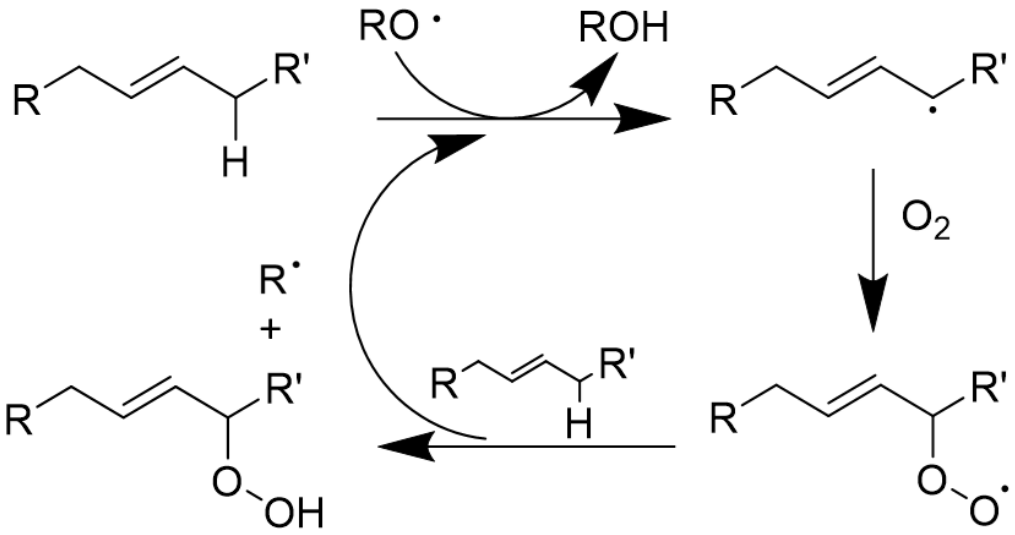

Figure 1.1. Mechanism of lipid peroxidation. Lipid peroxidation is initiated when hydrogen is abstracted from an unsaturated lipid by an oxidant (e.g. a free radical), producing a lipid radical. The addition of O_2 creates a lipid peroxyl radical, an oxidant that can propagate the reaction with surrounding lipids.

The aldehydes produced from lipid peroxidation include malondialdehyde (MDA), 4-hydroxynonenal (4HNE), acrolein, 4-oxo-2-nonenal, glyoxal, isolevuglandin, propanal, and hexanal[20-22]. MDA appears to be the most mutagenic product of lipid peroxidation and is one of the most popular clinical biomarkers of oxidative stress[23]. 4HNE is viewed as the most cyto- and genotoxic product of lipid peroxidation[24,25]. 4-hydroxyalkenals are produced in large amounts and have been described as second messengers of free radicals[4]. 4HNE inhibits coupled respiration in mitochondria and carbonylates mitochondrial proteins[26]. The toxicity of these aldehydes is due to their ability to propagate oxidative stress, form adducts with macromolecules, and act as signaling molecules involved in the regulation of transcription factors for cell proliferation/differentiation, cell survival, autophagy, senescence, apoptosis, and necrosis (adducts)[20]. As aldehydes are amphiphilic, they are able to diffuse passively across membranes and can therefore covalently modify macromolecules far from their site of origin[27].

The accumulation of lipid peroxidation products cause tissue and cellular dysfunction, playing a key role in aging[28] and most age-[29] and oxidative stress-related diseases. Classically, these include

neurodegenerative disease[30,31], metabolic syndrome[32], diabetes[33], and atherosclerosis[34,35]. Furthermore, evidence has pointed toward lipid peroxidation products contributing to fetal vascular dysfunction[36-38], renal disease[39], hepatic diseases[40], and cancer[41,42].

Proteins are also susceptible to oxidative stress. Amino acid residues of proteins are susceptible to oxidation by ROS, which usually results in aldehyde production[43]. Furthermore, aldehydes from any source, including lipid peroxidation products, can form adducts primarily at lysine, histidine, and cysteine residues, which cause protein dysfunction and may tag them for destruction[44]. Aldehyde-protein adducts have been implicated in a wide range of pathological conditions, in particular neurodegenerative diseases (including Alzheimer's disease, Parkinson disease, amyotrophic lateral sclerosis, Huntington disease, and down syndrome), atherosclerosis, and autoimmune diseases (Sjogren's syndrome, and systemic lupus erythematosus)[45].

Finally, autoxidation of carbohydrates is also a contributor to oxidative stress and aldehydic load. Glyoxal, a dialdehyde, is formed from glyceraldehyde *via* glycoaldehyde autoxidation, an intermediary metabolite of glyceraldehyde, fructose, and sorbitol metabolism[1]. Hydroxypyruvaldehyde, along with superoxide and H_2O_2, are formed from the autoxidation of glyceraldehyde and dihydroxyacetone. Methylglyoxal is also produced during the glycolytic metabolism of glucose from intermediates glyceradehyde-3-phosphate and dihydroxyacetone phosphate (DHAP). Glyoxal and methylglyoxal are potent glycating agents of proteins, nucleotides, and phospholipids forming advanced glycation endproducts (AGEs)[46], which have been implicated in the pathogenesis of many neurodegenerative and cardiovascular diseases[47-49]

1.1.2. Immune Response

Importantly, the inflammatory response of the immune system contributes a significant amount of oxidative products that lead to production of reactive aldehydes. Phagocytic immune cells including neutrophils, monocytes and macrophages produce an oxidative burst to kill invading bacteria, viruses, or tumorigenic cells[50] (Fig. 1.2). These cells possess NADPH oxidase, which catalyzes the reduction of O_2 to form $O_2^{-\bullet}$[51]. Superoxide dismutase (SOD) catalyzes the conversion of the highly reactive $O_2^{-\bullet}$ radical to O_2 and H_2O_2.

During phagocytosis, myeloperoxidase is released from the cytoplasmic granules of neutrophils and monocytes, which reacts with H_2O_2 to produce hypochlorous acid and other oxidative agents including chlorine, chloramines, hydroxyl radicals, singlet oxygen, and ozone[52]. While this oxidative burst plays an important role in the innate immune system's ability to kill invading pathogens, myeloperoxidase and ROS produced by this mechanism can be released to the outside of the cell, contributing to inflammatory damage of the host tissue[53].This reaction generates many reactive oxygen species which propagate autoxidation, and in turn generates α-hydroxy and α, β-unsaturated aldehydes in high yield[54-56]. Dysregulation of the myeloperoxidase-H_2O_2-chloride system has been associated with carcinogenesis, renal injury, lung injury, atherosclerosis, multiple sclerosis, Alzheimer's disease, and Parkinson's disease[52].

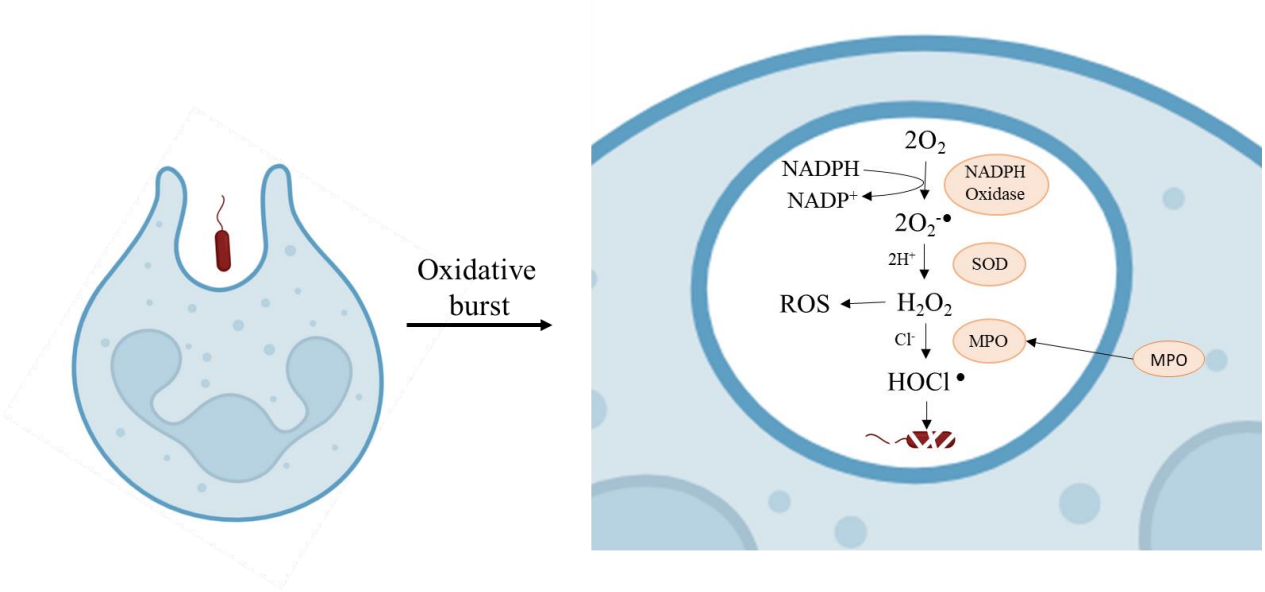

Figure 1.2. Oxidative burst mechanism of a phagocytic cell. This myeloperoxidase-H_2O_2-chloride system kills the engulfed pathogen, but also releases ROS outside of the cell, damaging the host tissue.

Again, due to the amphiphilic nature of aldehydes, including those produced from inflammatory processes, they can react with adjacent cells, propagating the pathology. In this case, plasma membrane proteins are the first targets for aldehyde-adduct formation[45].

1.1.3. Polyamine Catabolism

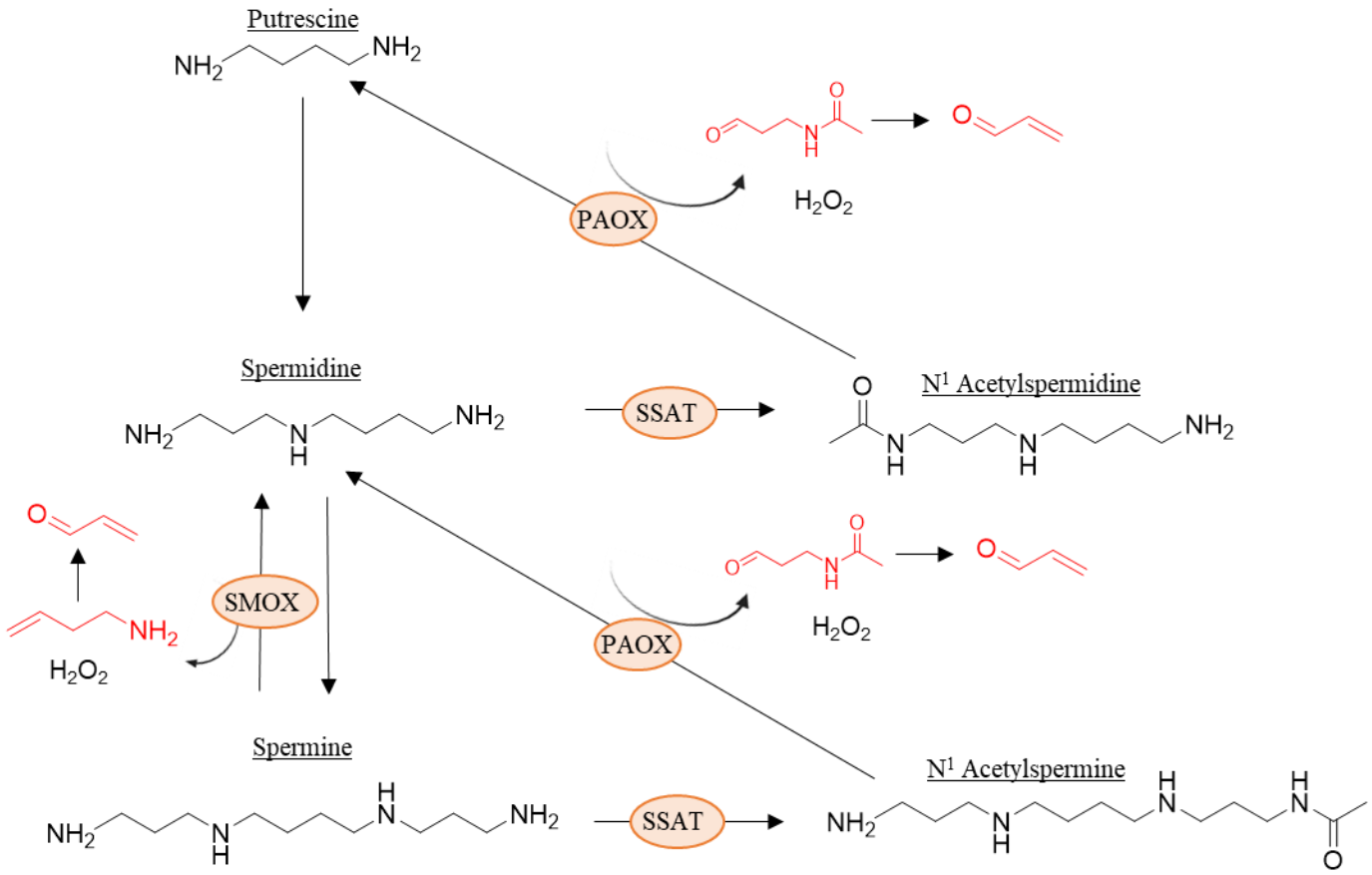

Figure 1.3. Catabolism of polyamines enzymatically produces aldehyde and ROS biproducts. Spermidine/spermine-N^1-acetyltransferase (SSAT) catalyzes the acetylation of spermidine and spermine. N^1 acetylpolyamine oxidase (PAOX) converts N^1 acetylspermine back to spermidine, and N^1 acetylspermidine back to putrescine, forming 3-acetoaminopropanal and H_2O_2 as bioproducts. The conversion of spermine to spermidine by spermine oxidase also produces 3-aminopropanal and H_2O_2 as biproducts. Both aldehyde biproducts are non-enzymatically converted to acrolein.

Polyamines are organic cations ubiquitous to all mammalian cells and are essential for cell growth and survival[57]. Putrescine, spermidine, and spermine are crucial for ion channel regulation, chromatin structure maintenance, DNA replication, transcription, and translation[57]. Polyamines also contribute to the oxidative

status of a cell, as they are free radical scavengers, but their catabolism also produces ROS and aldehydes as biproducts. Polyamine catabolism has two interconnected pathways, both of which result in the formation of H_2O_2 and aldehydes (Fig. 1.3). First, spermidine and spermine are acetylated by SSAT (spermidine/spermine-N^1-acetyltransferase). The acetylated polyamines can then be oxidized back to putrescine or spermidine by peroxisomal N_1-acetylpolyamine oxidase (PAOX), producing H_2O_2 and 3-acetoamidopropanal as biproducts. Second, spermine can be oxidized by spermine oxidase (SMOX) to form spermidine, producing H_2O_2 and 3-aminopropanal as biproducts. 3-aminopropanal spontaneously converts into acrolein, which is highly reactive and toxic[58]. SMOX is induced by inflammatory cytokines[59], and several researchers have suggested it may be the mechanism linking inflammation to oncogenesis, as unrepaired DNA damage from ROS and aldehyde biproducts of polyamine catabolism can cause mutations contributing to carcinogensis[60-62].

Polyamines are present at high concentration in the mammalian brain compared to other tissues[63]. Furthermore, the central nervous system has elevated levels of polyunsaturated lipids, contains large pools of redox-active transition metal ions[64], and a poor antioxidative defense system, making it very sensitive to oxidative mechanisms like polyamine catabolism, autoxidation, and lipid peroxidation[65]. Polyamine catabolism is induced during stroke due to the release of free polyamines from damaged RNA[66,67]. Furthermore, in this type of injury, acrolein is responsible for neuronal damage rather than ROS, indicating reactive aldehydes produced from polyamine catabolism may be more damaging to cells compared to ROS in the brain.

Polyamine catabolism plays an important role in the response to stressful stimuli, and its dysfunction contributes to the pathology of many conditions including cancer[61,68,69], psychiatric conditions[70,71], ischemia reperfusion injury[72,73], stroke[66], infection by helicobacter pylori[74], and traumatic brain injury (TBI)[75]. The pathophysiology of TBI is described further in chapter 5 of this thesis.

1.2. Pathological outcomes of oxidative stress: are aldehydes propagators of disease or consequential?

Aldehydes are not only products of these damaging pathways but are also propagators of oxidative stress and inflammation. For example, exposure to aldehydes elicits an inflammatory response (increase in macrophages, neutrophils, and cytokines)[76]. Excessive consumption of alcohol (which is metabolized to acetaldehyde by alcohol dehydrogenase), induces oxidative stress, inflammation in neuronal cells, and overall cognitive decline[77]. However, there exists a baseline physiological level of endogenous aldehydes in organisms, as they are biproducts of normal metabolic processes. At physiological levels, aldehydes are metabolized by various pathways (ALDHs, ALD, GST), and do not elicit any toxicity. At low levels, they initiate cell signaling in response to stress and initiate antioxidant systems, leading to cell survival. It is only when aldehydes are produced beyond this threshold that cell death is initiated[78]. The major challenge with the study of endogenous aldehydes is it is often difficult to determine whether they are involved in the initiation and propagation of disease or are a consequence of it. The tools developed in this thesis allow access to imaging of total aldehydic load *in vivo*, toward the better understanding of the physiological roles of aldehydes.

1.3. Models of endogenous aldehyde production

1.3.1. Mouse model of inflammation

A mouse model of systemic inflammation is frequently used in pre-clinical research to better understand the pathophysiology of inflammation, and to develop new drugs candidates. In this thesis, administration of exogenous endotoxin bacterial cell wall lipopolysaccharide (LPS) is used to induce systemic and neuroinflammation in mice. Shortly after administration of LPS, pro-inflammatory cytokines are released into circulation[79]. This pro-inflammatory response leads to increased generation of ROS and lipid peroxidation, and inflammatory cell infiltration[80]. These mechanisms lead to the increased production of aldehydes, as discussed above.

LPS treatment is also one of the most widely used animal models of peripherally induced neuroinflammation and neurodegeneration. Neuroinflammation plays an important role in the progression of neurodegenerative diseases like Alzheimer's disease, Parkinson's disease, and other neurodegenerative diseases[81-84]. This model induces activation of microglia, astrogliosis, pro-inflammatory cytokine release in the brain, leading to synaptic failure and cognitive dysfunction[85].

1.3.2. Aldehydes in fibrosis

Aldehydes are also formed during active fibrosis. The oxidation of collagen by lysyl oxidase (LOX) enzymes convert extracellular matrix lysine residues to allysine. Allysine covalently crosslinks collagen proteins by condensation reactions, stabilizing the fibrotic tissue[86].

This mechanism, along with the recent advances of molecular imaging of allysine, is reviewed in more detail in chapter 2 of this thesis.

1.3.3. Aldehyde formation in a model of drug toxicity

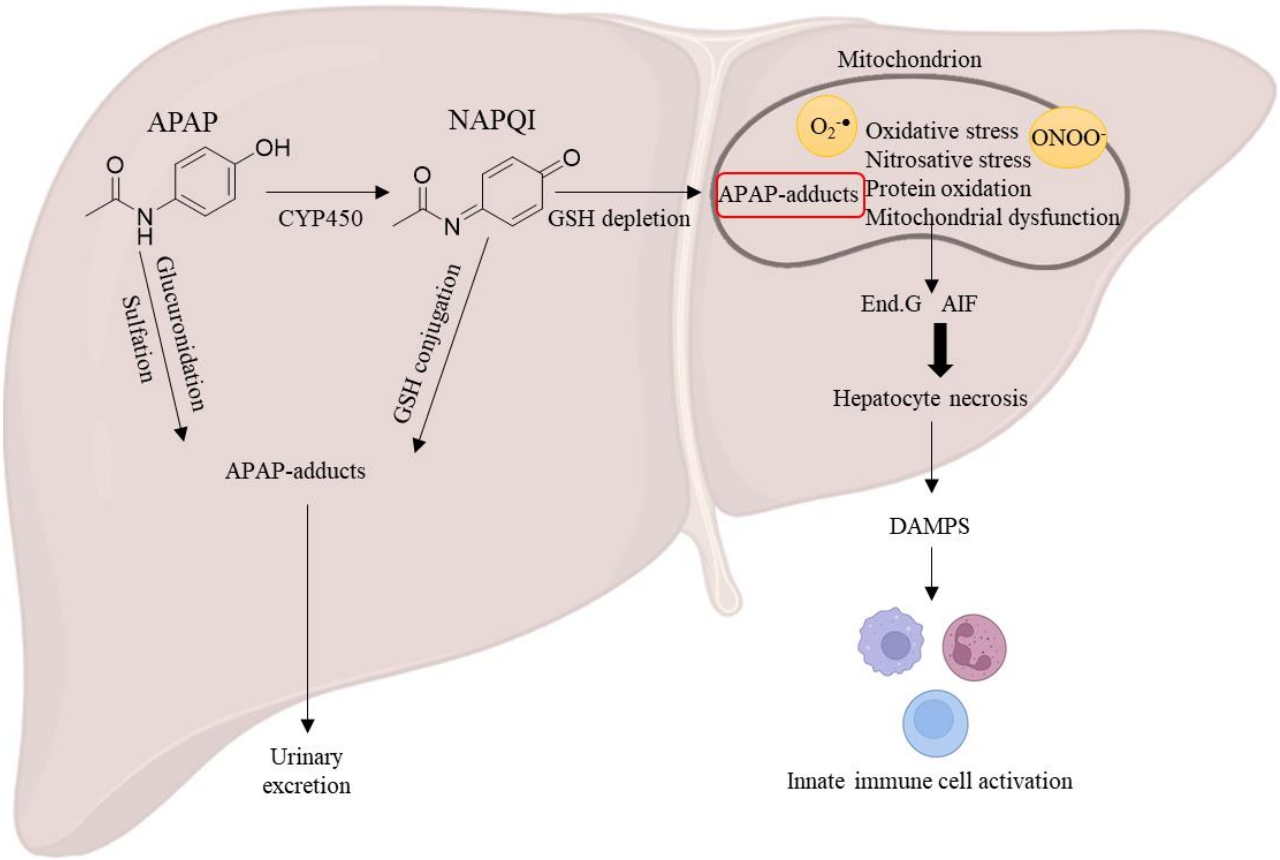

Figure 1.4. Metabolic action of acetaminophen (APAP)-induced hepatocyte necrosis and inflammatory response. At therapeutic doses, APAP is conjugated with glucuronide or sulfate and eliminated through the kidneys. Some APAP is metabolized by the action of cytochrome P450 (CYP450) into a reactive intermediate, *N*-acetyl-*p*-benzoquinone (NAPQI). NAPQI is then conjugated by glutathione (GSH) in the liver to form non-toxic cysteine conjugates and can be excreted. When APAP is consumed at high doses, GSH stores are rapidly depleted, leaving free reactive NAPQI to form mitochondrial APAP-protein adducts. These protein adducts in turn compromise respiration, leading to formation of free radicals. This oxidative stress leads to the oxidation of proteins and mitochondrial dysfunction resulting in a signaling cascade which further increases mitochondrial oxidative stress. Mitochondrial intermembrane proteins including endonuclease G (End.G) and apoptosis-inducing factor (AIF) are then released, inducing

nuclear DNA fragmentation, and finally programmed necrosis. Hepatocyte necrosis triggers the release of damage-associated molecular patterns (DAMPS), which initiates a sterile inflammatory response.

N-acetyl-*p*-aminophenol (APAP), or acetaminophen, is a widely used analgesic and antipyretic drug. APAP overdose is the most common cause of acute liver failure in the United States[87,88]. When a therapeutic dose of APAP is consumed, the majority of the drug is conjugated into non-toxic products and proceeds through renal clearance (Fig. 1.4). A small component is enzymatically converted by cytochrome P450 into a highly reactive metabolite, N-acetyl-*p*-benzoquinone imine (NAPQI)[89]. This metabolite, when present in minor quantities, is rapidly complexed by GSH, resulting in its clearance. However, in the event of an overdose of APAP, cellular GSH is rapidly depleted resulting in high levels of reactive NAPQI. The free NAPQI forms protein-adducts with mitochondrial proteins[90-92] within 30 minutes of overdose[93], which leads to mitochondrial oxidative stress and dysfunction, generation of ROS, and eventually hepatocyte necrosis. A subsequent sterile inflammatory response occurs[94], triggered by damage-associated molecular patterns (DAMPS), including the release of pro-inflammatory cytokines and activation of immune cells[95], ultimately producing more ROS. Currently, there exists one FDA-approved clinical intervention for an overdose of APAP, *N*-acetylcysteine (NAC), which facilitates scavenging of NAPQI and supports mitochondrial metabolism[96], but this antidote is limited by its narrow therapeutic window. This major drawback of the sole treatment for APAP overdose necessitates further investigation of APAP-induced hepatotoxicity.

A better understanding of the inflammatory mechanisms of APAP-induced hepatotoxicity is needed[97], and could be uncovered through *in vivo* molecular imaging of aldehydes. Wimborne *et al*. recently investigated the role of aldehydes in APAP toxicity in mice[98]. They found that 4-HNE protein adducts increased from 0.1% in control tissue to 7% two hours after APAP overdose. When ALDH2 was activated with an agonist Alda-1[99], the adducts were reduced to 1%. Six hours after treatment, 62% of tissue had polarized mitochondria, which was reduced to 33.5% with Alda-1. This study indicates that aldehydes mediate APAP toxicity, and that acceleration of ALDH2-mediated aldehyde degradation decreases APAP-induced liver injury.

1.4. Comparison of imaging modalities used in this thesis:

In this thesis, techniques of both anatomical imaging and molecular imaging are employed. Anatomical imaging is used to visualize the structure and morphology of tissues or organs within the body. This type of imaging requires high spatial resolution and is often used in conjunction with molecular imaging in order to provide anatomical reference. The anatomical imaging modalities used in this thesis are computed tomography (CT), and magnetic resonance imaging (MRI). Anatomical imaging has been instrumental in medicine since its advent, however, the development of novel molecular imaging techniques from advances in molecular and cell biology have drastically improved our understanding of complex biological phenomena. Molecular imaging is a non-invasive technique to visualize biochemical processes within living organisms,[100] is used clinically for diagnostics and therapy monitoring, and is widely used for pre-clinical research of many biological processes. Molecular imaging techniques often involve the use of targeted, specific imaging agents, such as radiotracers, fluorescent probes, and contrast agents, which selectively bind to a target of interest. These agents are detected with specialized cameras or detectors enabling positron emission tomography (PET), molecular MRI, and fluorescence microscopy, and provide researchers and clinicians with information on cellular function, metabolic activity, and molecular mechanisms in the body.

When developing a molecular imaging agent, choosing the right modality is crucial in the success of the probe. The factors to consider include required spatial resolution, temporal resolution, sensitivity, safety, depth of penetration, and whether this agent will be translated to the clinic (Table 1.1). Spatial resolution, often dictated by the size of pixel (or voxel) of an image, determines the quality of the image, and describes how small an object should be for detection. CT and MRI have ultra-high spatial resolution and are therefore excellent for anatomical imaging. Temporal resolution refers to the time needed to complete imaging. If dynamic imaging is required, temporal resolution increases. Sensitivity refers to the minimum concentration of probe required for detection, which depends on binding affinity of the probe and concentration of the target. PET has the highest sensitivity among molecular imaging modalities and is

therefore ideal for molecular targets expressed in low concentrations. Safety is important to consider, especially when the goal is clinical translation. If the toxicity of the probe is low, and therefore can be used safely in animal models, we next consider safety of the imaging modality (i.e. presence of ionizing radiation). CT and PET both expose imaging subjects to ionizing radiation. Depth of penetration is important to consider and is the main reason for the limited application of optical fluorescence in the clinic, as its depth of penetration is low, meaning its uses are limited to surface-level imaging. PET, CT, and MRI all have limitless depth of penetration.

Table 1.1. Overview of the molecular imaging modalities used in this thesis.

Modality	Use	Spatial resolution	Temporal resolution	Sensitivity	Safety	Depth of penetration	Clinical applicability
Positron emission tomography (PET)	Molecular	1-2mm (preclinical) 5-7mm (clinical)	Minutes	10^{-11} to 10^{-12} M	Ionizing radiation	Limitless	Yes
Computed Tomography (CT)	Anatomical	50-200µm (preclinical) 0.5-1mm (clinical)	Minutes	N/A	Ionizing radiation	Limitless	Yes
Magnetic Resonance Imaging (MRI)	Anatomical and Molecular	25-100µm (preclinical) ~1mm (clinical)	Minutes to hours	10^{-3} to 10^{-5} M	Good	Limitless	Yes
Optical fluorescence imaging	Molecular	2-3mm	Seconds to minutes	10^{-9} to 10^{-12}M	N/A	<1cm	Sometimes

*information in this table adapted from James and Gambhir, 2012[101]

1.4.1. Positron Emission Tomography (PET)

PET is a radionuclide imaging technique with high sensitivity, enabling whole-body imaging of molecular targets using nanomolar concentration of imaging agent. A radiotracer, targeted to a specific molecule or metabolic process, is injected into the subject. The radiotracer travels to the targeted molecule/process, and unused/unbound probe is cleared. Radioactivity at the sites of accumulation is detected by the PET camera, which forms an image based on concentration of the probe within the body. The radiotracer contains a radioactive isotope (e.g., [^{18}F], [^{89}Zr]), which emits a positron, which then travels a short distance before colliding with an electron from surrounding tissue. This is called an annihilation event, which results in the production of two gamma ray photons that travel 180° from each other, subsequently and coincidentally detected by the PET detector. These signals are back-calculated to the location of annihilation, and are reconstructed into tomographic images, reflecting the biodistribution of the radiotracer in the subject, thus providing information on the molecular or biochemical event the radiotracer was targeting[102]. The largest

benefit of PET is its excellent sensitivity, as it provides quantitative data. Due to its limited spatial resolution, PET is usually paired with another modality for anatomical imaging such as PET-MRI or PET-CT.

In this thesis, PET is used as the primary imaging modality for *in vivo* mapping of aldehydes (chapters 4 and 7), fructose metabolism (chapter 6), and long-term tracing of site-specific immunomodulators (chapter 8).

1.4.2. Computed Tomography (CT)

CT emits a narrow beam of x-rays while rotating around the subject, creating a three-dimensional image based on the different levels of x-ray attenuation of tissues of the body. Tissues that strongly absorb x-rays, like bone, result in high contrast. Conversely, tissue areas that x-rays easily pass through like air and fat, appear dark on the image. The result is a rapid high-contrast three-dimensional image with detailed morphological information and high spatial and temporal resolution.

CT is used in combination with PET to provide anatomical reference in chapter 6 of this thesis. Chapter 7 details the methodology for PET/CT imaging of multisubject small animals.

1.4.3. Magnetic Resonance Imaging (MRI)

MRI is more versatile than CT, as it can be used for both anatomical and molecular imaging. When a subject is placed into an MRI, which is composed of a large magnet, radiofrequency (RF) coils, and gradient coils, certain atomic nuclei with magnetic properties (most often ^{1}H) act as magnetic dipoles and align with the magnetic field. The nuclei align either parallel or antiparallel to the magnetic field, resulting in a small net difference in polarization, which generates an MR signal. Anatomical images are formed from the hydrogen signal in water in tissues. Pulse sequences, generated by the RF coils tip the magnetic dipoles out of alignment, and their relaxation back to equilibrium (longitudinal [T1], transverse [T2]) creates contrast between different tissues due to the differences in relaxation times. Pulse sequences are manipulated based on the tissue being imaged to increase contrast, including sequences that reveal physiological information.

This type of MR imaging is non-specific, as it does not target a specific substrate. With the use of molecular imaging contrast agents, more information can be revealed using MRI. Targeted Gd-based agents, for example, are capable of sensing metabolite levels, alterations in tissue pH, redox state, and oxygenation[103].

CEST (chemical exchange saturation transfer) MRI is a technique whereby a targeted probe containing an exchangeable ^{1}H temporarily saturates (i.e. net zero magnetization) a tissue by exchanging its proton with surrounding water molecules proportional to the concentration of the target, resulting in reduced or no image signal[104]. The benefit of CEST is not only to allow for specifically targeted molecular probes to be used, but sensitivity is amplified exponentially as ^{1}H transfer is continuous until a steady state is reached.

MRI is used in chapter 5 of this thesis for molecular imaging of aldehydes in a mouse model of concussion and is used in chapters 5 and 8 for anatomical imaging. Furthermore, the development of MRI probes for molecular imaging of aldehydes is reviewed in Chapter 2.

1.4.4. Optical Fluorescence Imaging (confocal microscopy)

Fluorescence microscopy involves using fluorescently tagged reporters or molecules (probes) to visualize molecular events or targets in living cells or *ex vivo* tissues in real time. This imaging modality can be highly sensitive, however, the use of low-energy photons limits the depth of penetration, rendering this technique virtually useless for deep tissues in human subjects. Depth of penetration can be gained by using specialized microscopes (e.g. confocal and two photon microscopy) and using near-infrared fluorescence to decrease scattering, attenuation, and autofluorescence. Its utility, at least in this thesis, lies in the ability to image biochemical processes in live cultured cells. When the fluorescent probe is added to the sample, application of an external light source (excitation) is absorbed by the fluorophore, and triggers an emission of light that is lower in energy (longer wavelength), revealing the location of probe accumulation. To decrease background signal, the probe needs sufficient time to bind to its target so the remainder can be cleared/washed, or an "activatable" probe is used, where the probe "turns on" when bound to its target, eliminating the need for washing. This type of molecular imaging uses activity-based sensing, which uses molecular reactivity for selective detection (i.e. fluorescence turn on) of an analyte[105].

In fluorescence microscopy, light passes through the entire field of view of the sample, and any emission from fluorescent molecules outside of the focal plane is also detected, adding blur to the image and reducing resolution. Confocal microscopes emit light from a laser that is reflected from a mirror to the objective lens which focuses the beam on a single point on the sample. A pinhole rejects out-of-focus light , allowing for higher resolution images in thicker samples[106]. The image is constructed as the illumination point moves over the sample, scanning an optical section (slice), with the ability to create a 3D image by collecting z-stacks. Overall, fluorescence microscopy provides a useful tool for evaluation of new imaging agents and understanding of molecular processes at the cellular and sub-cellular level.

In chapter 3 of this thesis, a fluorescent aldehyde-binding activity-based probe is described and used to image aldehydes in live cells in chapters 3 and 5.

1.5. Metabolism of fructose

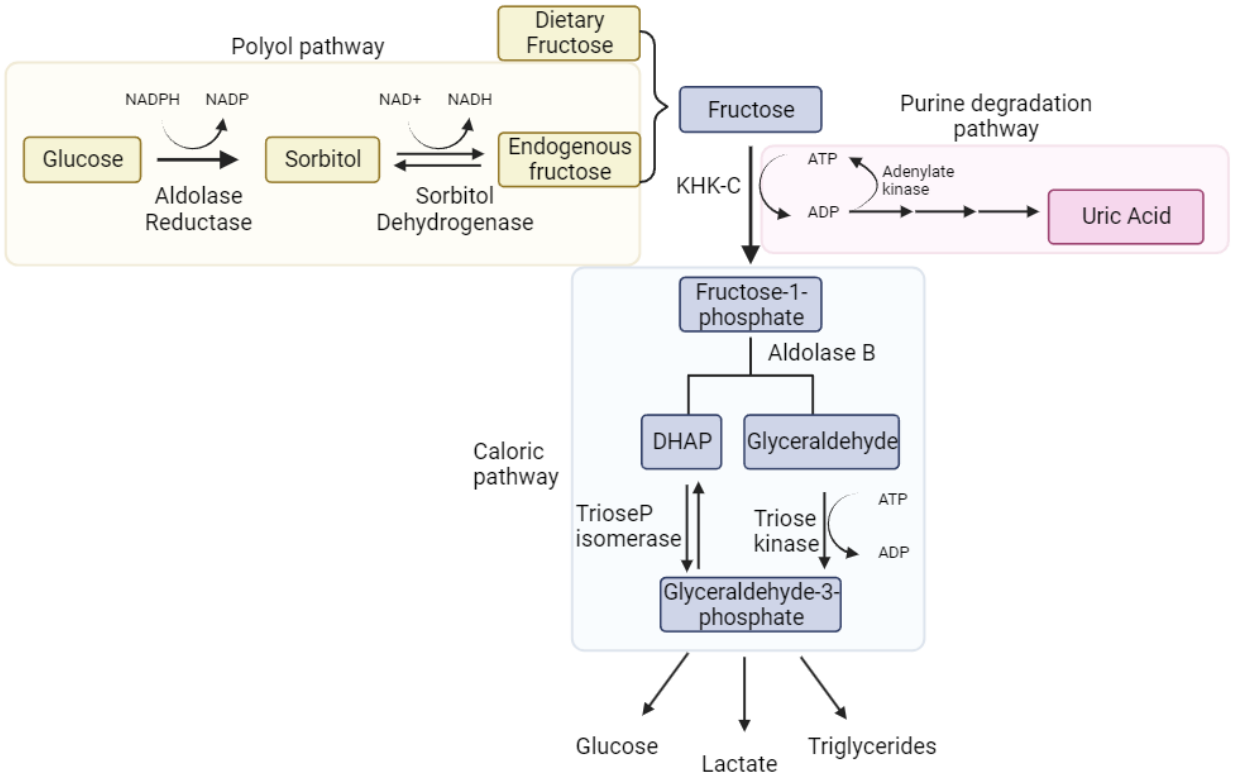

Figure 1.5. The metabolic pathways of fructose from glucose or dietary consumption. The polyol pathway (yellow) is a two-step mechanism whereby glucose is converted to sorbitol by aldolase reductase, then to fructose by sorbitol dehydrogenase. This endogenous fructose or dietary fructose enters the fructolysis pathway where it is converted into fructose-1-phosphate by ketohexokinase C-isoform (KHK-C). This step consumes adenosine triphosphate (ATP), and proceeds *via* the purine degradation pathway to produce uric acid (red), and *via* the caloric pathway (blue). In the caloric pathway, aldolase B converts fructose-1-phosphate into dihydroxyacetone phosphate (DHAP) and glyceraldehyde, which are enzymatically converted to glyceraldehyde-3-phosphate. From there, the production of energy sources like glucose, lactate, and triglycerides are produced by different metabolic pathways.

The polyol or sorbitol pathway is a two-step mechanism which converts glucose into fructose (Fig. 1.5.). During normoglycemic conditions, the glycolytic pathway converts glucose into ATP for energy, and produces NADPH. Excess glucose can be stored as glycogen or fatty acids. Under conditions where

hexokinase is saturated[107], for example under persistent hyperglycemia, the polyol pathway is upregulated. During this process, glucose is converted to sorbitol by aldol reductase, utilizing NADPH to drive the reaction. The sorbitol is then converted into fructose by sorbitol dehydrogenase, requiring NAD+ to drive the reaction, leading to NADH production. Fructose is then transported from the gut to the liver by the portal vein for metabolism, where it is immediately converted into fructose-1-phosphate by KHK-C. It is then split into glyceraldehyde and DHAP by aldolase. Glyceraldehyde is converted to glyceraldehyde-3-phosphate, which, along with dihydroxyacetone, can proceed by various metabolic pathways to produce energy substrates like glucose, glycogen, lactate, and fatty acids[108]. Fructose metabolism however, unlike glucose metabolism, is "unregulated," as it bypasses the rate-limiting step of phosphofructokinase (PFK), allowing for *de novo* lipogenesis in the liver.

Under diabetic conditions, ~30% of glucose is metabolized *via* the polyol pathway[109]. It is believed that this pathway plays a role in end-stage diabetes, as some tissues including the retina, kidneys, and Schwann cells do not possess sorbitol dehydrogenase, which results in toxic accumulation of sorbitol. Along with the accumulation of sorbitol, the endogenous production of fructose and NADH have also been implicated in the pathogenesis of diabetes. The result of these products is retinopathy[110,111], nephropathy[112], and neuropathy[113]. In other tissues, this pathway leads to overproduction of fructose, which is metabolized by KHK-C, requiring ATP. A large load of fructose can deplete ATP, relieved by aldenylate kinase producing AMP, which is turned into uric acid, correlating with hyperuricemia and hypertension[114]. Fructose can also glycate proteins *via* the Maillard reaction, leading to protein dysfunction[115]. In fact, fructose is a more potent glycating agent than other sugars[116,117]. This is where fructose and its metabolites (methylglyoxal, glyoxal, deoxyglucosone) form adducts with amino groups in proteins, DNA, and lipids, resulting advanced glycation end products[115]. Furthermore, the utilization of NADPH in the first step of the polyol pathway leads to less cofactor available for GSH reductase, a critical enzyme needed for the maintenance of the intracellular pool of GSH, thereby impairing the cell's response to oxidative stress[118].

The polyol pathway therefore functions to metabolize glucose when the primary glycolytic pathway and the NAD+:NADH redox balance is overwhelmed[119]. Although this metabolic pathway may be necessary at times for cell survival, the excessive consumption of NADPH leads to uncontrolled production of ROS[120], and the depletion of intracellular ATP and subsequent generation of uric acid activates various signaling pathways, leading to a burst of oxidative stress, especially in the mitochondria[121].

In 2023, a new mechanism by which fructose promotes metabolic complications was discovered by Helsley *et al*[122]. They found that fructose increases KHK-C, which can then increase lipogenic proteins, and increase triglyceride accumulation. KHK-C increases global protein acetylation and decreases SIRT2, the major cytoplasmic deacetylase. This mechanism explains how fructose increases lipogenesis, and decreases fatty acid oxidation.

1.5.1. Fructolysis in cardiac disorders

While it is generally accepted that excess fructose consumption leads to metabolic syndrome[123], type 2 diabetes[114], and nonalcoholic fatty liver disease[123], recent attention has been brought to the role of fructose in the pathogenesis of cardiometabolic diseases and cardiovascular diseases[124,125]. A large study of over 88,000 women followed for 24 years revealed those who consumed ≥2 servings per day of sugar-sweetened beverages (predominately sweetened with high-fructose corn syrup in the US, accounting for the majority of total dietary fructose intake), had a significantly increased risk of coronary heart disease compared with infrequent consumers[126].

Conditions that lead to a reduction in O_2 available to tissue activate hypoxia-inducible factor 1α (HIF1α), a transcription factor responsible for the activation of target genes which produce proteins responsible for various cellular processes for cell survival[127]. An important study published in 2015 shows that myocardial hypoxia in human and mouse models of pathological cardiac hypertrophy activates fructolysis through HIF1α activation of SF3B1, by mediating the splice switching of KHK-A (low affinity for fructose) to KHK-C (high affinity for fructose)[128]. Activated cardiac fructolysis mediated by this SF3B1-KHK-C axis ensures a high glycolytic turnover. Furthermore, excessive fructose production *via* the polyol pathway in

the liver can lead to systemic circulation of fructose[123], which drives fructose and glucose uptake by cardiomyocytes, leading to cardiac hypertrophy[128]. The HIF1α-driven conversion of fructose carbon into lipids also drives the accumulation of lipids in cardiac hypertrophy as the fructose-1-phosphate product DHAP is used for the glycerol backbone in triglyceride synthesis[128]. Lipid accumulation in the heart is considered pathologic and is a key feature of the diabetic heart[129].

A later study investigated whether transcriptional responses related to fructose metabolism were also seen following myocardial infarction (MI)[130]. Ischemic cardiac tissue showed an increase in HIF1α abundance as well as an increase in a direct target of HIF1α, indicating it was transcriptionally active at 1- and 3-days post-MI. MI causes chronic stabilization of HIF1α in the heart, which supports pathologic cardiac hypertrophy and contractile dysfunction. Considering the SF3B1-KHK-C axis is driven by HIF1α activation, there exists a link between hypoxia-mediated anabolic growth and fructolysis in the heart.[131].

1.5.2. Fructolysis in neurological disorders

In the last few years, research has been focused on the ability of fructose metabolism to induce neuroinflammation[132-134]. Activation of pro-inflammatory mediators is seen in the brains of rats fed high fructose diet, including increased expression of pro-inflammatory cytokines interleukin (IL6) and IL1β[135], tumour necrosis factor alpha (TNFα)[133], and increase in glial fibrillary acidic protein (GFAP)[133], suggesting cerebral fructose metabolism induces local gliosis and inflammation, which cause neuronal injury. The astrogliosis and inflammation initiated by fructose metabolism are mediated by an increase in toll-like receptor 4(TLR4), myeloid differentiation factor 88, and Nuclear Factor kappa B (NFκB) espression[136]. Histone deacetylase 3 (HDAC3) overexpression is also seen, which prolongs the inflammatory response by regulating NFκB-dependent transcription[136]. The activation of the TLR4/NFκB pathway induces microglia activation in the hippocampus, resulting in reduction of neurogenesis[137]. Indicators of mitochondrial dysfunction leading to oxidative stress are seen in the hippocampus even after short periods of fructose consumption in rats[133,138]. Increases in lipid peroxidation and nitrotyrosine are also elevated suggesting oxidative damage to proteins and lipids occur in the brain in response to high fructose feeding[133,139]. In

response to long-term high-fructose supplementation, rat hippocampus and cerebral cortex show higher level of ROS, lipid peroxides, and carbonyls, and lower GSH compared to controls[140].

Recently, a link has been proposed between Alzheimer's disease and cerebral fructose metabolism[141]. Cerebral metabolic dysfunction is a feature of Alzheimer's disease and other forms of vascular dementia as evidenced by brain glucose hypometabolism seen in regions of the brain in early stages of disease by [^{18}F]FDG-PET[142,143]. Cerebral insulin resistance can be defined as a failure of brain cells to respond normally to insulin, resulting in synaptic, metabolic, and immune dysfunction[144]. In 2008, Stranahan *et al*. discovered that rats fed with a high-fat, high-glucose and 20% high fructose diet to promote insulin resistance had reduced hippocampal synaptic plasticity and impaired cognitive performance[145]. This study provided evidence that insulin resistance promoted by excess dietary fructose intake[146] may have a profound effect on the hippocampus, one of the main regions of the brain affected by Alzheimer's disease[147]. Therefore, dietary intake of fructose is associated with cognitive dysfunction[148], which has been shown in many animal models[135,139,149-151] and in humans[152,153] . Insulin resistance affects similar brain regions as does Alzheimer's disease, supporting the hypothesis that insulin resistance from chronically elevated insulin levels, may promote neurodegenerative diseases[154]. While type 2 diabetes is associated with insulin resistance and is a risk factor for neurodegenerative dementias, especially Alzheimer's disease, these diseases may also occur in the absence of these conditions. Therefore, it has been proposed that the unifying link between this cerebral metabolic dysfunction and Alzheimer's disease may be due to intracerebral fructose metabolism[141]. Other risk factors for Alzheimer's disease including high glycemic diets[123,155,156], high salt diets (resulting in hyperosmolarity)[157-159], TBI[139,160,161], alcohol consumption[162,163], aging[164], and genetics [151], are also activators of endogenous fructose metabolism *via* the polyol pathway. Further support for this hypothesis includes increased levels of intracerebral polyol pathway intermediates in patients with Alzheimer's diesease[165].

The hypothesis that fructose metabolism in the brain is a driver of Alzheimer's disease is supported by numerous pieces of evidence. First, we know that the human brain is capable of producing endogenous

fructose *via* the polyol pathway[156], and consumption of dietary fructose remains high[166], which can cause cerebral insulin resistance[148]. This metabolism of fructose induces local inflammation and oxidative stress[133], and leads to a depletion of energy. The protection from this oxidative stress in neurons, unlike in other cells, is to use glucose in the pentose phosphate pathway to generate reduced GSH, thereby consuming the bioenergetic stores of glucose, necessitating another source of energy[167]. Glucose hypometabolism can be seen by [^{18}F]FDG PET scans of brains affected by Alzheimer's disease. This oxidative stress results in neuronal dysfunction and apoptotic death[167].

Several studies have also indicated that fructose metabolism exacerbates the pathology of brain injury[139,168,169]. TBI pathology is associated with a persistent metabolic crisis in the brain[170], where the control of brain glycolysis is dysregulated[171]. Furthermore, metabolic dysfunction like diabetes and insulin resistance are predictors of negative outcomes including mortality in TBI patients[172,173]. Agrawal *et al*. propose that dietary fructose consumption aggravates the deleterious effects of TBI on cognitive function by disrupting metabolic pathways that regulate plasticity and cognitive function[139]. Fructose metabolism disrupts insulin signaling in the brain[125], as well as brain-derived neurotrophic factor (BDNF) signaling, which participates as a neuromodulator important for neuronal plasticity[174]. From here, the effects of TBI and fructose are compounded as they both inhibit pathways associated with energy metabolism, decreasing oxidative phosphorylation and bioenergetics, resulting in loss of cognitive function and lipid peroxidation of the plasma membrane, evidenced by increased ROS[139].

Shraddha *et al*. propose another deleterious fructose mechanism associated with TBI *via* the liver[169]. TBI triggers a quick hepatic response, whereby chemokines are produced in the liver to respond to the trauma by regulating the central nervous system's (CNS) inflammatory response[175]. The authors make the connection between the liver and TBI since the liver is the primary site of fructose metabolism[176], leading to the hypothesis that the liver is the site for convergence of TBI and fructose metabolism on TBI pathology[169]. It is important to note however, that the primary site of fructose clearance is the small intestine, and fructose reaches the liver when intestinal KHK-C is saturated[177]. They report that fructose consumption

reduces insulin receptor signaling following TBI, more than TBI alone. Fructose consumption also potentiates the increase in hepatic TLR4 post-TBI, which exacerbates inflammatory processes. Finally, they show that hepatic lipid accumulation, under hormonal control, is higher post-TBI after fructose exposure, which is another piece of evidence indicating that metabolic perturbation induced by fructose metabolism potentiates the effects of TBI on systemic metabolism, thereby worsening the outcome of the injury.

More recently, Perez-Corredor *et al*. induced obesity in rats with a high fructose diet and subjected them to ischemic brain injury, followed by neurological and histological testing[168]. The fructose-consuming rats had worse neurological performance post-injury and exhibited neuronal loss. Cellular responses in this group included an increase in pro-inflammatory cytokine IL1β, microglial activation, loss of neuronal nuclear protein, decreased BDNF, destabilization of microtubules (microtubule-associated protein 2), and increased hyperphosphorylation of tau, all resulting in decreased plasticity and increased tauopathy. This study once again shows mortality and morbidity are increased after brain injury in fructose-fed animal models[168]. These studies suggest fructose metabolism reduces neural resilience and exacerbates pathophysiology following brain injury and may be a predictor of outcome.

1.5.3. Fructose as an oncologic driver

Fructose has also been implicated in oncogenesis and tumour growth, as the potential link between obesity and metabolic syndrome[178,179] with some types of cancer[180-182]. It has been estimated that only 45% of primary tumours are detectable by FDG-PET[183], and glucose transporter 1 (GLUT1) is only detected in 87 of 154 human malignant tumours[184], suggesting there may exist an alternate source of energy for oncogenesis. In 2010, Liu *et al*. proposed fructose may be an alternative substrate for pancreatic cancer cell proliferation[185]. In this study, the researchers were able to proliferate numerous lines of pancreatic cancer cells in fructose-containing media, just as they proliferate in traditional glucose-containing media. They found that fructose had a low contribution to glycolysis and fatty acid synthesis when compared to glucose, but fructose is preferentially used for nucleic acid synthesis *via* the pentose phosphate shunt to provide five-carbon pentose for RNA synthesis. With these results, the authors concluded that fructose metabolism

enables pancreatic cancer to proliferate more efficiently, potentially implicating fructose-mediated actions as novel therapeutic targets for pancreatic cancer therapy[185]. Goncalves *et al*. subjected mice genetically predisposed to developing intestinal tumours to either high-fructose diet or control diet. Mice fed a high fructose diet developed larger tumours of worse severity compared to control mice. The authors proposed that intratumoural fructolysis produces fructose-1-phosphate *via* KHK, which rapidly depletes ATP, leading to PFK activation and therefore increased glycolysis and fatty acid synthesis, which both support tumour growth[186]. This study therefore demonstrates that fructose metabolism can enhance tumour growth and suggests the inhibition of fructolysis may be a therapeutic target for slowing the growth of intestinal tumours. In 2022, Chen *et al*. showed that glioblastoma multiforme cells can switch from metabolizing glucose to fructose in response to glucose deprivation by increasing expression of GLUT5 and aldolase B, under control of stress-induced transcription factor ATF4[187]. Interestingly, GLUT5 and aldolase B expression correlated with poor prognosis in glioblastoma specimens.

The contributions of fructose metabolism to cancer growth are summarized in a review by Nakagawa *et al*.[188]. Fructose depletes intracellular ATP, which activates glycolysis[186]. Uric acid, formed *via* the pentose phosphate pathway forms mitochondrial ROS, which may contribute to cancer growth[189]. Lactate, an end-product of fructolysis, may contribute to angiogenesis[190], and may be used for immune evasion, metastasis, and self-sufficient metabolism[191]. Importantly, a call is made for PET fructose imaging as an alternative to [^{18}F]-FDG-PET imaging in the approximately 55% of cancers that may preferentially utilize fructose as an alternate energy source[188].

1.5.4. Development of metabolic imaging radiotracers

The switch from glucose to fructose metabolism in the above diseases, especially cancer, has driven the need for the development of metabolic fructose radiotracers for diagnostic imaging. One target has been GLUT receptors. [^{18}F]-labeled 2-deoxy-2-fluoro-D-glucose, or [^{18}F]-FDG is a radiolabeled glucose analog, and is the most commonly used radiopharmeceutical[192]. [^{18}F]-FDG has an [^{18}F] in place of a hydroxyl group at the 2-C position. It enters the cell *via* GLUT1 or GLUT3, is phosphorylated by hexokinase, and is trapped

in the cell until dephosphorylation by glucose-6-phosphatase, as it cannot be further metabolized by the glycolysis pathway. Intracellular FDG accumulation increases when there does not exist sufficient glucose-6-phosphatase, if there are excessive glucose transporters, and/or if there is a high glycolysis rate in the tissue. Typically, cancer cells possess some or all of these traits, making [^{18}F]-FDG an effective metabolic radiotracer for these cancers[193]. Many diseases do not present anatomical changes until later in disease stage, or never at all. Metabolic radiotracers like [^{18}F]FDG are therefore crucial to diagnose these diseases that would otherwise be missed by anatomical imaging alone like MRI or CT. [^{18}F]-FDG is used clinically for neurology[194], oncology[195], cardiology[196], and inflammatory conditions[197].

However, [^{18}F]-FDG is non-specific, as it is taken up by all cells that express these glucose transporters, creating high signal to noise ratio in some tissues (brain, muscles, salivary glands, heart, gastrointestinal system, urinary system, thyroid glands), and false positives[198]. Furthermore, false negatives are possible in tissues showing lack of radiotracer uptake, however these can just as well be malignancies with low glycolytic activities, for example in prostate cancer[199,200] and breast cancer[201]. Therefore, [^{18}F]-FDG uptake should only be indicative of a tissue's glycolytic activity, and further investigations are warranted.

Researchers have attempted to create a new diagnostic PET imaging agent for fructose metabolism to fill the gap that [^{18}F]-FDG leaves. Two iterations of this probe have been attempted: [^{18}F] 1-deoxy-1-fluoro-D-fructose([^{18}F]1-FDF)[202], where the [^{18}F] is installed at C_1, and [^{18}F] 6-deoxy-6-fluoro-D-fructose ([^{18}F]6-FDF)[203], with [^{18}F] installed at C_6. In theory, these radiolabeled fructose analogs would be taken up into cells by GLUT5 and GLUT2, and be trapped in the cell similar to the mechanism of [^{18}F]-FDG. The first attempt, [^{18}F]1-FDF, resulted in rapid clearance through the kidneys and liver *in vivo*, indicating intracellular trapping was not achieved. The second iteration, [^{18}F]6-FDF, demonstrated significant bone uptake, suggesting unwanted metabolic processing of the radiotracer.

In Chapter 6 of this thesis, a new metabolic fructose radiotracer, [^{18}F]4-FDF is presented and compared to [^{18}F]6-FDF and [^{18}F]FDG in a heterotopic hepatocarcinoma xenograft mouse model. Then, we compare our radiotracer with [^{18}F]-FDG in a mouse model of LPS-induced systemic inflammation. Mechanisms of

action are described in detail from metabolomics studies using heavy labelled [U^{13}C] radiotracer analogs. This novel radiotracer, [^{18}F]4-FDF, represents for the first time, a promising diagnostic radiotracer that traps and maps fructose uptake *in vivo* to complement [^{18}F]-FDG, thereby providing clinicians with a tool to visualize pathological fructolysis.

1.6. Site Specific Immunomodulators

In the 1890s, Dr. William Coley published papers detailing the research he conducted on patients with inoperable tumours[204,205]. Several physicians in the late 1800s had written reports about patients with inoperable or recurring tumours having undergone spontaneous remission after suffering from bacterial infections in the hospital. After recognizing this pattern, Coley conducted experiments whereby live bacterial cultures were injected into his patients to induce fever with the ultimate goal of curing the cancer. Erysipelas, a febrile skin infection caused by group A *Streptococcus*, appeared in the cases where tumour regression was observed. He proposed the toxins within the bacteria held curative properties, rather than the action of the bacteria on the body. If this hypothesis was true, the danger of bacterial infection, especially in the age before antibiotics[206], could be avoided, and dosing of the toxins could be regulated. From his own large-scale experiments and cases detailed by other physicians, Dr. Coley proposed a concoction for treatment of malignant sarcoma, later coined as "Coley's toxins", which included co-culture of heat-inactivated gram-positive *streptococcus* and heat-inactivated gram-negative *Serratia marcescens* to increase virulence. After successful cancer treatment of twenty patients, Coley proposed that these toxins elicit an antagonistic and specific influence on malignant tumours, and that the reaction to the toxins was systemic in nature.

While this was a major breakthrough in medicine, more sophisticated research was needed to properly evaluate the therapeutic and toxic effects of Coley's toxins, as the understanding of immunotherapy was still decades away. The advent of immunosuppressive cancer treatments like radiotherapy and later chemotherapy in the 1940s pushed Coley's toxins to the sidelines as the broad curative effects of these new treatments were more attractive than the selective use of the toxins. Coley's toxins were used for cancer

treatment by at least 42 physicians across Europe and North America until 1963, when the FDA declared Coley's toxins as a "new drug" in 1963, and could no longer be used in U.S. without rigorous clinical testing proving safety[207].

As immunosuppressants pose many risks for patients including nephrotoxicity, neurotoxicity, myelosuppression, and malignancy[208], many researchers are once again working on the development of new immunotherapies targeting specific tissues using microorganisms to stimulate the immune system[209-212]. The mechanism by which Coley's Toxins operates can be broken down by the two arms of the immune system: the non-specific innate immune response, and the specific adaptive immune response[213]. The innate immunity represents the first line of defense against pathogens, and includes physical barriers (epithelial cells), complement proteins, cytokines, chemokines, enzymes, and lipids. The innate immune system also relies on a family of pattern recognition receptors (PRRs) that detect pathogen-associated molecular patterns (PAMPs). Upon PAMP detection (from bacterial toxins, for example), PRRs trigger signaling cascades resulting in activation of pro-inflammatory molecules as an early response to infection[214], which is a pre-requisite for the second arm of the immune response, the adaptive immunity. Adaptive immunity is based on the activation of T and B cells, which target specific antigens and create immunologic memory in the case of re-exposure to pathogens[213]. For example, *Echerichia coli* has been used clinically to treat inflammatory bowel disease and irritable bowel syndrome[215,216]. *E. coli* is believed to mediate anti-inflammatory and barrier-protection effects[217,218]. Using synthetic biology, live biotherapeutics are being engineered to target specific mechanisms of disease[212]. Many current cancer immunotherapies focus on adaptive immunity and the elimination of immunosuppressive mechanisms of cancer[219]. Some researchers believe the key to immunotherapy is not only to focus on adaptive immunity, but also to include the innate immune system in the initial response, which has been effective in pre-clinical models[220].

The team of researchers at Qu Biologics take a unique approach to the historical immunotherapeutic approach with heat-inactivated bacterial therapies tuned to restore the function of the immune system in specific tissues. These therapies, named Site Specific Immunomodulators (SSIs), are designed to activate

the innate immune response in an organ-specific manner, based on the target of the bacteria from which the SSI is derived. Qu Biologics has developed two SSIs currently in clinical trials for ulcerative colitis/Chron's disease (QBECO)[221], and lung cancer (QBKPN)[222]. The current understanding of the mechanism of action of these SSIs is discussed in Chapter 8 of this thesis, along with my experimental approach to uncover the mechanisms of trafficking and differential biodistribution of the two SSIs using [^{89}Zr]-radiolabeled SSIs in mice.

1.7. Chapter 1 References

1 O'Brien, P. J., Siraki, A. G. & Shangari, N. Aldehyde Sources, Metabolism, Molecular Toxicity Mechanisms, and Possible Effects on Human Health. *Critical Reviews in Toxicology* **35**, 609-662, (2005).

2 Wood, P. L., Khan, M. A. & Moskal, J. R. The concept of "aldehyde load" in neurodegenerative mechanisms: cytotoxicity of the polyamine degradation products hydrogen peroxide, acrolein, 3-aminopropanal, 3-acetamidopropanal and 4-aminobutanal in a retinal ganglion cell line. *Brain research* **1145**, 150-156, (2007).

3 Ellis, E. M. Reactive carbonyls and oxidative stress: potential for therapeutic intervention. *Pharmacology & therapeutics* **115**, 13-24, (2007).

4 Esterbauer, H., Schaur, R. J. & Zollner, H. Chemistry and biochemistry of 4-hydroxynonenal, malonaldehyde and related aldehydes. *Free radical Biology and medicine* **11**, 81-128, (1991).

5 Lindahl, R. Aldehyde dehydrogenases and their role in carcinogenesis. *Critical reviews in biochemistry and molecular biology* **27**, 283-335, (1992).

6 Xie, Z., Baba, S. P., Sweeney, B. R. & Barski, O. A. Detoxification of aldehydes by histidine-containing dipeptides: from chemistry to clinical implications. *Chem Biol Interact* **202**, 288-297, (2013).

7 Edenberg, H. J. & McClintick, J. N. Alcohol Dehydrogenases, Aldehyde Dehydrogenases, and Alcohol Use Disorders: A Critical Review. *Alcoholism, clinical and experimental research* **42**, 2281-2297, (2018).

8 Hartley, D. P., Ruth, J. A. & Petersen, D. R. The hepatocellular metabolism of 4-hydroxynonenal by alcohol dehydrogenase, aldehyde dehydrogenase, and glutathione S-transferase. *Archives of biochemistry and biophysics* **316**, 197-205, (1995).

9 He, N.-G. *et al.* Transfection of a 4-Hydroxynonenal Metabolizing GlutathioneS-Transferase Isozyme, Mouse GSTA4-4, Confers Doxorubicin Resistance to Chinese Hamster Ovary Cells. *Archives of Biochemistry and Biophysics* **333**, 214-220, (1996).

10 Petersen, D. R. & Doorn, J. A. Reactions of 4-hydroxynonenal with proteins and cellular targets. *Free Radical Biology and Medicine* **37**, 937-945, (2004).

11 Zhang, J. *et al.* ROS and ROS-mediated cellular signaling. *Oxidative medicine and cellular longevity* **2016**, (2016).

12 Collin, F. Chemical basis of reactive oxygen species reactivity and involvement in neurodegenerative diseases. *International journal of molecular sciences* **20**, 2407, (2019).

13 Moldovan, L. & Moldovan, N. I. Oxygen free radicals and redox biology of organelles. *Histochemistry and cell biology* **122**, 395-412, (2004).

14 Sies, H. & Jones, D. P. Reactive oxygen species (ROS) as pleiotropic physiological signalling agents. *Nature reviews Molecular cell biology* **21**, 363-383, (2020).

15 Mailloux, R. J. An update on mitochondrial reactive oxygen species production. *Antioxidants* **9**, 472, (2020).

16 Juan, C. A., Pérez de la Lastra, J. M., Plou, F. J. & Pérez-Lebeña, E. The Chemistry of Reactive Oxygen Species (ROS) Revisited: Outlining Their Role in Biological Macromolecules (DNA, Lipids and Proteins) and Induced Pathologies. *International Journal of Molecular Sciences* **22**, 4642, (2021).

17 Niki, E. Lipid peroxidation: physiological levels and dual biological effects. *Free Radical Biology and Medicine* **47**, 469-484, (2009).

18 Zielinski, Z. A. M. & Pratt, D. A. Lipid Peroxidation: Kinetics, Mechanisms, and Products. *The Journal of Organic Chemistry* **82**, 2817-2825, (2017).

19 Yin, H., Xu, L. & Porter, N. A. Free radical lipid peroxidation: mechanisms and analysis. *Chemical reviews* **111**, 5944-5972, (2011).

20 Ayala, A., Muñoz, M. F. & Argüelles, S. Lipid peroxidation: production, metabolism, and signaling mechanisms of malondialdehyde and 4-hydroxy-2-nonenal. *Oxidative medicine and cellular longevity* **2014**, (2014).

21 Nam, T. G. Lipid peroxidation and its toxicological implications. *Toxicological research* **27**, 1-6, (2011).
22 Salomon, R. G. & Bi, W. Isolevuglandin adducts in disease. *Antioxid Redox Signal* **22**, 1703-1718, (2015).
23 Giera, M., Lingeman, H. & Niessen, W. M. Recent advancements in the LC-and GC-based analysis of malondialdehyde (MDA): a brief overview. *Chromatographia* **75**, 433-440, (2012).
24 Esterbauer, H., Eckl, P. & Ortner, A. Possible mutagens derived from lipids and lipid precursors. *Mutation Research/Reviews in Genetic Toxicology* **238**, 223-233, (1990).
25 Brambilla, G. *et al.* Cytotoxicity, DNA fragmentation and sister-chromatid exchange in Chinese hamster ovary cells exposed to the lipid peroxidation product 4-hydroxynonenal and homologous aldehydes. *Mutation Research/Genetic Toxicology* **171**, 169-176, (1986).
26 Curtis, J. M. *et al.* Downregulation of adipose glutathione S-transferase A4 leads to increased protein carbonylation, oxidative stress, and mitochondrial dysfunction. *diabetes* **59**, 1132-1142, (2010).
27 Negre-Salvayre, A., Coatrieux, C., Ingueneau, C. & Salvayre, R. Advanced lipid peroxidation end products in oxidative damage to proteins. Potential role in diseases and therapeutic prospects for the inhibitors. *British journal of pharmacology* **153**, 6-20, (2008).
28 Sohal, R. & Orr, W. Relationship between antioxidants, prooxidants, and the aging process. *Annals of the New York Academy of Sciences* **663**, 74-84, (1992).
29 Fleming, J., Miquel, J., Cottrell, S., Yengoyan, L. & Economos, A. Is cell aging caused by respiration-dependent injury to the mitochondrial genome? *Gerontology* **28**, 44-53, (1982).
30 Padurariu, M. *et al.* Changes of some oxidative stress markers in the serum of patients with mild cognitive impairment and Alzheimer's disease. *Neuroscience letters* **469**, 6-10, (2010).
31 Reed, T. T., Pierce, W. M., Markesbery, W. R. & Butterfield, D. A. Proteomic identification of HNE-bound proteins in early Alzheimer disease: Insights into the role of lipid peroxidation in the progression of AD. *Brain research* **1274**, 66-76, (2009).
32 Mattson, M. P. Roles of the lipid peroxidation product 4-hydroxynonenal in obesity, the metabolic syndrome, and associated vascular and neurodegenerative disorders. *Experimental gerontology* **44**, 625-633, (2009).
33 Negre-Salvayre, A., Salvayre, R., Augé, N., Pamplona, R. & Portero-Otin, M. Hyperglycemia and glycation in diabetic complications. *Antioxidants & redox signaling* **11**, 3071-3109, (2009).
34 Leitinger, N. Oxidized phospholipids as modulators of inflammation in atherosclerosis. *Current opinion in lipidology* **14**, 421-430, (2003).
35 McEwen, J. E., Zimniak, P., Mehta, J. L. & Reis, R. J. S. Molecular pathology of aging and its implications for senescent coronary atherosclerosis. *Current opinion in cardiology* **20**, 399-406, (2005).
36 Chekir, C. *et al.* Accumulation of advanced glycation end products in women with preeclampsia: possible involvement of placental oxidative and nitrative stress. *Placenta* **27**, 225-233, (2006).
37 Takacs, P. *et al.* Increased circulating lipid peroxides in severe preeclampsia activate NF-κB and upregulate ICAM-1 in vascular endothelial cells. *The FASEB Journal* **15**, 279-281, (2001).
38 Mehendale, S. *et al.* Fatty acids, antioxidants, and oxidative stress in pre-eclampsia. *International Journal of Gynecology & Obstetrics* **100**, 234-238, (2008).
39 Selvaraj, N., Bobby, Z., Koner, B. C. & Das, A. K. Reassessing the increased glycation of hemoglobin in nondiabetic chronic renal failure patients: a hypothesis on the role of lipid peroxides. *Clinica chimica acta* **360**, 108-113, (2005).
40 Wei, Y., Rector, R. S., Thyfault, J. P. & Ibdah, J. A. Nonalcoholic fatty liver disease and mitochondrial dysfunction. *World journal of gastroenterology: WJG* **14**, 193, (2008).
41 Seril, D. N., Liao, J., Yang, G.-Y. & Yang, C. S. Oxidative stress and ulcerative colitis-associated carcinogenesis: studies in humans and animal models. *Carcinogenesis* **24**, 353-362, (2003).
42 Klaunig, J. E. & Kamendulis, L. M. The Role of Oxidative Stress in Carcinogenesis. *Annual Review of Pharmacology and Toxicology* **44**, 239-267, (2004).

43 Wu, D. & Cederbaum, A. I. Alcohol, oxidative stress, and free radical damage. *Alcohol research & health* **27**, 277, (2003).
44 Yao, H. *et al.* Protein kinase Cζ mediates cigarette smoke/aldehyde-and lipopolysaccharide-induced lung inflammation and histone modifications. *Journal of Biological Chemistry* **285**, 5405-5416, (2010).
45 Pizzimenti, S. *et al.* Interaction of aldehydes derived from lipid peroxidation and membrane proteins. *Frontiers in physiology* **4**, 242, (2013).
46 Thornalley, P. J. Protein and nucleotide damage by glyoxal and methylglyoxal in physiological systems-role in ageing and disease. *Drug metabolism and drug interactions* **23**, 125-150, (2008).
47 Takeuchi, M. & Yamagishi, S.-i. Possible involvement of advanced glycation end-products (AGEs) in the pathogenesis of Alzheimer's disease. *Current pharmaceutical design* **14**, 973-978, (2008).
48 Ray, R., Juranek, J. K. & Rai, V. RAGE axis in neuroinflammation, neurodegeneration and its emerging role in the pathogenesis of amyotrophic lateral sclerosis. *Neuroscience & Biobehavioral Reviews* **62**, 48-55, (2016).
49 Frimat, M. *et al.* Kidney, heart and brain: three organs targeted by ageing and glycation. *Clinical science* **131**, 1069-1092, (2017).
50 Lam, G. Y., Huang, J. & Brumell, J. H. in *Seminars in immunopathology.* 415-430 (Springer).
51 Bokoch, G. M. & Zhao, T. Regulation of the phagocyte NADPH oxidase by Rac GTPase. *Antioxidants & redox signaling* **8**, 1533-1548, (2006).
52 Klebanoff, S. J. Myeloperoxidase: friend and foe. *Journal of leukocyte biology* **77**, 598-625, (2005).
53 Nussler, A., Wittel, U., Nussler, N. & Beger, H. Leukocytes, the Janus cells in inflammatory disease. *Langenbeck's archives of surgery* **384**, 222-232, (1999).
54 Anderson, D. G., Florang, V. R., Schamp, J. H., Buettner, G. R. & Doorn, J. A. Antioxidant-Mediated Modulation of Protein Reactivity for 3,4-Dihydroxyphenylacetaldehyde, a Toxic Dopamine Metabolite. *Chemical Research in Toxicology* **29**, 1098-1107, (2016).
55 Hazen, S. L. *et al.* p-Hydroxyphenylacetaldehyde, the major product of L-tyrosine oxidation by the myeloperoxidase-H2O2-chloride system of phagocytes, covalently modifies ε-amino groups of protein lysine residues. *Journal of Biological Chemistry* **272**, 16990-16998, (1997).
56 Hazen, S. L., Hsu, F. F., d'Avignon, A. & Heinecke, J. W. Human neutrophils employ myeloperoxidase to convert α-amino acids to a battery of reactive aldehydes: a pathway for aldehyde generation at sites of inflammation. *Biochemistry* **37**, 6864-6873, (1998).
57 Pegg, A. & McCann, P. P. Polyamine metabolism and function. *American Journal of Physiology-Cell Physiology* **243**, C212-C221, (1982).
58 Sharmin, S. *et al.* Polyamine cytotoxicity in the presence of bovine serum amine oxidase. *Biochemical and biophysical research communications* **282**, 228-235, (2001).
59 Babbar, N. & Casero Jr, R. A. Tumor necrosis factor-α increases reactive oxygen species by inducing spermine oxidase in human lung epithelial cells: a potential mechanism for inflammation-induced carcinogenesis. *Cancer research* **66**, 11125-11130, (2006).
60 Goodwin, A. C. *et al.* Polyamine catabolism contributes to enterotoxigenic Bacteroides fragilis-induced colon tumorigenesis. *Proceedings of the National Academy of Sciences* **108**, 15354-15359, (2011).
61 Goodwin, A. C. *et al.* Increased spermine oxidase expression in human prostate cancer and prostatic intraepithelial neoplasia tissues. *The Prostate* **68**, 766-772, (2008).
62 Chaturvedi, R. *et al.* Spermine oxidase mediates the gastric cancer risk associated with Helicobacter pylori CagA. *Gastroenterology* **141**, 1696-1708. e1692, (2011).
63 Seiler, N. Polyamine metabolism and function in brain. *Neurochemistry international* **3**, 95-110, (1981).
64 Yoo, J., Han, J. & Lim, M. H. Transition metal ions and neurotransmitters: coordination chemistry and implications for neurodegeneration. *RSC chemical biology* **4**, 548-563, (2023).

65 Coyle, J. T. & Puttfarcken, P. Oxidative stress, glutamate, and neurodegenerative disorders. *Science* **262**, 689-695, (1993).
66 Tomitori, H. *et al.* Polyamine oxidase and acrolein as novel biochemical markers for diagnosis of cerebral stroke. *Stroke* **36**, 2609-2613, (2005).
67 Nakamura, M. *et al.* Toxic acrolein production due to Ca2+ influx by the NMDA receptor during stroke. *Atherosclerosis* **244**, 131-137, (2016).
68 Coleman, C. S. *et al.* Targeted expression of spermidine/spermine N1-acetyltransferase increases susceptibility to chemically induced skin carcinogenesis. *Carcinogenesis* **23**, 359-364, (2002).
69 Tucker, J. M. *et al.* Potent modulation of intestinal tumorigenesis in Apcmin/+ mice by the polyamine catabolic enzyme spermidine/spermine N 1-acetyltransferase. *Cancer research* **65**, 5390-5398, (2005).
70 Sequeira, A. *et al.* Implication of SSAT by gene expression and genetic variation in suicide and major depression. *Archives of general psychiatry* **63**, 35-48, (2006).
71 Vaquero-Lorenzo, C. *et al.* Positive association between SAT-1− 1415T/C polymorphism and anxiety. *American Journal of Medical Genetics Part B: Neuropsychiatric Genetics* **150**, 515-519, (2009).
72 Zahedi, K. *et al.* Expression of SSAT, a novel biomarker of tubular cell damage, increases in kidney ischemia-reperfusion injury. *American journal of physiology-renal physiology* **284**, F1046-F1055, (2003).
73 Zahedi, K. *et al.* Spermidine/spermine-N 1-acetyltransferase ablation protects against liver and kidney ischemia-reperfusion injury in mice. *American Journal of Physiology-Gastrointestinal and Liver Physiology* **296**, G899-G909, (2009).
74 Chaturvedi, R. *et al.* Induction of polyamine oxidase 1 by Helicobacter pylori causes macrophage apoptosis by hydrogen peroxide release and mitochondrial membrane depolarization. *Journal of Biological Chemistry* **279**, 40161-40173, (2004).
75 Zahedi, K. *et al.* Polyamine catabolism is enhanced after traumatic brain injury. *Journal of neurotrauma* **27**, 515-525, (2010).
76 Ong, F. H., Henry, P. J. & Burcham, P. C. Prior exposure to acrolein accelerates pulmonary inflammation in influenza A-infected mice. *Toxicology letters* **212**, 241-251, (2012).
77 Yan, T. & Zhao, Y. Acetaldehyde induces phosphorylation of dynamin-related protein 1 and mitochondrial dysfunction via elevating intracellular ROS and Ca2+ levels. *Redox biology* **28**, 101381, (2020).
78 Siems, W. & Grune, T. Intracellular metabolism of 4-hydroxynonenal. *Molecular aspects of medicine* **24**, 167-175, (2003).
79 Remick, D. G., Newcomb, D. E., Bolgos, G. L. & Call, D. R. Comparison of the mortality and inflammatory response of two models of sepsis: lipopolysaccharide vs. cecal ligation and puncture. *Shock* **13**, 110-116, (2000).
80 Seemann, S., Zohles, F. & Lupp, A. Comprehensive comparison of three different animal models for systemic inflammation. *Journal of Biomedical Science* **24**, 60, (2017).
81 Eikelenboom, P. *et al.* Whether, when and how chronic inflammation increases the risk of developing late-onset Alzheimer's disease. *Alzheimer's research & therapy* **4**, 1-9, (2012).
82 Blandini, F. Neural and immune mechanisms in the pathogenesis of Parkinson's disease. *Journal of Neuroimmune Pharmacology* **8**, 189-201, (2013).
83 Evans, M., Couch, Y., Sibson, N. & Turner, M. Inflammation and neurovascular changes in amyotrophic lateral sclerosis. *Molecular and Cellular Neuroscience* **53**, 34-41, (2013).
84 Murta, V. & Ferrari, C. C. Influence of peripheral inflammation on the progression of multiple sclerosis: evidence from the clinic and experimental animal models. *Molecular and Cellular Neuroscience* **53**, 6-13, (2013).
85 Nava Catorce, M. & Gevorkian, G. LPS-induced murine neuroinflammation model: main features and suitability for pre-clinical assessment of nutraceuticals. *Current neuropharmacology* **14**, 155-164, (2016).

86 Tanzer, M. L. Cross-Linking of Collagen. *Science* **180**, 561-566, (1973).
87 Reuben, A., Koch, D. G. & Lee, W. M. Drug-induced acute liver failure: results of a US multicenter, prospective study. *Hepatology* **52**, 2065-2076, (2010).
88 Larson, A. M. *et al.* Acetaminophen-induced acute liver failure: results of a United States multicenter, prospective study. *Hepatology* **42**, 1364-1372, (2005).
89 Dahlin, D. C., Miwa, G. T., Lu, A. & Nelson, S. D. N-acetyl-p-benzoquinone imine: a cytochrome P-450-mediated oxidation product of acetaminophen. *Proceedings of the National academy of Sciences* **81**, 1327-1331, (1984).
90 Xie, Y. *et al.* Mitochondrial protein adducts formation and mitochondrial dysfunction during N-acetyl-m-aminophenol (AMAP)-induced hepatotoxicity in primary human hepatocytes. *Toxicology and applied pharmacology* **289**, 213-222, (2015).
91 Tirmenstein, M. A. & Nelson, S. D. Subcellular binding and effects on calcium homeostasis produced by acetaminophen and a nonhepatotoxic regioisomer, 3'-hydroxyacetanilide, in mouse liver. *Journal of Biological Chemistry* **264**, 9814-9819, (1989).
92 Hu, J., Ramshesh, V. K., McGill, M. R., Jaeschke, H. & Lemasters, J. J. Low dose acetaminophen induces reversible mitochondrial dysfunction associated with transient c-Jun N-terminal kinase activation in mouse liver. *Toxicological Sciences* **150**, 204-215, (2015).
93 Ramachandran, A. & Jaeschke, H. Oxidant stress and acetaminophen hepatotoxicity: mechanism-based drug development. *Antioxidants & redox signaling* **35**, 718-733, (2021).
94 Lawson, J. A., Farhood, A., Hopper, R. D., Bajt, M. L. & Jaeschke, H. The hepatic inflammatory response after acetaminophen overdose: role of neutrophils. *Toxicological sciences* **54**, 509-516, (2000).
95 Jaeschke, H., McGill, M. R. & Ramachandran, A. Oxidant stress, mitochondria, and cell death mechanisms in drug-induced liver injury: lessons learned from acetaminophen hepatotoxicity. *Drug metabolism reviews* **44**, 88-106, (2012).
96 Saito, C., Zwingmann, C. & Jaeschke, H. Novel mechanisms of protection against acetaminophen hepatotoxicity in mice by glutathione and N-acetylcysteine. *Hepatology* **51**, 246-254, (2010).
97 Larson, A. *et al.* in *Seminars in liver disease.* 221-234 (Thieme Medical Publishers 333 Seventh Avenue, New York, NY 10001, USA.).
98 Wimborne, H. J. *et al.* Aldehyde dehydrogenase-2 activation decreases acetaminophen hepatotoxicity by prevention of mitochondrial depolarization. *Toxicology and applied pharmacology* **396**, 114982, (2020).
99 Perez-Miller, S. *et al.* Alda-1 is an agonist and chemical chaperone for the common human aldehyde dehydrogenase 2 variant. *Nature structural & molecular biology* **17**, 159-164, (2010).
100 Massoud, T. F. & Gambhir, S. S. Molecular imaging in living subjects: seeing fundamental biological processes in a new light. *Genes & development* **17**, 545-580, (2003).
101 James, M. L. & Gambhir, S. S. A Molecular Imaging Primer: Modalities, Imaging Agents, and Applications. *Physiological Reviews* **92**, 897-965, (2012).
102 Phelps, M. E. Positron emission tomography provides molecular imaging of biological processes. *Proceedings of the National Academy of Sciences* **97**, 9226-9233, (2000).
103 De Leon-Rodriguez, L. M. *et al.* Responsive MRI agents for sensing metabolism in vivo. *Accounts of chemical research* **42**, 948-957, (2009).
104 Wu, B. *et al.* An overview of CEST MRI for non-MR physicists. *EJNMMI physics* **3**, 1-21, (2016).
105 Bruemmer, K. J., Crossley, S. W. & Chang, C. J. Activity-based sensing: a synthetic methods approach for selective molecular imaging and beyond. *Angewandte Chemie International Edition* **59**, 13734-13762, (2020).
106 Elliott, A. D. Confocal microscopy: principles and modern practices. *Current protocols in cytometry* **92**, e68, (2020).

107 Berrone, E., Beltramo, E., Solimine, C., Ape, A. U. & Porta, M. Regulation of intracellular glucose and polyol pathway by thiamine and benfotiamine in vascular cells cultured in high glucose. *Journal of Biological Chemistry* **281**, 9307-9313, (2006).
108 Khitan, Z. & Kim, D. H. Fructose: a key factor in the development of metabolic syndrome and hypertension. *Journal of nutrition and metabolism* **2013**, (2013).
109 Cheng, H.-M. & González, R. G. The effect of high glucose and oxidative stress on lens metabolism, aldose reductase, and senile cataractogenesis. *Metabolism* **35**, 10-14, (1986).
110 González, R. G., Barnett, P., Aguayo, J., Cheng, H.-M. & Chylack Jr, L. Direct measurement of polyol pathway activity in the ocular lens. *Diabetes* **33**, 196-199, (1984).
111 Kador, P. F. & Kinoshita, J. H. Role of aldose reductase in the development of diabetes-associated complications. *The American journal of medicine* **79**, 8-12, (1985).
112 Liu, H. *et al.* Genetic deficiency of aldose reductase counteracts the development of diabetic nephropathy in C57BL/6 mice. *Diabetologia* **54**, 1242-1251, (2011).
113 Ramasamy, R. & Goldberg, I. J. Aldose reductase and cardiovascular diseases, creating human-like diabetic complications in an experimental model. *Circulation research* **106**, 1449-1458, (2010).
114 Johnson, R. J. *et al.* Sugar, uric acid, and the etiology of diabetes and obesity. *Diabetes* **62**, 3307-3315, (2013).
115 Gugliucci, A. Formation of fructose-mediated advanced glycation end products and their roles in metabolic and inflammatory diseases. *Advances in nutrition* **8**, 54-62, (2017).
116 Schalkwijk, C. G., Stehouwer, C. D. & van Hinsbergh, V. W. Fructose-mediated non-enzymatic glycation: sweet coupling or bad modification. *Diabetes/metabolism research and reviews* **20**, 369-382, (2004).
117 Mastrocola, R. *et al.* Advanced glycation end products promote hepatosteatosis by interfering with SCAP-SREBP pathway in fructose-drinking mice. *American Journal of Physiology-Gastrointestinal and Liver Physiology* **305**, G398-G407, (2013).
118 Tang, W. H., Martin, K. A. & Hwa, J. Aldose reductase, oxidative stress, and diabetic mellitus. *Frontiers in pharmacology* **3**, 87, (2012).
119 Yan, L. j. Redox imbalance stress in diabetes mellitus: Role of the polyol pathway. *Animal models and experimental medicine* **1**, 7-13, (2018).
120 Du, X.-L. *et al.* Hyperglycemia-induced mitochondrial superoxide overproduction activates the hexosamine pathway and induces plasminogen activator inhibitor-1 expression by increasing Sp1 glycosylation. *Proceedings of the National Academy of Sciences* **97**, 12222-12226, (2000).
121 Lanaspa, M. A. *et al.* Counteracting roles of AMP deaminase and AMP kinase in the development of fatty liver. *PloS one* **7**, e48801, (2012).
122 Helsley, R. N. *et al.* Ketohexokinase-C regulates global protein acetylation to decrease carnitine palmitoyltransferase 1a-mediated fatty acid oxidation. *Journal of Hepatology* **79**, 25-42, (2023).
123 Lanaspa, M. A. *et al.* Endogenous fructose production and metabolism in the liver contributes to the development of metabolic syndrome. *Nature communications* **4**, 2434, (2013).
124 Malik, V. S. & Hu, F. B. Fructose and cardiometabolic health: what the evidence from sugar-sweetened beverages tells us. *Journal of the American College of Cardiology* **66**, 1615-1624, (2015).
125 Agrawal, R. & Gomez-Pinilla, F. 'Metabolic syndrome'in the brain: deficiency in omega-3 fatty acid exacerbates dysfunctions in insulin receptor signalling and cognition. *The Journal of physiology* **590**, 2485-2499, (2012).
126 Fung, T. T. *et al.* Sweetened beverage consumption and risk of coronary heart disease in women23. *The American Journal of Clinical Nutrition* **89**, 1037-1042, (2009).
127 Mirtschink, P. & Krek, W. Hypoxia-driven glycolytic and fructolytic metabolic programs: Pivotal to hypertrophic heart disease. *Biochimica et Biophysica Acta (BBA)-Molecular Cell Research* **1863**, 1822-1828, (2016).

128 Mirtschink, P. *et al.* HIF-driven SF3B1 induces KHK-C to enforce fructolysis and heart disease. *Nature* **522**, 444-449, (2015).
129 Regan, T. J. *et al.* Evidence for cardiomyopathy in familial diabetes mellitus. *The Journal of clinical investigation* **60**, 885-899, (1977).
130 Williams, A. L. *et al.* HIF1 mediates a switch in pyruvate kinase isoforms after myocardial infarction. *Physiological genomics* **50**, 479-494, (2018).
131 Mirtschink, P., Jang, C., Arany, Z. & Krek, W. Fructose metabolism, cardiometabolic risk, and the epidemic of coronary artery disease. *European heart journal* **39**, 2497-2505, (2018).
132 Mazzoli, A. *et al.* Adipose tissue and brain metabolic responses to western diet—is there a similarity between the two? *International Journal of Molecular Sciences* **21**, 786, (2020).
133 Cigliano, L. *et al.* Short-term fructose feeding induces inflammation and oxidative stress in the hippocampus of young and adult rats. *Molecular neurobiology* **55**, 2869-2883, (2018).
134 Spagnuolo, M. S. *et al.* A Short-Term Western Diet Impairs Cholesterol Homeostasis and Key Players of Beta Amyloid Metabolism in Brain of Middle Aged Rats. *Molecular Nutrition & Food Research* **64**, 2000541, (2020).
135 Hsu, T. M. *et al.* Effects of sucrose and high fructose corn syrup consumption on spatial memory function and hippocampal neuroinflammation in adolescent rats. *Hippocampus* **25**, 227-239, (2015).
136 Li, J. M. *et al.* Betaine recovers hypothalamic neural injury by inhibiting astrogliosis and inflammation in fructose-fed rats. *Molecular nutrition & food research* **59**, 189-202, (2015).
137 Xu, M.-X. *et al.* Up-regulated fractalkine (FKN) and its receptor CX3CR1 are involved in fructose-induced neuroinflammation: Suppression by curcumin. *Brain, behavior, and immunity* **58**, 69-81, (2016).
138 Jiménez-Maldonado, A., Ying, Z., Byun, H. R. & Gomez-Pinilla, F. Short-term fructose ingestion affects the brain independently from establishment of metabolic syndrome. *Biochimica et Biophysica Acta (BBA)-Molecular Basis of Disease* **1864**, 24-33, (2018).
139 Agrawal, R. *et al.* Dietary fructose aggravates the pathobiology of traumatic brain injury by influencing energy homeostasis and plasticity. *Journal of Cerebral Blood Flow & Metabolism* **36**, 941-953, (2016).
140 Yin, Q. *et al.* Lycopene attenuates insulin signaling deficits, oxidative stress, neuroinflammation, and cognitive impairment in fructose-drinking insulin resistant rats. *Neuropharmacology* **86**, 389-396, (2014).
141 Johnson, R. J. *et al.* Cerebral fructose metabolism as a potential mechanism driving Alzheimer's disease. *Frontiers in aging neuroscience* **12**, 299, (2020).
142 Marcus, C., Mena, E. & Subramaniam, R. M. Brain PET in the diagnosis of Alzheimer's disease. *Clinical nuclear medicine* **39**, e413, (2014).
143 Small, G. W. *et al.* Cerebral metabolic and cognitive decline in persons at genetic risk for Alzheimer's disease. *Proceedings of the National Academy of Sciences* **97**, 6037-6042, (2000).
144 Arnold, S. E. *et al.* Brain insulin resistance in type 2 diabetes and Alzheimer disease: concepts and conundrums. *Nature Reviews Neurology* **14**, 168-181, (2018).
145 Stranahan, A. M. *et al.* Diet-induced insulin resistance impairs hippocampal synaptic plasticity and cognition in middle-aged rats. *Hippocampus* **18**, 1085-1088, (2008).
146 Softic, S. *et al.* Fructose and hepatic insulin resistance. *Critical reviews in clinical laboratory sciences* **57**, 308-322, (2020).
147 Rao, Y. L. *et al.* Hippocampus and its involvement in Alzheimer's disease: a review. *3 Biotech* **12**, 55, (2022).
148 Beilharz, J. E., Maniam, J. & Morris, M. J. Diet-induced cognitive deficits: the role of fat and sugar, potential mechanisms and nutritional interventions. *Nutrients* **7**, 6719-6738, (2015).
149 Beilharz, J. E., Maniam, J. & Morris, M. Short-term exposure to a diet high in fat and sugar, or liquid sugar, selectively impairs hippocampal-dependent memory, with differential impacts on inflammation. *Behavioural brain research* **306**, 1-7, (2016).

150 Reichelt, A. C., Killcross, S., Hambly, L. D., Morris, M. J. & Westbrook, R. F. Impact of adolescent sucrose access on cognitive control, recognition memory, and parvalbumin immunoreactivity. *Learning & memory* **22**, 215-224, (2015).
151 Meng, Q. *et al.* Systems nutrigenomics reveals brain gene networks linking metabolic and brain disorders. *EBioMedicine* **7**, 157-166, (2016).
152 Pase, M. P. *et al.* Sugary beverage intake and preclinical Alzheimer's disease in the community. *Alzheimer's & Dementia* **13**, 955-964, (2017).
153 Ye, X., Gao, X., Scott, T. & Tucker, K. L. Habitual sugar intake and cognitive function among middle-aged and older Puerto Ricans without diabetes. *British journal of nutrition* **106**, 1423-1432, (2011).
154 Baker, L. D. *et al.* Insulin resistance and Alzheimer-like reductions in regional cerebral glucose metabolism for cognitively normal adults with prediabetes or early type 2 diabetes. *Archives of neurology* **68**, 51-57, (2011).
155 Roberts, R. O. *et al.* Relative intake of macronutrients impacts risk of mild cognitive impairment or dementia. *Journal of Alzheimer's disease* **32**, 329-339, (2012).
156 Hwang, J. J. *et al.* The human brain produces fructose from glucose. *JCI insight* **2**, (2017).
157 Lanaspa, M. A. *et al.* High salt intake causes leptin resistance and obesity in mice by stimulating endogenous fructose production and metabolism. *Proceedings of the National Academy of Sciences* **115**, 3138-3143, (2018).
158 Faraco, G. *et al.* Dietary salt promotes cognitive impairment through tau phosphorylation. *Nature* **574**, 686-690, (2019).
159 Liu, Y.-Z. *et al.* High-salt diet enhances hippocampal oxidative stress and cognitive impairment in mice. *Neurobiology of learning and memory* **114**, 10-15, (2014).
160 Andres-Hernando, A. *et al.* Protective role of fructokinase blockade in the pathogenesis of acute kidney injury in mice. *Nature communications* **8**, 14181, (2017).
161 Al-Dahhak, R., Khoury, R., Qazi, E. & Grossberg, G. T. Traumatic brain injury, chronic traumatic encephalopathy, and Alzheimer disease. *Clinics in geriatric medicine* **34**, 617-635, (2018).
162 Wang, M. *et al.* Elevated fructose and uric acid through aldose reductase contribute to experimental and human alcoholic liver disease. *Hepatology* **72**, 1617-1637, (2020).
163 Venkataraman, A., Kalk, N., Sewell, G., Ritchie, C. W. & Lingford-Hughes, A. Alcohol and Alzheimer's disease—does alcohol dependence contribute to beta-amyloid deposition, neuroinflammation and neurodegeneration in Alzheimer's disease? *Alcohol and Alcoholism* **52**, 151-158, (2017).
164 Kwee, I. L., Nakada, T. & Suzuki, N. 31P and 3-fluoro-3-deoxy-d-glucose 19F In vivo NMR spectroscopy of aged rat brain. *NMR in Biomedicine* **4**, 38-40, (1991).
165 Xu, C. *et al.* Increased serum levels of aldehydes are associated with cardiovascular disease and cardiovascular risk factors in adults. *Journal of Hazardous Materials* **400**, 123134, (2020).
166 Bray, G. A. Soft drink consumption and obesity: it is all about fructose. *Current opinion in lipidology* **21**, 51-57, (2010).
167 Herrero-Mendez, A. *et al.* The bioenergetic and antioxidant status of neurons is controlled by continuous degradation of a key glycolytic enzyme by APC/C–Cdh1. *Nature cell biology* **11**, 747-752, (2009).
168 Pérez-Corredor, P. A., Gutiérrez-Vargas, J. A., Ciro-Ramírez, L., Balcazar, N. & Cardona-Gómez, G. P. High fructose diet-induced obesity worsens post-ischemic brain injury in the hippocampus of female rats. *Nutritional Neuroscience* **25**, 122-136, (2022).
169 Rege, S. D. *et al.* Brain trauma disrupts hepatic lipid metabolism: blame it on fructose? *Molecular nutrition & food research* **63**, 1801054, (2019).
170 Vespa, P. *et al.* Metabolic crisis without brain ischemia is common after traumatic brain injury: a combined microdialysis and positron emission tomography study. *Journal of Cerebral Blood Flow & Metabolism* **25**, 763-774, (2005).

171 Kato, T. *et al.* Statistical image analysis of cerebral glucose metabolism in patients with cognitive impairment following diffuse traumatic brain injury. *Journal of neurotrauma* **24**, 919-926, (2007).
172 Ley, E. J. *et al.* Diabetic patients with traumatic brain injury: insulin deficiency is associated with increased mortality. *Journal of Trauma and Acute Care Surgery* **70**, 1141-1144, (2011).
173 Mowery, N. T. *et al.* Stress insulin resistance is a marker for mortality in traumatic brain injury. *Journal of Trauma and Acute Care Surgery* **66**, 145-153, (2009).
174 Bathina, S. & Das, U. N. Brain-derived neurotrophic factor and its clinical implications. *Archives of medical science : AMS* **11**, 1164-1178, (2015).
175 Anthony, D. C., Couch, Y., Losey, P. & Evans, M. C. The systemic response to brain injury and disease. *Brain, behavior, and immunity* **26**, 534-540, (2012).
176 Francey, C. *et al.* The extra-splanchnic fructose escape after ingestion of a fructose–glucose drink: An exploratory study in healthy humans using a dual fructose isotope method. *Clinical nutrition ESPEN* **29**, 125-132, (2019).
177 Jang, C. *et al.* The small intestine converts dietary fructose into glucose and organic acids. *Cell metabolism* **27**, 351-361. e353, (2018).
178 Hannou, S. A., Haslam, D. E., McKeown, N. M. & Herman, M. A. Fructose metabolism and metabolic disease. *The Journal of clinical investigation* **128**, 545-555, (2018).
179 Johnson, R. *et al.* Fructose metabolism as a common evolutionary pathway of survival associated with climate change, food shortage and droughts. *Journal of Internal Medicine* **287**, 252-262, (2020).
180 Michaud, D. S. *et al.* Dietary sugar, glycemic load, and pancreatic cancer risk in a prospective study. *Journal of the National Cancer Institute* **94**, 1293-1300, (2002).
181 Gatenby, R. A. & Gillies, R. J. Why do cancers have high aerobic glycolysis? *Nature reviews cancer* **4**, 891-899, (2004).
182 Hui, H. *et al.* Direct spectrophotometric determination of serum fructose in pancreatic cancer patients. *Pancreas* **38**, 706-712, (2009).
183 Lassen, U., Daugaard, G., Eigtved, A., Damgaard, K. & Friberg, L. 18F-FDG whole body positron emission tomography (PET) in patients with unknown primary tumours (UPT). *European Journal of Cancer* **35**, 1076-1082, (1999).
184 Godoy, A. *et al.* Differential subcellular distribution of glucose transporters GLUT1–6 and GLUT9 in human cancer: ultrastructural localization of GLUT1 and GLUT5 in breast tumor tissues. *Journal of cellular physiology* **207**, 614-627, (2006).
185 Liu, H. *et al.* Fructose induces transketolase flux to promote pancreatic cancer growth. *Cancer research* **70**, 6368-6376, (2010).
186 Goncalves, M. D. *et al.* High-fructose corn syrup enhances intestinal tumor growth in mice. *Science* **363**, 1345-1349, (2019).
187 Chen, C. *et al.* ATF4-dependent fructolysis fuels growth of glioblastoma multiforme. *Nature Communications* **13**, 6108, (2022).
188 Nakagawa, T. *et al.* Fructose contributes to the Warburg effect for cancer growth. *Cancer & Metabolism* **8**, 1-12, (2020).
189 Weinberg, F. *et al.* Mitochondrial metabolism and ROS generation are essential for Kras-mediated tumorigenicity. *Proceedings of the National Academy of Sciences* **107**, 8788-8793, (2010).
190 Kumar, V. S., Viji, R., Kiran, M. & Sudhakaran, P. Endothelial cell response to lactate: implication of PAR modification of VEGF. *Journal of cellular physiology* **211**, 477-485, (2007).
191 San-Millán, I. & Brooks, G. A. Reexamining cancer metabolism: lactate production for carcinogenesis could be the purpose and explanation of the Warburg Effect. *Carcinogenesis* **38**, 119-133, (2017).
192 Ido, T. *et al.* Labeled 2-deoxy-D-glucose analogs. 18F-labeled 2-deoxy-2-fluoro-D-glucose, 2-deoxy-2-fluoro-D-mannose and 14C-2-deoxy-2-fluoro-D-glucose. *Journal of Labelled Compounds and Radiopharmaceuticals* **14**, 175-183, (1978).

193 Suolinna, E.-M. *et al.* Metabolism of 2-[18F] fluoro-2-deoxyglucose in tumor-bearing rats: chromatographic and enzymatic studies. *International Journal of Radiation Applications and Instrumentation. Part B. Nuclear Medicine and Biology* **13**, 577-581, (1986).
194 Tai, Y. & Piccini, P. Applications of positron emission tomography (PET) in neurology. *Journal of neurology, neurosurgery, and psychiatry* **75**, 669, (2004).
195 Rohren, E. M., Turkington, T. G. & Coleman, R. E. Clinical applications of PET in oncology. *Radiology* **231**, 305-332, (2004).
196 Anagnostopoulos, C., Georgakopoulos, A., Pianou, N. & Nekolla, S. G. Assessment of myocardial perfusion and viability by positron emission tomography. *International journal of cardiology* **167**, 1737-1749, (2013).
197 Jamar, F. *et al.* EANM/SNMMI guideline for 18F-FDG use in inflammation and infection. *Journal of nuclear medicine : official publication, Society of Nuclear Medicine* **54**, 647-658, (2013).
198 Carter, K. R. & Kotlyarov, E. Common causes of false positive F18 FDG PET/CT scans in oncology. *Brazilian Archives of Biology and Technology* **50**, 29-35, (2007).
199 Von Mallek, D. *et al.* Technical limits of PET/CT with 18FDG in prostate cancer. *Aktuelle Urologie* **37**, 218-221, (2006).
200 Salminen, E., Hogg, A., Binns, D., Frydenberg, M. & Hicks, R. Investigations with FDG-PET scanning in prostate cancer show limited value for clinical practice. *Acta Oncologica* **41**, 425-429, (2002).
201 Lind, P., Igerc, I., Beyer, T., Reinprecht, P. & Hausegger, K. Advantages and limitations of FDG PET in the follow-up of breast cancer. *European journal of nuclear medicine and molecular imaging* **31**, S125-S134, (2004).
202 Haradahira, T. *et al.* Radiosynthesis, rodent biodistribution, and metabolism of 1-deoxy-1-[18F] fluoro-D-fructose. *Nuclear medicine and biology* **22**, 719-725, (1995).
203 Wuest, M. *et al.* Radiopharmacological evaluation of 6-deoxy-6-[18F] fluoro-D-fructose as a radiotracer for PET imaging of GLUT5 in breast cancer. *Nuclear medicine and biology* **38**, 461-475, (2011).
204 Coley, W. B. The therapeutic value of mixed toxins of the streptococcus of erysipelas and bacillus prodigiosus in the treatment of inoperable malignant tumors. *Am J Med Sci* **112**, 251-280, (1896).
205 Coley, W. B. The treatment of malignant tumors by repeated inoculations of erysipelas: With a report of ten original cases. 1. *The American Journal of the Medical Sciences (1827-1924)* **105**, 487, (1893).
206 Adedeji, W. A. THE TREASURE CALLED ANTIBIOTICS. *Annals of Ibadan postgraduate medicine* **14**, 56-57, (2016).
207 Jessy, T. Immunity over inability: The spontaneous regression of cancer. *Journal of natural science, biology, and medicine* **2**, 43, (2011).
208 McDermott, J. K. Complications of Immunosuppression. *Contemporary Heart Transplantation*, 205-222, (2020).
209 Baird, J. R. *et al.* Immune-mediated regression of established B16F10 melanoma by intratumoral injection of attenuated Toxoplasma gondii protects against rechallenge. *The Journal of Immunology* **190**, 469-478, (2013).
210 Aly, R. G., El-Enbaawy, M. I., Abd El-Rahman, S. S. & Ata, N. S. Antineoplastic activity of Salmonella Typhimurium outer membrane nanovesicles. *Experimental cell research* **399**, 112423, (2021).
211 Karpiński, T. M. & Adamczak, A. Anticancer activity of bacterial proteins and peptides. *Pharmaceutics* **10**, 54, (2018).
212 Charbonneau, M. R., Isabella, V. M., Li, N. & Kurtz, C. B. Developing a new class of engineered live bacterial therapeutics to treat human diseases. *Nature Communications* **11**, 1738, (2020).
213 Chaplin, D. D. Overview of the immune response. *Journal of allergy and clinical immunology* **125**, S3-S23, (2010).

214 Akira, S., Uematsu, S. & Takeuchi, O. Pathogen recognition and innate immunity. *Cell* **124**, 783-801, (2006).
215 Sonnenborn, U. Escherichia coli strain Nissle 1917—from bench to bedside and back: history of a special Escherichia coli strain with probiotic properties. *FEMS microbiology letters* **363**, fnw212, (2016).
216 Schultz, M. Clinical use of E. coli Nissle 1917 in inflammatory bowel disease. *Inflammatory bowel diseases* **14**, 1012-1018, (2008).
217 Fábrega, M.-J. *et al.* Intestinal anti-inflammatory effects of outer membrane vesicles from Escherichia coli Nissle 1917 in DSS-experimental colitis in mice. *Frontiers in microbiology* **8**, 1274, (2017).
218 Guo, S. *et al.* Escherichia coli Nissle 1917 protects intestinal barrier function by inhibiting NF-κB-mediated activation of the MLCK-P-MLC signaling pathway. *Mediators of inflammation* **2019**, (2019).
219 Thallinger, C. *et al.* Review of cancer treatment with immune checkpoint inhibitors: current concepts, expectations, limitations and pitfalls. *Wiener Klinische Wochenschrift* **130**, 85-91, (2018).
220 Uher, O. *et al.* Coley's immunotherapy revived: Innate immunity as a link in priming cancer cells for an attack by adaptive immunity. *Seminars in oncology* **46**, 385-392, (2019).
221 Sham, H. P. *et al.* Immune stimulation using a gut microbe-based immunotherapy reduces disease pathology and improves barrier function in ulcerative colitis. *Frontiers in immunology* **9**, 2211, (2018).
222 Bazett, M. *et al.* A novel microbe-based treatment that attenuates the inflammatory profile in a mouse model of allergic airway disease. *Scientific reports* **6**, 35338, (2016).

Thesis Objectives and Overview

Objectives and hypotheses

The first objective of this thesis is to develop a toolkit of molecular imaging probes across different modalities to better characterize the role of aldehydes in disease and injury. While the literature suggests aldehydes and their resulting adducts are implicated in many diseases, it is not well understood whether they are signaling mediators for pathological processes, if they propagate disease, or whether they are simply biproducts. With a molecular imaging toolkit, we can begin to visualize the spatial and temporal production of aldehydes in cells and *in vivo* following a range of cellular stressors, disease, and injury. I hypothesize that if aldehydes are endogenously produced following disease and injury, then the build-up of these aldehydes, or "total aldehydic load," can be used as an imaging biomarker for early diagnosis of these pathologies.

The second objective of this thesis is to investigate the metabolism of fructose in inflammatory disease. In order to accomplish this, a fructose-analog radiotracer that undergoes intracellular trapping in fructose-metabolizing cells must be developed. First, we must investigate why previous attempts by other researchers have been unsuccessful by following the metabolic pathway of the fructose analog. Second, we must improve on the design of the radiotracer for successful intracellular trapping. Once achieved, this radiotracer can be used to visualize the switch from glucose to fructose metabolism in various pathologies. I hypothesize that if cellular metabolism switches from glucose to fructose in disease, then a fructose-analog radiotracer can be used as a diagnostic imaging tool for these diseases.

The final objective of this thesis is to better characterize the trafficking and biodistribution of SSIs *in vivo*. This can be accomplished through radiolabeling the SSIs and subsequently tracking with PET imaging. The SSIs QBECO and QBKPN are used clinically to mediate the innate immune response in patients with UC and lung cancer, but the full mechanism of action is not understood. By mapping the biodistribution of these immunomodulators, we will begin to understand whether these SSIs behave like live bacterial pathogens, how they are trafficked to the targeted organ from site of injection, and how innate immune cells respond to the administration of the therapy. I hypothesize that if SSIs modulate the immune system in the same

organs as their live bacterial species from which they are derived, then differential distribution will be seen by PET imaging of the two radiolabeled-SSIs.

Overview

In this thesis, I use molecular imaging techniques to better understand the drivers of pathological inflammation described above using probes developed in our laboratory in various cell and animal models. In chapters 2-5, I focus on endogenous aldehydes as mediators, and potentially propagators of cellular stress, disease, and injury. Chapter 2 is a review article on MRI contrast agents for *in vivo* imaging of aldehydes. Included is an overview of endogenous aldehydes, the important considerations for creating an aldehyde-detecting molecular imaging probe, and a comprehensive review of all current aldehyde-binding MRI probes. Chapter 3 is a research article where we introduce an aldehyde-binding fluorogenic probe used to visualize total cellular aldehydic load. Chapter 4 is a research article introducing a PET radiotracer for *in vivo* imaging of total aldehydic load used in a mouse model of local aldehyde rich tissue, and an LPS model of systemic inflammation. Finally, Chapter 5 is a research article using a novel CEST-MRI probe to visualize aldehyde production in a mouse model of mild traumatic brain injury. These three aldehyde-binding molecular imaging agents comprise a new toolkit for imaging total aldehydic load in cells and *in vivo* towards better understanding the pathophysiology of aldehydes.

Chapter 6 of this thesis is a research article introducing a new metabolic fructose radiotracer for PET imaging. While it is well known that fructose metabolism plays a major role in many diseases, the development of radiotracers to visualize fructolysis *in vivo* has proved difficult. Through thoughtful consideration of its biochemical pathways and using metabolomics, we developed an [^{18}F]-labeled fructose analog that becomes trapped in cells undergoing fructolysis, allowing for mapping of systemic fructose metabolism. Mice bearing heterotopic xenografts of hepatocarcinoma, or LPS-induced neuroinflammation are imaged by PET/CT. The methodology for multisubject PET/CT imaging is outlined in chapter 7, along with an example of aldehyde imaging of mice with APAP overdose.

Finally, chapter 8 is a research article using PET to track the biodistribution of radiolabeled immunotherapies administered to mice. These immunotherapies, called SSIs, were developed by Qu Biologics. While these SSIs are in clinical trials, their trafficking and biodistribution are poorly understood. Using a radioligand with a long half-life, the SSIs were radiolabeled and tracked *in vivo* for 8 days, elucidating the differential biodistribution of the two SSIs.

Chapter 2: MRI Probes for In Vivo Aldehyde Sensing

Alexia Kirby[a,b], Mojmír Suchý[b,c], Adam J. Shuhendler[a,b,c]*

[a] A. Kirby, A. Shuhendler
Department of Biology
University of Ottawa
30 Marie Curie Pvt, Ottawa, Ontario, Canada, K1N 6N5
Email: adam.shuhendler@uottawa.ca

[b] A. Kirby, M. Suchy, A. Shuhendler
University of Ottawa Heart Institute
40 Ruskin Dr., Ottawa, ON, Canada, K1Y 4W7

[c] M. Suchy, A. Shuhendler
Department of Chemistry and Biomolecular Sciences
10 Marie Curie Pvt, Ottawa, Ontario, Canada, K1N 6N5

2.1. Introduction to the Review Article Presented in this Chapter

The development of aldehyde-trapping MRI probes has been an ongoing pursuit for the labs of Dr. Peter Caravan and Dr. Adam Shuhendler over the past decade. Although this class of probes has only been explored by these two groups, significant progress has been made toward imaging aldehydes in pre-clinical disease models by MRI. In this invited review written for the journal Analysis & Sensing, I discuss the need for aldehyde-detecting imaging agents, the requirements for development, and a comprehensive up to date summary of these probes.

2.2. Author Contributions

A.K. wrote the manuscript and made the figures. A.K, M.S. and A.S. edited the manuscript.

2.3. Copyright

Reproduced from Ref. ***Anal. Sens.*** 2024, e202300087. **https://doi.org/10.1002/anse.202300087**

2.4. Abstract

Endogenous aldehydes are produced *via* tightly regulated metabolic processes and are rapidly cleared by aldehyde dehydrogenases. However, dysregulation of these processes leads to accumulation of toxic aldehydes in affected tissues, resulting in electrophilic stress forming pathogenic DNA- and protein-adducts. The highly reactive aldehydes contribute to numerous pathologies including traumatic brain injury, cancer, cardiovascular diseases, and fibrosis. Due to their transient nature and electrophilicity, the development of molecular imaging probes with the ability to trap and detect aldehydes *in vivo* remains a challenge. Herein, two classes of aldehyde-mapping MRI probes are discussed: (1) gadolinium and manganese-containing macrocyclic MRI agents targeting extracellular aldehydes produced during active tissue fibrosis, and (2) metal-free hydrazoCEST-MRI agents for total intracellular aldehyde detection. This comprehensive review outlines the development, mechanisms, and potential applications of diverse MRI probes targeting aldehydes, aiming to advance non-invasive diagnostic tools, disease staging, and therapeutic interventions in multiple pathologies.

2.5. Introduction

Aldehydes are produced *in vivo* as intermediates of tightly regulated metabolic processes including the metabolism of carbohydrates, lipids, amino acids, biogenic amines, vitamins, steroids, and pharmacological agents[1]. At normal levels, these aldehydes are neutralized by numerous enzymatic and non-enzymatic mechanisms do not cause harm to cells or tissues. Some short-chain aldehydes act as regulatory molecules involved in cell signaling pathways[2-4]. Dysregulation of these metabolic processes, however, leads to a build-up of endogenous aldehydes through metabolic processes including lipid peroxidation[5], glycation[6], carbohydrate autoxidation[7,8], polyamine oxidation[9], and myeloperoxidase activity[10,11]. The resulting intracellular electrophilic aldehydes produced by these processes react directly with proteins, phospholipids, and DNA, forming adducts leading to protein dysregulation and DNA damage. There is accumulating evidence that these reactive aldehydes are mediators of many pathologies including mild cognitive impairment in early Alzheimer's disease[12], traumatic brain injury[13-18], cardiovascular disease[19-22], tissue fibrosis[23,24], and cancer[25-27].

Chronic tissue inflammation results in an accumulation of extracellular matrix (ECM) molecules that make up scar tissue[28]. While fibrosis is initially beneficial in wound-healing, progressive fibrosis due to unresolved inflammation leads to the replacement of normal tissue with scar tissue, eventually leading to organ failure and death. Pulmonary fibrosis[29], hepatic cirrhosis[30], atrial fibrillation[31], myocardial infraction[32], and diabetic nephropathy[33] are common diseases characterized by tissue fibrosis. During fibrosis, lysyl oxidase (LOX) and LOX-like enzymes are upregulated and catalyze the oxidation of lysine to the aldehyde allysine[34]. The highly reactive extracellular allysine participates in condensation reactions with other aldehyde residues, or with unmodified lysine residues, resulting in cross-linking of elastin and collagen[35] (**Fig.2.1**). When fibrogenesis is no longer active, LOX activity stops and allysine residues can spontaneously condense with peptidyl aldehydes (allysine aldol condensation) or with ε-amino groups of peptidyl lysine. During active fibrogenesis, the formation of allysine residues is faster than subsequent clearance reactions, thus creating an allysine-rich environment in actively fibrotic disease[36,37].

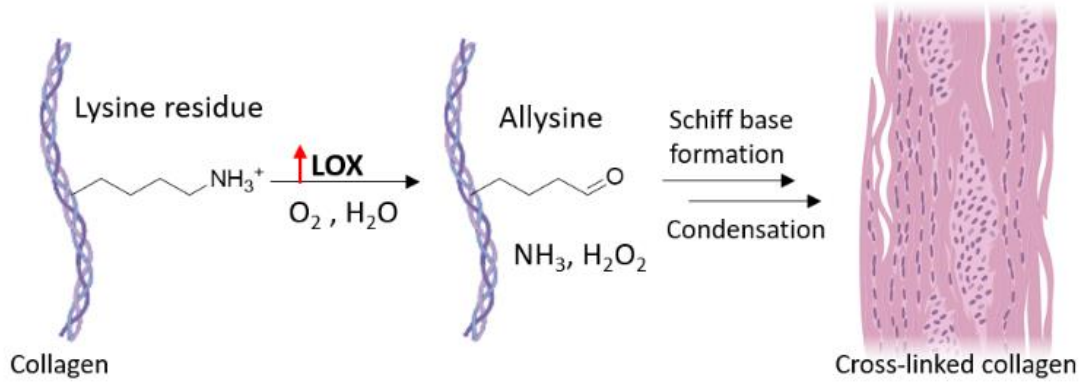

Figure 2.1. Allysine aldehydes are produced in fibrotic tissue. During active fibrosis, lysine residues are converted to allysine by lysyl oxidase (LOX) enzymes, creating allysine-rich tissue. The allysine aldehydes then undergo transformations with other allysine- or unmodified lysine residues, resulting in cross-linked collagen, forming scar tissue.

While fibrotic diseases account for nearly half of the deaths in the industrialized world[28,38], disease progression and response to treatment represents an unmet medical challenge[39]. Non-invasive imaging techniques like high resolution computed tomography (CT) may be used to classify the extent of fibrosis, but cannot assess disease activity and progression. Tissue biopsies can be performed to provide some insight on disease activity, but risk of complications and patient compliance are limiting factors. Non-invasive diagnostic tools are needed to determine molecular activity within the fibrous tissue in order to stage fibrotic disease and differentiate active *vs* stable scar tissue to better monitor disease progression and response to treatment. This is particularly important for pulmonary fibrosis, a respiratory disease caused by chronic lung injury. While CT can be used to diagnose pulmonary fibrosis and determine the extent of the disease[40], it cannot distinguish between old scar tissue and actively progressive fibrosis. Idiopathic pulmonary fibrosis is the most common interstitial lung disease and is associated with a high mortality rate[41]. Disease progression is highly unpredictable, and radiological diagnosis is difficult in early stages of the disease[42].

In addition to pulmonary fibrosis, non-alcoholic steatohepatitis (NASH) is a key chronic liver disease characterized by fibrosis, as well as steatosis and inflammation. NASH affects approximately 5% of the general population in the Western world[43]. Currently, diagnosis relies on an invasive biopsy that carried risk of complication[44]. Furthermore, it has been shown from tissue biopsy that fibrosis, rather than steatosis, is predictive of severe liver disease and mortality[45]. Current methods of detection (imaging, blood panels), is not sensitive for early disease, nor can they measure disease activity [46,47]. As LOX is a hallmark of fibrogenesis as discussed above, activity of LOX and its paralogs are increased in liver fibrogenesis[48]. Therefore, characterization of fibrosis *via* molecular imaging of LOX activity would provide a non-invasive technique for early detection and management of NASH.

2.6. Requirements for *in vivo* aldehyde sensing

A molecular imaging probe for aldehydes is used to visualize, characterize, and quantify aldehydes *in vivo* for biochemical, biological, diagnostic, and/or therapeutic application. Aldehydes are transient and highly electrophilic reactive intermediates and will rapidly modify biological nucleophiles like proteins and nucleic acids. A probe to detect aldehydes must undergo rapid, covalent, and irreversible reactions with aldehydes that are faster than the reaction of aldehydes with other endogenous compounds. If the probe contains a beacon moiety that must be cleared for safety (e.g., gadolinium), the aldehyde-probe complex must be stable long enough to be detected by MRI. The probe should proceed through a bimolecular mechanism without the requirement for an intermolecular catalyst to form a non-toxic and stable product under physiological conditions. The probe must be highly soluble and stable in water. High binding affinity is essential in order to capture the targeted aldehydes where they accumulate, and not be washed out immediately by circulation. High sensitivity is important as any small change from baseline may be important in detecting early disease. Finally, a significant signal enhancement with good signal to noise ratio must be observable by MRI upon reaction with aldehydes. For T1-shortening MRI contrast agents, this can take the form of changing from low relaxivity when unbound to high relaxivity when bound to aldehydes to produce sufficient contrast enhancement in diseased tissues. Alternatively, CEST-MRI agents

have been generated that only produce image contrast when bound to aldehydes, effectively invoking full signal turn-on upon hydrazone formation. For clinical translation, probe chemistry should be simple, robust, and amenable to large-scale production. Herein is a comprehensive review of aldehyde-mapping MRI probes developed to date, categorized into two classes of probes: (1) macrocyclic metal-based paramagnetic probes for extracellular aldehyde trapping, and (2) small molecule metal-free CEST-MRI probes for intracellular aldehyde detection (Fig.2.2). Probe design, characterization, *in vivo* testing, and applications for the two classes of probes are discussed.

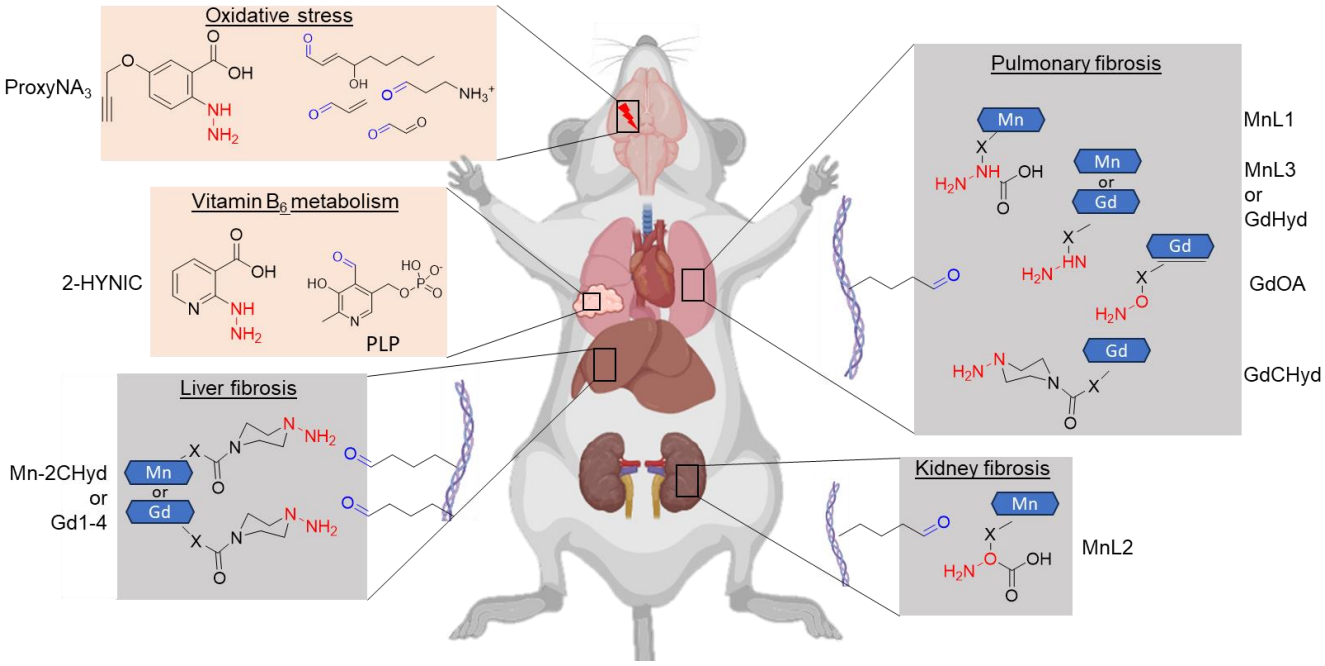

Figure 2.2. MRI probes for *in vivo* imaging of pathological endogenous aldehydes discussed in this review. These probes are designed to map intracellular (orange) or extracellular (grey) aldehydes *via* covalent binding of the warhead (red) with the targeted carbonyl (blue).

2.7. Current aldehyde-trapping MRI probes

2.7.1. Macrocyclic Metal-Based Compounds for Extracellular Aldehyde Trapping

While the value of molecular imaging of aldehydes has been widely recognized in the literature[49-51], the development of *in vivo* aldehyde probes has been limited due to the challenges listed above. Towards

accessing aldehydes as an imaging-based biomarker of disease, Caravan and co-workers have developed several MRI contrast agents targeting fibrotic tissue. Early generations of these MRI contrast agents were targeted to collagen deposition, providing a direct measure of a fibrotic burden, however no measure of dynamic changes occurring during fibrogenesis was possible[52,53]. To overcome this limitation, allysine-targeted MRI contrast agents have been developed.

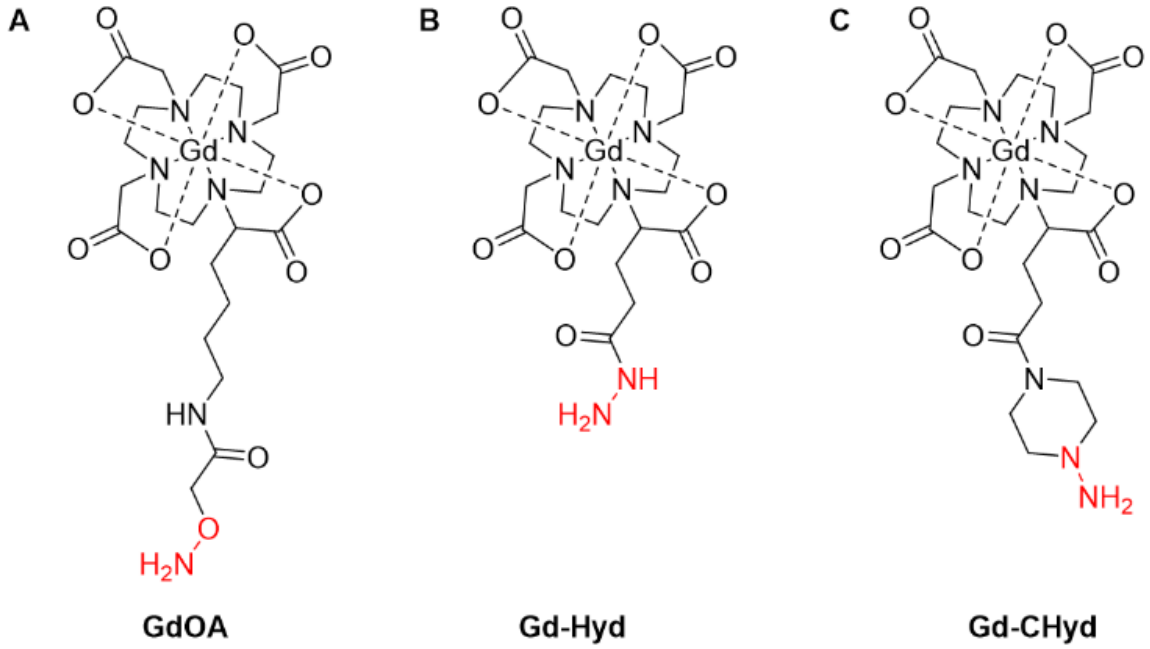

Figure 2.3. Gadolinium-based macrocyclic aldehyde-binding MRI compounds developed by the Caravan group for in vivo imaging of lung fibrosis. Structures from [54 55].

Since LOX-catalyzed lysine oxidation to allysine is faster than the subsequent formation of crosslinks, Waghorn *et al*. reasoned that an excess of allysine would be associated with active fibrinogenesis, while in stable disease all the allysine residues will be converted to cross-links[37]. They found that the concentration of allysine in healthy lung tissue was estimated to be ~ 80 nmol/g of tissue, while significant increase (~ 150 nmol/g of tissue) was observed in mice with fibrotic lungs (bleomycin injury, see below). These

concentrations of allysine in the tissue of interest are sufficiently high to be observed by Gd-enhanced MRI, supporting the hypothesis of differentiating active from passive fibrogenic disease.

Gd-based macrocyclic complexes are widely used as MRI contrast agents due to their high thermodynamic stability and kinetic inertness, good water solubility and rapid renal excretion[56]. In the first design for an *in vivo* aldehyde-binding MRI probe for imaging of fibrogenesis, Waghorn *et al.* developed GdOA: an oxyamine-functionalized probe derived from GdDOTA[54,57]. This novel probe bears an aliphatic side chain terminated by an oxyamine group capable of rapid and irreversible reaction with aldehydes to form oximes (GdOA, Fig.2.3A)[54]. A control compound was prepared with a non-reactive OCH3 group in place of the aldehyde-reactive -O-NH moiety. The relaxivity of GdOA was tested *in vitro* in the presence of naïve BSA or oxidized BSA (BSA-Ald). GdOA has low non-specific binding in the PBS-BSA solution, which increased by 90% in the presence of BSA-Ald. GdOA showed affinity to binding allysine-rich tissue, rapid blood clearance, and almost exclusive renal clearance. A bleomycin-induced mouse model of pulmonary fibrosis was used to test the ability of GdOA to detect fibrotic tissue *in vivo*. GdOA-injected mice showed a strong lung signal enhancement in injured mice compared to naïve mice, whereas the control probe, GdOX, showed similar enhancement in both treated and untreated mice. GdOA has also been validated in mouse models of nephritis, revealing its potential utility in detecting and staging renal fibrogenesis[58]. These results indicated that oxyamine functionalization was necessary for target binding, and that free allysine could now be accessed for molecular imaging of fibrogenic severity.

A second allysine-targeted MRI probe for fibrogenesis based on GdDOTA was designed by Chen *et al.*, this time functionalized with a hydrazide group instead of an oxyamine, which the authors named Gd-Hyd (Fig.2.3B)[55]. Hydrazines and hydrazides are capable of rapid reaction with aldehydes to form hydrazones. In the structure of Gd-Hyd, the aliphatic side chain was reduced to two carbons terminated by a hydrazide functional group [-(C=O)-NHNH2]. A control compound, devoid of reactivity toward aldehydes was also prepared (terminal amino group was replaced with N,N-dimetylamino group) and was denoted as Gd-DiMe.

A similar set of experiments to those associated with GdOA were performed with Gd-Hyd and corresponding unreactive control Gd-DiMe. While only a modest difference in relaxivity of the Gd-Hyd in the presence of oxidized BSA was observed *in vitro*, a remarkable 238% relaxivity increase (13.74 $mmol^{-1}s^{-1}$) was determined for the protein-bound fraction of Gd-Hyd. A decreased affinity to allysine-rich aortic tissue was associated with Gd-Hyd (Kd 650 μmol) as compared to GdOA (Kd 360 μmol). Importantly, specificity was demonstrated as there was no aorta binding when the unreactive control Gd-DiMe was used. Bleomycin-injured mice were again used as the *in vivo* model for pulmonary fibrosis. Mice that received Gd-Hyd exhibited a 3.8-fold increase in lung signal compared to mice injected with the control compound Gd-DiMe, and a 3.7-fold increase compared to sham mice. The use of Gd-Hyd to monitor response to treatment (disease regression) and disease progression was assessed in mouse models of pulmonary and hepatic fibrosis. Interestingly, Gd-Hyd is able to distinguish active pulmonary fibrosis from stable scar tissue, allowing for accurate detection and staging of fibrosis in multiple organs. Gd-Hyd has since been validated in various *in vivo* disease models of hepatic injury, fibrosis, and NASH to monitor disease progression and therapeutic response[53,59-61].

Replacement of the hydrazide moiety in Gd-Hyd with an N-aminopiperazine terminus resulted in the formation of Gd-Chyd (Fig.2.3C), an allysine-targeted MRI contrast agent with increased reactivity toward aldehydes[62]. The reaction between Gd-CHyd and small molecule aldehyde (2-formyl pyridine) was found to be ~1 order of magnitude faster under physiological temperature and pH, compared to the reaction with Gd-Hyd. Moreover, Gd-CHyd hydrazone was ~1 order of magnitude more stable (Kd 45 ± 16 μmol) compared to Gd-Hyd hydrazone (Kd 415 ± 63 μmol). The *in vitro* relaxivity enhancement was similar (~30%) when comparing the samples containing Gd-CHyd and Gd-Hyd in the presence of BSA or BSA-Ald, and binding with allysine-rich tissue was slightly enhanced with Gd-Chyd. An increased reactivity of Gd-CHyd toward aldehydes was demonstrated in an *in vivo* MRI study, wherein the efficiency of Gd-CHyd was compared with that of Gd-Hyd. In bleomycin-induced lung injury bearing mice, the lung signal intensity was stronger at all imaging time points when Gd-CHyd was used compared to Gd-Hyd. This

difference was attributed to slower washout of bound Gd-CHyd from the tissue due to the enhanced stability of the corresponding hydrazone. As expected, negligible lung signal enhancement is observed upon administration of Gd-CHyd to healthy mice. Overall, the set of aldehyde targeted Gd-based MRI contrast agents discussed herein (GdOA, Gd-Hyd and Gd-CHyd) represent a robust and reliable tool for detection and staging of fibrosis in different organs (lung, liver).

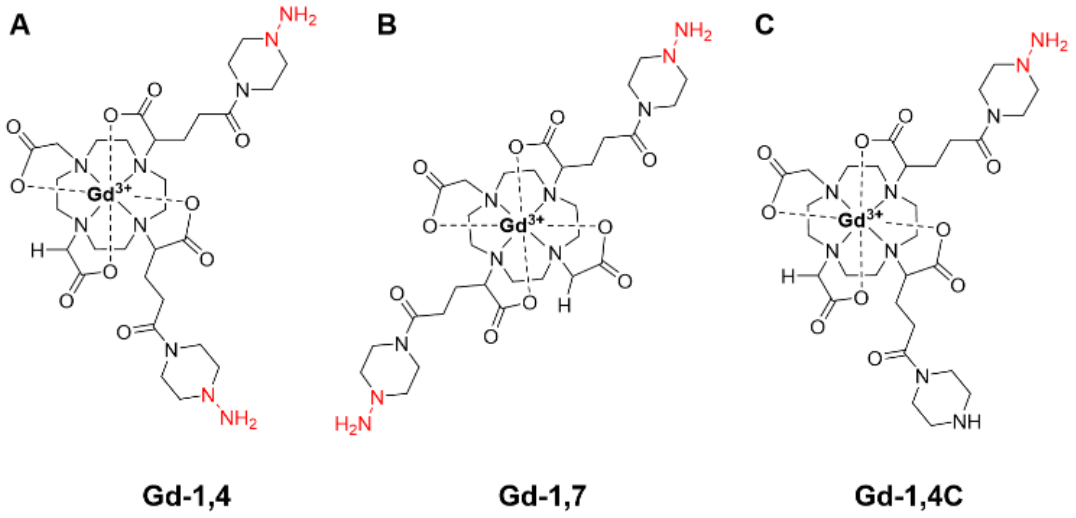

Figure 2.4. Gadolinium-based macrocyclic dual hydrazine aldehyde-binding (A,B) and mono-hydrazine (C) MRI contrast agents for *in vivo* imaging of liver fibrosis. Structures from [63].

During liver fibrogenesis, like in the lungs, collagen cross-linking is catalyzed by LOX by oxidizing lysine amino pairs in close proximity[64,65], producing extracellular allysine aldehyde pairs that are absent in normal liver tissue, potentially identifying a highly specific biomarker for active liver fibrogenesis. Ning *et al.* proposed an MRI probe with two hydrazine moieties that could covalently dually bond the allysine aldehyde pairs[63]. Upon cross-linking, probe tumbling in solution would cease upon binding into a rigid, bridged

biomolecular-probe complex, resulting in an increase in the tumbling time constant (τ_R) and a significant increase in relaxivity, since $r_1 \alpha \tau_R^{-1}$. In addition to the requirements in designing an aldehyde-reactive probe stated above, this probe also requires the two targeting groups to match the O-O distance of the paired allysine aldehyde residues (approximately 16.5 Å) on the oxidized collagen. Differentiating it from lung-targeted contrast agents, it must also undergo renal excretion, as hepatobiliary elimination would increase background liver signal. Two isomeric probes were prepared based on Gd-DOTA: two piperazino-hydrazine moieties on the α-carbons on two of the Gd-DOTA carboxylate arms to produce (1) *cis*-1,4-Gd-$(CHyd)_2$ (Gd-1,4) and (2) *trans*-1,7-Gd-$(CHyd)_2$ (Gd-1,7), where the N-N distance between the piperazino-hydrazine groups were 16.2 Å and 20.7 Å, respectively (Fig.2.4A,B). Two additional control compounds were prepared: (1)Gd-1,4C which replaces one piperazino-hydrazine arm with a piperazine moiety (Fig.2.4C), and (2)Gd-CHyd, as described above[62], bearing only one piperazino-hydrazine moiety (Fig.2.3C). The authors find that the introduction of the second hydrazine moiety resulted in faster hydrazone formation, increasing the on-rate (600%), decreasing off-rate (50%), and increasing affinity by two-fold for the aldehyde-binding compounds compared to their respective controls. Reactivity, affinity, and relaxivity were confirmed *in vitro* with BSA-Ald compared to PBS and unmodified BSA, and using Gd-DOTA, which lacks an aldehyde-binding moiety, as a negative control. As hypothesized, dual-binding probes Gd-1,4 and Gd-1,7 had higher protein-bound relaxivity compared to the monohydrazine probes on account of cross-linking induced τ_R enhancement. Finally, the probes were tested in a mouse model of CCl4-induced liver fibrogenesis. Both Gd-1,4 and Gd-1,7 exhibited enhancement in the liver, with a change in liver:muscle contrast:noise ratio of 2.5+/-1.0 and 1.3+/-0.4, respectively, which persisted for at least 45 minutes post-injection. Control groups receiving Gd-CHyd or Gd-DOTA, or vehicle control mice exhibited no liver enhancement. A blocking study confirmed specific binding of Gd-1,4 to fibrotic livers. In follow-up experiments, Gd-1,4 signal enhancement did not correlate with liver collagen content, but tracked with markers of active fibrogenesis (i.e. LOX, allysine aldehyde, and α-smooth muscle actin). Gd-1,4 was also shown to specifically bind *ex-vivo* human fibrotic lung tissue. Overall, Gd-1,4 is a highly sensitive MRI

contrast agent that binds extracellular allysine aldehyde pairs in fibrotic liver tissue, allowing for non-invasive hepatic fibrogenesis imaging, but does not report on fibrosis stage.

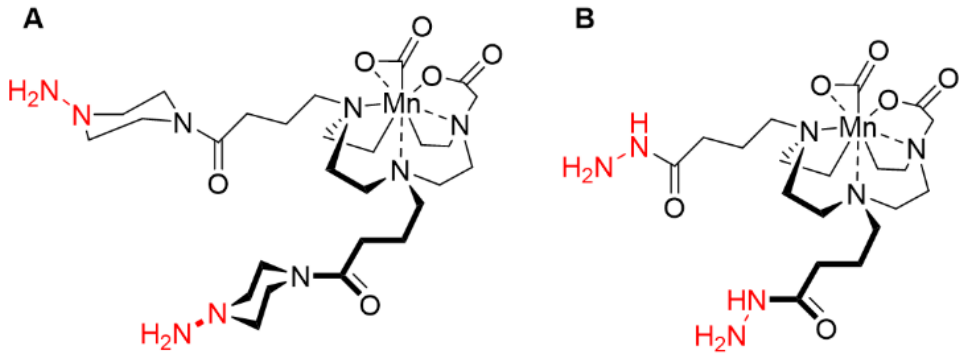

Figure 2.5. Manganese-based aldehyde-binding MRI probes for *in vivo* imaging of liver fibrosis. Structures from [66].

Caravan and coworkers next focused their efforts on creating a similar liver fibrosis-targeted MRI probe, but with manganese in place of gadolinium[66], considering the long-term safety concerns of Gd-based contrast agents[67]. An additional requirement is presented as free Mn^{2+} is taken up by normal hepatocytes, which would lead to high background signal, requiring high kinetic inertness to prevent the release of free Mn^{2+}. This time using *cis*-Mn-1,4-DO2A as a stable, inert starting point for probe design[68], the authors created two probes using the same dual-binding approach as with Gd-1,4. Two piperazino-hydrazine (Mn-2Chyd; Fig.2.5A), or hydrazide (Mn-2Hyd; Fig.2.5B) moieties were installed onto *cis*-Mn-1,4-DO2A. No free manganese was detected in *in vitro* experiments, supporting the kinetic inertness of the agents. Reactions with BSA-Ald and BSA indicated negligible non-specific binding, and a 103% increase in relaxivity of Mn-2CHyd with oxidized BSA. In healthy mice, Mn-2CHyd showed little enhancement to the liver over time. After determining Mn-2Chyd has high stability, high turn-on upon binding with the paired aldehydes, and low accumulation in healthy liver, it was tested in a mouse model of CCl4-induced liver fibrogenesis. Liver enhancement was seen in diseased liver with Mn-2CHyd compared to Gd-DOTA, and

compared to vehicle treated mice, indicating this probe is sensitive and specific for *in vivo* detection of liver fibrogenesis in mice.

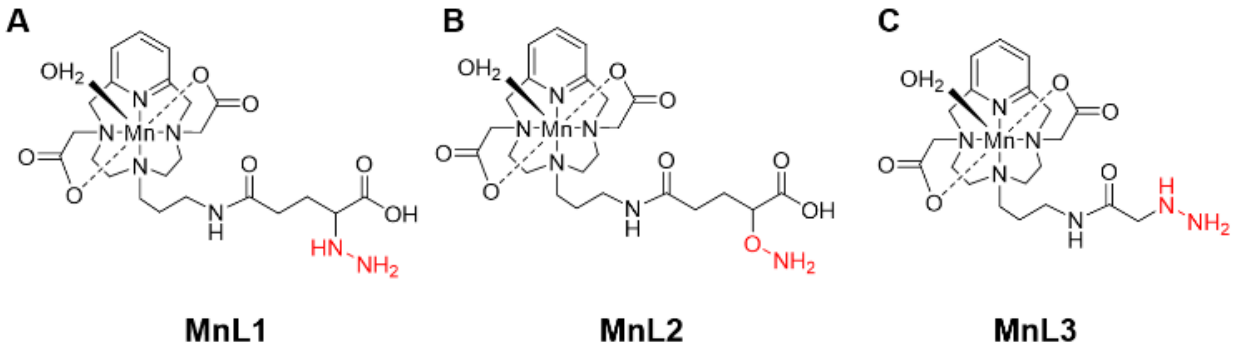

Figure 2.6. Extracellular aldehyde-targeting Mn-based MRI probes for *in vivo* imaging of lung, liver, and kidney fibrosis. Aldehyde-reactive groups are either an alkyl hydrazine (A,C), or α-carboxylate oxyamine (B). Structures from [69].

In 2023, three more Mn(II)-based MRI probes containing aldehyde-targeting groups were presented by Ma *et al.* for the imaging of allysine in fibroproliferative diseases[69]. These three probes allowed for the direct comparison between different aldehyde-targeting warheads: α-carboxylate alkyl hydrazine, α-carboxylate oxyamine, and alkyl-hydrazine (Fig.2.6). In a mouse model of pulmonary fibrosis, the three hydrazine/oxyamine probes had lung signal enhancement peak immediately post-injection as a result of aldehyde binding and non-specific distribution. The diseased lung signal enhancement from MnL1 and MnL3 steadily decreased over the scan time (110min), compared to MnL2, the more hydrolytically-stable oxyamine-bearing probe, which plateaued at 60 minutes post-injection as a result of specific binding and a very slow off rate. Despite MnL1 and MnL3 having similar affinity to aldehydes (Kd), MnL3 had higher signal enhancement of the fibrotic tissue at early timepoints compared to MnL1, which the authors attributed to the slower off-rate of MnL3. MnL3 was also 40% more sensitive in detecting fibrogenesis compared to MnL1. MnL3 was subsequently shown to map whole lung fibrosis disease activity, accurately correlating signal enhancement with disease severity. Given the hydrolytic stability of the oxime bond MnL2 forms with allysine, the authors proposed MnL2 may be used as a kidney fibrosis imaging agent as

the probe may remain bound longer than the time needed for non-specific renal signal to diminish. This hypothesis was tested in a mouse model of unilateral renal ischemia-reperfusion injury, and a comparison between MnL2 and GdOA (Fig. 2.3). The change in relaxation rate, ΔR1, was used as a measure of probe concentration in the tissue. The ΔR1 in the injured kidney was 30-40% higher following MnL2 injection compared to GdOA, due to the 4-fold higher condensation rate of MnL2, improving its performance as a probe for renal fibrogenesis.

This study highlights the importance of the correct choice of warhead for aldehyde-targeted probes depending on disease and tissue. In choosing a hydrazine, the fast hydrolysis of the hydrazone results in fibrolytic tissue enhancement quickly after i.v. administration and fast elimination, useful for lung and liver fibrosis mapping. In contrast, the hydrolytic stability of the oxyamine causes a delay in signal enhancement, which can be advantageous in imaging renal fibrosis, where non-specific clearance must occur before signal enhancement for diseased tissue can be evaluated.

2.7.2. Small Molecule Metal-Free Compounds for Intracellular Aldehyde Trapping

While the MRI probes above are useful in imaging fibrogenesis that occurs in the extracellular environment, the diversity of biogenic aldehydes produced in the early stages of many diseases and following injury leads to the aldehydic load hypothesis, which states the buildup of structurally diverse aldehydes as a whole (i.e. intracellular and extracellular) is what determines the fate or outcome of the cell or tissue[49,70,71]. Based on this aldehydic load hypothesis, Shuhendler and coworkers have developed α-carboxylate arylhydrazone-based aldehyde-targeting molecular imaging agents for optical imaging[72,73], positron emission tomography[74], and MRI[75,76]. Similar to many of the probes detailed above, the imaging agents created by this group also take advantage of the rapid reaction of aldehydes with hydrazines under physiological conditions. Unlike the aforementioned probes, Shuhendler *et al.* have developed metal-free contrast agents targeted toward all aldehyde species, that can bind aldehydes intracellularly, with the intention of imaging intracellular aldehyde-rich areas in the body. The group developed a new class of chemical exchange

saturation transfer (CEST)-MRI contrast agents termed Hydrazo-CEST, which selectively turns on in the presence of bioactive aldehydes. A CEST agent requires an exchangeable proton that dynamically exchanges with water. When a specific radiofrequency pulse is applied, the magnetization of the exchangeable pool of protons is saturated (i.e. nullified), which is detectable through the reduction of the surrounding water signal[77,78]. The α-carboxylate hydrazine-derived hydrazo-CEST probes rapidly activate in the presence of aldehydes under physiological conditions forming a hydrazone and remain stable for signal detection at 3T and 7T MRI. The first of these MRI agents is based on the N-amino anthranilic acid (NA_3) scaffold (Fig.2.7A). The proton on the ring-proximal nitrogen of an aryl hydrazone is exchangeable with water under modulation of the critical α-carboxylate group, making the resulting hydrazone amenable to detection by CEST-MRI[75]. The authors noted that the hydrazone, but not the hydrazine, provide CEST contrast, therefore creating a "turn on" mechanism upon reaction with aldehydes, favouring aliphatic over aromatic aldehydes. The probe was able to detect a variety of endogenous aldehydes with pathogenic potential *in vitro* and does not react with D-glucose under physiological conditions. This represents the first Hydrazo-CEST probe that elicits a turn-on mechanism with aldehydes that would be capable of mapping both freely diffusing small molecule aldehydes, and larger oxidized residues of biomacromolecules.

A second hydrazo-CEST agent, 2-hydrazinonicotininc acid (2-HYNIC) was developed in 2021 by Brun *et al.* (Fig. 2.7B)[76]. Compared to the first NA_3 agent resulting in signal turn on in when complexed to aliphatic aldehydes, 2-HYNIC resulted in signal generation when bound to aromatic aldehydes. Given the ability of 2-HYNIC to detect aromatic aldehydes, the authors chose to test metabolites of vitamin B_6, or pyridoxine (PN), as it is an essential nutrient needed for > 140 metabolic reactions occurring *in vivo*[79]. PN is actively transported into cells then oxidized to pyridoxal (PL), which is then phosphorylated to pyridoxal 5'-phosphate (PLP) by pyridoxal kinase (PDXK). Pyridoxal phosphatase can then dephosphorylate PLP back to PL to tightly control the pool of intracellular PLP. The dysregulation of this kinase-phosphatase-oxidase system has been associated with pathologies including neurodegeneration[80], neurotrauma severity[81], depression[82], pain[83], and cancer[84]. In particular, non-small cell lung cancer

patients with low PDXK expression have a poorer prognosis, with a higher chance of cancer cell resistance to therapy[84]. In particular, non-small cell lung cancer patients with low PDXK expression have a poorer prognosis, with a higher chance of cancer cell resistance to therapy[54]. PL-derived hydrazones produce a poor signal due to a non-planar conformation at physiological pH, but PLP-derived hydrazones provide substantial CEST-MRI signal at physiological pH as they maintain a planar conformation. The authors then tested whether 2-HYNIC could image intracellular PLP *in vitro* in two human non-small cell lung cancer lines. There was a substantial increase in contrast after incubation of 20 mM 2-HYNIC with both cell lines, with a greater increase in H460 large cell carcinoma than A549 adenocarcinoma. Liquid chromatography-mass spectrometry revealed that the intracellular PLP-to-PL ratio was greater in H460, which may explain the greater CEST signal in these cells. Finally, 2-HYNIC was used to image PLP in mice bearing A549 or H460 heterotopic xenografts. An increase in contrast was observed in the tumours, steadily increasing up to 60 min post-intravenous injection, with significantly greater contrast in the H460 tumours compared to the A549 tumours. H460 xenografts are more sensitive to chemotherapies, suggesting 2-HYNIC PLP mapping may be useful in predicting the efficacy of lung cancer chemotherapy.

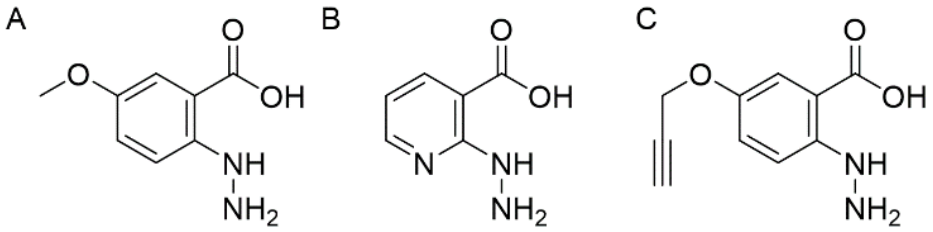

Figure 2.7. Chemical structures of (A) the first generation (NA3), (B) second generation (2-HYNIC), and (C) third generation (ProxyNA$_3$) CEST-MRI agents targeted to aldehydes developed by Shuhendler *et al.*[75,76,85]

A third Hydrazo-CEST MRI agent, 5-propargyloxy-N-aminoanthranilic acid (ProxyNA$_3$) (Fig. 2.7C) has been developed by Kirby *et al.* to rapidly and irreversibly bind aldehydes in the brain to map total aldehydic load following mild traumatic brain injury (mTBI)[85]. Concussion, or mTBI, often do not present with

external signs of trauma, and do not show signs of injury on anatomical scans like CT[86,87]. Diagnosis therefore relies on subjective patient-physician interviews of symptom evaluation and physical examination which leads to mTBI being highly underdiagnosed[88,89]. The neurometabolic cascade of mTBI results in the loss of ionic and cellular homeostasis, forming oxygen-centered free radicals[90]. In response to the formation of free radicals, several processes including lipid peroxidation and polyamine catabolism lead to downstream production of aldehydes[90,91]. ProxyNA$_3$ targets these endogenously formed aldehydes following brain injury, allowing for the visualization of trauma using total cerebral aldehydic load as a biomarker. The authors tested ProxyNA$_3$ on a mouse model of mTBI, where awake mice were subjected to a controlled, closed head impact and evaluated for behavioural deficits. The mice underwent ProxyNA$_3$ CEST-MRI before, and 2- and 7- days post-injury. The aldehyde-targeted probe was able to pass the blood-brain-barrier and bind to intracerebral aldehydes, effectively mapping the increase in total aldehydes in the brain two days post-mTBI. The production of aldehydes by neurons was confirmed in a cell model of concussion by microscopy using a fluorogenic aldehyde probe[72], and an inflammatory response was confirmed by immunofluorescence staining of glial fibrillary acidic protein (GFAP) at 7 days post-injury. ProxyNA3 therefore represents an MRI agent that maps total aldehydic load in the brain as a biomarker for mTBI.

2.8. Summary and Outlook

Non-invasive imaging of aldehydes *in vivo* may allow for early detection of many diseases leading to better staging, management, and therefore prognosis. In this review, two classes of aldehyde-targeted MRI probes were discussed. First, a class of gadolinium- and manganese-based probes with aldehyde-targeting moieties of hydrazines, hydrazides, or oxyamines are presented. These probes are designed to remain in the extracellular space as to target the aldehyde-bearing, protein-bound allysine residues, which are the result of LOX-catalyzed lysine oxidation in tissues with active fibrosis. Dual-functionalized probes were developed to increase reactivity, affinity, and relaxivity upon binding the target allysine for imaging of

active fibrosis. These probes were used to map the presence of allysine in mouse models of fibrosis of the lungs, liver, and kidney, allowing for disease staging, and quantifying progression, and regression of fibrosis.

Second, a group of hydrazoCEST agents are presented as a novel class of small molecule metal-free CEST MRI probes for imaging total aldehydic load. These probes are designed to cross the cell membrane, giving them the unique ability to map total intracellular aldehydes, which are increased in many cases of disease and injury. These probes are based on an N-aminoanthranilic acid scaffold, with the aldehyde-binding moiety of hydrazine combined with an α-carboxylic acid necessary for CEST signal production. The hydrazine binds aldehydes, forming a stable hydrazone, and creating a turn-on CEST signal. The probes are designed with different use-cases in mind, to favour either aromatic or aliphatic aldehydes. The aromatic-favouring 2-HYNIC was used to map PLP activity in two xenograft mouse models of lung cancer, while the aliphatic-favouring ProxyNA3 was used to map aldehydic load in the brain following injury in a mouse model of mTBI.

The aldehyde-targeted probes discussed here present a large clinically-translatable toolkit for the non-invasive detection of a wide array of diseases. Unlike traditional receptor-targeted molecular imaging probes that rely on specific binding to a desired substrate, these probes bind to a wide array of diverse aldehydes, allowing for the *in vivo* mapping of total aldehydic load. Work in this field is ongoing to characterize the application of these probes in other clinically-relevant pathologies. In selecting an approach for aldehyde mapping, it is important to consider both the localization of the target aldehydes of interest (i.e. intracellular vs. extracellular), as well as the expected concentration of aldehydic load under the disease conditions of interest. Aldehyde levels can reach several hundred μM in disease[92], which should be contrasted with the inherent sensitivity of Gd- or Mn-based contrast agents (tens of μM)[93] and CEST contrast agents (high μM to low mM)[94]. It should also be noted that both the τ_R-driven contrast enhancement of MnLx-based probes and the resolution of HydrazoCEST contrast production are both field-strength

dependent. These imaging approaches are likely more impactful at lower field (~1.5 T) used clinically, but less suited to the increasingly higher fields used for preclinical work (>7.0 T). As aldehydes may play a key role in the progression of disease, future work may explore the potential for these aldehyde-binding agents to be used as a therapeutic tool sequester aldehydes minimizing their downstream effects. Other imaging modalities like positron emission tomography for mapping aldehydes are being explored to broaden the applications of this class of diagnostic imaging agents[74,95]. Future work is needed to fully characterize all biochemical processes with endogenous aldehyde biproducts in order to identify more diseases with aldehyde-rich signals for which these probes can be used as early detectors of disease.

2.9. References

1 O'Brien, P. J., Siraki, A. G. & Shangari, N. Aldehyde Sources, Metabolism, Molecular Toxicity Mechanisms, and Possible Effects on Human Health. *Critical Reviews in Toxicology* **35**, 609-662, (2005).

2 Backos, D. S., Fritz, K. S., Roede, J. R., Petersen, D. R. & Franklin, C. C. Posttranslational modification and regulation of glutamate–cysteine ligase by the α, β-unsaturated aldehyde 4-hydroxy-2-nonenal. *Free Radical Biology and Medicine* **50**, 14-26, (2011).

3 Usatyuk, P. V. & Natarajan, V. Role of mitogen-activated protein kinases in 4-hydroxy-2-nonenal-induced actin remodeling and barrier function in endothelial cells. *Journal of Biological Chemistry* **279**, 11789-11797, (2004).

4 Usatyuk, P. V. & Natarajan, V. Hydroxyalkenals and oxidized phospholipids modulation of endothelial cytoskeleton, focal adhesion and adherens junction proteins in regulating endothelial barrier function. *Microvascular research* **83**, 45-55, (2012).

5 Barrera, G. *et al.* Lipid peroxidation-derived aldehydes, 4-hydroxynonenal and malondialdehyde in aging-related disorders. *Antioxidants* **7**, 102, (2018).

6 Hayashi, N. *et al.* Acetaldehyde-derived advanced glycation end-products promote alcoholic liver disease. *PloS one* **8**, e70034, (2013).

7 Yang, K., Feng, C., Lip, H., Bruce, W. & O'Brien, P. J. Cytotoxic molecular mechanisms and cytoprotection by enzymic metabolism or autoxidation for glyceraldehyde, hydroxypyruvate and glycolaldehyde. *Chemico-biological interactions* **191**, 315-321, (2011).

8 Thornalley, P., Wolff, S., Crabbe, J. & Stern, A. The autoxidation of glyceraldehyde and other simple monosaccharides under physiological conditions catalysed by buffer ions. *Biochimica et Biophysica Acta (BBA)-General Subjects* **797**, 276-287, (1984).

9 Stewart, T. M., Dunston, T. T., Woster, P. M. & Casero, R. A. Polyamine catabolism and oxidative damage. *Journal of Biological Chemistry* **293**, 18736-18745, (2018).

10 Heinecke, J. W. Pathways for oxidation of low density lipoprotein by myeloperoxidase: tyrosyl radical, reactive aldehydes, hypochlorous acid and molecular chlorine. *Biofactors* **6**, 145-155, (1997).

11 Hazen, S. L., Hsu, F. F., d'Avignon, A. & Heinecke, J. W. Human neutrophils employ myeloperoxidase to convert α-amino acids to a battery of reactive aldehydes: a pathway for aldehyde generation at sites of inflammation. *Biochemistry* **37**, 6864-6873, (1998).

12 Tao, R. *et al.* In Situ Imaging of Formaldehyde in Live Mice with High Spatiotemporal Resolution Reveals Aldehyde Dehydrogenase-2 as a Potential Target for Alzheimer's Disease Treatment. *Analytical Chemistry* **94**, 1308-1317, (2022).

13 Knopp, R. C. *et al.* Interaction of oxidative stress and neurotrauma in ALDH2−/− mice causes significant and persistent behavioral and pro-inflammatory effects in a tractable model of mild traumatic brain injury. *Redox Biology* **32**, 101486, (2020).

14 Cebak, J. E., Singh, I. N., Hill, R. L., Wang, J. A. & Hall, E. D. Phenelzine protects brain mitochondrial function in vitro and in vivo following traumatic brain injury by scavenging the reactive carbonyls 4-hydroxynonenal and acrolein leading to cortical histological neuroprotection. *Journal of neurotrauma* **34**, 1302-1317, (2017).

15 Hall, E. D., Vaishnav, R. A. & Mustafa, A. G. Antioxidant therapies for traumatic brain injury. *Neurotherapeutics* **7**, 51-61, (2010).

16 Shao, C., Roberts, K. N., Markesbery, W. R., Scheff, S. W. & Lovell, M. A. Oxidative stress in head trauma in aging. *Free Radical Biology and Medicine* **41**, 77-85, (2006).

17 Wood, P. L., Khan, M. A. & Moskal, J. R. Mechanism of action of the disease-modifying anti-arthritic thiol agents D-penicillamine and sodium aurothiomalate: restoration of cellular free thiols and sequestration of reactive aldehydes. *European journal of pharmacology* **580**, 48-54, (2008).

18 Ivanova, S. *et al.* Cerebral ischemia enhances polyamine oxidation: identification of enzymatically formed 3-aminopropanal as an endogenous mediator of neuronal and glial cell death. *The Journal of experimental medicine* **188**, 327-340, (1998).
19 Kattoor, A. J., Pothineni, N. V. K., Palagiri, D. & Mehta, J. L. Oxidative stress in atherosclerosis. *Current atherosclerosis reports* **19**, 1-11, (2017).
20 Antoniak, D. T., Duryee, M. J., Mikuls, T. R., Thiele, G. M. & Anderson, D. R. Aldehyde-modified proteins as mediators of early inflammation in atherosclerotic disease. *Free radical biology & medicine* **89**, 409-418, (2015).
21 Xu, C. *et al.* Increased serum levels of aldehydes are associated with cardiovascular disease and cardiovascular risk factors in adults. *Journal of Hazardous Materials* **400**, 123134, (2020).
22 Nair, J., De Flora, S., Izzotti, A. & Bartsch, H. Lipid peroxidation-derived etheno-DNA adducts in human atherosclerotic lesions. *Mutation Research/Fundamental and Molecular Mechanisms of Mutagenesis* **621**, 95-105, (2007).
23 Shearn, C. T. *et al.* Cholestatic liver disease results increased production of reactive aldehydes and an atypical periportal hepatic antioxidant response. *Free Radical Biology and Medicine* **143**, 101-114, (2019).
24 Zhong, Y. *et al.* Lysyl oxidase regulation and protein aldehydes in the injured newborn lung. *American Journal of Physiology-Lung Cellular and Molecular Physiology* **322**, L204-L223, (2022).
25 Fuchs, P., Loeseken, C., Schubert, J. K. & Miekisch, W. Breath gas aldehydes as biomarkers of lung cancer. *International Journal of Cancer* **126**, 2663-2670, (2010).
26 Hu, W. *et al.* The major lipid peroxidation product, trans-4-hydroxy-2-nonenal, preferentially forms DNA adducts at codon 249 of human p53 gene, a unique mutational hotspot in hepatocellular carcinoma. *Carcinogenesis* **23**, 1781-1789, (2002).
27 Young, O., Crotty, T., O'Connell, R., O'Sullivan, J. & Curran, A. J. Levels of oxidative damage and lipid peroxidation in thyroid neoplasia. *Head & Neck: Journal for the Sciences and Specialties of the Head and Neck* **32**, 750-756, (2010).
28 Rockey, D. C., Bell, P. D. & Hill, J. A. Fibrosis—a common pathway to organ injury and failure. *New England Journal of Medicine* **372**, 1138-1149, (2015).
29 Ahluwalia, N., Shea, B. S. & Tager, A. M. New therapeutic targets in idiopathic pulmonary fibrosis. Aiming to rein in runaway wound-healing responses. *American journal of respiratory and critical care medicine* **190**, 867-878, (2014).
30 Schuppan, D. & Afdhal, N. H. Liver cirrhosis. *The Lancet* **371**, 838-851, (2008).
31 Burstein, B. & Nattel, S. Atrial fibrosis: mechanisms and clinical relevance in atrial fibrillation. *Journal of the American College of Cardiology* **51**, 802-809, (2008).
32 Jugdutt, B. I., Joljart, M. J. & Khan, M. I. Rate of collagen deposition during healing and ventricular remodeling after myocardial infarction in rat and dog models. *Circulation* **94**, 94-101, (1996).
33 Sugimoto, H., Grahovac, G., Zeisberg, M. & Kalluri, R. Renal fibrosis and glomerulosclerosis in a new mouse model of diabetic nephropathy and its regression by bone morphogenic protein-7 and advanced glycation end product inhibitors. *Diabetes* **56**, 1825-1833, (2007).
34 Rucker, R. B. *et al.* Copper, lysyl oxidase, and extracellular matrix protein cross-linking. *The American journal of clinical nutrition* **67**, 996S-1002S, (1998).
35 Baker, A., Bird, D., Lang, G., Cox, T. & Erler, J. Lysyl oxidase enzymatic function increases stiffness to drive colorectal cancer progression through FAK. *Oncogene* **32**, 1863-1868, (2013).
36 Chen, H. H. *et al.* Molecular imaging of oxidized collagen quantifies pulmonary and hepatic fibrogenesis. *JCI Insight* **2**, e91506, (2017).
37 Waghorn, P. A., Oliveira, B. L., Jones, C. M., Tager, A. M. & Caravan, P. High sensitivity HPLC method for determination of the allysine concentration in tissue by use of a naphthol derivative. *Journal of Chromatography B* **1064**, 7-13, (2017).

38 Friedman, S. L., Sheppard, D., Duffield, J. S. & Violette, S. Therapy for fibrotic diseases: nearing the starting line. *Science translational medicine* **5**, 167sr161-167sr161, (2013).
39 Mehal, W. Z., Iredale, J. & Friedman, S. L. Scraping fibrosis: expressway to the core of fibrosis. *Nature medicine* **17**, 552-553, (2011).
40 Noble, P. W., Barkauskas, C. E. & Jiang, D. Pulmonary fibrosis: patterns and perpetrators. *The Journal of clinical investigation* **122**, 2756-2762, (2012).
41 Zheng, Q. *et al.* Mortality and survival in idiopathic pulmonary fibrosis: a systematic review and meta-analysis. *ERJ open research* **8**, (2022).
42 Cottin, V. & Richeldi, L. Neglected evidence in idiopathic pulmonary fibrosis and the importance of early diagnosis and treatment. *European Respiratory Review* **23**, 106-110, (2014).
43 Younossi, Z. M. *et al.* The global epidemiology of nonalcoholic fatty liver disease (NAFLD) and nonalcoholic steatohepatitis (NASH): a systematic review. *Hepatology* **77**, 1335-1347, (2023).
44 Tapper, E. B. & Lok, A. S.-F. Use of liver imaging and biopsy in clinical practice. *New England Journal of Medicine* **377**, 756-768, (2017).
45 Hagström, H. *et al.* Fibrosis stage but not NASH predicts mortality and time to development of severe liver disease in biopsy-proven NAFLD. *Journal of hepatology* **67**, 1265-1273, (2017).
46 Tapper, E. B. & Loomba, R. Noninvasive imaging biomarker assessment of liver fibrosis by elastography in NAFLD. *Nature reviews Gastroenterology & hepatology* **15**, 274-282, (2018).
47 Sanyal, A. J. *et al.* Non-invasive biomarkers of nonalcoholic steatohepatitis: the FNIH NIMBLE project. *Nature medicine* **28**, 430-432, (2022).
48 Chen, W. *et al.* Lysyl oxidase (LOX) family members: rationale and their potential as therapeutic targets for liver fibrosis. *Hepatology* **72**, 729-741, (2020).
49 Yuen, L. H., Saxena, N. S., Park, H. S., Weinberg, K. & Kool, E. T. Dark hydrazone fluorescence labeling agents enable imaging of cellular aldehydic load. *ACS chemical biology* **11**, 2312-2319, (2016).
50 Chen, J. *et al.* Toward a biomarker of oxidative stress: a fluorescent probe for exogenous and endogenous malondialdehyde in living cells. *Analytical Chemistry* **87**, 8052-8056, (2015).
51 Brewer, T. F. & Chang, C. J. An aza-cope reactivity-based fluorescent probe for imaging formaldehyde in living cells. *Journal of the American Chemical Society* **137**, 10886-10889, (2015).
52 Zhou, I. Y., Catalano, O. A. & Caravan, P. Advances in functional and molecular MRI technologies in chronic liver diseases. *Journal of Hepatology* **73**, 1241-1254, (2020).
53 Zhou, I. Y. *et al.* Advanced MRI of Liver Fibrosis and Treatment Response in a Rat Model of Nonalcoholic Steatohepatitis. *Radiology* **296**, 67-75, (2020).
54 Waghorn, P. A. *et al.* Molecular Magnetic Resonance Imaging of Lung Fibrogenesis with an Oxyamine-Based Probe. *Angewandte Chemie International Edition* **56**, 9825-9828, (2017).
55 Chen, H. H. *et al.* Molecular imaging of oxidized collagen quantifies pulmonary and hepatic fibrogenesis. *JCI insight* **2**, (2017).
56 Ramalho, J. *et al.* Gadolinium-based contrast agent accumulation and toxicity: an update. *American Journal of Neuroradiology* **37**, 1192-1198, (2016).
57 Bousquet, J.-C. *et al.* Gd-DOTA: characterization of a new paramagnetic complex. *Radiology* **166**, 693-698, (1988).
58 Chen, Y.-C. *et al.* Molecular MR imaging of renal Fibrogenesis in mice. *Journal of the American Society of Nephrology* **34**, 1159-1165, (2023).
59 Erstad, D. J. *et al.* Molecular magnetic resonance imaging accurately measures the antifibrotic effect of EDP-305, a novel farnesoid X receptor agonist. *Hepatol Commun* **2**, 821-835, (2018).
60 Ferreira, D. S. *et al.* Molecular Magnetic Resonance Imaging of Liver Fibrosis and Fibrogenesis Is Not Altered by Inflammation. *Invest Radiol* **56**, 244-251, (2021).
61 Waghorn, P. A. *et al.* Quantitative, noninvasive MRI characterization of disease progression in a mouse model of non-alcoholic steatohepatitis. *Scientific Reports* **11**, 6105, (2021).

62 Akam, E. A. *et al.* Improving the reactivity of hydrazine-bearing MRI probes for in vivo imaging of lung fibrogenesis. *Chemical Science* **11**, 224-231, (2020).
63 Ning, Y. *et al.* Molecular MRI quantification of extracellular aldehyde pairs for early detection of liver fibrogenesis and response to treatment. *Science Translational Medicine* **14**, eabq6297, (2022).
64 Kawahara, K. *et al.* Spatiotemporal regulation of PEDF signaling by type I collagen remodeling. *Proceedings of the National Academy of Sciences* **117**, 11450-11458, (2020).
65 Yamauchi, M. & Sricholpech, M. Lysine post-translational modifications of collagen. *Essays in biochemistry* **52**, 113-133, (2012).
66 Ning, Y. *et al.* Dual Hydrazine-Equipped Turn-On Manganese-Based Probes for Magnetic Resonance Imaging of Liver Fibrogenesis. *Journal of the American Chemical Society* **144**, 16553-16558, (2022).
67 Kanal, E. Gadolinium based contrast agents (GBCA): Safety overview after 3 decades of clinical experience. *Magnetic resonance imaging* **34**, 1341-1345, (2016).
68 Garda, Z. *et al.* Physico-chemical properties of MnII complexes formed with cis- and trans-DO2A: thermodynamic, electrochemical and kinetic studies. *Journal of Inorganic Biochemistry* **163**, 206-213, (2016).
69 Ma, H. *et al.* Tailored Chemical Reactivity Probes for Systemic Imaging of Aldehydes in Fibroproliferative Diseases. *Journal of the American Chemical Society* **145**, 20825-20836, (2023).
70 Wood, P. L., Khan, M. A. & Moskal, J. R. The concept of "aldehyde load" in neurodegenerative mechanisms: cytotoxicity of the polyamine degradation products hydrogen peroxide, acrolein, 3-aminopropanal, 3-acetamidopropanal and 4-aminobutanal in a retinal ganglion cell line. *Brain research* **1145**, 150-156, (2007).
71 Ellis, E. M. Reactive carbonyls and oxidative stress: potential for therapeutic intervention. *Pharmacology & therapeutics* **115**, 13-24, (2007).
72 Suchý, M. *et al.* Methyl 5-MeO-N-aminoanthranilate, a minimalist fluorogenic probe for sensing cellular aldehydic load. *Organic & biomolecular chemistry* **17**, 1843-1853, (2019).
73 Lazurko, C. *et al.* Fingerprinting Biogenic Aldehydes Through Pattern Recognition Analyses of Excitation-Emission Matrices. *ChemBioChem* **40**, 543-554, (2019).
74 Kirby, A., Suchý, M., Brouwer, A. & Shuhendler, A. Mapping aldehydic load in vivo by positron emission tomography with [18 F] NA 3 BF 3. *Chemical Communications* **55**, 5371-5374, (2019).
75 Dang, T. *et al.* Hydrazo-CEST: Hydrazone-Dependent Chemical Exchange Saturation Transfer Magnetic Resonance Imaging Contrast Agents. *Chemistry – A European Journal* **24**, 9148-9156, (2018).
76 Brun, E. M. S. P.-T. *et al.* Mapping vitamin B 6 metabolism by hydrazoCEST magnetic resonance imaging. *Chemical Communications* **57**, 10867-10870, (2021).
77 Ward, K., Aletras, A. & Balaban, R. S. A new class of contrast agents for MRI based on proton chemical exchange dependent saturation transfer (CEST). *Journal of magnetic resonance* **143**, 79-87, (2000).
78 Bar-Shir, A., Bulte, J. W. M. & Gilad, A. A. Molecular Engineering of Nonmetallic Biosensors for CEST MRI. *ACS Chemical Biology* **10**, 1160-1170, (2015).
79 Percudani, R. & Peracchi, A. A genomic overview of pyridoxal-phosphate-dependent enzymes. *EMBO reports* **4**, 850-854, (2003).
80 Miller, J., Green, R., Mungas, D., Reed, B. & Jagust, W. Homocysteine, vitamin B6, and vascular disease in AD patients. *Neurology* **58**, 1471-1475, (2002).
81 Kuypers, N. J. & Hoane, M. R. Pyridoxine administration improves behavioral and anatomical outcome after unilateral contusion injury in the rat. *Journal of neurotrauma* **27**, 1275-1282, (2010).
82 Mikkelsen, K., Stojanovska, L. & Apostolopoulos, V. The effects of vitamin B in depression. *Current medicinal chemistry* **23**, 4317-4337, (2016).

83 Niculescu, A. *et al.* Towards precision medicine for pain: diagnostic biomarkers and repurposed drugs. *Molecular psychiatry* **24**, 501-522, (2019).
84 Galluzzi, L. *et al.* Prognostic impact of vitamin B6 metabolism in lung cancer. *Cell reports* **2**, 257-269, (2012).
85 Kirby, A. *et al.* Aldehydic load as an objective imaging biomarker of mild traumatic brain injury. *bioRxiv*, 2024.2004.2016.589820, (2024).
86 Haydel, M. J. *et al.* Indications for computed tomography in patients with minor head injury. *New England Journal of Medicine* **343**, 100-105, (2000).
87 Homer, C. J. & Kleinman, L. Technical report: minor head injury in children. *Pediatrics* **104**, e78-e78, (1999).
88 Cassidy, J. D. *et al.* Incidence, risk factors and prevention of mild traumatic brain injury: results of the WHO Collaborating Centre Task Force on Mild Traumatic Brain Injury. *Journal of rehabilitation medicine* **36**, 28-60, (2004).
89 Stephenson, S., Langley, J. & Cryer, C. Effects of service delivery versus changes in incidence on trends in injury: a demonstration using hospitalised traumatic brain injury. *Accident Analysis & Prevention* **37**, 825-832, (2005).
90 Yates, N. J. *et al.* Repeated mild traumatic brain injury in female rats increases lipid peroxidation in neurons. *Experimental brain research* **235**, 2133-2149, (2017).
91 Zahedi, K. *et al.* Polyamine catabolism is enhanced after traumatic brain injury. *Journal of neurotrauma* **27**, 515-525, (2010).
92 Niki, E. Lipid peroxidation: physiological levels and dual biological effects. *Free Radical Biology and Medicine* **47**, 469-484, (2009).
93 Caravan, P. Strategies for increasing the sensitivity of gadolinium based MRI contrast agents. *Chemical Society Reviews* **35**, 512-523, (2006).
94 Liu, G. & van Zijl, P. C. in *Molecular Imaging* 325-341 (Elsevier, 2021).
95 Wahsner, J. *et al.* 68Ga-NODAGA-indole: an allysine-reactive positron emission tomography probe for molecular imaging of pulmonary fibrogenesis. *Journal of the American Chemical Society* **141**, 5593-5596, (2019).

Chapter 3: Methyl 5-MeO-*N*-aminoanthranilate, a minimalist fluorogenic probe for sensing cellular aldehydic load

Mojmír Suchý,[a,c] Caitlin Lazurko,[a] Alexia Kirby,[b,c] Trina Dang,[a] George Liu,[a] and Adam J. Shuhendler[a,c*]

[a]Department of Chemistry & Biomolecular Sciences, University of Ottawa, Ottawa, ON, Canada.

[b]Department of Biology, University of Ottawa, Ottawa, ON, Canada

[c]University of Ottawa Heart Institute, Ottawa, ON, Canada

*Corresponding author: Adam Shuhendler (adam.shuhendler@uottawa.ca)

3.1. Introduction to the Research Article Presented Within this Chapter

An early goal of the Molecular Medicine Lab was to develop tools to image aldehydes in live cells and animals as a biomarker for oxidative stress and its associated pathologies. As aldehydes are transient, highly electrophilic products of cell stress, a trapping moiety must bind rapidly, covalently, and irreversibly to aldehydes, proceed through a bimolecular mechanism, and be stable and non-toxic in physiological conditions. These challenging requirements are likely the cause of the lack of imaging probes for aldehydes in the literature. An earlier publication from the group showed a similar probe, 5-MeO-*N*-aminoanthranilic acid, reacts with endogenous aldehydes and produces a CEST-MRI signal. 5-MeO-*N*-aminoanthranilate was then prepared, and its fluorescent properties were studied upon reaction with different biogenic aldehydes. The work presented in this chapter represents the evaluation of 5-MeO-*N*-aminoanthranilate as a fluorogenic probe for the mapping of aldehydic load in live cells.

3.2. Author Contributions

MS, AK and AS designed experiments and wrote the manuscript. MS, CL, TD and GL performed chemistry experiments. AK developed methodology, cell models, and performed all experiments on cells, including microscopy, and analysis of micrographs.

3.3. Copyright

3.4. Abstract

Methyl 5-MeO-*N*-aminoanthranilate, a fluorogenic probe comprising a single substituted benzene ring has been applied towards the fluorescence detection of endogenous carbonyls through rapid, catalyst-free complexation of these bio-derived markers of cell stress under physiological conditions. The products formed during the reaction between the probe and aldehydic products of lipid peroxidation, including malondialdehyde and long-chain aliphatic aldehydes relevant to the oxidative decomposition of cell membranes, have been evaluated. Live cell imaging of diethyl maleate-induced oxidative stress with or

without pretreatment with α-tocopherol was carried out, with the result suggesting that the presented molecule might serve as a minimalist molecular probe capable of cellular "Aldehydic Load" detection by fluorescence microscopy. This work also outlines functional constraints of the fluorogenic probe (i.e. intramolecular cyclization), providing a realistic evaluation of methyl 5-MeO-*N*-aminoanthranilate for fluorescence-based aldehyde detection.

3.5. Introduction

Anthranilic acid (**1a**, Figure 3.1) and methyl anthranilate (**1b**, Figure 3.1) are among the simplest naturally occurring fluorophores, exhibiting long excited state life times (8.7 ns) along with high quantum yields in aqueous solution ($\Phi \sim 0.60$).[1] Although these properties appear to make the anthranilic acid-based fluorophores attractive probes for molecular biology, their use in the context of the development of imaging probes is still in its infancy.[2,3] This can be in part attributed to the fact that anthranilic acid-based fluorophores require high energy excitation (320 - 350 nm) and emit in the violet to blue region (λ_{em} 410 – 470 nm).[1] Moreover, the synthetic methodologies describing their incorporation into larger molecular entities are rather limited.[4,5]

Kool and co-workers have recently shown that substituted anthranilic acids can auto-catalyze the reaction between hydrazines and carbonyl compounds (aldehydes and ketones denoted herein as carbonyls) to form hydrazones.[6,7] When anthranilic acid is converted into the corresponding hydrazine (*N*-aminoanthranilic acid, **1c**, Figure 3.1), the rate of the reaction with carbonyls increases dramatically even surpassing that associated with strain-promoted "click" reactions, which makes *N*-aminoanthranilates attractive reactive head-groups for the rapid, catalyst-free trapping of biogenic carbonyls under physiological conditions.[8,9]

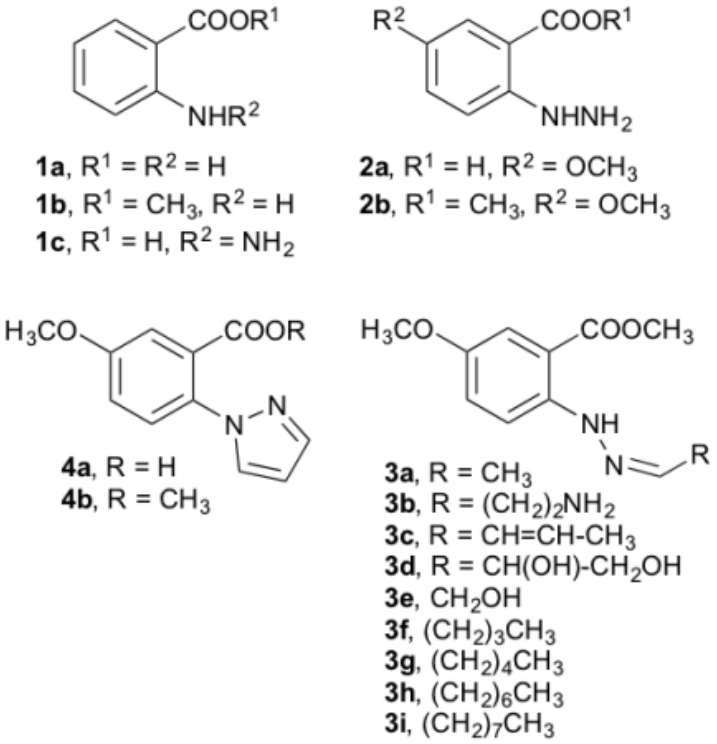

Figure 3.1 Structures of anthranilic acids and anthranilates 1a-1c, 2a, 2b, hydrazones 3a-3i, pyrazoles 4a and 4b.

It is now well established that the exposure of humans to carbonyls has a negative impact on health and well-being.[10] Although some carbonyls are present in the environment as a consequence of industrial operations (e. g. acetone, formaldehyde), many simple carbonyls (e. g. acetaldehyde, glyceraldehyde, pyruvate) are also produced endogenously *via* tightly regulated metabolic pathways.[10] Increased production of carbonyls upon the disruption of homeostasis often times underlies early stages of various pathologies, including diabetes (e. g. acetone),[11] cancer (e. g. simple aliphatic aldehydes)[12] cardiovascular diseases [e. g. acrolein, malondialdehyde (MDA)][13] or traumatic brain injury (e. g. 3-aminopropanal).[14] The ability to properly design, synthesize and evaluate molecular probes capable of *in vitro* or *in vivo* mapping of total endogenous carbonyls

(denoted herein as Aldehydic Load) is of significant interest to the scientific community,[15-19] as the outcomes of these research efforts are expected to facilitate our fundamental understanding of, and ability to diagnose, a wide range of illnesses affecting a significant part of the global population.

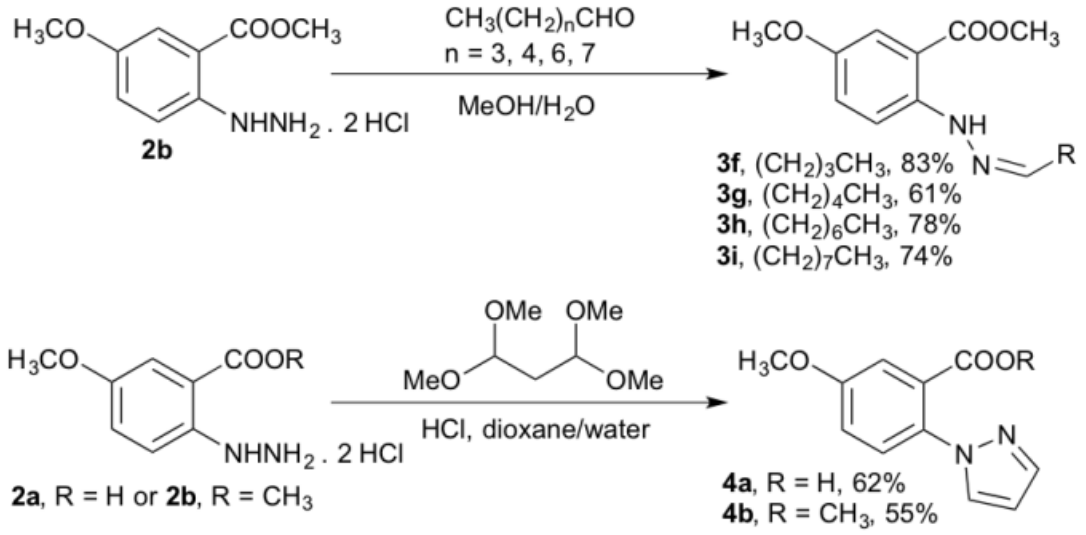

Scheme 3.1 Preparation of hydrazones **3f-3i** and pyrazoles **4a** and **4b**

The development of molecular imaging probes capable of reporting on Aldehydic Load at both the *in vitro* and *in vivo* scales is one of the key research avenues currently pursued in our laboratory. We have recently shown that 5-MeO-*N*-aminoanthranilic acid (**2a**, Figure 3.1) a simple anthranilic acid-based hydrazine can act as a Chemical Exchange Saturation Transfer Magnetic Resonance Imaging (CEST MRI) contrast agent upon reaction with endogenous aldehydes (e.g. acetaldehyde, 3-aminopropanal).[9] During the course of our studies, we have also prepared methyl 5-MeO-*N*-aminoanthranilate (**2b**, Figure 3.1) and allowed it to react with several endogenous carbonyls. The majority of the products we obtained upon reaction with aldehydes (hydrazones **3a-3e**, Figure 3.1) were found to fluoresce in the blue to blue-green region of the spectrum; therefore we decided to study their fluorescence in greater detail. As described recently, we have acquired excitation-emission matrices (EEM) associated with compounds **3a-3e** (Figure 3.1), and have concurrently developed a novel pattern matching algorithm for the fluorescent fingerprinting of biogenic

carbonyls.[20] This approach allowed us to determine both the total amount of aldehyde (i.e. Aldehydic Load), as well as the identity of individual components of carbonyl mixtures. As an expansion to our previous studies, we are describing herein the fluorescence properties associated with hydrazones derived from longer chain aliphatic aldehydes as putative end-products of lipid peroxidation (compounds **3f-3i**, Figure 3.1), and validating the use of **2b** as a fluorogenic probe capable of mapping Aldehydic Load *via* live cell microscopy in a model of oxidative stress. We have also carried out detailed mechanistic studies to elucidate the mechanism of the reaction between methyl 5-MeO-*N*-aminoanthranilate (**2b**, Figure 3.1) and the dialdehyde MDA to form a pyrazole ring through an *in situ* detected hydrazone intermediate. The further understanding of the reaction mechanisms of methyl 5-MeO-*N*-aminoanthranilate with biogenic carbonyls reported in this work supports the utility of this minimalist fluorogenic probe, and advocates for its value as a novel tool for studying the chemical biology of lipid peroxidation in live cells.

3.6. Results and Discussion

3.6.1. Preparation of hydrazone/pyrazole standards and evaluation of their fluorescent properties

Chemical synthesis of the probes was carried out as outlined in Scheme 3.1. Reaction of methyl 5-MeO-*N*-aminoanthranilate (**2b**) with simple longer chain aliphatic aldehydes (pentanal, hexanal, octanal, nonanal) afforded hydrazones **3f-3i** in good yields (61-83%). The final compounds were purified by flash column chromatography (FCC) and were obtained as inseparable mixtures of *E* and *Z* isomers in approximately a 2:3 ratio (major isomer not identified). Observed results are in contrast with the synthesis of previously described hydrazones (**3a-3e**, Figure 3.1),[20] which were obtained either as a single isomer, or where the amount of the minor isomer was negligible (< 5%). Fluorescence spectra of hydrazones **3f-3i** were acquired in phosphate buffered saline (1 × PBS, pH 7.2) containing up to 10% DMSO (Figure 3.2), and relative quantum yields (Φ) were determined using harmane as a standard (Table 3.1).[21]

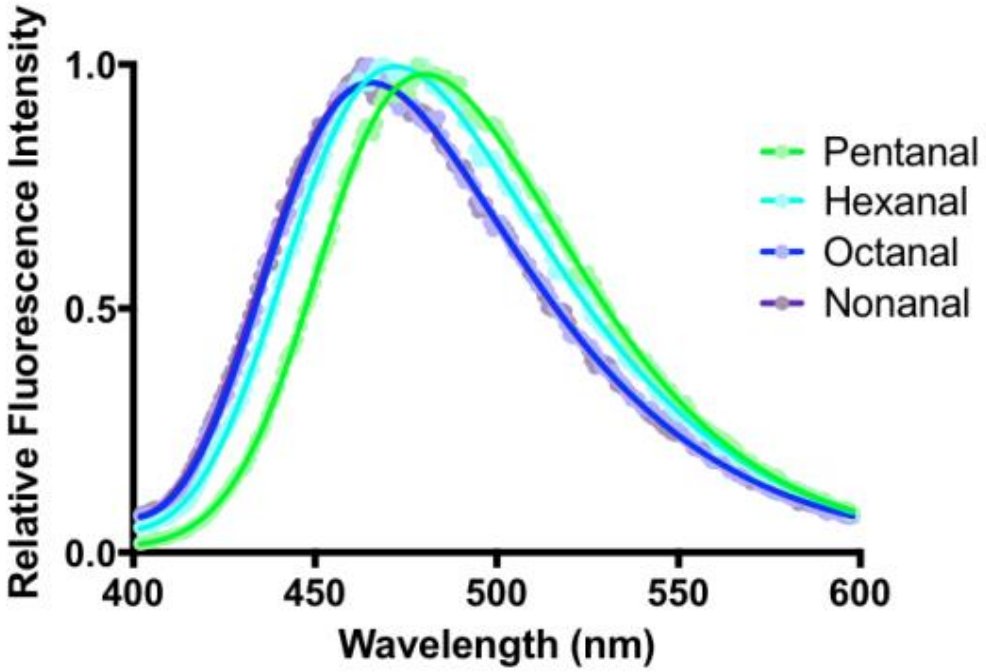

Figure 3.2 Emission scans for hydrazones derived from 2b and aliphatic aldehydes 3f (green), 3g (cyan), 3h (blue), and 3i (purple) acquired with lex = 370 nm

Table 2.1 Fluorescence properties associated with hydrazones 3f-3i

Compound	f(harmane)	l_{ex} (nm)	e (m^2mol^{-1})	l_{em} (nm)	Stoke's Shift (nm)
3f	0.17	372	5631	480	108
3g	0.08	376	7107	475	99
3h	0.08	377	8410	467	90
3i	0.06	378	8025	466	88

While the excitation wavelengths appear to be independent of the hydrazone structure and only vary by 6 nm, the emission wavelengths as well as Stoke's shifts decrease slightly with increasing length of the carbon chain. Fluorescence quantum yields were found to be relatively low, possibly a

consequence of the presence of two inseparable isomers, and decreased with an increased length of aldehyde carbon chain. When 5-MeO-*N*-aminoanthranilic acid (**2a**) or methyl 5-MeO-*N*-aminoanthranilate (**2b**) were treated with MDA tetramethyl acetal, pyrazoles **4a** and **4b** were obtained in moderate yield (Scheme 3.1) upon purification by FCC as described recently.[21]

3.6.2. Pyrazole formation from MDA and methyl-5-MeO-*N*-aminoanthranilate (2b) proceeds through a long-lived fluorescent hydrazone intermediate

Malondialdehyde (MDA, **5**, Scheme 3.2), a terminal product of polyunsaturated fatty acid peroxidation mediated by reactive oxygen species (ROS) is regarded as a classical marker of oxidative stress.[22] MDA occurs as an equilibrium of two tautomers (Scheme 3.2), is a known mutagen,[23,24] and has been associated with early stages of various pathologies (e. g. cancer,[25] atherosclerosis,[26] stroke,[27] Alzheimer's disease[28]). MDA has classically been assayed in cells or tissue extracts through treatment with thiobarbituric acid (**6**, Scheme 3.2) with the formation of a red coloured dye **7** under harsh conditions.[29]

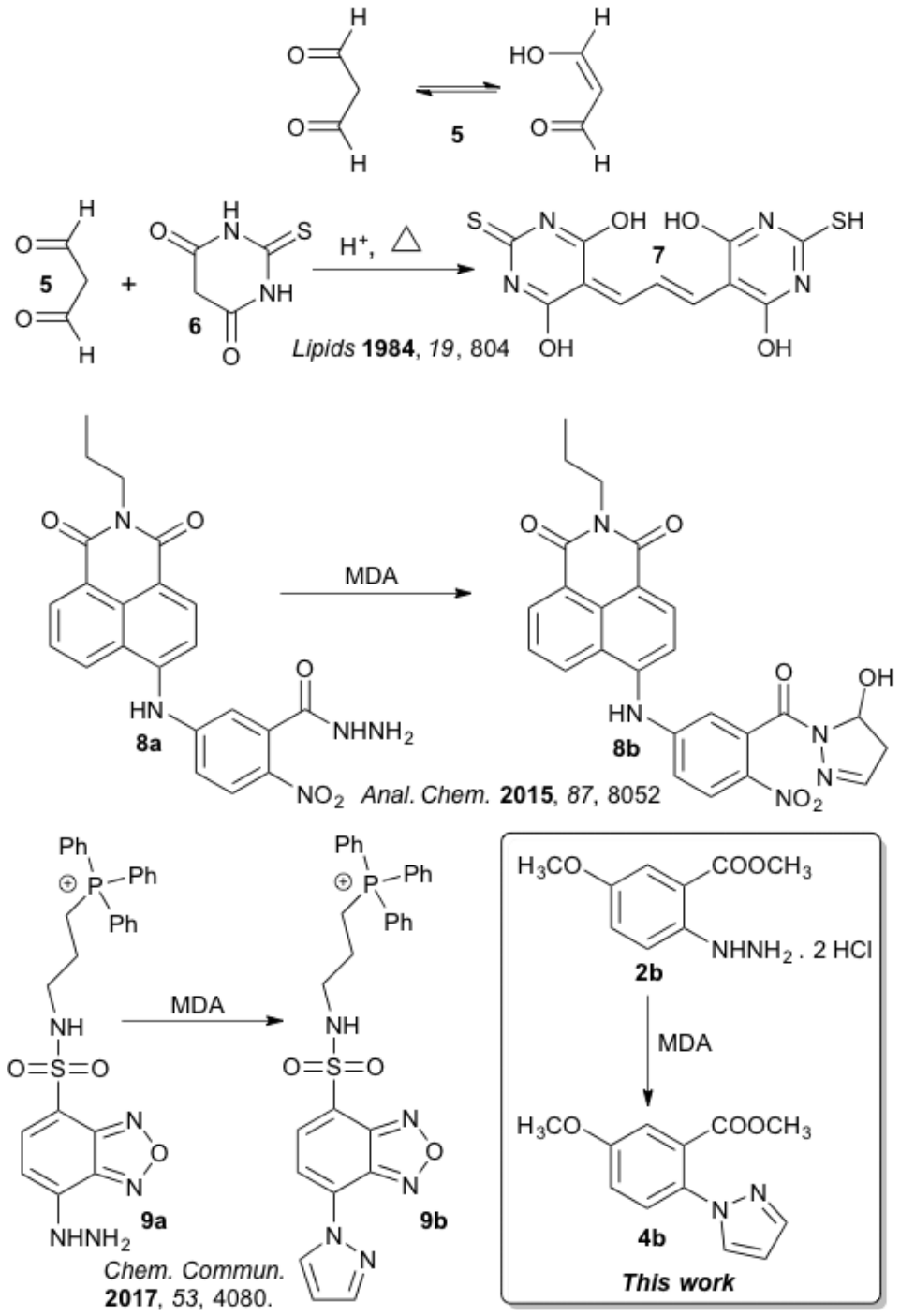

Scheme 3.2 Structure of MDA, colourimetric (**6** → **7**) and fluorogenic probes (**8a** → **8b**; **9a** → **9b**) used for its detection previously. The fluorogenic probe (**2b** → **4b**) investigated in this work is structurally simpler than previous probe examples.

The development of a molecular imaging probe capable of *in situ* complexation of MDA in live cells in order to more accurately map concentrations has been challenging due to the high reactivity of MDA in living systems, which is partly attributable to its presence in two tautomeric forms.[30] Recent efforts toward this end include two green fluorescent probes (**8a**,[31] **9a**,[32] Scheme 3.2), bearing a hydrazide/hydrazine subunit reported to quench fluorescence *via* photoinduced electron transfer (PET). Upon reaction with MDA, a five-membered pyrazolidine/pyrazole ring is formed (compounds **8b**, **9b**, Scheme 3.2), limiting PET to result in a strong fluorescence turn-on.[31,32] Both **8a** and **9a** show excellent selectivity toward MDA, as no fluorescence response is observed upon exposure to other carbonyls.[31,32] Interestingly, this observation is in contrast with our results using methyl 5-MeO-*N*-aminoanthranilate (**2b**), wherein the reaction with a range of simple endogenous carbonyls leads to the formation of fluorescent hydrazones (e. g. compounds **3a-3i**).[20] Although the detailed mechanism of the fluorescence signal turn on associated with the **8a** → **8b** transformation has been proposed based on NOESY measurements,[31] no evidence for the suggested mechanism associated with the signal turn on upon **9a** → **9b** conversion has been provided.[32] Due to differential aldehyde selectivity of **2b** relative to **8a** and **9a**, a detailed mechanistic evaluation of the reaction of MDA with 5-MeO-*N*-aminoanthranilic acid (**2a**) and methyl 5-MeO-*N*-aminoanthranilate (**2b**) was undertaken.

Compound **2b** (Figure 3.1, Scheme 3.2) contains a hydrazine subunit and is known to form a pyrazole ring (compound **4b**, Scheme 3.2) upon exposure to MDA.[20] The structure of pyrazole **4b** is simple, with well-resolved resonances in its ^{1}H NMR spectrum,[20] which permitted a detailed ^{1}H NMR-based kinetic analysis to be carried out in order to fully understand the transformation of 5-MeO-*N*-aminoanthranilic acid (**2a**) and methyl 5-MeO-*N*-aminoanthranilate (**2b**) to pyrazoles **4a** and **4b** upon reaction with MDA.

Since the main chemical shift differences due to pyrazole formation were expected in the aromatic region (6 – 8 ppm), only changes occurring within this range are depicted in Figure 3.3 and discussed below. Note that full views of the spectra can be found in Supporting Figures S1 and S2. Briefly, within this region both hydrazines **2a** and **2b** exhibit three distinct signals (**2a**, d, 7.26 ppm, J = 3 Hz, H^6; d, 7.08 ppm, J = 9 Hz, H^3; dd, 7.01 ppm, J = 9, 3 Hz, H4; **2b**, d, 7.52 ppm, J = 3 Hz, H6; dd, 7.20 ppm, J = 9, 3 Hz, H4; d, 7.05 ppm, J = 9 Hz, H3) fully consistent with the substitution pattern present in **2a** and **2b**.

Baseline 1H-NMR were acquired of separate solutions of 1 mg of **2a** or **2b** in 1 × PBS, pH 7.2 containing 10% DMSO-D6, followed by the addition of 1 drop of a 1 M solution of MDA tetramethyl acetal in 1 M HCl, known to form MDA in situ.[33] Further acquisitions of ^{1}H NMR spectra occurred immediately (1 min), 2 min, 4 min, 20 min and, for compound **2b** only, 2 h after MDA addition (Figure 3.3). To allow for this rapid spectral acquisition following addition of MDA, neither locking of the signal nor shimming was carried out. The reaction of hydrazines **2a** and **2b** with MDA led to the rapid formation (within 1 min) of new peaks associated with a putative pyrazole ring, as well as a slight change in benzene ring chemical shifts associated with starting materials **2a** and **2b**. Three new signals at ca. 7.8 (HC), 7.7 (HA) and 6.5 ppm (HB) are observed in both instances and their intensity increases with time (Figure 3.3). The presence of the new signals is fully consistent with the formation of the pyrazole scaffold in both, **4a** and **4b** (see the Experimental and ESI for the details), with only slight changes in chemical shifts (≤ 0.1 ppm) between the products of the reactions observed at the terminal time points (**4a**, 20 min; **4b**, 2 h) and corresponding pyrazole standards **4a** and **4b** having their spectra acquired under identical conditions.

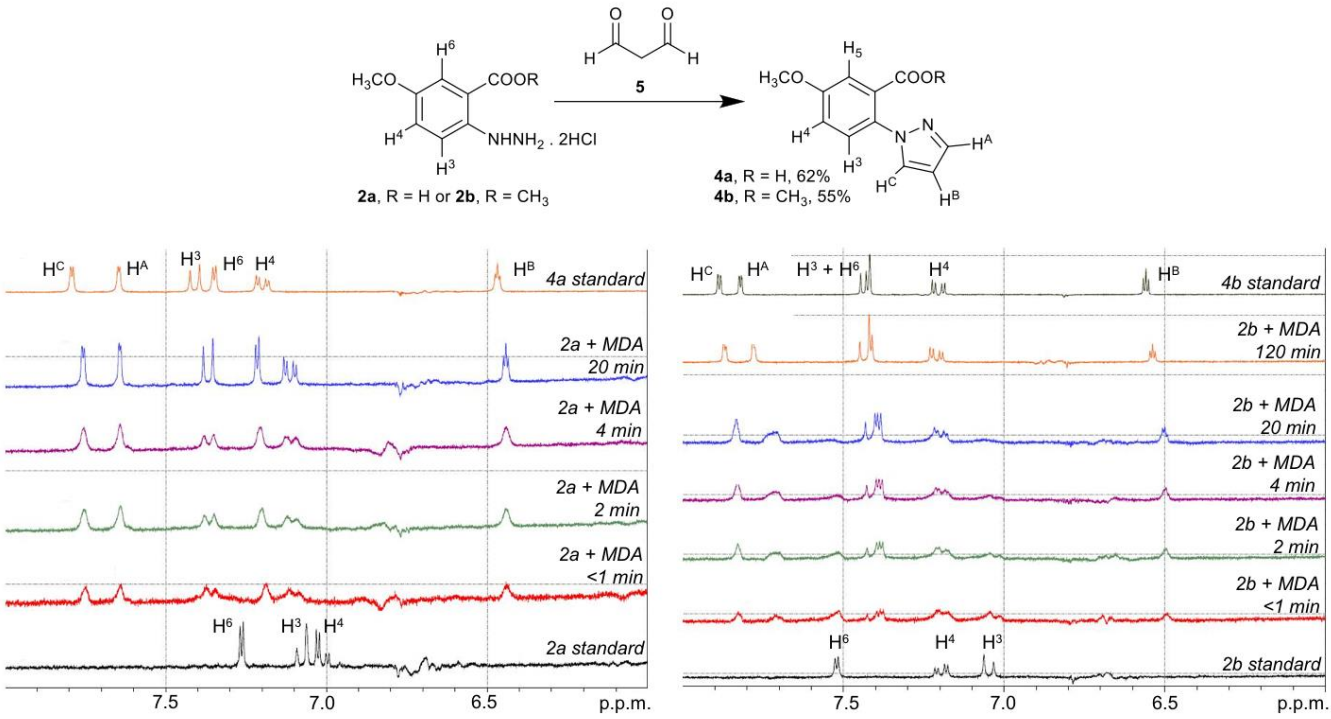

Figure 3. 3 Detailed ^{1}H NMR analysis of the reactions between 5-MeO-N-aminoanthranilic acid (2a) and MDA (left), or methyl 5-MeO-N-aminoanthranilate (2b) and MDA (right). Spectra shown are before MDA addition (black), and <1 min (red), 2 min (green), 4 min (purple), 20 min (blue), and 2 h (orange) after MDA addition. Brown and grey spectra are those of authentic standards **4a** (left) or **4b** (right).

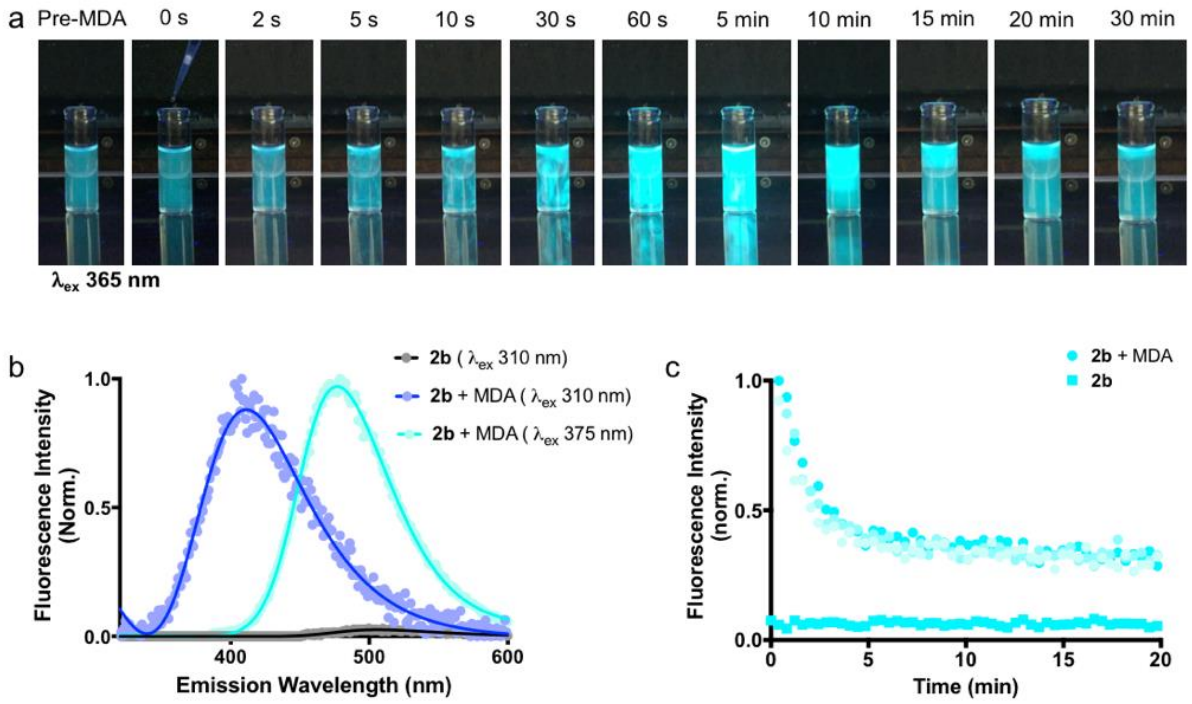

Figure 3.4 Methyl 5-MeO-N-aminoanthranilate (2b) as a fluorogenic probe for the detection of MDA. (**a**) MDA was added to a 25 mM PBS solution of **2b** (pH 7.2) under illumination at 365 nm, and photographed at indicated time points. (**b**) Emission spectra of 1 mM **2b** (black), or **2b** after 1 min incubation with 5 eq. MDA at 37 °C and excited at 310 nm (blue) or 375 nm (cyan). (**c**) Formation and rapid decay of short lived intermediate **10** formed in the reaction between methyl 5-MeO-*N*-aminoanthranilate (**2b**) and MDA followed by fluorescence spectroscopy with l_{ex}/l_{em} = 375/480 nm. Kinetics of 25 mM **2b** alone (squares) and **2b** + MDA (circles) are shown, with three individual trials of **2b** + MDA shown (light, medium, and dark cyan).

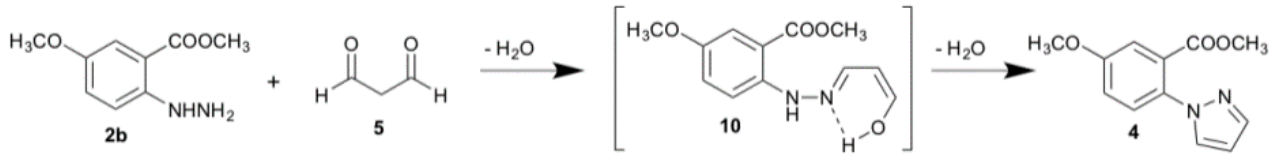

Scheme 3.3 Reaction between hydrazine **2b** and MDA proceeds *via* short lived intermediate 10

This deviation in chemical shift is likely caused by the fact that the spectrometer was not shimmed prior to the acquisition of spectra during the time-course study. Consistent with our previous observations,[9] the reaction of hydrazine **2a** with MDA occurred very rapidly and only traces of the hydrazone intermediate can be observed as a small shoulder associated with the signal at ca. 7.7 ppm (H^A) in the NMR spectra acquired at earlier time points up until 4 min (Figure 3.3, left). However, the signal observed at 7.7 ppm (H^A) was of particular interest in the NMR spectra associated with hydrazine **2b** wherein the signal is broad and unresolved even after 20 min of reaction, and a distinct doublet is observed after 2 h (Figure 3.3, right). This observation prompted us to propose that a short-lived hydrazone intermediate is present in solution and observable by NMR spectroscopy.

In order to further investigate the formation and fate of the proposed hydrazone intermediate observed by ^{1}H NMR spectroscopy, we performed an identical experiment to that performed for the NMR study however using fluorescence spectroscopy as read out. Fluorescence spectra associated with pyrazoles **4a** and **4b** were measured in 1 × PBS, pH 7.2, containing 10% DMSO (Figures ESI47 and 48). Pyrazole **4a** is a weak ($\Phi < 0.02$, harmane) blue fluorophore (λ_{ex} 258 nm, λ_{em} 391 nm, Stoke's shift 133 nm), which precluded a detailed investigation of the reaction of **2a** with MDA by fluorescence spectroscopy. However, the replacement of the carboxylic acid moiety in pyrazole **4b** with the ester leads to a significant increase (>20 fold) in quantum yield (Φ 0.45, harmane)[20] as well as a red shift of both excitation and emission wavelengths (**4b**, λ_{ex} 307 nm, λ_{em} 410 nm, Stoke's shift 103 nm), allowing for a detailed fluorescence-guided investigation of the reaction between methyl 5-MeO-*N*-aminoanthranilate (**2b**) and MDA.

Upon mixing hydrazine **2b** with MDA under illumination by UV lamp (λ_{ex} 365 nm), the evolution of blue-green fluorescence was observed within 1 minute (Figure 3.4a), which was red-shifted relative to the expected fluorescence of the synthesized pyrazole standard, compound **4b** (λ_{em} 410 nm). Detailed measurement of the fluorescence associated with the obtained mixture revealed two

fluorescent species in solution: one with spectral properties expected from compound **4b** (λ_{ex} 307 nm, λ_{em} 410 nm), and the other with λ_{ex} 371 nm as an optimal excitation wavelength and associated emission at λ_{em}478 nm (Stoke's shift 107 nm, Figure 3.4b). When the mixture was left at room temperature (rt) for 30 minutes, the initially observed blue-green fluorescence was no longer visible, but instead the mixture produced a deep blue fluorescence with photophysical properties matching those of **4b**. Fluorescence kinetic measurements were carried out that recapitulated these qualitative observations (Figure 3.4c). An initial formation of the blue-green fluorescent species takes place rapidly, followed by a rapid decrease of the fluorescent signal at λ_{em} 480 nm by 50% within 5 minutes, and then a slower decrease over a longer period of time.

Considering the results of the fluorescence-based kinetic study along with those from the detailed NMR experiment, a mechanism for the reaction of **2b** with MDA is proposed (Scheme 3.3). While we believe that an identical mechanism operates in the case of the transformation **2a** → **4a** supported by the NMR study, we were unable to support this hypothesis by fluorescence measurements. The reaction of **2b** with MDA leads to the formation of the hydrazone intermediate **10**, which is transiently stabilized by the presence of a hydrogen bond between the terminal hydrazone nitrogen and the hydroxyl group of the enol tautomer of intermediate **10**. The enol tautomer would be favoured by the intramolecular hydrogen bond resulting in a pseudo-aromatic six-membered ring. The nucleophilic attack of the ring-proximal nitrogen group present in the hydrazone moiety onto the electrophilic carbonyl would then take place, ultimately leading to the formation of pyrazole **4b** (Scheme 3.3). Importantly, the intensity of the observed blue-green emission peak was dependent on MDA concentration, supporting the hypothesis that the observed fluorescence was associated with a semi-stable reaction intermediate **10** (Figure 3.5).

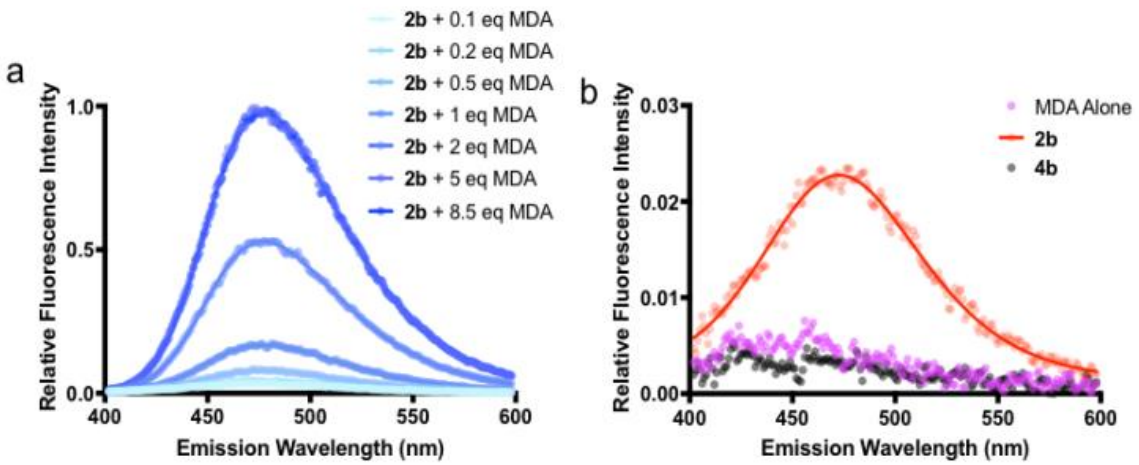

Figure 3.5 The formation of the fluorescent hydrazone intermediate 10 is dependent upon MDA concentration. (a) A 1 mM solution of **2b** in PBS (pH 7.2) was mixed with the indicated molar equivalents of MDA and an emission scan was recorded immediately after mixing usingl_{ex} 375 nm (blue curves). (b) Emission scans for MDA alone (open circles), **2b** alone (red), and the pyrazole standard **4b** (black) are also shown. Note the difference in the y-axis scaling between panels a and b.

3.6.3. Cyclization of methyl 5-MeO-*N*-aminoanthranilate (2b) in PBS buffer

During our initial experiments involving solutions of methyl 5-MeO-*N*-aminoanthranilate dihydrochloride (**2b**) in PBS, we noted the evolution of deep-blue fluorescence over 5 min from an initially non-fluorescent probe stock solution. To understand this phenomenon, we evaluated the stability of hydrazine **2b** in PBS at 37 °C (Figure 3.6). A significant (~ 10 fold) fluorescence signal increase (λ_{em} 421 nm) was observed within 5 minutes of incubation, which continued to increase over time. It is known that heating *N*-aminoanthranilic acids (e. g. **2a**) in concentrated HCl results in the formation of indazoles.[34] This reaction involves a strong mineral acid-catalyzed intramolecular nucleophilic attack of the terminal hydrazine nitrogen onto the carbonyl group with the formation of a tetrahedral intermediate, followed by its collapse and subsequent aromatization to afford blue fluorescent indazoles. Our hypothesis (Figure 3.6) was that a similar reaction was

taking place when hydrazine **2b** is dissolved in PBS buffer. Although the solution of **2b** is neutral (pH ~ 7.2), the concentration of **2b** is low enough (10^{-6} M) to favour intramolecular reactions. Importantly, the ester moiety makes the carbonyl group in **2b** more prone to intramolecular nucleophilic attack by the terminal hydrazine nitrogen since methanol is a relatively better leaving group, facilitating the collapse of the tetrahedral intermediate. We have prepared indazole **11** (in 31% yield, Figure 3.6) by heating 5-MeO-*N*-aminoanthranilic acid (**2a**) according to a previous method,[34] and compared the fluorescence emission spectra (λ_{em} 421 nm) of **11** to those obtained by simple incubation of **2b** in PBS. As shown in Figure 3.6, a good match in emission maxima between standard **11** and stock solution containing **2b** was observed upon excitation at 310 nm. Excitation at higher wavelengths (λ_{ex} 375 nm) required to induce hydrazone fluorescence, resulted in background levels (Figures ESI49a) fluorescence emission from the indazole. Furthermore, the *pseudo*-first order rate constant for the cyclization reaction in PBS (k_{obs} = 0.009 ± 0.002 min^{-1}) was 10-fold lower than that for hydrazone formation with hexanal as a test aldehyde (k_{obs} = 0.100 ± 0.002 min^{-1}) as determined by previously published methods (Figures ESI49b).[8,9] Together, this suggests that indazole formation, while limiting levels of **2b** in PBS, would not result in artifactual fluorescence emission upon aldehyde sensing with compound **2b**. Importantly, the spontaneous cyclization of **2b** can be significantly limited by preparation of stock solutions in DMSO and guarding them from light, where cyclization to **11** was found to be slow (< 5% conversion after 24 h) as indicated by ^{1}H NMR inspection.

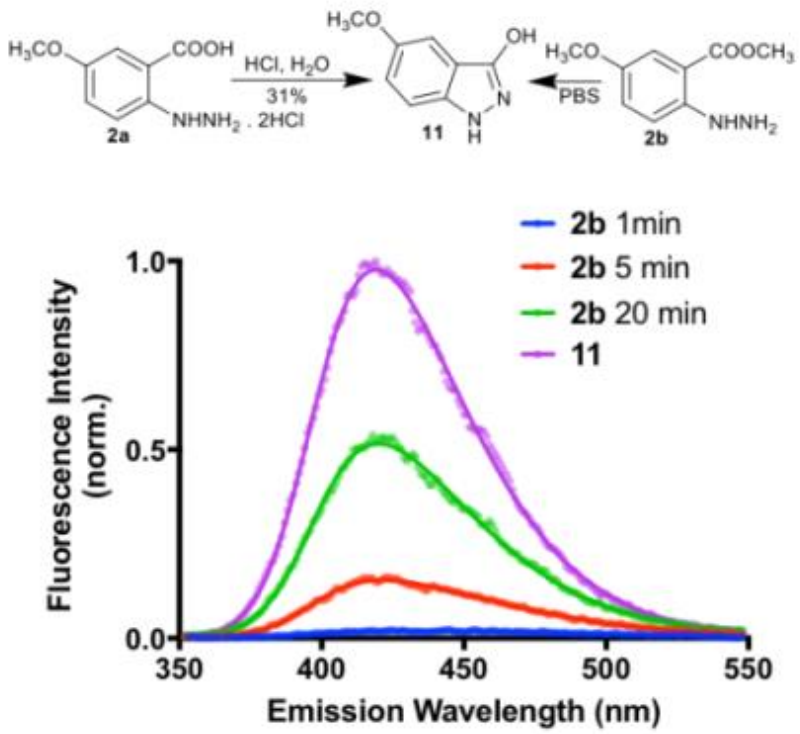

Figure 3.6 Cyclization of methyl 5-MeO-N-aminoanthranilate (2b) in PBS solution. Probe **2b** was incubated at 37°C in PBS (pH 7.2) for 1 (blue), 5 (red), and 20 min (green), and an emission scan was recorded with l_{ex} 310 nm. The emission spectrum of the standard indazole**11** is shown for comparison

3.6.4. Specificity of fluorogenic response of hydrazone 2b to biogenic carbonyls, metabolites, and ions

In addition to MDA, we assayed the fluorogenic response of hydrazine **2b** towards endogenous carbonyl compounds, including aliphatic aldehydes (formaldehyde, acetaldehyde, pentanal, hexanal, octanal, nonanal), more complex aldehyde metabolites (glyoxal, methylglyoxal, crotonaldehyde, glyceraldehyde), cofactors (pyridoxal phosphate), and ketones (acetone, pyruvate, butanedione, acetylacetone), glutathione, and biogenic cations (Ca^{2+}, Cu^{2+}, Fe^{3+}, Mg^{2+}, Mn^{2+}, Zn^{2+}, Figure 3.7). Among the carbonyls examined, hydrazine **2b** showed limited fluorescence signal turn-on in the presence of ketones, glutathione and some complex aldehydes (crotonaldehyde,

glyoxal, pyridoxalphosphate). While some biogenic metal cations (Ca^{2+}, Fe^{3+}, Mg^{2+}) appeared to produce negligible fluorescence in the presence of **2b**, a moderate fluorescence signal turn-on is observed from Cu^{2+}, Mn^{2+} and Zn^{2+} (Figure 3.7). This weak fluorescence response is possibly attributable to the suitability of both the hydrazino- and methyloxycarbonyl groups as ligands for Cu^{2+}, Mn^{2+} and Zn^{2+}, possibly promoting the formation of metal complexes in solution. In addition to glyceraldehyde and methylglyoxal, simple aliphatic aldehydes (formaldehyde, acetaldehyde, pentanal, hexanal, octanal, and nonanal) showed a substantial fluorescence signal turn-on upon reaction with hydrazine **2b** (Figure 3.7).

From a diagnostic standpoint, increased concentrations of pentanal, hexanal, octanal and nonanal were found in the exhaled breath of lung cancer patients when compared to healthy smoker and non-smoker volunteers.[12] While the formation of hexanal results from the oxidative cleavage of linoleic or arachidonic acid[35] and hexanal is considered a general marker of oxidative stress,[36] other aldehydes might also result from lipid peroxidation if specific unsaturated fatty acids are present in tumour cell membranes. Derivatization of these aliphatic aldehydes as biomarkers of lung cancer and analysis by fluorescent methods may present an alternative to tandem gas chromatography mass spectrometry (GC-MS) analysis currently used.[12,37] Compared to GC-MS analysis requiring expensive instrumentation, as well as sample processing leading to potential inaccuracies, fluorescence assays are significantly easier to perform and may be better suited to the point-of-care determination of longer chain aliphatic aldehydes. Future studies will seek to apply fluorescence-based aldehyde fingerprinting that uses **2b** as derivatizing agent for the identification of hydrazones **3f-3i** in complex mixtures to rapidly determine their identities with a low-cost technique.[20] Overall our results indicate that hydrazine **2b** could serve as a fluorogenic probe for Aldehydic Load, providing for the detection of a range of aliphatic aldehydes and MDA, which comprise catabolic products of lipid peroxidation.

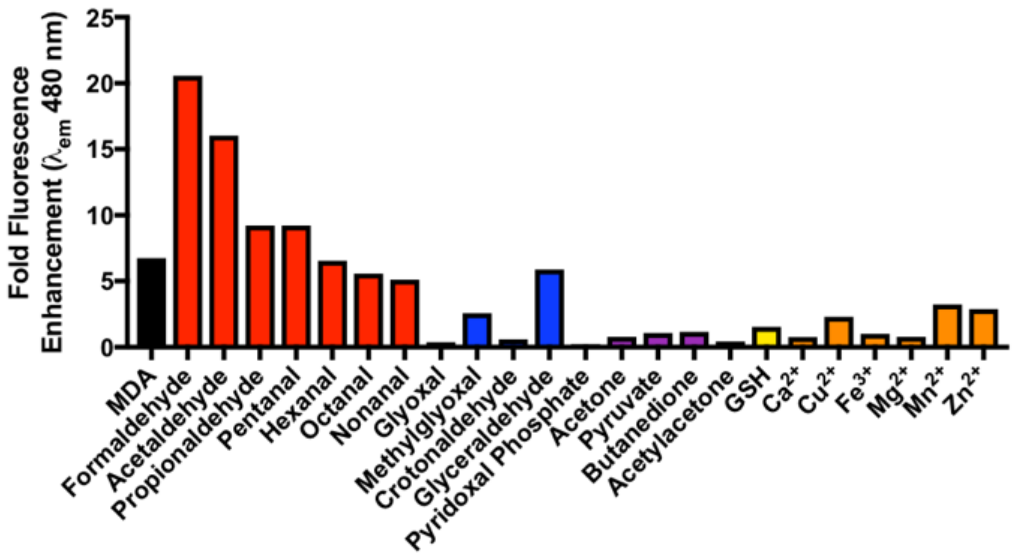

Figure 3.7 Methyl 5-MeO-N-aminoanthranilate (2b) shows broad specificity to aliphatic aldehydes. The fold fluorescence enhancement relative to **2b** alone was recorded with l_{ex}/l_{em} 375/480 nm following 1 min of incubation of 1mM solutions of **2b** in PBS (pH 7.2) with 5 eq. of MDA (black bar), simple aliphatic aldehydes (red bars), dialdehydes and more complex aldehydes (blue bars), ketones (purple bars), glutathione (yellow bar) and biogenic metal cations (orange bars).

3.6.4. Imaging Aldehydic Load changes due to lipid peroxidation by live cell microscopy

While there are a variety of biochemical processes that can result in the production of aldehydes in cells and tissues, the major source of aliphatic aldehydes is the decomposition of the cell membrane due to lipid peroxidation.[22] Since the fluorogenic response of **2b** to aldehydes spans a broad range of potential products of lipid peroxidation to yield fluorescent hydrazones with spectral properties amenable to conventional fluorescence microscopy (i.e. λ_{ex} 370 nm, λ_{em} 480 nm), we sought to apply this probe to live cell imaging. A well-characterized model of lipid peroxidation was implemented, comprising human HEK293 cells treated with diethyl maleate (DEM), which perturbs cellular redox status with the endpoint of cell membrane catabolism through oxidative lipid degradation, and/or witha-tocopherol (a-TOH),

nature's most effective antioxidant previously shown to limit DEM-induced lipid peroxidation in HEK293 cells.[38] Cells were either left untreated (Figure 3.8b, g, l), or were treated with 1.5 mM DEM for 1 h (Figure 3.8c, h, m) or 2 h (Figure 3.8d, i, n) in order to induce lipid peroxidation prior to incubation with **2b** for 5 min. Micrographs show limited fluorescence in untreated HEK293 cells, which is expected due to a homeostatic flux of metabolic aldehydes and carbonyls such as glyceraldehyde and pyruvate. However, a substantial fluorescence enhancement is observed after 1 h of DEM treatment in some cells, which continues to increase in both intensity and frequency after 2 h of incubation. In order to reduce aldehydic load, HEK293 cells were treated with 10 mM a-TOH for 24 h and left untreated (Fig. 3.8 a, f, l) or treated with 1.5 mM DEM for 1 h (Fig. 3.8 e, j, o) prior to incubation with **2b** for 5 min. A reduction of aldehydic load was observed following both treatments, with a-TOH reducing DEM-induced aldehyde production, as well as homeostatic aldehyde production in the cultured cells. Although the specific identity of the aldehydes contributing to the fluorescence enhancement observed in HEK293 cells cannot be determined using **2b**, the broad reactivity of the probe for aliphatic aldehydes in general provides a measure of Aldehydic Load, an important emerging biomarker for studying a range of diseases.[16,39]

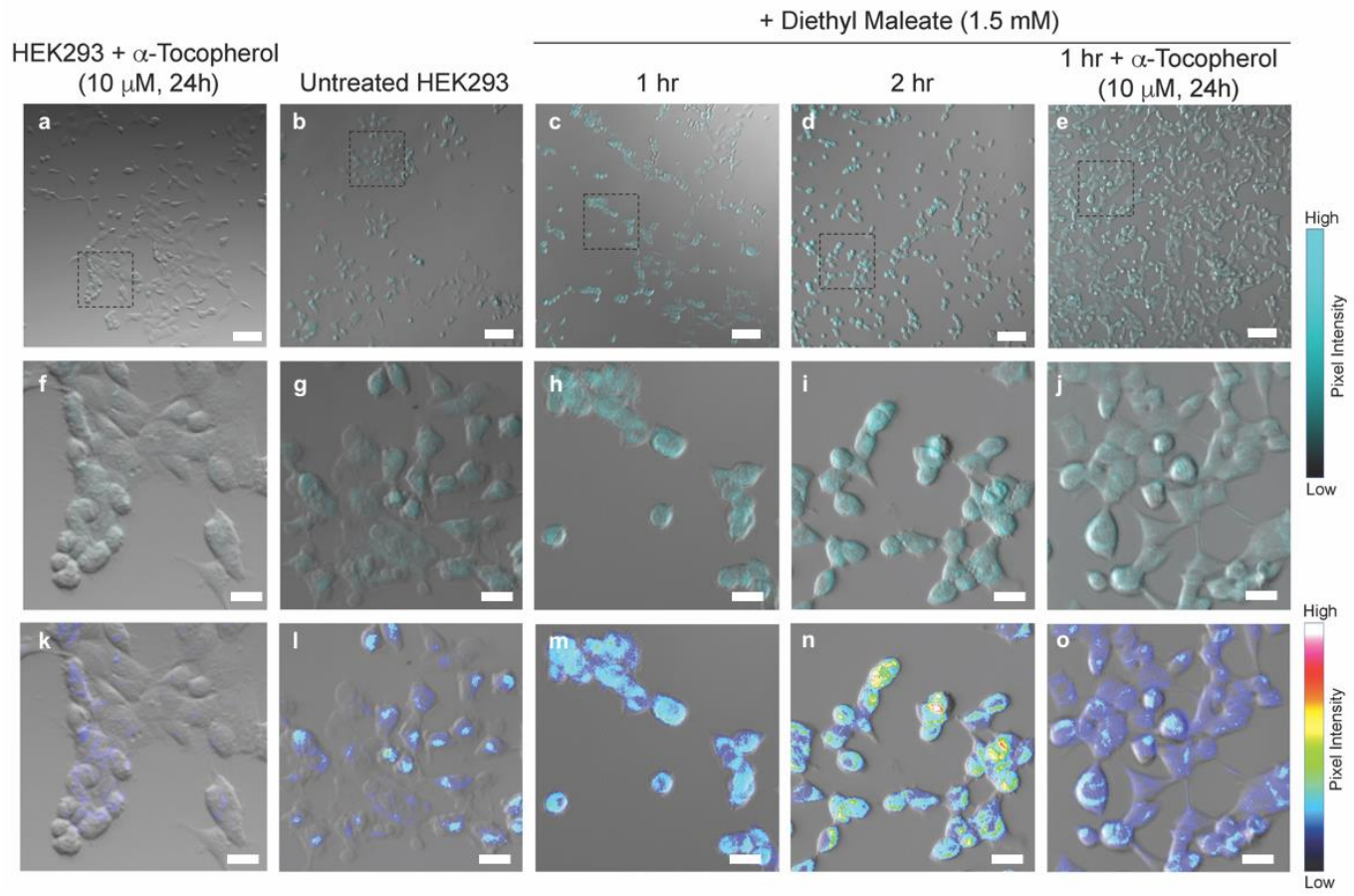

Figure 3.8 Live cell microscopy of HEK293 cells incubated with diethyl maleate (DEM) to induce lipid peroxidation, and/or α-tocopherol (α-TOH) as an anti-oxidant. HEK293 cells were either left untreated (b, g, l), treated with 1.5 mM diethyl maleate for 1 h (c, h, m) or 2 h (d, i, n), or treated with a-tocopherol (10 mM, 24 h) (a, f, k) alone or prior to DEM (1.5 mM, 1 h) (e, j, o) and were then incubated with 100 mM **2b** for 5 min prior to imaging. The fluorescence micrographs overlayed on DIC images for the full field of view (top), as well as a zoom region (middle) are shown. Zoom region is indicated by black dashed boxes. Heat map overlay of the fluorescence intensity shows relative distribution of imaging signal intensity in HEK293 cells (bottom). Scale bars for panels a-c = 100 mm, and panels d-I = 25 mm. All images were acquired with 405 nm excitation laser, and an emission window of 420 to 520 nm.

3.7. Conclusions

The use of methyl 5-MeO-N-aminoanthranilate dihydrochloride (**2b**) as a fluorogenic probe capable of detecting endogenous aldehydes was examined in detail. The current work complements a previous description of **2b** in the context of fluorescent fingerprinting of aldehydes[20], and seeks to fully describe its intra- and intermolecular reactivity, as well as the utility of **2b** for live cell microscopy of aldehydic load. The reaction of **2b** with MDA (formed in situ from MDA tetramethyl acetal) was found to produce a blue fluorescent pyrazole **4b** (λem 410 nm, Φ 0.45), proceeding through a blue-green fluorescent hydrazone intermediate 10. The simple structures of both **2b** and **4b** facilitated a detailed ^{1}H NMR-based mechanistic evaluation of the reaction, presenting evidence of the hydrazone intermediate that was also supported by fluorescence spectroscopy studies. The selectivity of **2b** toward the detection of cellular components was also evaluated, revealing that in addition to MDA, a significant fluorogenic response is observed with simple aliphatic aldehydes. Longer chain aliphatic aldehydes, produced, for example, during lung cancer progression, led to the formation of fluorescent hydrazones (**3f-3i**), emitting in the "far" blue region (λem 466-480 nm). Quantum yields associated with these fluorophores were found to be modest (Φ 0.06-0.17), attributable to the occurrence of hydrazones as inseparable mixtures of E- and Z-isomers. One caveat for the use of **2b** for Aldehydic Load imaging derives from the instability of hydrazine **2b** in aqueous solution and the minute time-scale lifetime of the hydrazone intermediate 10, limiting detection reliability to within 5 min of probe application. Even with this caveat in place, Aldehydic Load enhancement following oxidative stress-induced lipid peroxidation was successfully imaged through live cell microscopy of HEK293 cells treated with DEM. Overall our results present a detailed evaluation of the reaction between a fluorogenic hydrazine-derived probe and MDA, and might provide a useful guideline for the development of rapid and easy to perform fluorescence assays for point-of-care detection of Aldehydic Load relevant to a variety of diseases. The uniqueness of methyl 5-MeO-*N*-aminoanthranilate derives from its minimal nature: facile synthesis for easy accessibility, simple wash-free implementation for live cell microscopy, and broad aliphatic aldehyde binding for total aldehyde load mapping. In effect, the minimalism of the probe maximizes its application to evaluate the chemical

biology of carbonyls. Future studies will involve chemical modifications of **2b** to prevent the spontaneous cyclization in PBS, the formation of fluorescent molecules emitting at longer wavelengths (λem > 500 nm), and the application of **2b** to interrogate the chemical biology of endogenous aldehydes in cellular models of disease.

3.8. Experimental

3.8.1 General experimental procedures

Reagents were commercially available, except for 5-MeO-*N*-aminoanthranilic acid (**2a**),[9] methyl 5-MeO-*N*-aminoanthranilate dihydrochloride (**2b**),[20] pyrazoles **4a**, **4b**[20] and indazole **11**[34] which were prepared according to the literature procedures. All solvents were HPLC grade except for water (18.2 MΩ cm millipore water). Solvents were removed under reduced pressure in a rotary evaporator, aqueous solutions were lyophilized and organic extracts were dried over Na_2SO_4. Flash column chromatography (FCC) was carried out using silica gel (SiO_2), mesh size 230 - 400 Å. Thin-layer chromatography (TLC) was carried out on Al backed silica gel plates with compounds visualised by anisaldehyde stain, 5% ninhydrin stain, and UV light. NMR spectra were recorded on a 300 or 400 MHz spectrometers, for ^{1}H NMR spectra δ values were recorded as follows: DMSO-D_6 (2.50 ppm); for ^{13}C (93.75 or 125 MHz) δ DMSO-D_6 (39.50 ppm). Mass spectra (MS) were obtained using electron impact (EI). Steady state fluorescence spectra were acquired on a Cary Eclipse fluorescence spectrophotometer, using 1 × PBS, pH 7.2 containing up to 10% DMSO. Quantum yields were determined as described previously,[40] using harmane as a standard.[21]

3.8.2. Reaction of 2b with aliphatic aldehydes (pentanal, hexanal, octanal, nonanal)

Aliphatic aldehydes (pentanal, 53 μL; hexanal, 61 μL; octanal, 78 μL; nonanal, 86 μL; 0.5 mmol each) were added to separated stirred solutions of methyl 5-MeO-*N*-aminoanthranilate dihydrochloride (**2b**, 132 mg, 0.5 mmol) in MeOH (5 mL) and water (1.25 mL). The mixtures were stirred for 18 h at rt; MeOH was evaporated, the residues were diluted with brine (30 mL) and were

extracted with EtOAc (2 × 30 mL). Combined organic extracts were dried, were concentrated and the residues were subjected to FCC on 40 g SiO_2 as follows: hydrazone **3f**, hexanes/EtOAc (4 : 1); hydrazones **3g–3i**, hexanes/EtOAc (9 : 1). Evaporation of the eluates afforded hydrazones**3f-3i**.

3.8.2.1. Hydrazone 3f.

yellow oil, mixture of *E*- and *Z*-isomers, 110 mg, 83%. ^{1}H NMR δ (DMSO-D_6) 10.51 (s, D_2O exch., 0.4H); 10.33 (s, D_2O exch., 0.6H); 7.53 (d, *J* = 9.0 Hz, 0.4H); 7.43 (d, *J* = 9.0 Hz, 0.6H); 7.37 (t, *J* = 5.0 Hz, 0.6H); 7.32 (d, *J* = 3.0 Hz, 0.4H); 7.27 (d, *J* = 3.0 Hz, 0.6H); 7.18 (dd, *J* = 9.0, 3.0 Hz, 0.4H); 7.14 (dd, *J* = 9.0, 3.0 Hz, 0.6H); 6.59 (t, *J* = 5.0 Hz, 0.4H); 3.86 (s, 1.2H); 3.83 (s, 1.8H); 3.72 (s, 1.2H); 3.71 (s, 1.8H); 2.23 (m, 2H); 1.45 (m, 4H); 0.90 (m, 3H). ^{13}C NMR δ (DMSO-D_6) 167.9, 167.4, 150.9, 150.4, 144.2, 142.8, 142.4, 142.3, 123.2 (2 × C), 114.8, 114.7, 112.6 (2 × C), 108.8, 108.1, 55.4 (2 × C), 52.2, 51.9, 31.5, 28.5, 27.5, 26.1, 22.0, 21.7, 13.8, 13.7. HRMS (EI) m/z; found 264.1473 [M+] (calcd 264.1474 for $C_{14}H_{20}N_2O_3$), LRMS (EI) m/z (rel. abundance): 264 [M+] (100), 180 (87), 164 (24), 150 (49), 122 (53).

3.8.2.2. Hydrazone 3g.

yellow oil, mixture of *E*- and *Z*-isomers, 85 mg, 61%. ^{1}H NMR δ (DMSO-D_6) 10.51 (s, D_2O exch., 0.4H); 10.33 (s, D_2O exch., 0.6H); 7.53 (d, *J* = 9.0 Hz, 0.4H); 7.47 (d, *J* = 9.0 Hz, 0.6H); 7.37 (t, *J* = 5.0 Hz, 0.6H); 7.32 (d, *J* = 3.0 Hz, 0.4H); 7.27 (d, *J* = 3.0 Hz, 0.6H); 7.18 (dd, *J* = 9.0, 3.0 Hz, 0.4H); 7.14 (dd, *J* = 9.0, 3.0 Hz, 0.6H); 6.58 (t, *J* = 5.0 Hz, 0.4H); 3.86 (s, 1.2H); 3.83 (s, 1.8H); 3.72 (s, 1.2H); 3.71 (s, 1.8H); 2.22 (m, 2H); 1.53 (m, 2H); 1.33 (m, 4H); 0.89 (m, 3H). ^{13}C NMR δ (DMSO-D_6) 167.9, 167.4, 150.9, 150.4, 144.2, 142.8, 142.4, 142.3, 123.2, 123.1, 114.8, 114.7, 112.7, 112.6, 108.8, 108.2, 55.4 (2 × C), 52.2, 51.9, 31.7, 31.0, 30.8, 26.3, 26.0, 25.0, 21.9, 21.8, 13.9, 13.8. HRMS (EI) m/z; found 278.1638 [M+] (calcd 278.1630 for $C_{15}H_{22}N_2O_3$), LRMS (EI) m/z (rel. abundance): 278 [M+] (100), 180 (83), 164 (43), 150 (37), 122 (38).

3.8.2.3. Hydrazone 3h.

yellow oil, mixture of *E*- and *Z*-isomers, 119 mg, 78%. ^{1}H NMR δ (DMSO-D_6) 10.51 (s, D_2O exch., 0.4H); 10.32 (s, D_2O exch., 0.6H); 7.53 (d, *J* = 9.0 Hz, 0.4H); 7.47 (d, *J* = 9.0 Hz, 0.6H); 7.37 (t, *J* = 5.0 Hz, 0.6H); 7.32 (d, *J* = 3.0 Hz, 0.4H); 7.28 (d, *J* = 3.0 Hz, 0.6H); 7.18 (dd, *J* = 9.0, 3.0 Hz, 0.4H); 7.14 (dd, *J* = 9.0, 3.0 Hz, 0.6H); 6.59 (t, *J* = 5.0 Hz, 0.4H); 3.86 (s, 1.2H); 3.83 (s, 1.8H); 3.72 (s, 1.2H); 3.71 (s, 1.8H); 2.23 (m, 2H); 1.53 (m, 2H); 1.32 (m, 8H); 0.85 (m, 3H). ^{13}C NMR δ (DMSO-D_6) 167.9, 167.4, 150.9, 150.4, 144.2, 142.8, 142.4, 142.3, 123.2, 123.1, 114.8, 114.6, 112.6 (2 × C), 108.8, 108.1, 55.4 (2 × C), 52.1, 51.9, 31.8, 31.2, 31.1, 28.8, 28.6, 28.5, 28.4, 26.4, 26.3, 25.4, 22.1 (2 × C), 13.9 (2 × C). HRMS (EI) m/z; found 306.1953 [M+] (calcd 306.1943 for $C_{17}H_{26}N_2O_3$), LRMS (EI) m/z (rel. abundance): 306 [M+] (100), 180 (79), 164 (34), 150 (36), 122 (40).

3.8.2.4. Hydrazone 3i.

yellow oil, mixture of *E*- and *Z*-isomers, 119 mg, 74%. ^{1}H NMR δ (DMSO-D_6) 10.51 (s, D_2O exch., 0.4H); 10.32 (s, D_2O exch., 0.6H); 7.52 (d, *J* = 9.0 Hz, 0.6H); 7.47 (d, *J* = 9.0 Hz, 0.4H); 7.37 (t, *J* = 5.5 Hz, 0.4H); 7.32 (d, *J* = 3.0 Hz, 0.6H); 7.27 (d, *J* = 3.0 Hz, 0.6H); 7.18 (dd, *J* = 9.0, 3.0 Hz, 0.6H); 7.14 (dd, *J* = 9.0, 3.0 Hz, 0.4H); 6.59 (t, *J* = 5.5 Hz, 0.6H); 3.86 (s, 1.8H); 3.83 (s, 1.2H); 3.72 (s, 1.8H); 3.70 (s, 1.2H); 2.22 (m, 2H); 1.53 (m, 2H); 1.36 (m, 10H); 0.85 (m, 3H). ^{13}C NMR δ (DMSO-D_6) 167.9, 167.4, 151.0, 150.5, 144.2, 142.8, 142.4 (2 × C), 123.2, 123.1, 114.8, 114.7, 112.7, 112.6, 108.8, 108.2, 55.4 (2 × C), 52.1, 51.9, 31.8, 31.3, 31.2, 28.9, 28.8, 28.7, 28.6 (3 × C), 26.4, 26.3, 25.4, 22.1 (2 × C), 13.9 (2 × C). HRMS (EI) m/z; found 320.2081 [M+] (calcd 320.2100 for $C_{18}H_{28}N_2O_3$), LRMS (EI) m/z (rel. abundance): 320 [M+] (32), 180 (52), 164 (19), 150 (22), 122 (21).

3.8.3. Reaction of 2a and 2b with MDA – detailed kinetic analysis

3.8.3.1. NMR study.

Separate solutions of **2a** or **2b** (1 mg each) in 1 × PBS, pH 7.2 containing 10% DMSO-D_6 were prepared and the ^{1}H NMR spectra were acquired. The tubes were then removed from the spectrometer, 1 drop of 1 M solution of MDA tetramethyl acetal in 1 M HCl (known to form MDA *in situ*)[24] was added and ^{1}H NMR spectra were acquired immediately (1 min) and then after 2, 4, 20 and 120 (**2b** only) minutes. Separate solutions of pyrazoles **4a**, **4b** and MDA (controls) were prepared and analyzed under identical conditions.

3.8.3.2. Fluorescence study.

A 10 mM stock solution of **2b** was prepared in DMSO, and 5 uL was added to 1 × PBS, pH 7.2, in a 1 cm path length quartz cuvettes, followed by mixing by inversion. To this solution, 50 µL of 1 M solution of MDA tetramethyl acetal in 1 M HCl was added,[33] immediately followed by 5 µL of 10 M NaOH to neutralize the solution (as confirmed by a pH paper). Fluorescence emission was recorded on a fluorescence spectrophotometer with $\lambda_{ex}\backslash\lambda_{em}$ 310\410 nm and 375\475 nm and slit widths of 5 nm. Readings were acquired concurrently every 10 sec for 45 min, the experiment was repeated three separate times.

3.8.4. Hydrazine 2b as a fluorogenic probe for Aldehydic Load

3.8.4.1. Detection of MDA

The samples were prepared as follows: 100 µL of the solution of **2b** (10^{-5} M) in DMSO was mixed with 1 × PBS (pH 7.2) and a stock solution of MDA[24] was added to achieve the final volume of 1 mL (final concentration of **2b** in the sample is 10^{-6} M). Seven separate samples were prepared, the concentrations of MDA were 10^{-7} M (0.1 eq), 2×10^{-7} M (0.2 eq), 5×10^{-7} M (0.5 eq), 10^{-6} M (1 eq), 2×10^{-6} M (2 eq), 5×10^{-6} M (5 eq), 8.5×10^{-6} M (8.5 eq). The pH in the samples containing

larger amounts of MDA stock solution (> 2 eq) was adjusted (to reach ~ pH 7.2) by the addition of saturated $NaHCO_3$ solution (10 – 20 μL). Control samples containing just hydrazine **2b**, pyrazole **4b** and MDA (final concentration of 10^{-6} M) were also prepared. Each sample was analyzed right after preparation (within 1 min) by fluorescence scans (λ_{ex} 371 nm or 307 nm). All measurements were performed at 37 °C. The same temperature was maintained to keep the MDA stock solution as well as PBS. The stock solution of hydrazine **2b** in DMSO was stored at rt in the dark (flask wrapped in Al foil). Bell-type curves were fitted to raw data points of emission scans using standard protocols in GraphPad Prism v.7.0c.

3.8.4.2. Response to other carbonyls, metal ions and biologically relevant molecules

The samples containing **2b** (final concentration 10^{-6} M) were prepared as described above. A solution of 5 eq of the analyte of interest was added (final concentration 5×10^{-6} M), the fluorescence scans (λ_{ex} 371 nm) were performed as described above.

3.8.4.3. Instability of 2b in PBS

A solution of hydrazine **2b** in DMSO (100 μL) was mixed with PBS (overall volume 1 mL, final concentration 10^{-6} M, 37 °C). The fluorescence scans (λ_{ex} 327 nm) were performed immediately (1 min), then after 5 and 20 min. A sample containing indazole **11** was prepared and analyzed under identical conditions.

3.8.4.4. Live-cell microscopy study

HEK293 cells were a gift from the lab of Dr. D. A. Pratt (University of Ottawa). Cells were cultured in Minimal Essential Medium supplemented with 10% v/v Fetal Calf Serum and 1% v/v Pen Strep antibiotic solution at 37°C in a 5% CO_2 atmosphere. Cells were plated at 25000 cells/well in a 24-well tissue culture-treated polystyrene plate overnight prior to use for microscopy. Growth medium

was changed prior to treatment with 10mM a-TOH for 24 h, or 1.5 mM DEM for 1 and 2 h. At indicated time points, media was removed and replaced with 1 × Hank's Balanced Salt Solution, pH 7.2, and 10 mL of a solution of **2b** in DMSO (final concentration of **2b** = 100 mM) was added. Imaging was performed on a Zeiss LSM 880 confocal microscope fitted with live cell incubator chamber using 405 nm excitation laser line, and 10x objective lens. Both, differential interference contrast (DIC) and fluorescence images were acquired. All image analysis was performed using ImageJ v1.45S.

3.9. Supplementary Materials

Electronic supplementary information (ESI) available: Full spectral characterization of hydrazones 3f–3i, fluorescence spectra associated with pyrazoles 4a and 4b, full view of the 1 H NMR spectra associated with the detailed kinetic analysis. See DOI: 10.1039/c8ob02255k

3.10. Conflicts of interest

The authors declare no competing financial interest.

3.11. Acknowledgements

We wish to acknowledge Professor Jeffrey Keillor for allowing us to use his Cary Eclipse Fluorescence Spectrophotometer for the duration of this work. This work was supported by an NSERC Discovery Grant RGPIN 2015-05796 (A.J.S.), the Canada Research Chairs Program 950-230754 (A.J.S.), and the Canadian Institutes of Health Research PJT376892 (A.J.S.), the financial support provided by these agencies is gratefully acknowledged.

3.12. Notes and References

1 Abou-Zied, O. K., Al-Busaidi, B. Y. & Husband, J. Solvent effect on anthranilic acid spectroscopy. *The Journal of Physical Chemistry A* **118**, 103-109, (2014).

2 Duval, R. & Duplais, C. Fluorescent natural products as probes and tracers in biology. *Natural product reports* **34**, 161-193, (2017).

3 Coburn, C. *et al.* Anthranilate fluorescence marks a calcium-propagated necrotic wave that promotes organismal death in C. elegans. *PLoS biology* **11**, e1001613, (2013).

4 KANIŞKAN, N., Kokten, S. & Çelik, İ. A new protocol for the synthesis of primary, secondary and tertiary anthranilamides utilizing N-(2-aminoarylacyl) benzotriazoles. *Arkivoc* **2012**, (2012).

5 McKay, C. S. & Finn, M. Polyvalent catalysts operating on polyvalent substrates: A model for surface-controlled reactivity. *Angewandte Chemie* **128**, 12833-12839, (2016).

6 Crisalli, P. & Kool, E. T. Importance of ortho proton donors in catalysis of hydrazone formation. *Organic letters* **15**, 1646-1649, (2013).

7 Crisalli, P. & Kool, E. T. Water-soluble organocatalysts for hydrazone and oxime formation. *The Journal of organic chemistry* **78**, 1184-1189, (2013).

8 Kool, E. T., Park, D.-H. & Crisalli, P. Fast hydrazone reactants: electronic and acid/base effects strongly influence rate at biological pH. *Journal of the American Chemical Society* **135**, 17663-17666, (2013).

9 Dang, T. *et al.* Hydrazo-CEST: Hydrazone-Dependent Chemical Exchange Saturation Transfer Magnetic Resonance Imaging Contrast Agents. *Chemistry – A European Journal* **24**, 9148-9156, (2018).

10 O'Brien, P. J., Siraki, A. G. & Shangari, N. Aldehyde Sources, Metabolism, Molecular Toxicity Mechanisms, and Possible Effects on Human Health. *Critical Reviews in Toxicology* **35**, 609-662, (2005).

11 Owen, O. *et al.* Acetone metabolism during diabetic ketoacidosis. *Diabetes* **31**, 242-248, (1982).

12 Fuchs, P., Loeseken, C., Schubert, J. K. & Miekisch, W. Breath gas aldehydes as biomarkers of lung cancer. *International Journal of Cancer* **126**, 2663-2670, (2010).

13 Antoniak, D. T., Duryee, M. J., Mikuls, T. R., Thiele, G. M. & Anderson, D. R. Aldehyde-modified proteins as mediators of early inflammation in atherosclerotic disease. *Free Radical Biology and Medicine* **89**, 409-418, (2015).

14 Ivanova, S. *et al.* Cerebral ischemia enhances polyamine oxidation: identification of enzymatically formed 3-aminopropanal as an endogenous mediator of neuronal and glial cell death. *Journal of Experimental Medicine* **188**, 327-340, (1998).

15 Brewer, T. F. & Chang, C. J. An aza-cope reactivity-based fluorescent probe for imaging formaldehyde in living cells. *Journal of the American Chemical Society* **137**, 10886-10889, (2015).

16 Yuen, L. H., Saxena, N. S., Park, H. S., Weinberg, K. & Kool, E. T. Dark hydrazone fluorescence labeling agents enable imaging of cellular aldehydic load. *ACS chemical biology* **11**, 2312-2319, (2016).

17 Brewer, T. F., Burgos-Barragan, G., Wit, N., Patel, K. J. & Chang, C. J. A 2-aza-Cope reactivity-based platform for ratiometric fluorescence imaging of formaldehyde in living cells. *Chemical science* **8**, 4073-4081, (2017).

18 Bruemmer, K. J., Green, O., Su, T. A., Shabat, D. & Chang, C. J. Chemiluminescent Probes for Activity-Based Sensing of Formaldehyde Released from Folate Degradation in Living Mice. *Angewandte Chemie* **130**, 7630-7634, (2018).

19 Yang, M., Fan, J., Zhang, J., Du, J. & Peng, X. Visualization of methylglyoxal in living cells and diabetic mice model with a 1, 8-naphthalimide-based two-photon fluorescent probe. *Chemical science* **9**, 6758-6764, (2018).

20 Lazurko, C. *et al.* Fingerprinting Biogenic Aldehydes Through Pattern Recognition Analyses of Excitation-Emission Matrices. *ChemBioChem* **40**, 543-554, (2019).

21 Pardo, A., Reyman, D., Poyato, J. & Medina, F. Some β-carboline derivatives as fluorescence standards. *Journal of luminescence* **51**, 269-274, (1992).
22 Zielinski, Z. A. & Pratt, D. A. Lipid peroxidation: Kinetics, mechanisms, and products. *The Journal of organic chemistry* **82**, 2817-2825, (2017).
23 Pluskota-Karwatka, D. *et al.* Identification of Adducts Formed in the Reactions of Malonaldehyde–glyoxal and Malonaldehyde–methylglyoxal with Adenosine and Calf Thymus DNA. *Chemistry & Biodiversity* **7**, 959-974, (2010).
24 Salus, K., Hoffmann, M., Siodła, T., Wyrzykiewicz, B. & Pluskota-Karwatka, D. Synthesis, structural studies and stability of model cysteine containing DNA–protein cross-links. *New Journal of Chemistry* **41**, 2409-2424, (2017).
25 Gönenç, A., Özkan, Y., Torun, M. & Şimşek, B. Plasma malondialdehyde (MDA) levels in breast and lung cancer patients. *Journal of clinical pharmacy and therapeutics* **26**, 141-144, (2001).
26 Viigimaa, M. *et al.* Malondialdehyde-modified low-density lipoproteins as biomarker for atherosclerosis. *Blood Pressure* **19**, 164-168, (2010).
27 Bir, L. S., Demir, S., Rota, S. & Köseoglu, M. Increased serum malondialdehyde levels in chronic stage of ischemic stroke. *The Tohoku journal of experimental medicine* **208**, 33-39, (2006).
28 Hajimohammadreza, I. & Brammer, M. Brain membrane fluidity and lipid peroxidation in Alzheimer's disease. *Neuroscience letters* **112**, 333-337, (1990).
29 Nair, V. & Turner, G. A. The thiobarbituric acid test for lipid peroxidation: structure of the adduct with malondialdehyde. *Lipids* **19**, 804-805, (1984).
30 Janero, D. R. Malondialdehyde and thiobarbituric acid-reactivity as diagnostic indices of lipid peroxidation and peroxidative tissue injury. *Free radical biology and medicine* **9**, 515-540, (1990).
31 Chen, J. *et al.* Toward a biomarker of oxidative stress: a fluorescent probe for exogenous and endogenous malondialdehyde in living cells. *Analytical Chemistry* **87**, 8052-8056, (2015).
32 He, L., Yang, X., Xu, K. & Lin, W. A mitochondria-targeted fluorescent probe for imaging endogenous malondialdehyde in HeLa cells and onion tissues. *Chemical Communications* **53**, 4080-4083, (2017).
33 Tsuruta, Y. *et al.* Determination of malondialdehyde by high-performance liquid chromatography using 4-(2-phthalimidyl) benzohydrazide as a pre-column fluorescent labelling reagent. *Analyst* **119**, 1047-1050, (1994).
34 Baiocchi, L., Corsi, G. & Palazzo, G. Synthesis, properties, and reactions of 1H-indazol-3-ols and 1, 2-dihydro-3H-indazol-3-ones. *Synthesis* **1978**, 633-648, (1978).
35 Shahidi, F. Headspace volatile aldehydes as indicators of lipid oxidation in foods. *Headspace Analysis of Foods and Flavors: Theory and Practice*, 113-123, (2001).
36 Corradi, M. *et al.* Comparison between exhaled and sputum oxidative stress biomarkers in chronic airway inflammation. *European Respiratory Journal* **24**, 1011-1017, (2004).
37 Poli, D. *et al.* Determination of aldehydes in exhaled breath of patients with lung cancer by means of on-fiber-derivatisation SPME–GC/MS. *Journal of Chromatography B* **878**, 2643-2651, (2010).
38 Li, B., Zheng, F., Chauvin, J.-P. R. & Pratt, D. A. The medicinal thiosulfinates from garlic and Petiveria are not radical-trapping antioxidants in liposomes and cells, but lipophilic analogs are. *Chemical Science* **6**, 6165-6178, (2015).
39 Ellis, E. M. Reactive carbonyls and oxidative stress: potential for therapeutic intervention. *Pharmacology & therapeutics* **115**, 13-24, (2007).
40 Eaton, D. International union of pure and applied chemistry organic chemistry division commission on photochemistry: reference materials for fluorescence measurement. *Journal of Photochemistry and Photobiology B: Biology* **2**, 523-531, (1988).

Chapter 4: Mapping Aldehydic Load *In vivo* By Positron Emission Tomography with [^{18}F]Na_3BF_3

Alexia Kirby,[a‡] Mojmír Suchý,[b,c‡] Andrea Brouwer,[b] and Adam Shuhendler[a,b,c*]

[a]Dept. of Biology, University of Ottawa, Ottawa, Ontario, Canada.

[b]Dept. of Chemistry and Biomolecular Sciences, University of Ottawa, Ottawa, Ontario, Canada.

[c]University of Ottawa Heart Institute, Ottawa, Ontario, Canada.

‡ Authors contributed equally to this work.
* Corresponding author: adam.shuhendler@uottawa.ca

4.1. Introduction to the Research Article Presented within this Chapter

In continuing with the pursuit of imaging aldehydes, our group sought to create an imaging probe capable of mapping aldehydic load in a living animal. In this article, we present a new radiotracer, [^{18}F]*N*-aminoanthranilic acid trifluoroborate [^{18}F]NA_3BF_3 capable of binding aldehydes *in vivo* for visualization by PET. The radiotracer is a derivative of the fluorophore presented in Chapter 3 of this thesis. This study is the first to present an aldehyde-targeted PET radiotracer that enters the cell and is capable of mapping systemic inflammation using total aldehydic load as a biomarker.

4.2. Author Contributions

AK, MS, and AS designed the study and wrote the manuscript. AK and AB prepared the aldehyde-expressing microparticles. AK performed experiments for characterization of microparticles, and cell uptake study. MS conducted all other chemistry and radiochemistry. AK and AS performed all animal experiments and data analysis.

4.3. Copyright

4.4. Abstract

A new radiotracer, [^{18}F]NA_3BF_3, capable of rapid, stable, and catalyst-free complexation of aldehydes *in vivo* is reported. [^{18}F]NA_3BF_3 was shown to bind aldehydes in live subjects using locally administered aldehyde-presenting microparticles, and was then applied to mapping aldehydic load in a mouse model of sepsis. [^{18}F]NA_3BF_3 may enable the direct investigation of the chemical biology of aldehydes in living subjects, and may open avenues for the adoption of endogenous aldehydic load as an imaging biomarker of inflammatory pathology.

4.5. Main text

Aldehydes are ubiquitous contributors to normal biochemistry that are maintained at innocuous levels through tight regulatory controls.[1] Dysregulation of these controls, occurring very early on in a range of diseases and acutely following injury, leads to elevations in various aldehydes that can result in the initiation and propagation of pathology.[2-6] The diversity of aldehydes with pathogenic potential supports the importance of the aldehydic load hypothesis: the concerted build-up of structurally diverse biogenic aldehydes as a whole can define the fate or outcome of the cell or tissue.[7-9] Therefore the ability to map total tissue aldehyde content *via* live animal imaging, and not a single aldehyde species, may provide a more molecularly holistic imaging biomarker under the aldehydic load hypothesis.

We have previously shown that biogenic aldehydes can be rapidly complexed to form hydrazones under physiological conditions by *N*-amino anthranilic acids without added catalyst.[10] Our results reaffirm previous work demonstrating that hydrazone formation can proceed at rates rivaling strain-promoted azide-alkyne cycloaddition "click" reactions as a result of intramolecular acid catalysis provided by an *ortho*-carboxylate.[11-13] In addition to rate acceleration, the *ortho*-carboxylate was also shown to increase the stability of the hydrazone product (beyond 60 min), as well as the extent of reaction completion, through putative intramolecular hydrogen bonding.[10] Due to both the rapid rate of reaction and product longevity, a radiofluorinated radiotracer for aldehyde imaging was developed utilizing the *N*-amino anthranilic acid scaffold (Figure 4.1).

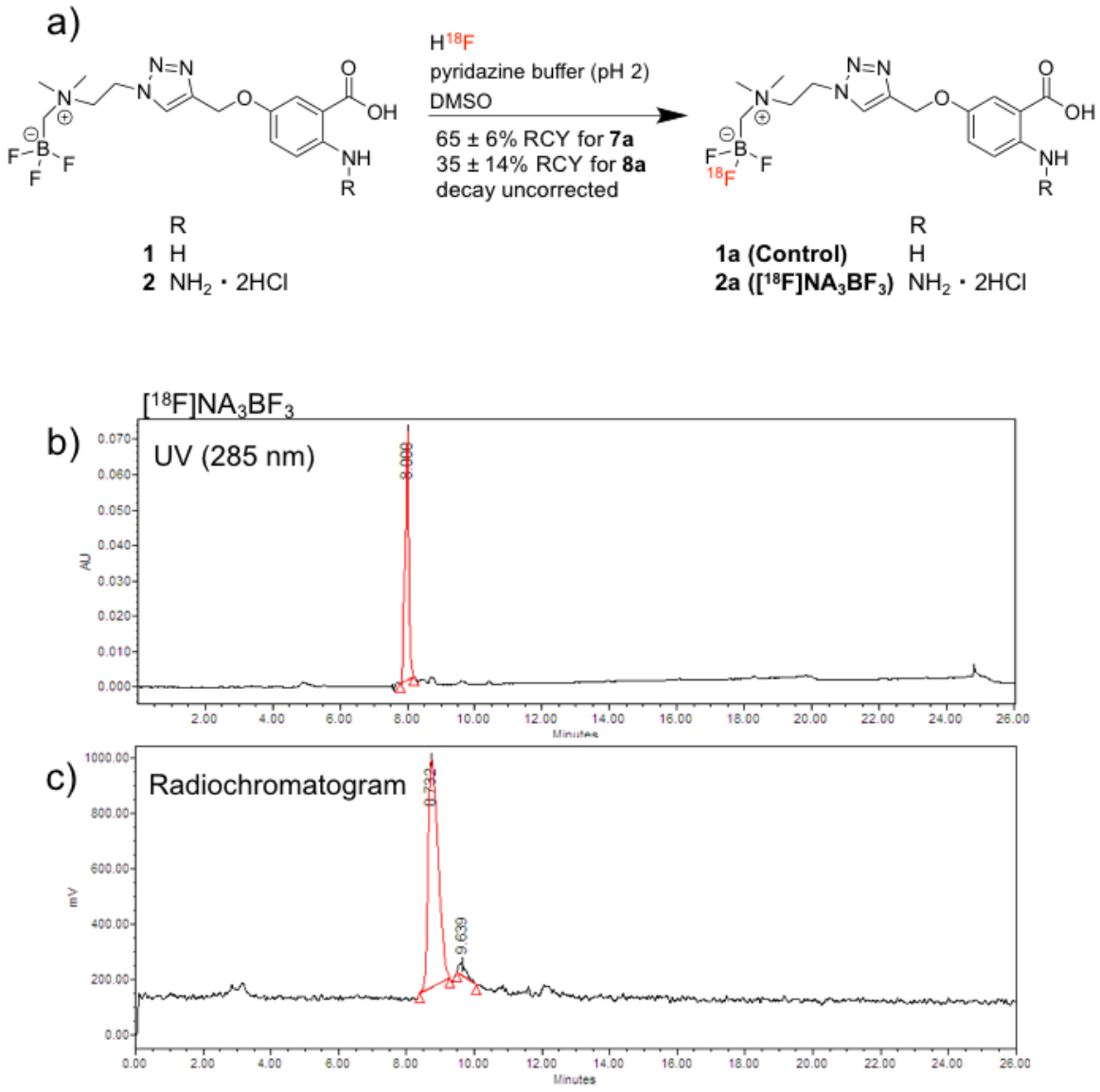

Figure 4.1. Radiosynthesis of [^{18}F]NA_3BF_3 and control probe. (**a**) Radiosynthetic scheme for the F-[^{18}F] exchange facilitated by the organotrifluoroborate prosthesis for both the unreactive control radiotracer (compound **1a**) and the reactive [^{18}F]NA_3BF_3 (compound **2a**). The product of radiosynthesis of [^{18}F]NA_3BF_3 was analysed by HPLC with both UV (285 nm) (**b**) and radiodetectors (**c**).

Radiofluorination was achieved *via* the aqueous organotrifluoroborate technique,[14-16] which was predicated upon earlier SiFA-based isotope exchange-mediated radiolabelling methodology.[17] Following the installation of an alkynyl moiety on 5-hydroxy anthranilic acid as described

previously,[18] the zwitterionic alkylammonium-methyltrifluoroborate, prepared in 4 steps from 2-*N,N*-dimethylethanol[14,19] and required for radiofluorination was incorporated through copper-assisted azide-alkyne cycloaddition to form the anthranilic acid **1**. Full synthetic details are provided in the Supporting Information. The application of a diazotization/reduction cascade of the anthranilic acid **1** (Figure 4.1) to the *N*-amino anthranilate, as previously reported,[10] led to the formation of the radiolabeling precursor **2**. Radiolabeling of compound **1** through isotope exchange in pyridazine buffer (pH 2)[14,20] yielded a non-reactive control radiotracer **1a**, while radiolabelling of compound **2** yielded the aldehyde-active radiotracer [^{18}F]NA_3BF_3 (compound **2a**) in good radiochemical yield (decay uncorrected, compound **1a**, 65 ± 6%, n = 3; compound **2a**, 35 ± 14%, n = 11) and purity (Figure 4.1, Supporting Figure S1, Supporting Table S1). While we report moderate molar activities from our radiosynthetic procedure, attributable to the low molecular mass of the precursor utilized, radiosynthesis optimization could yield clinically relevant molar activities and yields, for example through implementation of ^{18}F trapping on micro-QMA cartridges.[16] [^{18}F]NA_3BF_3 was also found to be stable in serum with no loss of probe at 120 min (Supporting Figure S2). Importantly, a significant enhancement in [^{18}F]NA_3BF_3 retention was observed in a cell culture model of electrophilic stress (Supporting Figure S3),[21] supporting the capability of [^{18}F]NA_3BF_3 to detect intracellular aldehydes and thus aldehydic load.

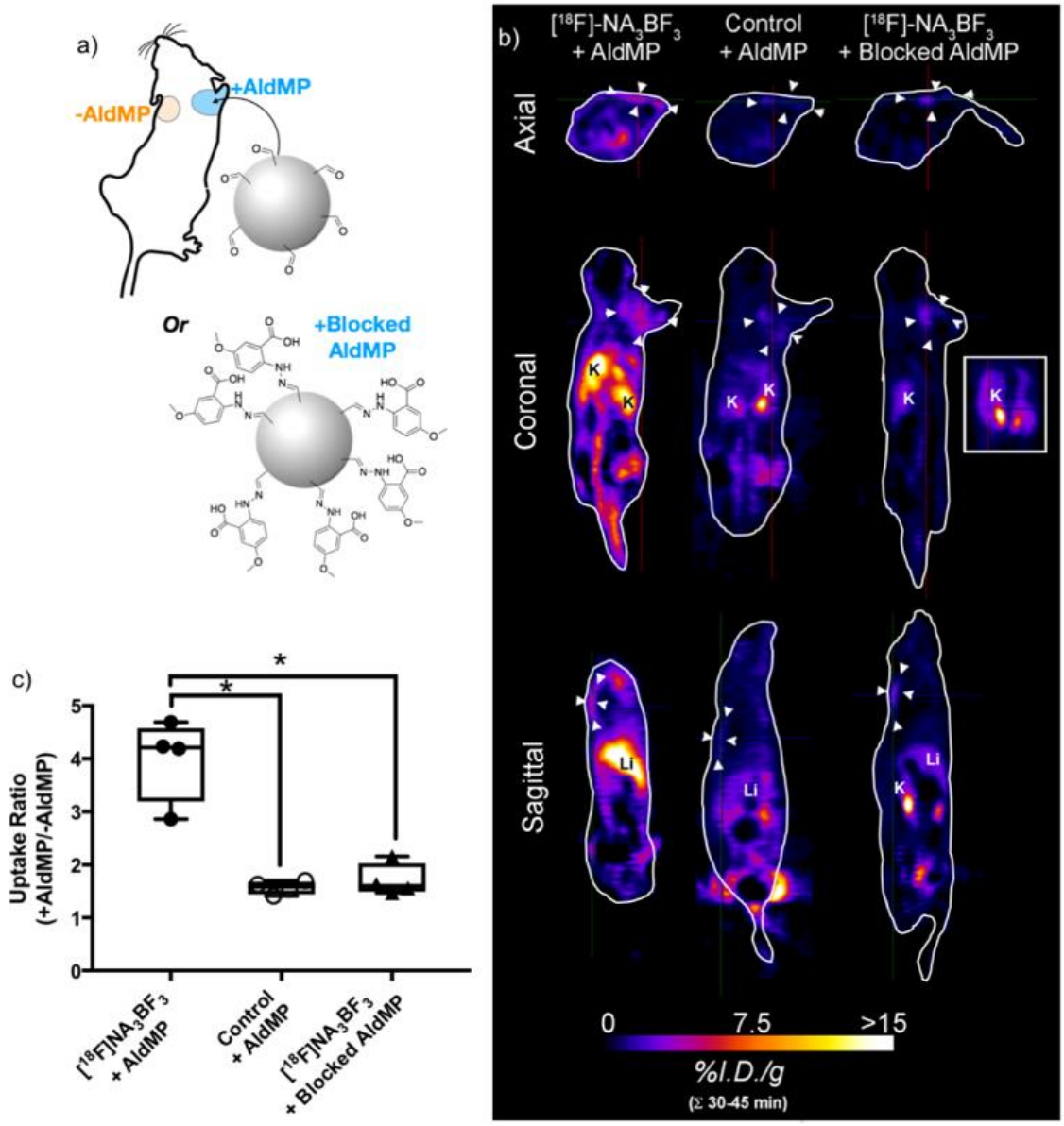

Figure 4.2. [^{18}F]NA_3BF_3 is retained in aldehyde-rich environments *in vivo.* (**a**) Experimental design for the *in vivo* assessment of aldehyde reactivity of [^{18}F]NA_3BF_3, illustrating the subcutaneous injection of AldMP or AldMP pre-saturated with 5-MeO-N-aminoanthranilate (i.e. blocked AldMP) dispersed in saline (blue), or of saline vehicle alone (orange), in the shoulders of Balb/C mice. (**b**) Results of PET following the generation of the mouse models illustrated in panel (**a**) receiving *i.v.* [^{18}F]NA_3BF_3 following AldMP (*left*) or blocked AldMP (*right*) subcutaneous injections, or receiving the unreactive control (compound **1a**) in AldMP-bearing mice (*middle*). Images are summed from 30 to 45 min post-radiotracer

injection. Inset shows kidney uptake of [^{18}F]NA_3BF_3 in blocked AldMP-bearing mice. Arrowheads indicate boundaries of AldMP injection. K: kidney, Li: liver. (**c**) Quantitative analysis of the uptake ratio between the +AldMP and -AldMP shoulders of mice receiving either unreactive control (compound **1a**) or [^{18}F]NA_3BF_3 summed from 30-45 min post-injection. Individual data points are shown, as well as box and whisker plots (horizontal line = mean, box = standard deviation, and whiskers = min/max range). * $p<0.05$ by two-tailed t-test, $n = 4$ mice per group.

In order to demonstrate the fast kinetics of hydrazone formation between the *N*-amino anthranilic acid group and aldehydes *in vivo*, which were previously only shown *in vitro*,[10,13] we synthesized aldehyde-bearing microparticles (AldMP) from glutaraldehyde according to previous reports (Supporting Figure S4a).[22,23] The presentation of aldehydes on the AldMP surface was tested using an aldehyde-conditional fluorophore,[21,24] methyl 5-methoxy-*N*-aminoanthranilate (Supporting Figure S4b). Fluorescence was observed only in the presence of AldMP (Supporting Figure S4b, *middle*). A blocked AldMP sample was prepared by pre-saturating AldMP with a non-fluorogenic sensor analog (5-methoxy-*N*-aminoanthranilic acid), which prevented sensor turn on. Altogether, these data support the hypothesis that AldMP present aldehyde groups on their surface.

In order to directly assess the ability of [^{18}F]NA_3BF_3 to bind aldehydes *in vivo*, an AldMP or blocked AldMP suspension in saline, or saline vehicle alone was injected *subcutaneously* (s.c.) above the shoulders of female Balb/C mice, providing known "aldehyde-rich" (+AldMP) and "aldehyde-poor" (-AldMP) regions (Figure 4.2a). Within 30 minutes of AldMP injection, mice received either [^{18}F]NA_3BF_3 (compound **2a**) (182 ± 9 mCi) (Figure 4.2b, *left and right*) or control radiotracer **1a** (174 ± 13 mCi) (Figure 4.2b, *middle*) by *intravenous* (i.v.) injection, followed by dynamic PET imaging for 60 minutes post-injection. In mice administered [^{18}F]NA_3BF_3, radiotracer uptake was observed in the shoulder bearing AldMP, as well as in the kidneys, liver, and circulation even at 60 minutes after AldMP injection (Figure 4.2b, *left*). The inoculation of mouse shoulders with AldMP pre-labeled with [^{18}F]NA_3BF_3 also showed signal loss from the site of injection and

concurrent liver and kidney uptake (Supporting Figure S5), supporting the systemic distribution of AldMP, which was expected due to both the low-micron particle size, which is amenable to systemic absorption,[25] and the tendency for polyglutaraldehyde linkages to degrade under physiological conditions.[26] The use of pre-labelled AldMP served only to demonstrate that the microparticles were absorbed systemically following subcutaneous injection, but not to mimic the systemic labelling shown in Fig. 4.2b.

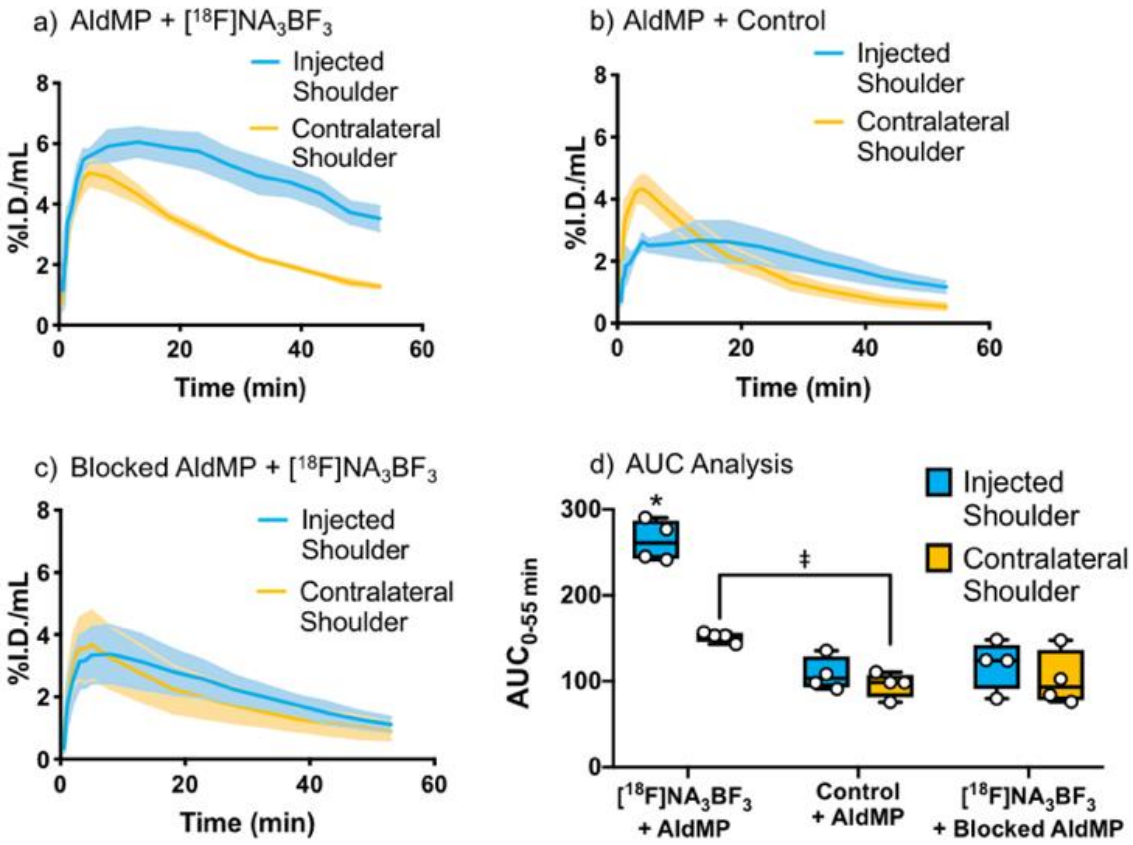

Figure 4.3. Time-activity curves for radiotracer retention *in vivo*. Activity was determined for microparticle-bearing shoulder (injected shoulder, blue) and saline-bearing shoulder (contralateral shoulder, orange) for mice receiving [^{18}F]NA_3BF_3 (**a** and **c**) or control radiotracer (**b**). Dark line and shaded region represent mean ± s.d. for n = 4 mice *per* group. (**d**) The area under the time-activity curve (AUC) was calculated over the duration of the imaging experiment (45 min) for the injected (blue) and contralateral (orange) shoulders for the treatments in panels **a-c**. Individual data points are shown, as well as box and whisker plots (horizontal line = mean, box = standard deviation, and whiskers = min/max range). * significant difference relative to all other groups (p<0.05 by two-way ANOVA). ‡ significant difference between indicated groups (p < 0.05 by two-way ANOVA).

Limited radiotracer uptake was observed following administration of the control compound **1a** (Figure 4.2b, *middle*), which is unable to form hydrazones. Similarly, uptake of [^{18}F]NA_3BF_3 was

limited in mice hosting pre-blocked AldMP (Figure 4.2b, *right*). The ratio of radiotracer uptake between the "aldehyde-rich" and "aldehyde-poor" shoulders of mice (i.e. the uptake ratio) was quantified (Figure 4.2c), resulting in a significantly greater uptake ratio following [^{18}F]NA_3BF_3 administration than that found in mice receiving the control radiotracer (3.99 ± 0.79 *vs.* 1.57 ± 0.13, $p < 0.05$). The uptake ratio was similarly significantly greater for AldMP-bearing mice relative to those receiving blocked AldMP following [^{18}F]NA_3BF_3 administration (3.99 ± 0.79 *vs.* 1.71 ± 0.31, $p < 0.05$).

Radiotracer accumulation was also examined dynamically for the three treatment groups tested, evaluating regions of interest in the shoulder receiving microparticles and the contralateral shoulder (Figure 4.3 *blue vs. orange*). While contralateral shoulder uptake remained relatively consistent between treatments, a substantial enhancement of uptake and prolongation of retention of radiotracer was only observed in the shoulder of mice bearing AldMP and receiving [^{18}F]NA_3BF_3 (Figure 4.4a). Considering the limited radiotracer uptake for the blocked AldMP-bearing mice (Figure 4.2b *right*, Figure 4.3c), these observations provide initial evidence that [^{18}F]NA_3BF_3 accumulation and retention is associated with local tissue aldehyde content.

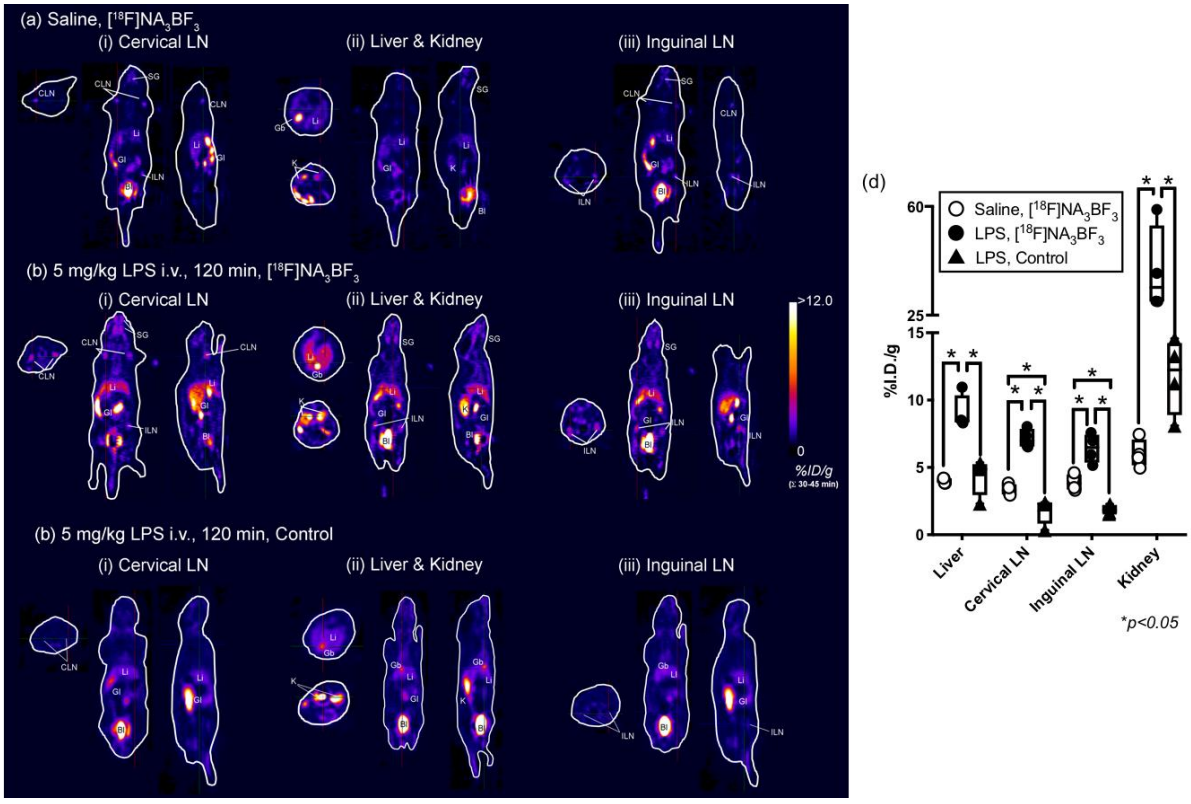

Figure 4.4. The uptake of [^{18}F]NA_3BF_3 increases in liver, kidney, and lymph nodes following acute sepsis. Orthogonal views of representative mice showing the differential uptake of [^{18}F]NA_3BF_3 2 hours following i.v. treatment with saline **(a)** or 5 mg/kg LPS **(b)**, or of control probe (**1a**) following 5 mg/kg LPS, focusing on anatomical regions of the cervical lymph node (*i*), liver and kidney (*ii*), and inguinal lymph node (*iii*). Images are summed acquisitions 30 to 45 min post-radiotracer injection. CLN: cervical lymph node, SG: salivary gland, Li: Liver, GI: Gastrointestinal tract, ILN: inguinal lymph node, K: kidney, Bl: bladder. **(d)** Radiotracer uptake was quantified in liver, cervical and inguinal LN, and kidney of mice receiving [^{18}F]NA_3BF_3 following saline (white circles) or 5 mg/kg LPS (black circles) treatment, or control probe (**1a**) following 5mg/kg LPS (black triangles). Individual data points are shown, as well as box and whisker plots (horizontal line = mean, box = standard deviation, and whiskers = min/max range). * $p < 0.05$ by tissue-wise ANOVA followed by Tukey's HSD test, $n = 4$ mice per group.

[^{18}F]NA_3BF_3 was then applied to image systemic inflammation in a mouse model of sepsis induced by i.v. injection of bacterial cell wall lipopolysaccharide (LPS), which is known to induce lipid peroxidation in liver and kidney, and to increase aldehyde load.[27-31] Balb/C mice were administered either saline (Figure 4.4a) or 5 mg/kg LPS i.v. (Figure 4.4b, c) 2 hr prior to imaging. Mice received [^{18}F]NA_3BF_3 (136 ± 15mCi) (Figure 4.4a, b) or control probe **1a** (150 ± 32 mCi) (Figure 4.4c) i.v., and PET was performed 30 min afterward. In mice receiving saline, [^{18}F]NA_3BF_3 uptake was observed in the gall bladder, proximal gastrointestinal (G.I.) tract, renal pelvis and bladder, suggesting both renal and G.I. tract elimination (Figure 4.4a, d). Following the induction of sepsis, a significant increase in [^{18}F]NA_3BF_3 uptake was observed in the liver, renal cortex and medulla, as well as cervical and inguinal lymph nodes (Figure 4.4b, d). The elevated uptake of [^{18}F]NA_3BF_3 in the liver and kidneys was expected.[29-31] Importantly, liver and kidney uptake of control probe following LPS treatment was significantly reduced relative to [^{18}F]NA_3BF_3, and lymphoid uptake was significantly lower than both LPS- and saline-treated mice receiving [^{18}F]NA_3BF_3 (Figure 4.4c, d). Lymphoid responses to LPS have been reported, including the induction of lymphocyte apoptosis as early as 1 h post-LPS injection,[32] and the upregulation of membrane receptors for LPS (toll-like receptors 2 and 4), pro-inflammatory signals and transcription factors (e.g. NFkB, and IkBa), and pro-inflammatory cytokines (e.g. TNF-a) within 3 hours of LPS administration.[33] Through [^{18}F]NA_3BF_3-mediated mapping of endogenous aldehyde production, support is provided for the local enhancement of lymph node aldehydes, in addition to hepatic and renal aldehydes, due to LPS-induced sepsis as a result of the activation of this inflammatory cascade.

This work has introduced a novel radiotracer, [^{18}F]NA_3BF_3, capable of mapping endogenous aldehydes in living subjects by PET. Radiofluorination of the *N*-amino anthranilic acid-based precursor compound was accomplished through an organotrifluoroborate isotope exchange mechanism with good radiochemical yields. Utilizing aldehyde-presenting microparticles, support was drawn for the ability of the *N*-amino anthranilic acid-based probe to bind aldehydes *in vivo*,

since administration of only the hydrazine-bearing radiotracer **2a**, but not the amine-bearing control compound **1a**, resulted in enhanced uptake, and only when free aldehyde groups were present (i.e. no retention enhancement was observed using blocked AldMP). Finally, [^{18}F]NA_3BF_3 was applied to a mouse model of sepsis and was capable of mapping early (within 3 h of LPS administration) aldehyde production in the liver and kidney, as well as lymphoid tissues, anatomical sites previously shown to induce pro-inflammatory signals and cytokines with LPS treatment.[32,33] With [^{18}F]NA_3BF_3, aldehyde biomarkers of lipid peroxidation and oxidative stress comprising endogenous aldehydic load may now be imaged *in vivo* while capitalizing on the high sensitivity (sub-pmol) and quantitative nature of PET.

4.6. Supplementary Materials

Electronic supplementary information (ESI) available: Experimental methods, syntheses, and compound characterization. See DOI: 10.1039/c9cc01831j.

See also Appendix to Chapter 4 included in this thesis.

4.7. Conflicts of Interest

There are no conflicts to declare.

4.8. Acknowledgements

We acknowledge Prof. Benjamin Rotstein for providing access to the shielded fume hood for radiosynthesis, and Daniel Duan and Tayebeh Hadizad at the Radiochemistry Facility at the University of Ottawa Heart Institute for the production of radiofluorine. This work was supported by NSERC Discovery Grant RGPIN 2015-05796 (A. J. S.), the Canada Research Chairs Program 950-230754 (A. J. S.), and the Canadian Institutes of Health Research PJT376892 (A. J. S.), and student support from the Ontario Graduate Scholars program (A. K.), and NSERC for an Undergraduate Summer Research Award (A. B.).

4.9. Notes and References

1 O'Brien, P. J., Siraki, A. G. & Shangari, N. Aldehyde Sources, Metabolism, Molecular Toxicity Mechanisms, and Possible Effects on Human Health. *Critical Reviews in Toxicology* **35**, 609-662, (2005).

2 Antoniak, D. T., Duryee, M. J., Mikuls, T. R., Thiele, G. M. & Anderson, D. R. Aldehyde-modified proteins as mediators of early inflammation in atherosclerotic disease. *Free Radical Biology and Medicine* **89**, 409-418, (2015).

3 Burke, W. J. *et al.* Neurotoxicity of MAO metabolites of catecholamine neurotransmitters: role in neurodegenerative diseases. *Neurotoxicology* **25**, 101-115, (2004).

4 Burke, W. J. *et al.* Aggregation of α-synuclein by DOPAL, the monoamine oxidase metabolite of dopamine. *Acta neuropathologica* **115**, 193-203, (2008).

5 Cristofori, L. *et al.* Biochemical analysis of the cerebrospinal fluid: evidence for catastrophic energy failure and oxidative damage preceding brain death in severe head injury: a case report. *Clinical biochemistry* **38**, 97-100, (2005).

6 Panneton, W. M., Kumar, V., Gan, Q., Burke, W. J. & Galvin, J. E. The neurotoxicity of DOPAL: behavioral and stereological evidence for its role in Parkinson disease pathogenesis. *PloS one* **5**, e15251, (2010).

7 Wood, P. L., Khan, M. A. & Moskal, J. R. The concept of "aldehyde load" in neurodegenerative mechanisms: cytotoxicity of the polyamine degradation products hydrogen peroxide, acrolein, 3-aminopropanal, 3-acetamidopropanal and 4-aminobutanal in a retinal ganglion cell line. *Brain research* **1145**, 150-156, (2007).

8 Yuen, L. H., Saxena, N. S., Park, H. S., Weinberg, K. & Kool, E. T. Dark hydrazone fluorescence labeling agents enable imaging of cellular aldehydic load. *ACS chemical biology* **11**, 2312-2319, (2016).

9 Ellis, E. M. Reactive carbonyls and oxidative stress: potential for therapeutic intervention. *Pharmacology & therapeutics* **115**, 13-24, (2007).

10 Dang, T. *et al.* Hydrazo-CEST: Hydrazone-Dependent Chemical Exchange Saturation Transfer Magnetic Resonance Imaging Contrast Agents. *Chemistry – A European Journal* **24**, 9148-9156, (2018).

11 Crisalli, P. & Kool, E. T. Importance of ortho proton donors in catalysis of hydrazone formation. *Organic letters* **15**, 1646-1649, (2013).

12 Kölmel, D. K. & Kool, E. T. Oximes and hydrazones in bioconjugation: mechanism and catalysis. *Chemical reviews* **117**, 10358-10376, (2017).

13 Kool, E. T., Park, D.-H. & Crisalli, P. Fast hydrazone reactants: electronic and acid/base effects strongly influence rate at biological pH. *Journal of the American Chemical Society* **135**, 17663-17666, (2013).

14 Liu, Z. *et al.* An Organotrifluoroborate for broadly applicable one-step 18F-labeling. *Angewandte Chemie International Edition* **53**, 11876-11880, (2014).

15 Liu, Z. *et al.* One-step 18F labeling of biomolecules using organotrifluoroborates. *Nature protocols* **10**, 1423-1432, (2015).

16 Perrin, D. M. Organotrifluoroborates as prosthetic groups for single-step F18-labeling of complex molecules. *Current Opinion in Chemical Biology* **45**, 86-94, (2018).

17 Schirrmacher, R. *et al.* 18F-labeling of peptides by means of an organosilicon-based fluoride acceptor. *Angewandte Chemie International Edition* **45**, 6047-6050, (2006).

18 McKay, C. S. & Finn, M. Polyvalent catalysts operating on polyvalent substrates: A model for surface-controlled reactivity. *Angewandte Chemie* **128**, 12833-12839, (2016).

19 Bernhard, Y. *et al.* Direct subphthalocyanine conjugation to bombesin vs. indirect conjugation to its lipidic nanocarrier. *Organic & Biomolecular Chemistry* **14**, 4511-4518, (2016).

20 Kommidi, H. *et al.* 18F-Radiolabeled Panobinostat Allows for Positron Emission Tomography Guided Delivery of a Histone Deacetylase Inhibitor. *ACS medicinal chemistry letters* **9**, 114-119, (2018).
21 Suchý, M. *et al.* Methyl 5-MeO-N-aminoanthranilate, a minimalist fluorogenic probe for sensing cellular aldehydic load. *Org Biomol Chem* **17**, 1843-1853, (2019).
22 Margel, S., Zisblatt, S. & Rembaum, A. Polyglutaraldehyde: A new reagent for coupling proteins to microspheres and for labeling cell-surface receptors. II. Simplified labeling method by means of non-magnetic and magnetic polyglutaraldehyde microspheres. *Journal of immunological methods* **28**, 341-353, (1979).
23 Rembaum, A., Margel, S. & Levy, J. Polyglutaraldehyde: A new reagent for coupling proteins to microspheres and for labeling cell-surface receptors. *Journal of immunological methods* **24**, 239-250, (1978).
24 Lazurko, C. *et al.* Multifunctional nano and collagen-based therapeutic materials for skin repair. *ACS Biomaterials Science & Engineering* **6**, 1124-1134, (2019).
25 Oussoren, C., Zuidema, J., Crommelin, D. & Storm, G. Lymphatic uptake and biodistribution of liposomes after subcutaneous injection.: II. Influence of liposomal size, lipid composition and lipid dose. *Biochimica et Biophysica Acta (BBA)-Biomembranes* **1328**, 261-272, (1997).
26 Adami, R. C. & Rice, K. G. Metabolic stability of glutaraldehyde cross-linked peptide DNA condensates. *Journal of pharmaceutical sciences* **88**, 739-746, (1999).
27 Hung, Y.-L. *et al.* Corylin protects LPS-induced sepsis and attenuates LPS-induced inflammatory response. *Scientific reports* **7**, 46299, (2017).
28 Liu, J. *et al.* CEST MRI of sepsis-induced acute kidney injury. *NMR in Biomedicine* **31**, e3942, (2018).
29 Liu, H. *et al.* The SMAC mimetic birinapant attenuates lipopolysaccharide-induced liver injury by inhibiting the tumor necrosis factor receptor–associated factor 3 degradation in Kupffer cells. *Immunology letters* **185**, 79-83, (2017).
30 Peavy, D. L. & Fairchild, E. J. Evidence for lipid peroxidation in endotoxin-poisoned mice. *Infection and immunity* **52**, 613-616, (1986).
31 Requintina, P. J. & Oxenkrug, G. F. Differential effects of lipopolysaccharide on lipid peroxidation in F344N, SHR rats and BALB/c mice, and protection of melatonin and NAS against its toxicity. *Annals of the New York Academy of Sciences* **993**, 325-333, (2003).
32 Norimatsu, M., Ono, T., Aoki, A., Ohishi, K. & Tamura, Y. In-vivo induction of apoptosis in murine lymphocytes by bacterial lipopolysaccharides. *Journal of medical microbiology* **43**, 251-257, (1995).
33 Wang, J. *et al.* Anti-inflammatory activity of curcumin-loaded solid lipid nanoparticles in IL-1β transgenic mice subjected to the lipopolysaccharide-induced sepsis. *Biomaterials* **53**, 475-483, (2015).

Appendix to Chapter 4

Supplementary Material for:

Mapping Aldehydic Load *In vivo* By Positron Emission Tomography with [^{18}F]NA3BF3

Alexia Kirby*, Mojmír Suchý*, Andrea Brouwer, Adam Shuhendler

*authors contributed equally

General Synthetic Procedures

Reagents were commercially available, or prepared as stated below. All solvents were HPLC grade except for water (18.2 MΩ cm millipore water), CH_2Cl_2 and Et_2O (dried over Al_2O_3 in a solvent purification system). Solvents were removed under reduced pressure in a rotary evaporator, aqueous solutions were lyophilized and organic extracts were dried over Na_2SO_4. Flash column chromatography (FCC) was carried out using silica gel (SiO_2), mesh size 230 - 400 Å. Thin-layer chromatography (TLC) was carried out on Al backed silica gel plates with compounds visualized by anisaldehyde stain, 5% ninhydrin stain, and UV light. HPLC purification (Method A) was performed using a Luna C_{18} 100 Å column (particle size 5 μm; 21.2 × 250 mm). Mobile phase for Method A was 0 min, 99% H_2O – 1% MeCN to 25 min, 100% MeCN, linear gradient and 10 mL/min flow rate. HPLC analysis associated with the radiolabeling (Method B) was performed using a Luna C_{18} 100 Å column (particle size 5 μm; 4.6 × 250 mm). Mobile phase for Method B was 0 min, 99% H_2O – 1% MeCN to 21 min, 100% MeCN, linear gradient and 1 mL/min flow rate. NMR spectra were recorded on a 300 or 400 MHz spectrometers for ^{1}H NMR spectra δ values were recorded as follows: DMSO-D_6 (2.50 ppm), D_2O (4.79 ppm), CD_3OD (3.31 ppm); for ^{13}C (93.75 or 125 MHz) δ DMSO-D_6 (39.50 ppm), CD_3OD (49.00 ppm). Mass spectra (MS) were obtained using electron impact (EI) or electrospray ionisation (ESI). Synthetic procedures associated with this work can be found in Scheme 1 in the main text.

Preparation of 5-*O*-propargyl-*N*-Boc-anthranilic acid (2)

5-*O*-Propargyl-*N*-Boc-anthranilic acid (**2**) was prepared in four steps from 5-hydroxyanthranilic acid (**1**) as described in ref.[1]; spectral characteristics of all of the intermediates and the 5-*O*-propargyl-*N*-Boc-anthranilic acid (**2**) were in agreement with those described previously.[1]

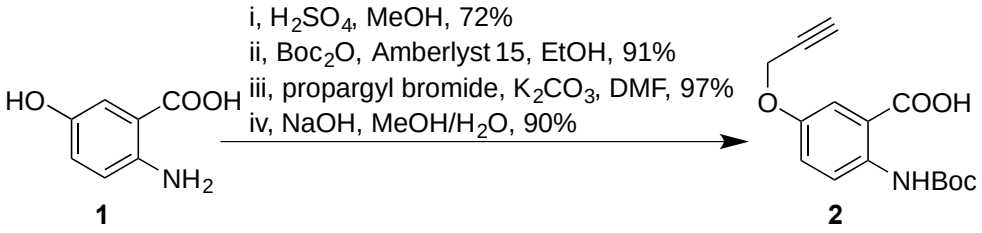

Scheme S4.1

Preparation of 5-*O*-propargyl-anthranilic acid (3)

TFA (500 µL) was added to a stirred suspension of 5-*O*-propargyl-*N*-Boc-anthranilic acid (**2**, 29 mg, 0.1 mmol) in CH_2Cl_2. The mixture was stirred for 1 h at room temperature (rt), volatiles were evaporated and the residue was co-evaporated with CH_2Cl_2 (3 × 50 mL). 5-*O*-propargyl-anthranilic acid (**3**) was obtained in quantitative yield as a white solid and was used for the subsequent step without further purification. Spectral characteristics of 5-*O*-propargyl-anthranilic acid (**3**) were in agreement with those described previously.[1]

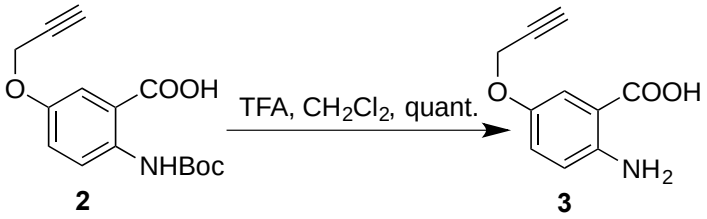

Scheme S4.2

Preparation of 2-azido-*N*,*N*-dimethylethaneamine (5)

This material was prepared according to the procedure described in ref.[2], which was modified as follows. A stirred solution of *N*,*N*-dimethylaminoethanol (**4**, 2 mL, 20 mmol) in dry CH_2Cl_2 (8 mL) was cooled to 0 ºC, while being flushed with N_2. $SOCl_2$ (1.6 mL, 22 mmol) was added dropwise over 5 min period. The cooling bath was removed and the mixture was stirred for 2 h at rt (N_2 atmosphere). The mixture was diluted with EtOH (10 mL), was concentrated to ca. one third of its original volume and was set aside for 18 h at 3 ºC. Colorless needles formed; they were filtered off with suction, were washed with cold Et_2O and were dried to afford *N*,*N*-dimethylamino-2-chloroethaneamine dihydrochloride (1.58 g, 55%); its spectral characteristics were in agreement with those described in ref.[2]

NaN_3 (902 mg, 13.88 mmol) was added to a stirred solution of *N*,*N*-dimethylamino-2-chloroethaneamine dihydrochloride (1 g, 6.94 mmol)in water (4 mL). The mixture was stirred for 18 h at 80 ºC, was cooled to rt and was treated with a solution of NaOH (279 mg, 6.94 mmol) in water (1 mL). The resulting mixture was stirred for 2 h at rt, was transferred into a separatory funnel and was extracted with EtOAc (4 × 10 mL). Combined organic extract was dried and concentrated to leave *N*,*N*-dimethylamino-2-azidoethaneamine (**5**, 315 mg, 40%) as colourless oil; its spectral characteristics were in agreement with those described in ref.[2]

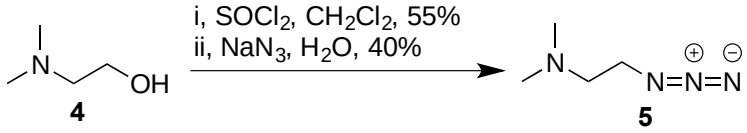

Scheme S4.3

Reaction of *N*,*N*-dimethylamino-2-azidoethaneamine (5) with iodomethylboronylpinacolate

Modified literature protocol[3] was used to perform this reaction. Iodomethylboronic acid pinacol ester (510 μL, 2.76 mmol) was added dropwise (over 1 min period) to a solution of *N*,*N*-dimethylamino-2-azidoethaneamine (**5**, 315 mg, 2.76 mmol) in dry Et_2O (12 mL). The mixture was stirred for 18 h at rt,

separated white precipitate was filtered off, was washed with ice-cold Et_2O and was dried to afford intermediate **5a**. No spectral characterization of intermediate **5a** is provided in the original reference.[3] Intermediate **5a**; white solid, 885 mg, 84%. ^{1}H NMR δ (D_2O) 3.91 (m, 2H); 3.69 (m, 2H); 3.22 (s, 6H); 3.10 (s, 2H); 1.20 (s, 12H).^{13}C NMR δ (D_2O) 75.7, 63.7, 54.2, 45.0, 23.8. ^{11}B NMR δ (D_2O) 26.9 (s).

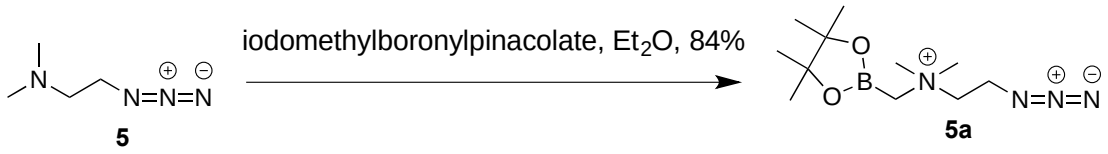

Scheme S4.4

Preparation of trifluoroborate azide6

Modified literature protocol was used to perform this reaction.[3] A solution (3 M in water) of KHF_2 (1.2 mL, 3.6 mmol) was added to a Falcon tube containing a stirred suspension of intermediate **5a**(225 mg, 0.59 mmol) in water (800 µL). The mixture was stirred for 2 h at 45 ºC, was cooled to room temperature and the pH was adjusted to ~7 (several drops of conc. NH_4OH). The reaction mixture was passed through a C_{18} normal phase SiO_2Seppak cartridge directly attached to QMA ion-exchange cartridge. The cartridges wee eluted with water (5 × 1 mL), the aqueous solution was extracted with Et_2O (6 × 5 mL) to remove the pinacol formed during the reaction. The aqueous solution was lyophilized to afford 330 mg of a white solid residue containing ca. 33% of trifluoroborate azide**6** along with other inorganic material (mainly KI). This material was used for the subsequent step without further purification. No spectral characterization (except for ESI-MS) of trifluoroborate azide**6** is provided in the original reference.[3] ^{1}H NMR δ (D_2O) 3.89 (t, J = 5.5 Hz, 2H); 3.51 (t, J = 6.5 Hz, 2H); 3.11 (s, 6H); 2.56 (m, 2H). ^{13}C NMR δ (D_2O) 64.0, 53.9, 44.9. ^{11}B NMR δ (D_2O) 2.1 (m).^{19}F NMR δ (D_2O) -136.9 (m).

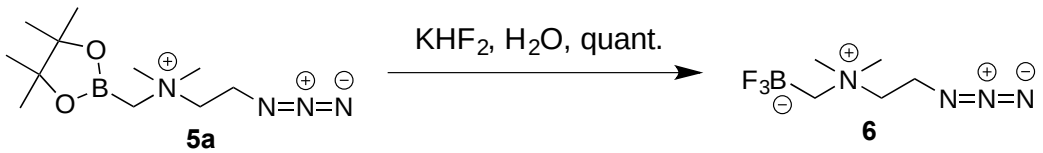

Scheme S4.5

Click reaction between 5-*O*-propargyl-anthranilic acid (3) and trifluoroborate azide6 to yield 7

This reaction was carried out as two batches run in parallel. Separate round bottom flasks containing 5-*O*-propargyl-anthranilic acid (**3**, 19 mg, 0.1 mmol) were charged with the lyophilized mixture containing ~ 33% of trifluoroborate azide (**6**, 58 mg, 0.1 mmol). DMSO (1.5 mL) was added into each flask, followed by the addition of $(BimC4A)_3$ (16 mg, 0.02 mmol). 1 M solutions of $CuSO_4 \cdot 5H_2O$ (50 μL, 0.05 mmol) and sodium ascorbate (100 μL, 0.1 mmol) were added and the reaction mixtures were stirred for 18 h at 50 ºC. The mixtures were cooled to rt, were diluted with water (10 mL), were transferred into Falcon tubes and were centrifuged (5 min at 5,000 rpm). The supernatants were combined and were subjected to preparative HPLC purification (Method A, General experimental procedures). The fractions containing the peak with t_R ~ 15 min were combined and were lyophilized to afford 39 mg of the solid residue. The residue was dissolved in water (15 mL) and was subjected to repeated preparative HPLC purification under identical conditions. The fractions containing the peak with t_R ~ 15 min were combined and were lyophilized to afford the desired anthranilic acid-derived trifluoroborate. A small amount of the product was aliquoted into Eppendorf tubes, so that each tube contained 0.09 mg (2.32×10^{-7} mol) of the anthranilic acid-derived trifluoroborate; this was used for the radiofluorination as described below. Anthranilic acid-derived trifluoroborate**7**; pale yellow fluffy solid, 29 mg, 38%. ^{1}H NMR δ (CD_3OD) 8.14 (s, 1H); 7.47 (d, J = 3.0 Hz, 1H); 7.06 (dd, J = 9.0, 3.0 Hz, 1H); 6.81 (d, J = 9.0 Hz, 1H); 5.13 (s, 2H); 4.98 (t, J = 7.0 Hz, 2H); 3.87 (t, J = 7.0 Hz, 2H); 3.09 (s, 3H); 2.54 (m, 2H).^{11}B NMR δ (CD_3OD) 2.1 (m). ^{19}F NMR δ (CD_3OD) -140.8 (m).HRMS (ESI) *m/z* found 410.1578 $[M + Na]^+$ (calcd 410.1587 for $C_{15}H_{21}BF_3N_5O_3Na$).

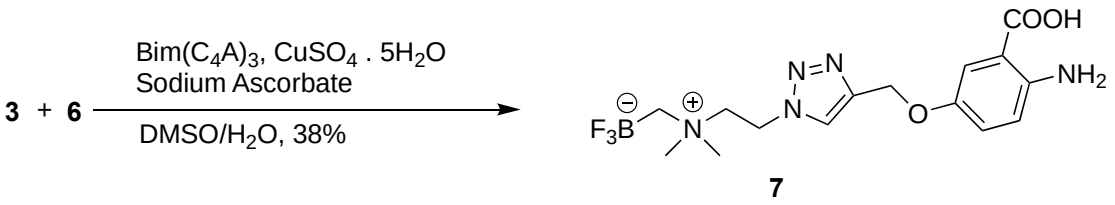

Scheme S4.6

Diazotization and reduction of anthranilic acid-derived trifluoroborate 7 to yield 8

A solution of **7** (14 mg, 3.6 × 10^{-5} mol) in 6 M HCl and MeOH (120 µL each) was cooled to 4 ºC, followed by the addition of a solution of $NaNO_2$ (54 µL, 1 M in water, 5.4 × 10^{-5} mol). The mixture was stirred for 40 min at 4 ºC, followed by the addition of a solution of $SnCl_2 \cdot 2H_2O$ (16 mg, 7.2 × 10^{-5} mol) in 6 M HCl (120 µL). The stirring continued for further 30 min at rt. The mixture was diluted with water (10 mL) and was subjected to preparative HPLC purification (Method A, General experimental procedures). The fractions containing the peak with t_R ~ 13 min were combined, one drop of 6 M HCl was added followed by lyophilization. The material was then aliquoted into Eppendorf tubes, so that each tube contained 0.1 mg (2.1 × 10^{-7} mol) of hydrazine-derived trifluoroborate; this was used for the radiofluorination as described below. Hydrazine-derived trifluoroborate dihydrochloride**8**; white fluffy solid, 1.3 mg, 8%. ^{1}H NMR δ (CD_3OD) 8.18 (s, 1H); 7.69 (d, *J* = 3.0 Hz, 1H); 7.33 (dd, *J* = 9.0, 3.0 Hz, 1H); 7.10 (d, *J* = 9.0 Hz, 1H); 5.22 (s, 2H); 4.99 (t, *J* = 7.0 Hz, 2H); 3.87 (t, *J* = 7.0 Hz, 2H); 3.11 (s, 3H); 2.53 (m, 2H). ^{11}B NMR δ (CD_3OD) 1.5 (m). ^{19}F NMR δ (CD_3OD) -140.6 (m). HRMS (ESI) *m/z* found 403.1891 $[M+ H]^+$ (calcd 403.1877 for $C_{15}H_{23}BF_3N_6O_3$).

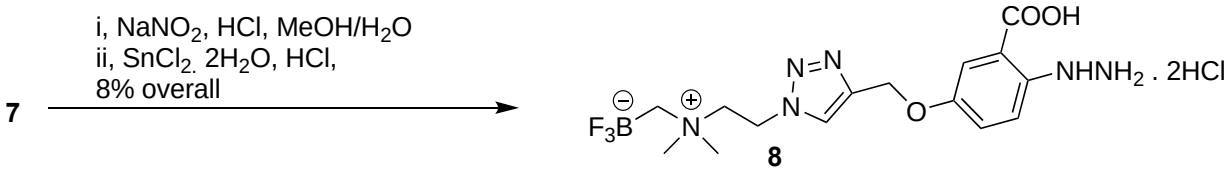

Scheme S4.7

The identity of the hydrazine-derived trifluoroborate dihydrochloride was also verified by reaction with acetaldehyde which occurred instantaneously[4] as follows: Small amount of the HPLC fraction containing the hydrazine-derived trifluoroborate dihydrochloride (50 μL) was treated with 3 drops of a solution of acetaldehyde and formic acid (1 drop each) in MeOH (500 μL); resulting solution was analyzed by HR-ESI-MS. HRMS (ESI) *m/z* found 429.2036 $[M + H]^+$ (calcd 429.2033 for $C_{17}H_{25}BF_3N_6O_3$).

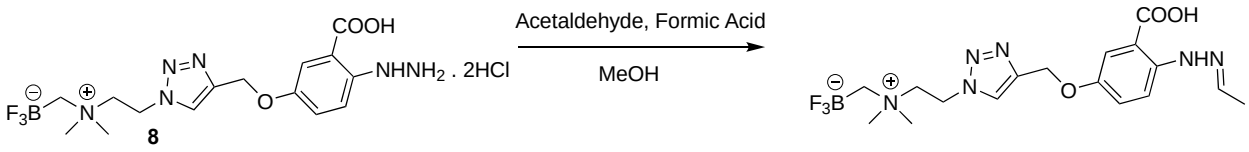

8

Scheme S4.8

Radiolabeling of hydrazine-derived trifluoroborate dihydrochloride and hydrazine-derived anthranilic acid

The radiolabeling protocols were adopted from the previously described methods.[3,5,6] Multiple radiolabelings were performed as described below and shown in the Supporting Scheme S4.9; the results are summarized in the Supporting Table S4.1.

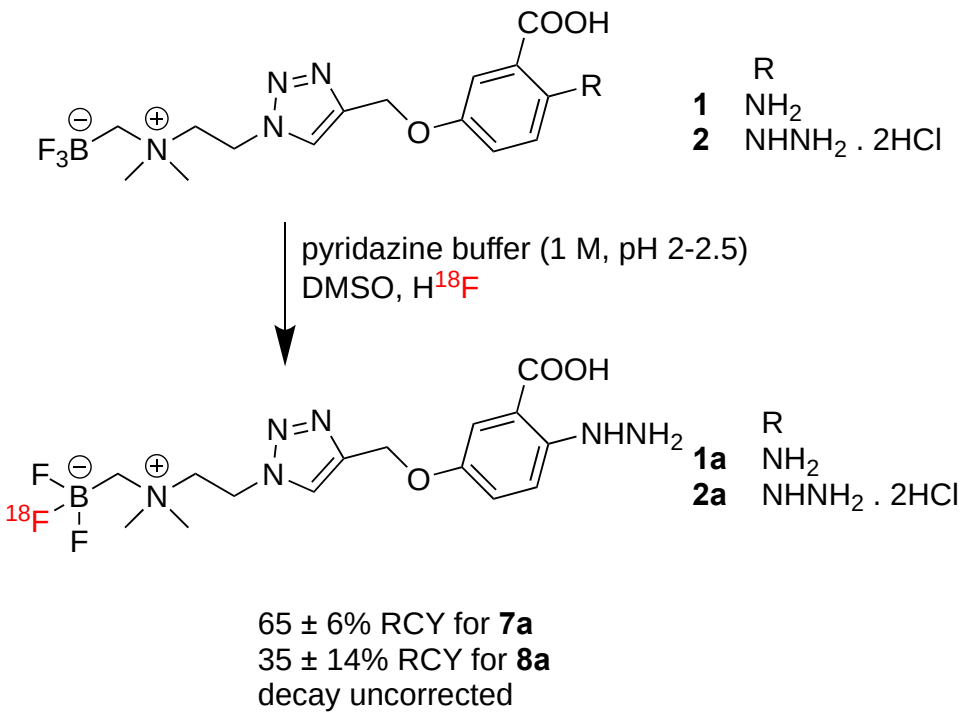

Scheme S4.9

Concentration of the [^{18}F] HF solution

A 0.1 M solution of $NaHCO_3$ (10 µL)[5] was added to a cyclotron produced solution of [^{18}F]HF in water (~ 250 µL, 30 – 50 mCi) in a Falcon tube (5 mL). The mixture was heated at 105 – 110 ºC (sand bath) under stream of nitrogen. The heating was stopped when the residual volume in the tube was ~ 50 µL. Resulting solution was used for the radiofluorination as described below.

Radiofluorination of hydrazine-derived trifluoroborate dihydrochloride

An aliquot of hydrazine-derived trifluoroborate dihydrochloride (**8**) (0.1 mg, 2.1×10^{-7} mol) in an Eppendorf tube was dissolved in 1 M pyridazine buffer (pH 2 – 2.5, 10 µL)[3,5] and DMSO (5 µL).[6] A concentrated [^{18}F]HF solution (15 µL) was added and the mixture was heated for 10 min at 95 – 100 ºC (sand bath). The reaction was quenched with 1 M $NaHCO_3$ solution (100 µL) and saline (500 µL) and was loaded on an acidic Sep-Pak light alumina cartridge. The cartridge was eluted with saline, 5 fractions (500 µL each) were obtained. The activity in each fraction was measured, revealing that the substantial amount

of the radiotracer was consistently found in fractions 1 and2. The identity and purity of the radiotracer was verified by radio-HPLC (Method B, t_R 8.7 min) and by comparison with the corresponding cold standard (t_R8.6 min), as depicted in Figure 4.1 of the main text. The material in these fractions was used for *in vivo* studies, as well as for calculating the decay uncorrected radiochemical yield (RCY) and molar activity (MA). The results are summarized in the Supporting Table 3.1.

Radiofluorination of anthranilic acid-derived trifluoroborate

An aliquot of anthranilic acid-derived trifluoroborate (**7**) (0.09 mg, 2.32×10^{-7} mol) in an Eppendorf tube was dissolved in 1 M pyridazine buffer (pH 2 – 2.5, 10 µL)[3,5] and DMSO (5 µL).[6] A concentrated [^{18}F]HF solution (15 µL) was added and the mixture was heated for 10 min at 95 – 100 ºC (sand bath). The reaction was quenched with 1 M $NaHCO_3$ solution (100 µL) and saline (500 µL) and was loaded on an acidic Sep-Pak light alumina cartridge. The cartridge was eluted with saline, 5 fractions (500 µL) were obtained. The activity in each fraction was measured, revealing that the substantial amount of the radiotracer was consistently found in fractions 1 and 2. The identity and purity of the radiotracer was verified by radio-HPLC (Method B, t_R 8.0 min) and by comparison with the corresponding cold standard (t_R 7.9 min), as depicted in Supporting Figure S1. The material in these fractions was used for *in vivo* studies, as well as for calculating the decay uncorrected radiochemical yield (RCY) and specific activity. The results are summarized in the Supporting Table 1.

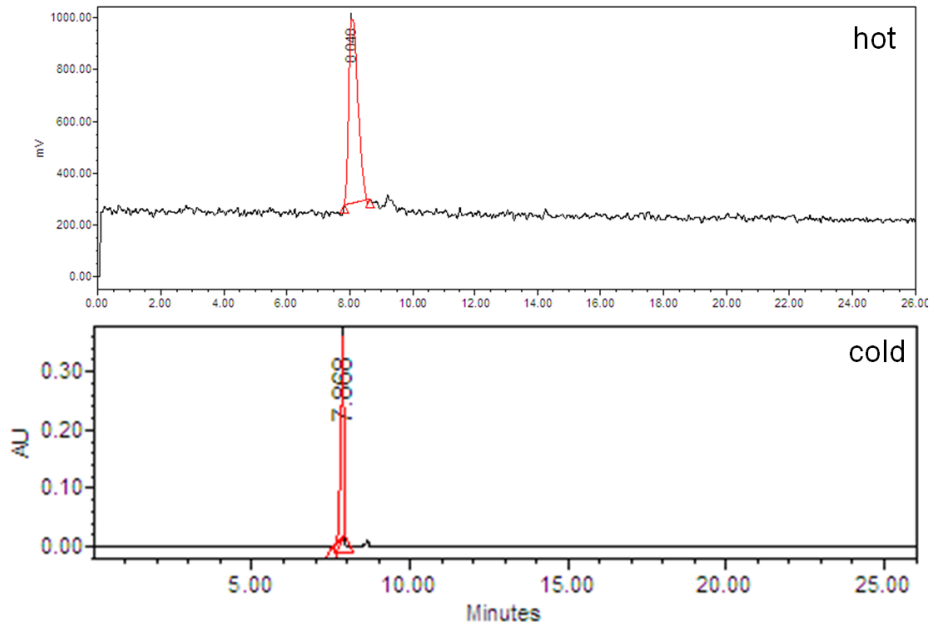

Figure S4.1: HPLC traces of [^{18}F]-anthranilic acid-derived trifluoroborate (**1a**) (top) and the corresponding radiofluorination precursor/cold standard **1** (bottom); due to the interference of pyridazine with the UV trace, the cold standard sample was prepared by dissolving an aliquot (0.1 mg) in 100 µL 1 M $NaHCO_3$/400 µL saline/500 µL water.

Supporting Table S4.1: Radiolabeling of hydrazine-derived trifluoroborate dihydrochloride (**2**) and anthranilic acid-derived trifluoroborate (**1**).

Precursor Used	Initial Activity (mCi)	Activity after 10 min (mCi)	Activity in Fraction 1 (mCi)	Activity in Fraction 2 (mCi)	Overall Activity (mCi)	Decay Uncorrected Radiochemical Yield (%)	Molar Activity (mCi/μmol)
2	5.20	4.85	1.04	0.99	2.03	42	9.64
2	4.60	4.23	0.84	0.85	1.69	40	8.04
2	3.13	2.96	0.70	0.74	1.44	49	6.85
2	8.14	7.33	0.42	0.55	0.97	13	4.64
2	5.28	4.77	0.31	0.40	0.71	15	3.37
2	12.96	12.33	1.24	1.45	2.69	22	12.81
2	14.72	14.06	1.51	1.45	2.96	21	14.10
2	8.72	8.53	1.86	1.75	3.61	42	17.19
2	8.88	8.72	2.03	2.08	4.11	46	19.57
2	4.76	4.60	1.03	1.04	2.07	45	9.86
2	5.46	5.24	1.39	1.29	2.68	51	12.76
1	2.36	2.23	0.55	0.73	1.28	58	5.53
1	3.23	3.05	1.03	1.03	2.06	68	8.88
1	4.52	4.04	1.49	1.26	2.75	68	11.85

Synthesis and Characterization of Polyglutaraldehyde Microparticles (AldMP)

AldMP were prepared as previously described.[7] Briefly, a solution comprising 100 mL of 5% v/v glutaraldehyde in water (70% aqueous glutaraldehyde solution) with 1% w/v Pluronic F127 was bubbled with N_2 and stirred for 10 min. 10 N NaOH was added dropwise to this solution until the pH of the solution was confirmed to be pH 11. The solution was stirred at room temperature overnight, with the pH being assessed 1, 2, and 4 hr after the initial addition of NaOH to maintain the solution at pH 11. The milky solution was washed three times with water by centrifugation (3500rpm for 10min). In order to acquire SEM images, particles were freeze dried and applied to an aluminum sample holder. The sample was then

coated with 5 nm of gold using an EM ACE200 vacuum coater (Leica Microsystems, Inc., Concord ON, Canada). Micrographs were then acquired on a JSM-7500F FESEM (Jeol USA, Inc., Peabody MA, USA) using 2.00 kV acceleration voltage and 20.0 uA under 4.4×10^{-4} Pa vacuum. Aldehyde presentation on theAldMP surface was evaluated using a fluorophore, methyl 5-methoxy-*N*-aminoanthranilate, as previously reported.[8] A DMSO solution of methyl 5-methoxy-*N*-aminoanthranilate was added to a suspension of AldMP diluted to approximately 1% w/v in 1× PBS, or to an equal volume of 1×PBS to a final concentration of 100 mM. The solution was mixed briefly by agitation and placed on a transilluminator with excitation wavelength of 302 nm immediately after mixing.

Serum Stability Study

A solution of **8a** in saline (300 μL) was added to a tube containing freshly thawed mouse serum (1 mL), to reach the activity of 206 μCi. Samples were withdrawn at 0 min (200 μL, 25.7 μCi), 30 min (250 μL, 26.0 μCi), 60 min (300 μL, 26.1 μCi) and 120 min (400 μL, 24.1 μCi), they were diluted with water to reach the final volume 1 mL, were filtered (Pasteur pipette with a cotton plug) and were analyzed by HPLC.

Cell Uptake Study

HEK293 cells ($1´10^6$ cells/mL) were plated in Eagle's Modified MEM supplemented with non-essential amino acids and FBS, and kept overnight in a humidified incubator at 37°C and 5% CO_2 atmosphere. Cells were treated with DMSO (vehicle) or a DMSO solution of diethyl maleate (DEM) to a final concentration of 1.5 mM for 1 or 2 hr. To each well was added 5 μCi/mL of $[^{18}F]NA_3BF_3$, and cells were incubated for 30 min. Cells were washed with cold DPBS three times, and lysed and lifted with RIPA buffer. One-half of the RIPA solution was counted on a Packard Cobra Quantum 5200 gamma counter, while the other half was subjected to protein quantitation by Bradford Assay following standard procedures.

Animal Models and Imaging

All animal work was approved by the IACUC of the University of Ottawa under AUP sc-3036, and ensures that experimental protocols and animal welfare meet that standards set out by the Canadian Council on

Animal Care. Female Balb/C mice (8 weeks old, Charles River Laboratories, Sherbrooke QC, Canada) were acclimated for 1week prior to experimentation. For studies involving AldMP, mice received an injection of a saline suspension of AldMP (50 mL, 10% w/v) or saline alone s.c. above the right and left shoulders, respectively. Tail veins were cannulated and mice received approximately 180 mCi of either [^{18}F]NA_3BF_3 (**2a**,*n*=4) or control probe (compound **1a**) (*n*=4) 30 min after AldMP injection. For pre-labeled AldMP study, [^{18}F]NA_3BF_3 (200 mCi/50mL particles) and AldMP solution was incubated at room temperature for 10 min, and washed twice by pelleting (3500 rpm, 5min) and resuspending in saline. PET imaging was performed on an InveonD-PET small animal imaging system (Siemens, Munich, Germany) from 30 to 45 min following radiotracer administration. For studies involving sepsis, mice received i.v. administration of either 5 mg/kg E. coli bacterial cell wall lipopolysaccharide O55:B5 in saline (*n*=4), or saline alone (*n*=4). Two hours later, tail veins were cannulated and mice received approximately 180 mCi of [^{18}F]NA_3BF_3, followed 30 min later by a 15 min static PET scan. All PET images were acquired using Inveon Acquisition Workstation software and were reconstructed using a 3D-OSEM algorithm with attenuation correction. Data were analyzed and images were generated using VivoQuant v 2.5 (inviCRO LLC, Boston MA, USA).

Statistics

Uptake ratio was compared between the control compound (**1a**) and [^{18}F]NA_3BF_3(**2a**) using a two-tailed t-test, and radiotracer uptake differences after sepsis was evaluated by ANOVA followed by Tukey's Test for HSD. All statistical analyses were performed with GraphPad Prism v.7 (GraphPad Software, La Jolla CA, USA).

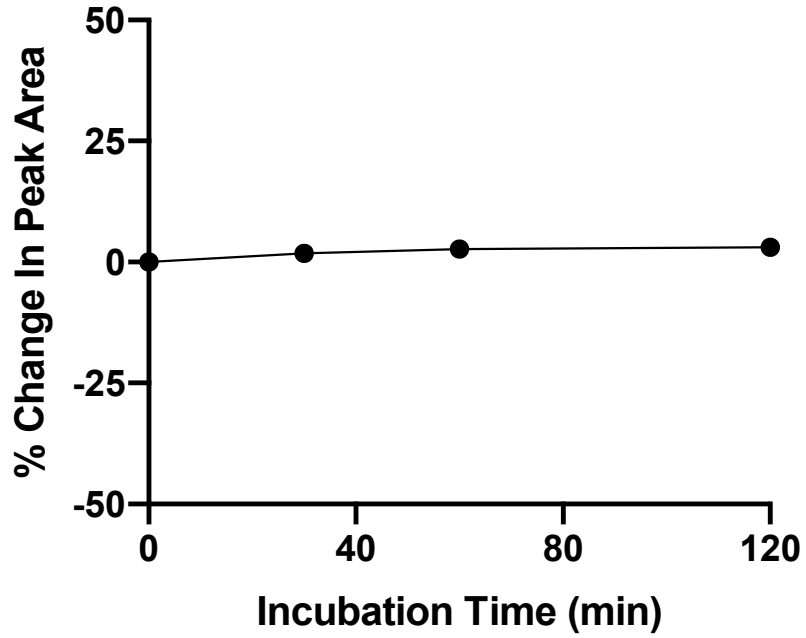

Figure S4.2. Serum stability of [^{18}F]NA_3BF_3. The stability of the radiotracer, [^{18}F]NA_3BF_3, was assayed in mouse serum at 37°C. Samples were extracted and analyzed by HPLC, with the resulting change in peak area plotted over time.

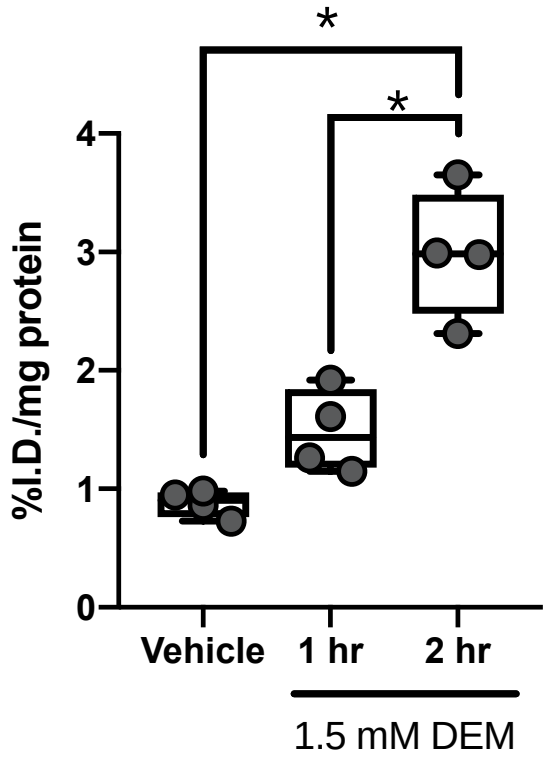

Figure S4.3. Uptake of [^{18}F]NA_3BF_3 in HEK293 cells following electrophilic stress. Cell uptake is shown following incubation of [^{18}F]NA_3BF_3 for 30 min with HEK293 cells treated with DMSO (vehicle), or with 1.5 mM DEM for 1 or 2 hr. Individual data points are shown, as well as box and whisker plots (horizontal line = mean, box = standard deviation, and whiskers = min/max range). * significant difference (p<0.05 by two-way ANOVA).

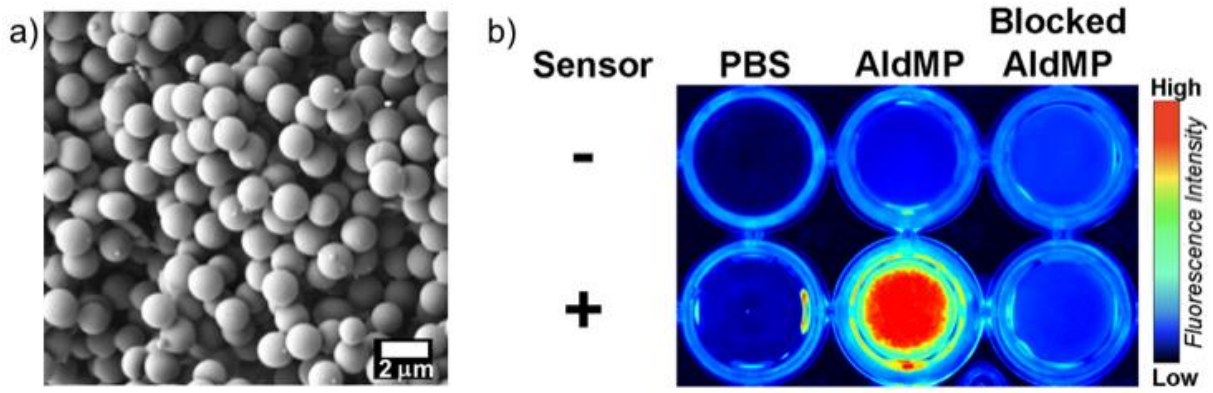

Figure S4.4. Morphological and functional characterization of (poly)glutaraldehyde microparticles (AldMP). An emulsion polymerization method was utilized for the preparation of AldMP. (**a**) SEM of AldMP was acquired with 5 nm gold coating, and shows spherical microparticles less than 2 µm in diameter. (**b**) The presentation of aldehydes on the surface of AldMP was verified using an aldehyde-sensitive fluorogenic probe methyl 5-methoxy-*N*-aminoanthranilate (i.e. sensor). The samples pictured contain PBS (*left*), AldMP (*middle*), and AldMP pre-saturated with *N*-amino anthranilic acid (Blocked AldMP, *right*) either without (*top row*) or with (*bottom row*) the addition of aldehyde-reactive fluorogenic sensor.

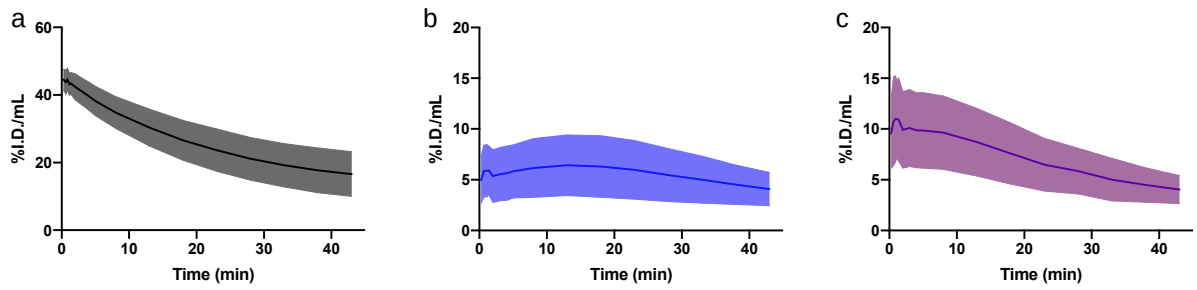

Figure S4.5. Kinetics of AldMP pre-labeled with [^{18}F]NA_3BF_3. AldMP were pre-inucbated with [^{18}F]NA_3BF_3, washed, and inoculated into the shoulder of Balb/C mice at a dose of 20 mCi per animal. Dynamic PET imaging was initiated 30 min post-injection. The quantity of AldMP was determined for the injected shoulder (a, black), the liver (b, blue) and the kidney (c, purple). Data represent the mean±s.d. for n=4 mice.

References

1 McKay, C. S. & Finn, M. Polyvalent catalysts operating on polyvalent substrates: A model for surface-controlled reactivity. *Angewandte Chemie* **128**, 12833-12839, (2016).

2 Bernhard, Y. *et al.* Direct subphthalocyanine conjugation to bombesin vs. indirect conjugation to its lipidic nanocarrier. *Organic & Biomolecular Chemistry* **14**, 4511-4518, (2016).

3 Liu, Z. *et al.* An Organotrifluoroborate for broadly applicable one-step 18F-labeling. *Angewandte Chemie International Edition* **53**, 11876-11880, (2014).

4 Dang, T. *et al.* Hydrazo-CEST: Hydrazone-Dependent Chemical Exchange Saturation Transfer Magnetic Resonance Imaging Contrast Agents. *Chemistry – A European Journal* **24**, 9148-9156, (2018).

5 Liu, Z. *et al.* One-step 18F labeling of biomolecules using organotrifluoroborates. *Nature protocols* **10**, 1423-1432, (2015).

6 Kommidi, H. *et al.* 18F-Radiolabeled Panobinostat Allows for Positron Emission Tomography Guided Delivery of a Histone Deacetylase Inhibitor. *ACS medicinal chemistry letters* **9**, 114-119, (2018).

7 Margel, S., Zisblatt, S. & Rembaum, A. Polyglutaraldehyde: A new reagent for coupling proteins to microspheres and for labeling cell-surface receptors. II. Simplified labeling method by means of non-magnetic and magnetic polyglutaraldehyde microspheres. *Journal of immunological methods* **28**, 341-353, (1979).

8 Lazurko, C. *et al.* Fingerprinting Biogenic Aldehydes Through Pattern Recognition Analyses of Excitation-Emission Matrices. *ChemBioChem* **40**, 543-554, (2019).

Chapter 5: Aldehydic load as an objective imaging biomarker of mild traumatic brain injury by CEST-MRI

Alexia Kirby[1,2], Cian Ward[1], Nicholas D. Calvert[2,3], Ryan Daniel[1], Joseph Wai-Hin Leung[1,4], Ashwin Sharma[1], Mojmír Suchý[2,3], Cassandra Donatelli[1], Jing Wang[4,5,6], Emily Standen[1], Adam J. Shuhendler[1,2,3,6]*

[1]Department of Biology, University of Ottawa; Ottawa, ON, Canada.

[2]University of Ottawa Heart Institute; Ottawa, ON, Canada.

[3]Department of Chemistry and Biomolecular Sciences; University of Ottawa, Ottawa, ON, Canada;

[4]Regenerative Medicine Program, Ottawa Hospital Research Institute, Ottawa, ON, Canada;

[5]Department of Cellular and Molecular Medicine, University of Ottawa; Ottawa, ON, Canada;

[6]Brain and Mind Research Institute, University of Ottawa; Ottawa, ON, Canada.

*Corresponding author: Adam Shuhendler (adam.shuhendler@uottawa.ca)

5.1. Introduction to the Research Article Presented Within this Chapter

Following the development and characterization of aldehyde-targeting probes for fluorescence microscopy and PET, a third modality was added to the aldehyde imaging toolkit in this present chapter: MRI. The clinical diagnosis of mild traumatic brain injury (mTBI), or concussion, relies on subjective diagnostic scoring and often leads to missed diagnoses and therefore worse patient outcomes. Following brain injury, oxidative damage to cells leads to downstream production of toxic, endogenous aldehydes. We created a new CEST-MRI agent, ProxyNA$_3$, that maps total aldehydic load as a quantitative biomarker for mTBI. We document the production of aldehydes in a 3D cell model of concussion and can objectively identify mTBI in a mouse model 2 days post-injury. Our research supports the use of ProxyNA$_3$ as an objective diagnostic neuroimaging tool for mTBI that may lead to better personalized medicine.

5.2. Author Contributions

A.K., R.D., and A.S. developed *in vivo* mouse model of mTBI. A.K., C.W., A.S. and N.D.C. contributed to corticomimetic scaffold development. J.W. and J.L. performed primary cortical precursor cell dissections. M.S. and N.C. performed all chemistry for probe preparation. A.K., R.D., C.D., and E.S. conducted UTM experiments. A.K. performed histology, microscopy, and molecular biology procedures. A.K. and A.J.S. conducted MR imaging, performed statistical analysis, data interpretation, and drafting of manuscript.

5.3. Copyright

5.4. Abstract

Concussion, or mild traumatic brain injury (mTBI), yields complex neurological impairment from biomechanical forces without structural brain damage. An objective diagnostic tool for concussion is needed, and the search for diagnostic biomarkers is ongoing. A collagen-based 3D corticomimetic scaffold afforded an *in vitro* model of concussion, which confirmed increased aldehyde production in live neurons

following impact. To evaluate total aldehyde levels *in vivo* following mTBI, a novel CEST-MRI contrast agent, ProxyNA$_3$, has been implemented in a new model of closed-head, awake, single-impact concussion yielding transient behavioural deficits was developed in aged and young mice with aldehyde dehydrogenase 2 (ALDH2) deficiency. MRI signal enhancement significantly increased at two days post-injury and decreased to baseline seven days post-injury in all mice. An increase in astrocyte activation at seven days post-injury confirms the onset of a neuroinflammatory response following aldehyde production in the brain. The data suggest that advanced age and ALDH2 deficiency contribute to increased aldehydic load following mTBI. Overall, ProxyNA$_3$ was capable of mapping concussion-associated aldehydes, supporting its application as an objective diagnostic tool for concussion.

5.5. Introduction

More than 50 million people worldwide experience a Traumatic Brain Injury (TBI) each year, with mild TBI (mTBI) accounting for up to 90% of those cases [1]. The incidence of sports-related concussions has also been on the rise, with a more than 100% increase from 2001 to 2012 in North America [2]. It is important to note that mTBI statistics are prone to diagnostic and selection biases, as concussions are underreported, underdiagnosed, and misdiagnosed [1,3]. Objective, unambiguous diagnosis is crucial for safe return to activities to avoid further exacerbation of symptoms and development of neurological deficits later in life [4,5].

Currently, the detection of intracranial injuries relies on head Computed Tomography (CT), which may result in unnecessary ionizing radiation in young individuals with mTBI [6]. Studies show 85-99% of adults and 93-100% of children with mTBI have no intracerebral lesions, in which cases cranial CT scans could be avoided [7,8]. Unlike more severe TBIs, concussions often do not present visible physical trauma or external signs of injury with a delayed onset of symptoms that vary widely [9]. Currently, there is no single objective diagnostic tool for concussions, but instead diagnosis relies on a combination of medical history, physical examination, symptom evaluation, and, in some cases, neuroimaging to rule out more severe

traumatic brain injury [10]. A direct, imaging-based assessment of brain health after mTBI is an outstanding clinical need.

The pathophysiology of mTBIs derives from the neurometabolic cascade of concussion, propagating from irregular ionic flux due to lipid membrane mechanoporation, resulting in an energy crisis, altered intracellular redox state, and formation of reactive oxygen species [11]. The induced oxidative stress promotes polyamine catabolism and lipid peroxidation, resulting in the production of a diverse array of biogenic aldehydes detectable in rodents, human plasma, and human cerebral spinal fluid within 72 hours post-brain injury [12-17]. Scavenging aldehydes in the early hours following TBI can have neuroprotective effects [18], suggesting aldehydes are not only markers of injury, but also early propagators of pathogenesis.

While aldehydes play a significant role in the early stages of TBI neuropathy [19-21], it is not yet clear whether advanced age leads to worse clinical outcomes following head injury, as TBI studies often exclude older adults due to pre-existing neurological conditions [22]. Preclinical evidence exists supporting an increase in oxidative damage, lowered antioxidant capacities, and increased tissue loss in aged rats compared to young rats following moderate TBI [21]. The redox stress hypothesis of aging proposes a shift from predominately anti-oxidant to more pro-oxidant redox state as age progresses [23], increasing aldehyde production as secondary messengers of pathology, amplifying injury [24,25]. With the recent shift of increased incidence of TBI in the older population [26], there is an urgent need for more investigation into this under-researched topic [27]. The progressive decline of aldehyde metabolism with advancing age is, in part, due to a reduced activity of aldehyde dehydrogenases (ALDH), a family of enzymes responsible for the elimination of endogenous aldehydes [28]. Mitochondrial ALDH2 plays a major role in the detoxification of aldehydes derived from lipid peroxidation [29,30]. Given the redox hypothesis of aging, and evidence supporting aldehydes as propagators of injury, we hypothesize that older individuals will have a greater neural aldehyde load following mTBI, which may lead to more severe outcomes.

While the neurometabolic cascade of concussion has been shown to result in the elevated production of aldehydes that can serve as a potential mTBI biomarker, detecting and imaging aldehydic load in live

subjects remains a challenge, hindering their use as diagnostic tools. In this study, the generation of aldehydes following mechanical injury of neurons has been shown, and the diagnostic potential of aldehydic load as a biomarker for mTBI has been demonstrated. A novel chemical exchange saturation transfer (CEST) magnetic resonance imaging (MRI) contrast agent, 5-propargyloxy-*N*-aminoanthranilic acid ($ProxyNA_3$), has been developed to map aldehydic load in a mouse model of mTBI, affording the use of pathology-associated aldehydes as imaging biomarkers for concussion.

5.6. Results

5.6.1. Imaging aldehydes *in vitro* in a 3D corticomimetic scaffold after concussive impact

A three-dimensional collagen-based scaffold was prepared to mimic the biomechanical (i.e., stress/strain) properties of mouse cortical brain tissue. The corticomimetic scaffold consisted of two parts (Fig. 5.1A, top): a stiffer outer ring comprised of glutaraldehyde-crosslinked collagen necessary to mimic mouse cortical brain mechanics and provide overall structural support to the construct; and a gel-like inner plug comprised only of collagen, which optimally promoted the growth and survival of stem cell-derived mammalian cortical neurons (Fig. S1). In order to mimic mouse cortical brain tissue, the Young's Modulus of a fresh punch of mouse cortical tissue was determined using a universal testing machine (UTM) (Fig. 5.1B). We determined that a corticomimetic scaffold comprised of an outer ring of 8.1 mg/mL collagen + 0.75 wt% glutaraldehyde, and inner plug of 2 mg/mL collagen best mimics the biomechanical properties of mouse cortical brain (Fig. 5.1B). In maintaining the formulation of the inner plug at 2 mg/mL collagen with no cross-linker, the growth of primary neural stem cell-derived mouse cortical neurons (Fig. 5.1C and D) and induced pluripotent stem cell (iPSC)-derived human cortical neurons (Fig. S2) was promoted. Using NeuO as a fluorescent neuronal marker [31], confocal microscopy revealed both mouse (Fig. 5.1C) and human (Fig. S2) neurons had migrated throughout the scaffold, resulting in neurite outgrowth. The application of live/dead staining confirmed the cells were alive, with very minimal death seen after seven days post-seeding (Fig. 5.1D and Fig. S2).

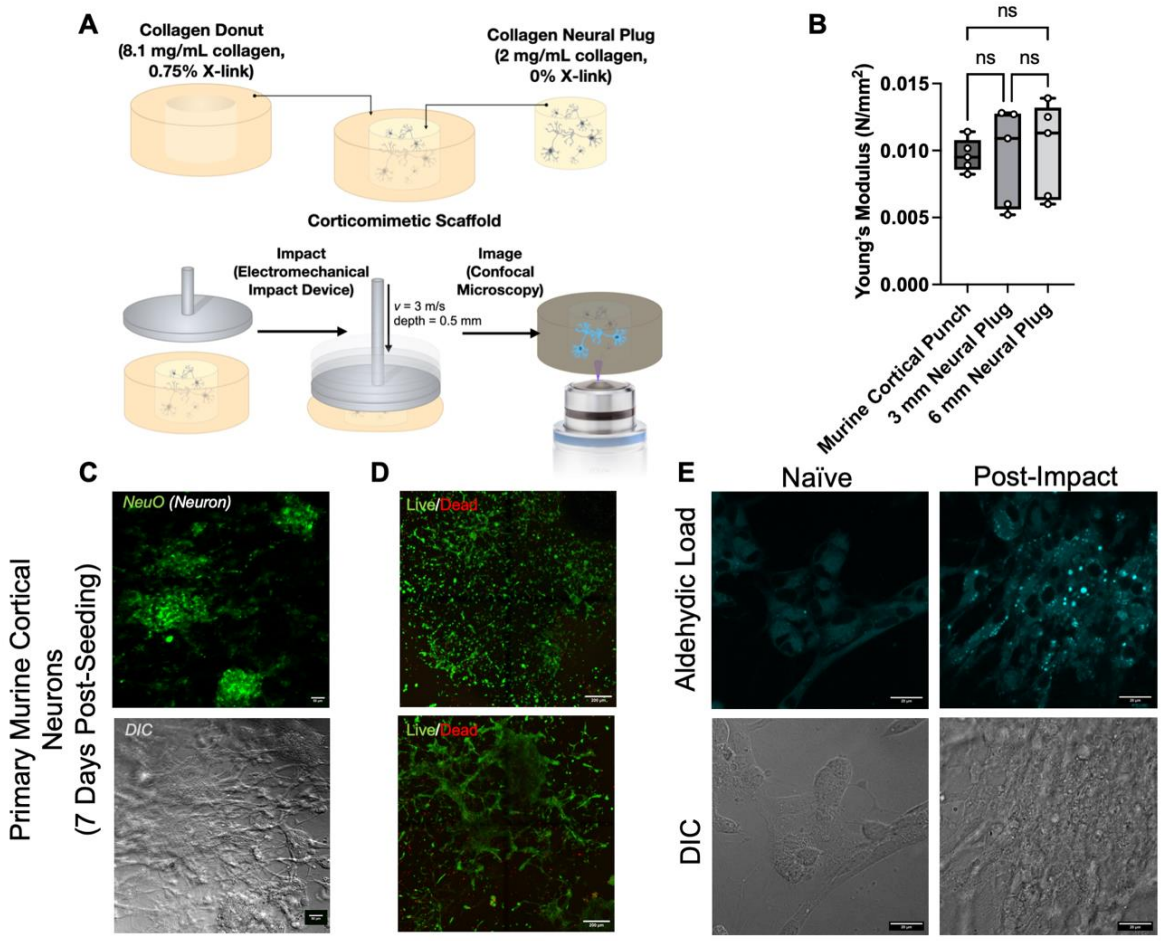

Fig. 5.1. Aldehydes are produced following concussion-like impact in primary neurons growing in a corticomimetic scaffold. (A) Formulation of corticomimetic scaffold with crosslinked collagen exterior, and collagen interior containing primary mouse neurons. The scaffold was impacted with a concussion-like force followed by confocal microscopy with an aldehyde-binding fluorophore 5MeONA$_3$ (**B**) Young's Modulus of the corticomimetic scaffold with two different sized interior plugs compared to a murine cortical punch. Data are shown in a box plot with individual values, n=5 per group, $p<0.05$. (**C**) Confocal microscope images showing NeuO fluorescent staining (top) of primary mouse cortical neurons seven days after seeding into corticomimetic scaffold to confirm differentiation of neurons. Differential interference contrast (DIC; bottom) shows elongation of cells within 3D scaffold. Scale bar = 50µM (**D**) Evaluation of cell death at three- and seven-days post-seeding of primary mouse cortical neurons into corticomimetic

scaffold. Scale bar = 200μM. (**E**) Representative confocal images of primary neurons pre- (left) and post- (right) concussion-like impact after incubation with $5MeONA_3$ for fluorescent staining of aldehydes (top) and DIC of cells showing morphological changes pre- and post-impact. Scale bar = 20μM.

With the ability to support primary neuron culture in a scaffold recapitulating mouse cortical brain rheological properties, the corticomimetic scaffold was then applied for biomarker testing post-concussion (Fig. 5.1A). A custom impactor tip affixed to an electromechanical impactor (Leica Inc.) produced a force to compress but not tear the scaffold, and to mimic a previously-reported concussion-like strain of 26% thickness [32]. A cell-penetrable, aldehyde-conditional fluorogenic probe ($5MeONA_3$) [33] afforded the mapping of total aldehydic load in the corticomimetic scaffolds by confocal microscopy before and 10 minutes post-impact (Fig. 5.1E). Every post-impact scaffold exhibited an increase in aldehyde signal over the baseline, pre-impact levels present as a result of normal metabolism. Interestingly, the aldehydes presented as round, punctate foci within the cytosol (Fig. 5.1E). In primary neurons cultured in a corticomimetic scaffold, total aldehydic load increases after a concussive-like impact, supporting the role for aldehydes as a biomarker for cell injury following mTBI.

5.6.2. Development of an awake closed head impact mouse model of mTBI

The use of an awake, closed head impact (ACHI) mouse model of concussion is important to provide behavioural and neuroimaging outcomes most relevant to human injury. Many rodent models of TBI have been developed [34,35], however surgical manipulation, head fixation, and the use of neuroprotective anesthesia make these models less translatable to humans. Linear and rotational acceleration of the head are a fundamental characteristic of mTBI [36], which is lost with fixed-head or surgical models. The use of anesthesia provides neuroprotection [37,38], which alters the biochemical and behavioural outcomes of the impact. Furthermore, an awake model provides the opportunity to perform behavioural testing immediately after injury, which is a crucial timepoint as many symptoms of concussion in humans are commonly identified immediately after impact [39-41]. By adapting two previously described procedures [42,43], a new ACHI

mouse model of mTBI is developed, eliminating limitations of surgical, fixed head, and anesthetized models.

Impact velocity is a crucial variable for a reproducible mTBI. Velocities of 2.35 to 6m/s have been previously described in the literature (Table S4.1). A suitable ACHI model would elicit some behavioural phenotype, but cause no blood-brain barrier (BBB) leakage, no skull fracture or intracranial hemorrhaging, and no severe reaction including seizure, paralysis, or death [44]. The ACHI model was initially developed on 8–10-week-old healthy, wild type (WT) Balb/c mice (Fig. S3A). A single impact with velocities of 2.35, 5.0, or 6.0 m/s were evaluated (n=5 mice/group). Mice receiving impacts at 6.0m/s showed paralysis of limbs, inability to regain righting reflex, and intermittent apnea. Post-mortem dissection revealed skull fracture and intracerebral hemorrhaging of the right cortex, indicating 6.0 m/s resulted in TBI, not mTBI. No such damage was observed during post-mortem gross evaluation of the brains of mice receiving 2.35 or 5.0 m/s impacts.

As behavioural deficits are a hallmark of rodent concussion [34], grid walk (Fig. S3B,C) and neurological severity score (NSS; Fig. S3D-H) tests were conducted before impact, immediately after regaining righting reflex following impact, and at 1-, 4-, and 24-hours post-injury (Fig. 5.2 A-C). NSS consists of a series of 5 objective pass or fail tests used to assess balance, cognition, reflexes, and exploratory behavior. A higher score indicates a greater deficit, with a score of 5 being the most severe. Sham mice (restrained with no impact) had a baseline average score of 0.2±0.4, which did not significantly change at any evaluation timepoint. The NSS of mice receiving an impact of 5m/s significantly increased to 3.8±0.4 ($p<0.05$) immediately after impact and returned to baseline for all subsequent time points (average 0.8 to 1.2; $p>0.05$) (Fig. 5.2A). There was no change in NSS for mice receiving 2.35 m/s impact. The grid walk test assesses acute deficits in motor coordination and overall activity level [45]. The percentage of foot faults compared to number of total forelimb steps and percent time active was counted from a 3-minute video (Movies S1,S2). For mice receiving a 5 m/s impact, forelimb foot-faults increased significantly over baseline (18.8±16.4%

vs. 6.0±0.19%, $p<0.05$) (Fig. 5.2B), and activity time decreased significantly (40.6±17.6% *vs.* 85.8±25.4%, $p<0.05$) immediately after impact (Fig. 5.2C).

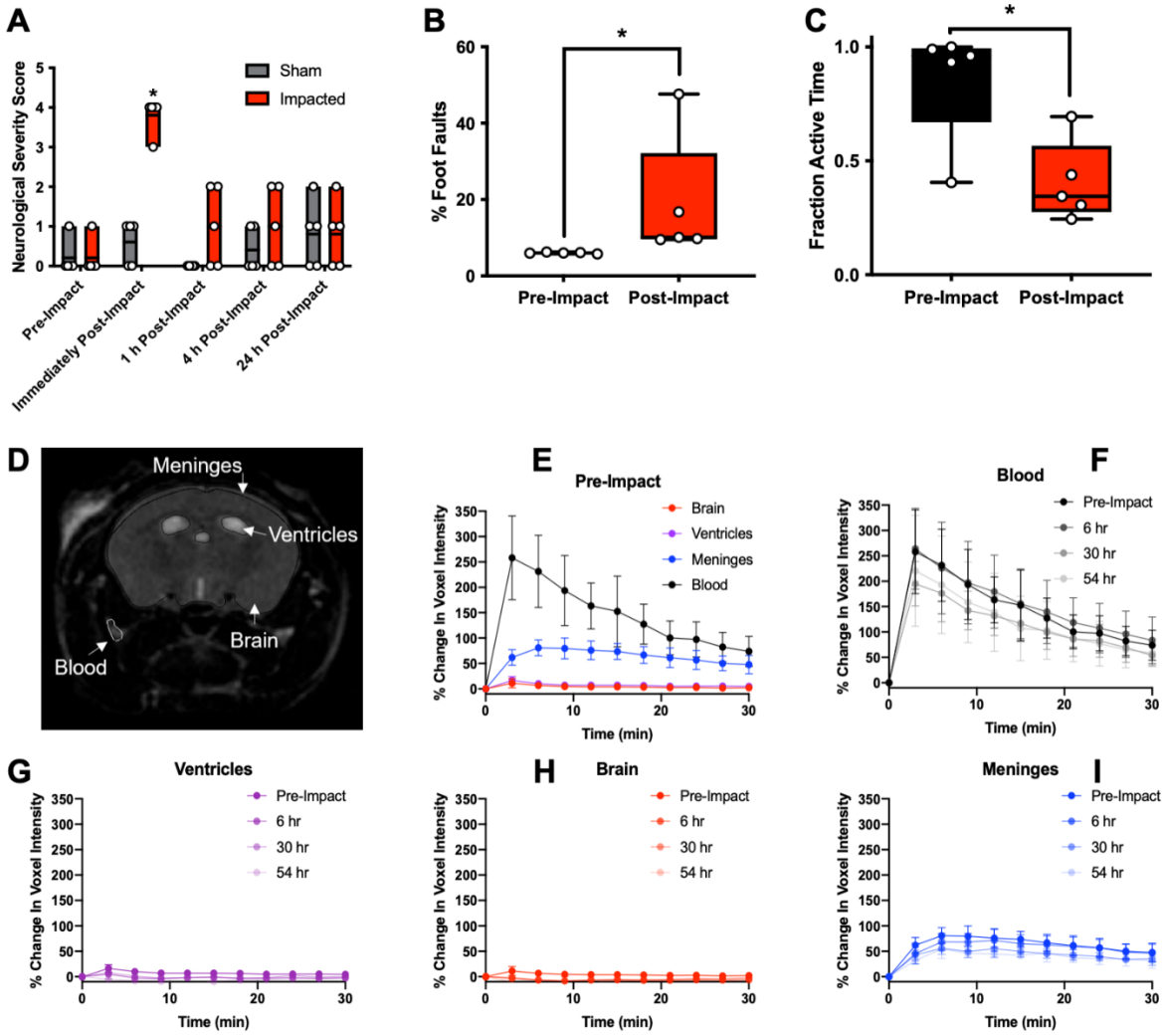

Fig 5.2. Mice exhibit changes in behaviour but not blood-brain barrier permeability after mTBI. (**A**) Mice underwent behavioural testing for neurological severity score (NSS) comprised of 5 pass-or-fail tests including beam walk, hindlimb reflex, startle reflex, escape paradigm, and balance test. A point was awarded for every test failed, with a score of 5 representing the more severe behavioural deficit. Individual data points (n=5 per group) and box plots are shown. Sham mice were restrained, but not impacted. * $p<0.05$. (**B-C**) Results from 3-minute grid walk test for pre- and post-impact mice (n=5 per group). (B) Percentage of foot faults of total forelimb steps before and after ACHI. (C) Time active including walking, grooming, and exploratory behaviour during the three-minute grid walk challenge is

shown. Statistical analysis was performed using a One-Tailed Wilcoxon Test, * denotes $p< 0.05$. (**D**) Regions of interest (brain, ventricles, meninges, and blood) were drawn to evaluate contrast enhancement following intravenous gadolinium-based contrast agent pre- and post- impact. (**E-I**) Dynamic contrast enhanced MRI was performed pre-and post-impact at various timepoints. Percent change in voxel intensity after gadobutrol injection in each of the ROIs from images acquired (E) five days pre-impact and (F-I) at timepoints of 6 hours-, 30 hours-, and 54 hours post-impact. Data are shown as means +/- standard deviation. Each data point represents the analysis of ROIs on 6 slices per brain MRI. $P>0.05$ using GLM repeated measures, n=5 mice.

Following the observation of behavioural sequelae to ACHI at 5.0 m/s, BBB integrity was assessed with DCE-MRI [46,47]. Four regions of interest were analyzed for contrast enhancement pre- and post-impact: ventricles, middle cerebral artery as a proxy for blood, the meninges, and the remaining brain structures (Fig. 5.2D) [48]. Pre-impact, blood contrast increased (246%) (Fig. 5.2E), with no significant change in contrast enhancement in the brain tissue or ventricles ($p>0.05$). There was a significant increase in contrast in the meninges by 6 minutes after gadobutrol injection, however the lack of extravasation, retention in the subarachnoid space and steady clearance over time signifies an intact BBB [47]. Post-ACHI, there were no significant changes in contrast enhancement in blood (Fig. 5.2F), ventricles (Fig. 5.2G), brain (Fig. 5.2H), and meninges (Fig. 5.2I) relative to pre-impact, suggesting ACHI does not cause disruption of BBB integrity, supporting the mild severity of our model recapitulating concussion. Overall, we have shown that a single-impact ACHI mouse model with impact velocity of 5.0m/s, depth of impact of 7mm, and dwell time of 0.3s results in transient behavioural deficits without overt signs of skull damage, without intracranial hemorrhage, and without compromising BBB integrity.

5.6.3. CEST-MRI mapping of total aldehydic load *in vivo* following mTBI

We have previously reported *N*-aminoanthranilic acids as aldehyde-conditional CEST-MRI contrast agents, where MRI contrast is produced only upon reaction of the probe with aldehydes to form a hydrazone (Fig. 5.3A) [49]. The reactive *ortho* acid hydrazine moiety has been shown to effectively bind aldehydes *in vivo* [50,51], and here we introduce ProxyNA$_3$ to map aldehydic load after mTBI. Two hypotheses were evaluated in the current study: (1) brain aldehydic load increases in aged relative to younger mice following concussion; (2) ALDH2 is involved in concussion-related pathogenic aldehyde metabolism. In order to evaluate these hypotheses, WT C57Bl/6, and previously reported C57Bl/6 mice harboring heterozygous or homozygous knockouts of ALDH2 were employed [52]. ALDH2 is normally expressed in the liver but not the brain [53] (Fig. 5.3B). Within these three groups, mice were evaluated when either young (<20 weeks) or of advanced age (>65 weeks). Four male mice were induced to ACHI from each cohort (total of n=24 mice) and underwent behavioural testing at two timepoints (pre- and post-impact), and *in vivo* MRI at three timepoints (pre-injury, two days-, and seven days-post injury) (Fig. 5.3C). An additional 6 mice from each group were used for histological evaluation at each of pre-injury, two days-, and seven days-post injury (n=36) (Fig. 5.3C).

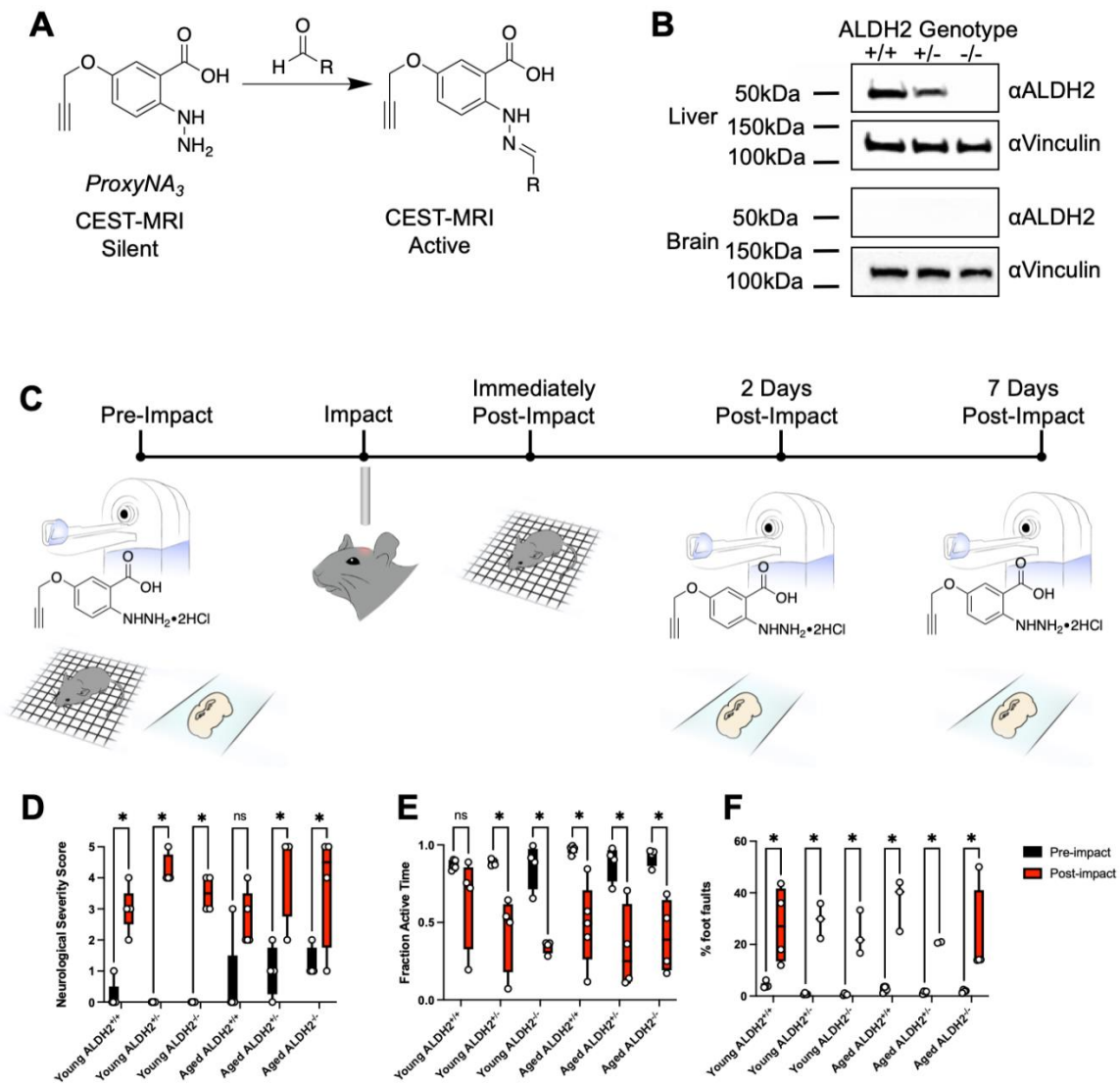

Fig 5.3. Experimental procedure for evaluation of mTBI in ALDH2-/- mouse model using behavioural tests, histology, and ProxyNA3 CEST-MRI. (**A**) Chemical structure of ProxyNA$_3$ in its unbound, silent state (left), and its CEST-MRI active state, upon reaction with aldehyde (right). (**B**) Western blots showing protein levels of ALDH2 in the liver (top) and brain (bottom) tissues from transgenic mice with ALDH2 $^{+/+}$, $^{+/-}$, and $^{-/-}$ genotypes. Vinculin was used as a loading control protein. (**C**) Experimental design for all testing done pre- and post-impact for *in vivo* mouse model of mTBI. CEST-

MRI with ProxyNA$_3$ was performed pre- and at two- and seven days post-impact. Behavioural tests, denoted by grid-walk symbol, was performed pre- and immediately post-impact. A separate cohort of mice were used for immunohistological examination at the same timepoints as MRI. (**D**) Results of neurological severity score (NSS) comprised of 5 pass-or-fail tests pre-impact (black) and post-impact (red). A point was awarded for every test failed, with a score of 5 representing the most severe behavioural deficit. (**E-F**) Immediately after NSS test, mice were placed on a raised grid with video recording for 3 minutes. A researcher blindly scored (E) the fraction of time spent active and (F) the total number of foot faults divided by total number of forelimb steps. Groups of mice were chosen by age (young <16 weeks; aged >65 weeks) and by genotype. Individual data points (n=4 per group) and box plots are shown. * $p<0.05$, 2-way ANOVA followed by Tukey-corrected multiple comparisons test.

All mice had an increased NSS immediately after impact compared to baseline (Fig. 5.3D). The increase was statistically significant in all cohorts except for the aged WT mice ($p=0.063$). All mice had a decreased fraction of time spent active during the grid walk (Fig. 5.3E), with only the young WT cohort failing to reach statistical significance($p=0.749$). Every group had a significant increase in number of foot faults on the grid walk following injury compared to baseline (Fig. 5.3F). The results of the behavioural testing confirmed transient sensorimotor deficits indicative of mTBI across all groups of mice tested.

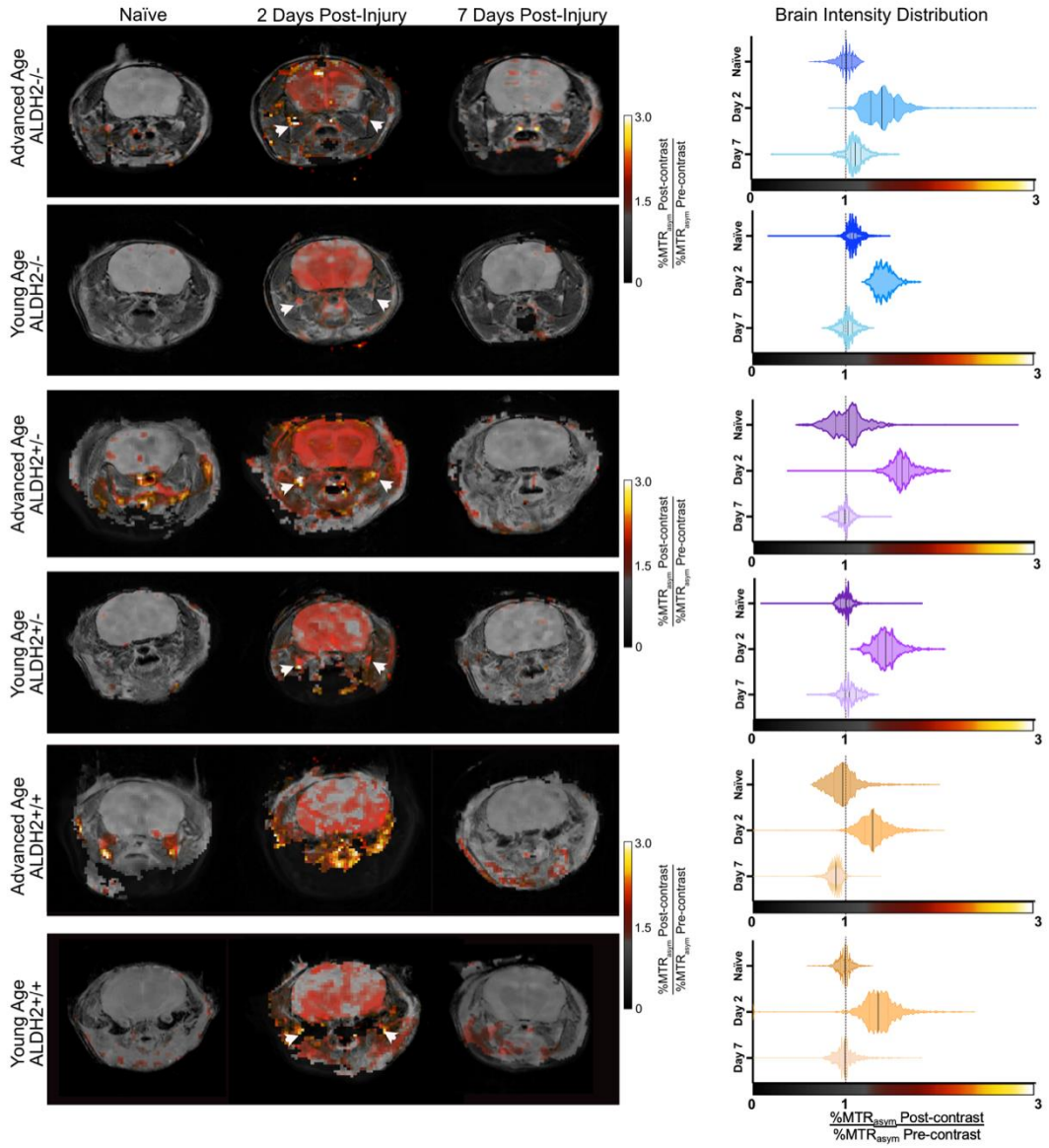

Fig 5.4. Mapping of brain aldehydes by ProxyNA$_3$ in a mouse model of mTBI. CEST-MRI (average %MTR$_{asym}$ normalized to pre-contrast signal) after ProxyNA$_3$ injection mapped onto axial T$_2$-weighted image of mice of identified age group and ALDH2 deficiency (left). A representative image of a mouse from each cohort is shown longitudinally across timepoints (pre-impact, two days post-impact, and 7 days post-impact). Arrowheads indicate vascular signal derived from ProxyNA$_3$-aldehyde adducts. Violin plots showing voxel-wise intensity distribution for the corresponding mouse at each timepoint. Solid line= median, dashed lines = 25th and 75th %ile.

CEST-MRI was performed before and after injection of ProxyNA$_3$ to map total aldehydic load in a single axial slice of the brain. While brain aldehyde levels were low before impact (naïve), normalized %MTR$_{asym}$ increased significantly over the whole brain slice and vasculature in all mice at two-days post-impact (Figs. 5.4, S4). However, by day seven post-impact, aldehyde signal decreased to baseline levels, suggesting that aldehydes are transiently present in the brain following mTBI in mice. Young WT mice have less aldehyde signal compared to all other groups (Fig. 5.5A). Aged WT mice have less aldehydes compared to all other aged mice, with both cohorts of aged ALDH2 deficient mice having the greatest aldehyde signal two days post-injury. When grouped by age-only, young mice have significantly less aldehyde-derived imaging signal compared to aged mice two days post-injury (Fig. 5.5B). ALDH2 deficient mice (both ALDH2 $^{+/-}$ and $^{-/-}$) had significantly more aldehyde signal compared to WT mice (Fig. 5.5C). These data suggest that more toxic endogenous aldehydes are produced following mTBI in aged individuals, and those with ALDH2 deficiency.

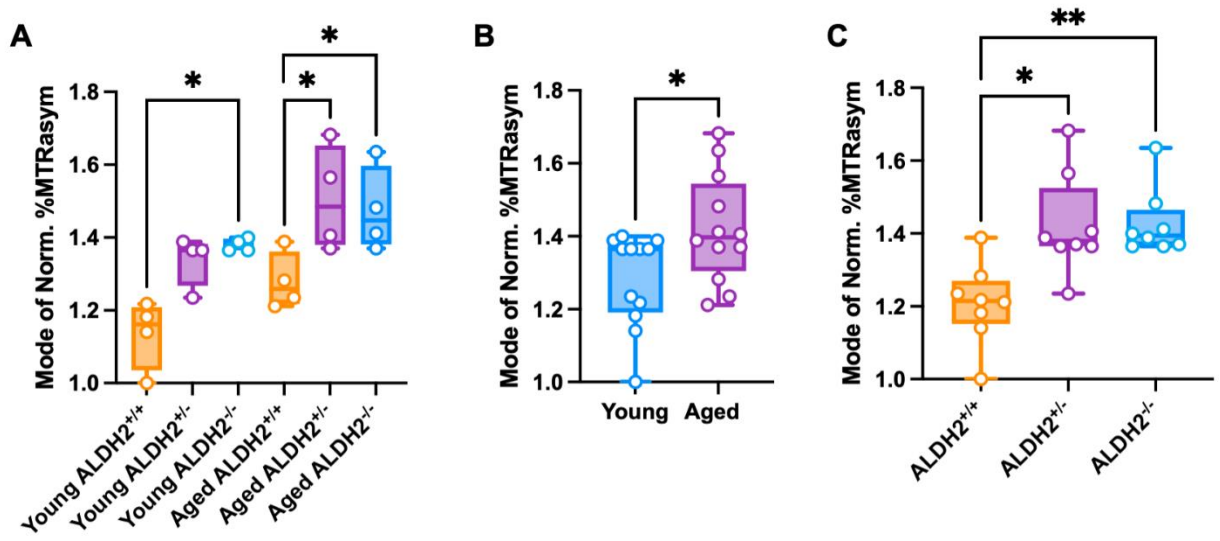

Fig 5.5. Aldehyde production post-concussion is affected by age and ALDH2 genotype. Box plots of voxel-wise intensity distribution of aldehyde signal following ProxyNA$_3$ CEST-MRI at day two post-mTBI. Mice are grouped by age and genotype. Data are presented as modes of normalized %MTR$_{asym}$. (**A**) Comparison of aldehyde signal two days post-impact between all groups of mice, n=4 per group. (**B**) Comparison of young (<16 weeks) and aged (>65 weeks) mice, n=12 per group. (**C**) Comparison of aldehyde signal between groups of either wild type (ALDH2$^{+/+}$) or transgenic mice with lower ALDH2 expression (ALDH2$^{+/-}$), or complete knockouts (ALDH2$^{-/-}$). *<0.05, (A, C) Brown-Forsythe ANOVA and Dunnett's T3 multiple comparison, (B) two-tailed Mann-Witney U-test.

5.6.4. Aldehydes precede astrogliosis in the pathogenesis of mTBI

Astrocyte activation, an active proponent in the propagation and regulation of neuroinflammation [54], was quantified by immunohistological staining for glial fibrillary acidic protein (GFAP) in brains of mice pre- and at two timepoints post-injury (Fig. 5.3C). Hippocampal astrogliosis appeared seven days post-injury for both young mice (Fig. 5.6A) and those of advanced age (Fig. 5.6B) independent of ALDH2 genotype. A region of hippocampus from each image was quantified by measuring GFAP density, the mean integrated density of GFAP signal divided by the mean integrated density of DAPI signal, which estimates the astrocyte activation normalized to number of cells (Fig. 5.6C). There was no significant difference in GFAP

density by age and by genotype. The only variable influencing the measure being time relative to ACHI, with GFAP density increasing from 1.9±0.26 to 2.7 ± 0.78 ($p<0.05$) at 7-days post-impact. These results suggest an activation of a hippocampal inflammatory response seven days after injury, proceeding the elevation of aldehydic load (Fig. 5.6D).

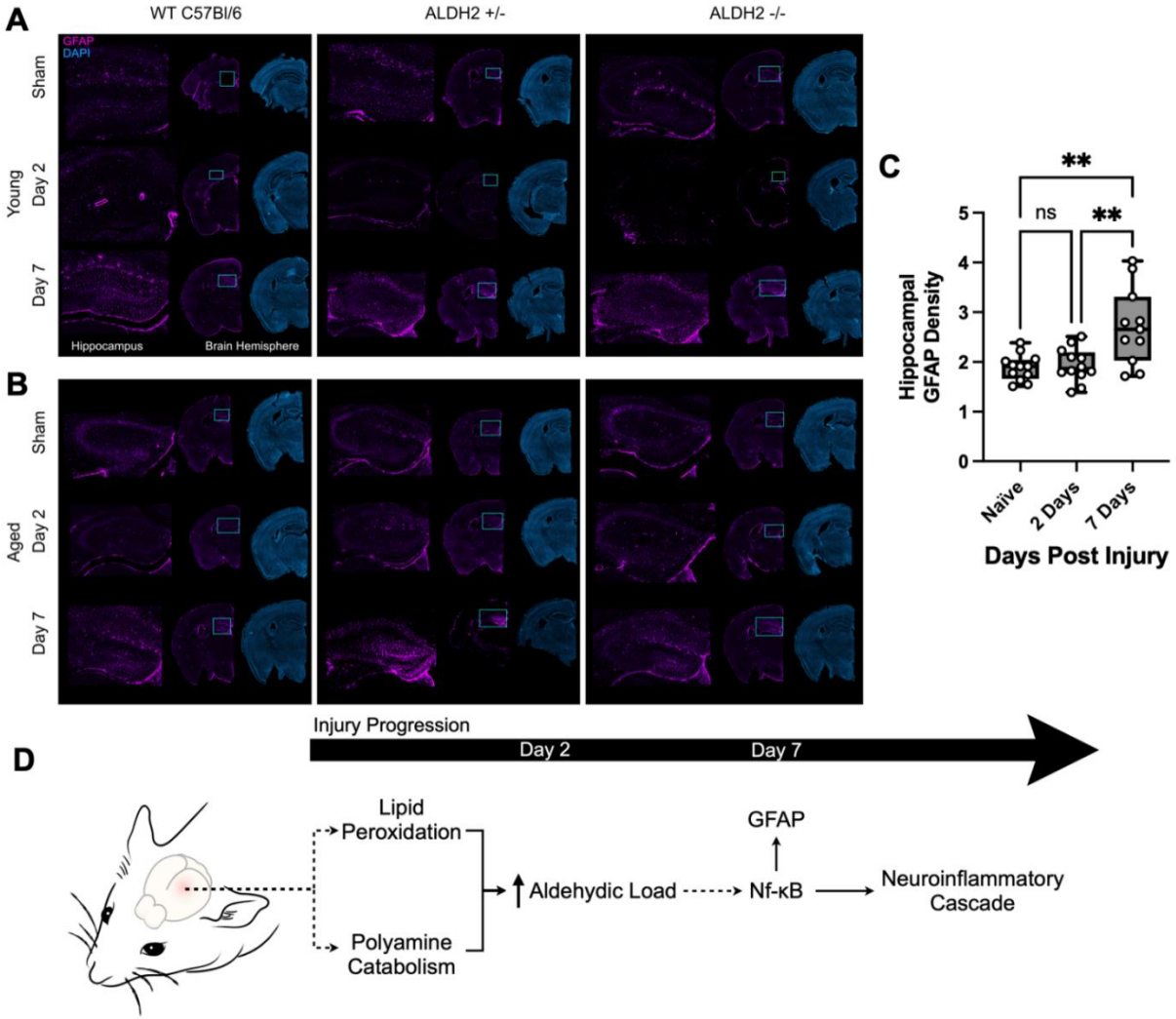

Fig 5.6. Astroglial activation increases 7 days post-impact, following increase in aldehydic load during the neuroinflammatory cascade driving mTBI. The brains of mice were excised at day two- and day seven- post-impact, or without impact (sham). Brain sections were fluorescently probed with anti-GFAP antibody to visualize astrocyte activation and DAPI. A representative image is shown for a mouse in each cohort based on genotype, age, and timepoint. (**A**) Young mice (<16 weeks) and (**B**) old mice (>65 weeks) all show an increase in GFAP signal in the hippocampus at seven days post-injury, but not at two days post-injury compared to sham mice. (**C**) Quantification of GFAP density in a region of the hippocampus from each mouse with no impact, or two- and seven-days post-impact (n=12 per group; **p<0.01, ns, non-significant, one-way ANOVA with *post-hoc* Tukey's test. (**D**) Proposed causative role

of aldehydes, produced from oxidative events, in the pathogenesis of mTBI: initial creation of aldehyde-rich tissue, followed by astrogliosis (Nf-κB-driven GFAP expression), and progression of the neuroinflammatory cascade.

5.7. Discussion

Our corticomimetic scaffold was designed to mimic the mechanical properties of cortical brain tissue upon compression (Fig. 5.1B), and support the growth of primary neurons using existing mammalian cell culture infrastructure and commercially-sourced collagen. The collagen-based 3D scaffold offers some practical advantages over bioprinted or silk-based scaffolds [55-57] by reducing infrastructure-need, process complexity, and time-to-finished product [56,58-60]. This higher-throughput, cost-effective method may improve *in vitro* testing of CNS-injury models, and, through co-culture of neurons with astrocytes and microglia, provide a more complete examination of the neurometabolic cascade following injury. In the current study, this scaffold allowed for imaging of aldehydic load in primary mouse cortical neurons before and after concussion-like impact. Naïve, unimpacted cells have some background level of aldehydes due to normal metabolic processes, consistent with our previous findings [33]. Following impact, the cells have a marked increase in aldehyde-rich foci within the cytoplasm of cells (Fig. 5.1E), likely due to both lipid peroxidation and polyamine catabolism [16,17,33]. Future work will aim to determine the nature of these aldehyde-dense foci.

In recent years, one focus of TBI diagnostic research has been the discovery of blood-based biomarkers, including several astroglial and neuronal biomarkers S100B, GFAP and UCH-L1 [61]. Such blood tests provide no spatial dimension to the diagnosis (i.e., implicated brain regions) and only indicate that an injury has occurred. Molecular imaging of aldehydes fills this gap, providing information about severity, and location of injury, which will not only diagnose with high sensitivity, but will aid in the prognosis and personalized treatment planning following mTBI. The ALERT-TBI study identified a prespecified cut-off value for serum GFAP and UCH-L1 to predict intracranial injury on head CT [62], which contributed to the FDA approval of the first blood test for avoidance of unnecessary CT in adults following head trauma in

2018. Studies on serum and plasma GFAP to discriminate mTBI with and without CT abnormalities are emerging [63-65], with GFAP continuing to outperform other biomarkers [66,67]. Although blood GFAP level shows promise, there are some limitations regarding its utility for concussion diagnosis. GFAP levels in the blood may be sensitive to intracranial pathologies that are not seen on CT, and there is continuing debate on how the mechanisms by which GFAP and its breakdown products exit the cell and enter the bloodstream. Importantly, GFAP expression increases with age in the healthy population [68], reducing the specificity of a blood-based test in older individuals [69,70]. In general, fluid biomarkers have limitations, including short half-life in biofluid, sources for generation outside of the CNS, delayed appearance in the circulation, and dependence on age, sex, and co-morbidities [71,72].

ALDH2 deficiency affects 560 million people worldwide, making it one of the most prevalent hereditary disorders [73]. The results from this study indicate a potential increased risk for more severe outcomes for the population with ALDH2 deficiencies and those of advanced age. Mice with ALDH2 deficiency had a larger increase in aldehydes two days post-mTBI compared to WT mice (Fig. 5.5. A, C). Furthermore, aged mice had more brain aldehydes post-injury compared to young mice (Fig. 5.5 B). Previous studies have shown that aged mice have decreased ALDH2 activity and increased HNE (4-hydroxynonenal) protein adducts compared to young mice [74], which exacerbates the increase in mitochondrial ROS production and accumulation of aldehydes that comes with age [75]. Together, these findings support our imaging results to suggest that the ability to clear these aldehydes is decreased with reduction in ALDH2 activity due to a genetic mutation (ALDH2 deficiency) and/or advanced age. If aldehydes are propagators of disease, the inability to quickly clear aldehydes produced in the brain following mTBI may exacerbate post-impact pathophysiology and/or delay recovery. Now that aldehydes have been determined to be an early biomarker for mTBI, further testing should be done to elucidate the pathogenic role of aldehydes in the neurometabolic cascade and if there is an increased risk of more severe symptoms, including PCS, following mTBI in the aged and ALDH2-deficient populations.

It is known that oxidative stress leads to profound activation of NF-κB, a family of transcription factors that play important roles in stress responses, inflammation, and apoptosis [76,77]. Various oxidants, cytokines, chemokines, and growth factors induce molecular signals that lead to activation of NF-κB [78], a central step in pro-inflammatory reactive astrocytosis [79-81], reactive gliosis, and cellular atrophy [82,83]. Several studies have shown a link between NF-κB and GFAP upregulation following TBI in cells and *in vivo*, with NF-κB-induced astrocyte activation driving edema [84]. Interestingly, inhibition of ALDH2 activity results in enhanced nuclear translocation, and therefore activation, of NF-κB [85]. Inhibition of NF-κB has also been shown to reduce astrogliosis in mice [86]. While it is not clear exactly how oxidative stress activates various protein kinases upstream to NF-κB, evidence implicates stress-derived aldehydes in the activation of the signaling cascade that eventually activates NF-κB [87-89]. We propose that the link between initial mTBI-induced injury and NF-κB signaling is mediated by aldehydes as secondary messengers. Lipid peroxidation-derived aldehydes are known to act as toxic secondary messengers to propagate redox signals leading to cellular and tissue injury [90-92]. Our data directly support the hypothesis (Fig. 5.4 and 5.6) that mTBI-induced aldehyde production precedes GFAP overexpression, the result of NF-κB activation, which contributes to reactive gliosis and inflammation in the brain to propagate trauma-induced injury.

A limitation of the current study is that the earliest timepoint for *in vivo* aldehyde mapping was two days post-injury. CEST-MRI will be repeated at shorter post-injury intervals to assess how early acute aldehyde production occurs. Our study did not explore sex differences in aged and ALDH2$^{-/-}$ mice. Some literature suggests ALDH2 polymorphisms may affect women more than men [93], although the effect of sex is likely different in mice compared to humans [75]. Moreover, the CEST-MRI technique used for *in vivo* imaging was limited to a single slice, preventing whole-brain analysis. Efforts are ongoing to translate the ProxyNA$_3$ probe chemistry described here to a radiotracer for positron emission tomography (PET). Not only would a radiotracer similar to ProxyNA$_3$ described herein allow for quantitative whole-body mapping of aldehydic load following mTBI, but its successful implementation could be more rapidly translated to human use [94-96].

The current study represents the first steppingstone in the application of aldehydic load as a biomarker for the objective diagnostic imaging of mTBI. Here, we propose a novel 3D *in vitro* model of concussion, which supported the use of aldehydes as a biomarker for mTBI. A new mouse model of ACHI was developed resulting in behavioural and histological sequalae recapitulating mTBI. Using this model, ProxyNA$_3$ CEST-MRI was used to map the increase in aldehydic load in the brain following concussion. Future iterations of this imaging tool may be used in a clinical setting not only telling that mTBI occurred, but also mapping the severity and location of damage, and leading to improved treatment outcomes *via* personalized concussion medicine.

5.8. Materials and Methods

5.8.1. Animals

All procedures for animal experimentation were conducted under Animal Use Protocol SCe-4019 approved by the IACUC at the University of Ottawa. Mice were housed under 12 hr light/dark cycle, and ambient temperature of 20-24°C and 45 to 65% humidity. All mice were provided access to food (Rodent Laboratory Chow) and water *ad libitum*. The ALDH2 knockout mice have a C57BL/6 background and were generated as previously described [52], and kindly provided by Dr. Brian Bennett (Queen's University, Kingston, Canada). Heterozygous and knockout mice were generated by breeding heterozygotes, genotyping offspring with extracted DNA from ear punches or tail snips by PCR [97]. Wild type mice were obtained from Charles River Laboratories (MA, USA).

5.8.2. Statistical Analysis

Statistical analyses were performed using Prism (v. 9.5.0, GraphPad, Inc.). Two-group comparisons were performed by two-tail Student's t-test. Comparisons across more than two groups was performed by one-way ANOVA followed by Tukey's test for honestly significant differences. Normality was assumed where appropriate for all data sets. Prior to ANOVA, Levene's test was used to confirm equal variance, and visual quantile-quantile plot analysis was used to confirm homoscedasticity.

5.8.3. Corticomimetic Scaffold

5.8.3.1. Donut Scaffold Exterior Preparation

All steps were performed in a biological safety cabinet. Stock glutaraldehyde solution is diluted to 0.75% in a final volume of 30μL using PBS (Gibco). Stock 1M NaOH solution was used to neutralize collagen solution. Fibricol Type I collagen (Advanced Biomatrix) was added to a glass vial containing a magnetic stir bar and then supplemented with 10X DMEM and glutaraldehyde on ice. Collagen hydrogel was neutralized to a pH of 7.6 using 1.0M NaOH and left on ice in the dark for 15 minutes before dispensing the gel in 500 μL aliquots into 20 mm diameter coverwell imaging chambers (Electron Microscopy Sciences). Dispensed gels were incubated at 37ºC overnight in a HERAcell 150 incubator (Thermo Fisher) in the coverslips to solidify. Solidified scaffolds were removed from the coverslips, placed in a 6 well tissue culture plate (VWR) and covered in 20% glycine for 1 hour at 37ºC, 5.0% CO_2 to quench unreacted glutaraldehyde. Collagen gel exteriors were then washed with three volumes of 3mL PBS (Gibco), before being placed back in their original coverslips. Using a 3.0 mm diameter disposable biopsy punch (Miltex), the centers of each cross-linked collagen gel was removed. Punched collagen hydrogels were then covered in neurobasal media and incubated at 37ºC while the second collagen matrix was being prepared.

5.8.3.2. Primary cell culture

Primary cortical precursors were obtained from E11-12 cortices dissected from CD-1 mice (Charles River Laboratories) as previously described[98]. Briefly, embryos were transferred to ice-cold Hanks' balanced salt solution (HBSS) (Fisher Scientific), meninges were removed, and cerebral cortices were isolated from the brain. The cortical tissue was mechanically triturated with a plastic pipette and seeded directly into a 24-well plate (Thermo Fisher Scientific), pre-coated with 15% poly-L-ornithine (PLO) (Sigma-Aldrich) and 5% laminin (Thermo Fisher Scientific). The cortical precursors were cultured following a neurosphere assay protocol[99] in a neurobasal medium (Thermo Fisher Scientific) containing 500μM GlutaMAX supplement (Thermo Fisher Scientific), 2% B27 supplement (Thermo Fisher Scientific), 1% penicillin/streptomycin (Thermo Fisher Scientific), 40ng/mL endothelial growth factor (EGF; Thermo

Fisher Scientific), and 40 ng/ml FGF2 (PeproTech). The seeded 24 well plate was incubated at 37ºC, 5.0% CO_2 for six days, with Neurobasal media changed daily. When the cells formed neurospheres (approximately six days after seeding), they were trypsinized, pelleted by centrifugation (110 x g for 15 min) at room temperature and resuspended in the appropriate volume of neurobasal medium to give a concentration of 1.28×10^6 cells/mL. Cortical precursor resuspension was kept on ice until needed.

5.8.3.3. Donut scaffold interior preparation

A second collagen matrix was prepared by diluting Fibricol Type I collagen (Advanced Biomatrix) in the appropriate volume of 0.01M HCl to give a collagen concentration of 2.0 mg/mL. Collagen solution was mixed using a magnetic stir bar and was supplemented with 10X DMEM and neutralized to a pH of 7.2-7.6 using 1.0 M NaOH. After neutralization, cortical precursor cell suspension was added to give a final cell concentration of 1,000,000 cells. Sterile water was added to the collagen solution to give a final volume of 625 µL and the solution was mixed gently with a magnetic stir bar. Cortical precursor-seeded collagen was left on ice in the dark for 15 minutes before aliquoting in 30 µL volumes to fill the centers of the donut exteriors. Donut scaffolds were incubated for 1.5 hours at 37ºC, 5.0% CO_2 before being removed from their coverslips, placed in a 6 well tissue culture plate (VWR) and covered in Neurobasal Medium (Gibco) supplemented with 2% B27, 1% Penicillin/Streptomycin (Gibco), GlutaMAX (Gibco), 40ng/mL FGF2 (PeproTech) and 40ng/mL EGF (Thermo-Fisher) and incubated at 37ºC, 5.0% CO_2 for four days before imaging or performing any further experiments.

5.8.3.4. Mechanical testing with UTM

Scaffolds or 6 mm punches of dissected fresh mouse cortical brain tissue were placed on a Fisherbrand double frosted microscope slide (Fisher Scientific) in the center of an adhesive, water-tight silicone gasket (Electron Microscopy Sciences). PBS was added to surround, but not submerge the scaffolds/brain tissue. The soaked material was then compressed 50% of its thickness five times using a UTM. The UTM recorded the thickness and standard force of the tested material. All material was tested in quintuplicate.

UTM settings:

Speed at starting position is 100mm/min, with a pre-load force of 0.002N, and pre-load speed of 50mm/min. A cyclic loading measurement phase with 5 cycles was applied with a strain of 50% at a speed of 3%/s, and a hold time of 1s at the point of load application and load removal of the cycles. The upper force limit was set to 20N.

5.8.3.5. Compression testing data analysis

The Young's Modulus value was used to evaluate the stiffness of the scaffolds and cortical brain tissue. Young's Modulus was determined by taking the slope of the linear portion of a stress vs strain graph of the first compression of the material. Strain was measured as a percentage of the gel's thickness and stress was calculated as the applied force per unit of material area. Young's Modulus data across varying materials was compared using a Kruskal- Wallis non-parametric test to determine significance between the multiple experimental groups. When a Kruskal-Wallis test identified significance between experimental groups, a Benjamini-Hochberg test was performed to give adjusted p-values of each experimental group. Using the adjusted p-values of the Benjamini-Hochberg test, a Dunn's post-hoc test was used to find significance between experimental groups. All statistical analysis was performed on R.

5.8.3.6. Compression and confocal imaging

Live/dead staining: Mouse primary neuron cells isolated and seeded into scaffolds as previously described were washed with PBS and then incubated with 1 mL of PBS containing calcein-acetoxymethyl ester (calcein-AM, 2 μM) and ethidium homodimer-1 (EthD-1, 4 μM) for 30 min under cell culture conditions. The scaffolds were washed gently three times with PBS and mounted onto a polymer-bottom 24 well plate (Ibidi). Scaffolds were imaged using a Zeiss LSM 880 confocal microscope with excitation/emission (ex./em.) and multi-bandpass filters (MPB) for calcein-AM set to 495/515 nm MBP 488nm and EthD-1 set to 495/635 nm MBP 458/561nm, respectively. Tile-scanned (3x3) Z-stacked images were acquired on 20x objective within the depth range of coherent light. Live cells fluoresced green (calcein-AM) and dead cells fluoresced red (EthD-1). Images were presented as maximum intensity projections (MIPs) of the Z-stacks.

NeuO: Cells are incubated with 0.25μM NeuO in cell culture medium at 37°C for 1 hour. The imaging medium was then replaced with fresh culture medium and incubated at 37°C for 2 hours before imaging. Confocal imaging was performed using a 20X objective with ex/em set to 488/557nm with multi-bandpass filter (MBP) of 488nm.

5MeONA$_3$: Images of live cells within the scaffold were taken after incubation 5MeONA$_3$ for aldehyde detection, before and after impact. The cell-seeded scaffold was placed in a well of a 12 well polymer-bottom plate and submerged in phenol-free media. Images were taken at 10X, 20X, or 64X objective at multiple depths of focus, with ex/em set to 405/420-520nm and MBP 405nm. After pre-impact imaging, the scaffold was removed from the well containing media and placed on a microscope slide and positioned under a custom-made 30mm tip for the impactor device. The depth was set to 0.5mm, velocity 4m/s and dwell time 0.3s. After impact, the gel was placed back into the well containing phenol red-free media to proceed with post-impact imaging.

5.8.4. mTBI mouse model

Model development including optimization of impact parameters, behavioral tests, and DCE-MRI was performed on WT Balb/c mice.

4.8.4.1 Awake closed head impact:

Unanesthetized mice were placed head-first into a conical restraint bag and held in a prone position by the base of the tail and hindlimbs (Fig. S3A). The head of the mouse was positioned under the tip (5mm diameter) of the impactor (Leica Impact One Electromagnetic Impactor). The mouse was held over a sheet of filter floss to allow free linear and rotational movement of the head and neck. The velocity, depth, and dwell time were set (see Table S1) and the impact was performed, with the tip making contact around the site of bregma. Immediately after impact, the mice were given a subcutaneous bolus of buprenorphrine (0.01mg/kg) and placed in the supine position until righting reflex was regained. Sham mice were placed

in restraint bag and held under impactor for 30 seconds, then removed from the bag to simulate the stress associated with handling.

Neurological Severity Score (NSS): The neurological severity score (NSS) is made up of a variety of tasks used to assess a rodent's balance, normal behavior, cognition, and reflexes (Supporting Fig. S3B-H). The procedure was adapted from previous studies [100-103]. Tasks were judged in a pass/fail format with zero points being awarded for completing the task and one point being awarded for failing to complete the task. As such, higher NSS is used to indicate greater deficits in the abilities mentioned above, with a maximum composite score of 5. For model development, mice performed the NSS immediately after impact, and at 1-, 4- and 24-hours post-impact. Note for the cohort of mice impacted at 2.35 m/s, the NSS was not performed immediately after impact. Each of the tasks incorporated in the NSS are outlined below in the order in which they were performed:

1. Hindlimb Reflex. A mouse was raised approximately 60 cm in the air by the tail (Supporting Fig. S3D). A point was awarded if the mouse failed to extend both forelimbs and hindlimbs, and instead crossed its limbs.

2. Startle Reflex. A mouse was placed on the flat surface of the lab bench and one researcher clapped over top of the mouse, while the other researcher observed for the presence of a normal startle reflex (Supporting Fig. S3E). A point was awarded if the mouse failed to display a proper startle reflex.

3. Escape Paradigm. A mouse was placed in the center of a cylinder with a diameter of 30 cm, a height of 20 cm and a small door (5 cm^2) to allow the mouse to escape (Supporting Fig. S3F). A point was awarded if the mouse failed to successfully exit the door during a 3-minute period.

4. Balance Test. A mouse was placed in the center of a meter stick positioned on its side (width of 0.6 cm) that was being held by a researcher in between an empty cage and the rodent's home cage (Fig. S3G). A point was awarded if the mouse failed to balance on the meter stick in a perched position for a period of 10 seconds.

5. Beam Walk Test. Using the same meter stick from task 4., the mouse was again placed in the center of the stick that was supported by an empty cage and the rodent's home cage that was placed 60 cm away (Fig. S3H). This time the meter stick was in the flat position (width of 2.5 cm). If the mouse failed to traverse 30 cm in either direction on the stick during a 3-minute period, a point was awarded.

Grid walk: Our modified grid walk test was used as an additional measure for acute deficits in motor coordination, as well as a measure of activity level[104]. The mouse was placed in the center of a 21 cm^2 grid (1/2-inch hole size) elevated 30 cm in the air (Fig. S3B-H). A video camera was positioned at a 45-degree angle underneath the grid for visualization. Mice were recorded for a 3-minute period 24 hours before impact and immediately after the NSS was performed post-concussive impact. Analysis was performed by a blinded researcher watching the videos frame by frame. The total number of forelimb strides were recorded, and the total number of forelimb foot faults were recorded. A foot fault was defined as anytime the mouse misplaced one of its forelimbs allowing it to pass directly through the grid (Fig. S3B *vs.* C). The activity level of the mouse was also recorded during the 3-minute period. Being active was defined when any part of the mouse was moving, which included exploratory behavior, such as just moving the head. The percentage of forelimb foot faults was calculated by dividing the number of forelimb foot faults by the total number of forelimb steps. The percentage of time active was calculated by dividing the total time spent active by the 3-minute recording period.

5.8.5. Probe preparation

$5MeONA_3$ [33] was synthesized as previously described; spectral characterization match that previously reported.

$ProxyNA_3$ was prepared from 5-*O*-propargyl-*N*-Boc-anthranilic acid previously prepared by us [51] by modification of an existing literature protocol [105]. A one pot reaction involving Boc deprotection and a diazotization/reduction cascade resulted in $ProxyNA_3 \cdot 2\ HCl$ (Scheme 1).

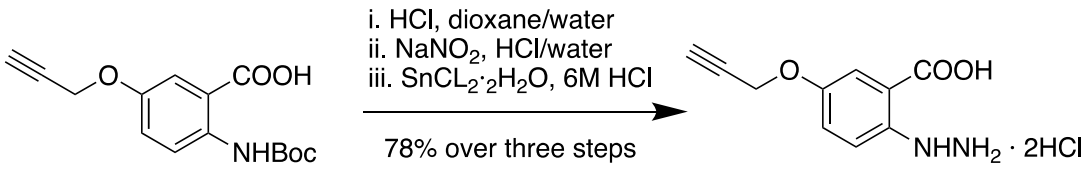

Scheme 1 Synthesis of ProxyNA$_3$

General synthetic procedures: Reagents were commercially available or prepared as stated below. All solvents were HPLC grade except for water (18.2 MΩ cm MilliQ water). Solvents were removed under reduced pressure in a rotary evaporator. Thin-layer chromatography (TLC) was carried out on Al backed silica gel plates with compounds visualised by anisaldehyde stain, 5% ninhydrin stain, and UV light. Melting points (mp) were obtained on EZ-Melt apparatus and are uncorrected. NMR spectra were recorded on a 300 MHz spectrometer for ^{1}H NMR spectra δ values were recorded as follows: DMSO-D$_6$ (2.50 ppm); for ^{13}C (93.75 MHz) δ DMSO-D$_6$ (39.50 ppm). Mass spectra (MS) were obtained using electron impact (EI).

ProxyNA$_3$: Concentrated HCl (3 mL) was added to a stirred solution of 5-*O*-propargyl-*N*-Boc-anthranilic acid (291 mg, 1 mmol) in dioxane (2.5 mL). The mixture was stirred for 45 minutes at 80 ºC, was cooled to 0 ºC and an ice-cold solution of $NaNO_2$ (76 mg, 1.1 mmol) in water (500 μL) was added. The stirring continued for 1 h at 0 ºC, an ice-cold solution of $SnCl_2 \cdot 2H_2O$ (451 mg, 2 mmol) in 6 M HCl (1 mL) was added, the cooling bath was removed, and the stirring continued for 1 h at room temperature. The mixture was set aside for 1 h at 3ºC, separated solid was filtered with suction, was washed with an ice-cold diluted HCl and was dried to afford 5-*O*-propargyl-*N*-aminoanthranilic acid dihydrochloride, orange solid, mp. 220-222 ºC, 217 mg, 78%. ^{1}H NMR (DMSO-D$_6$) δ 10.28 (br s, D$_2$O exch., 3H); 8.82 (br s, D$_2$O exch., 1H); 7.50 (d, *J* = 2.5 Hz, 1H); 7.30 (dd, *J* = 7.0, 2.5 Hz, 1H); 7.18 (d, *J* = 7.0 Hz, 1H); 4.81 (d, *J* = 2.0 Hz, 1H); 3.58 (t, *J* = 2.0 Hz, 1H). ^{13}C NMR (DMSO-D$_6$) δ 168.4, 150.9, 142.0, 122.0, 116.6, 116.5, 115.5, 79.1, 78.5,

56.0. HRMS (EI) *m/z*; found 206.0710 [M^+] (calcd 206.0691 for $C_{10}H_{10}N_2O_3$). LRMS (EI) *m/z* (rel abundance) 206 [M^+] (10), 131 (10). NMR spectra can be found in Supporting Figures 5 and 6.

5.8.6. *In vivo* imaging

5.8.6.1. Dynamic Enhanced Contrast Magnetic Resonance Imaging (DCE-MRI)

The experimental design for DCE-MRI was adapted from a previous study[106]. The experiments were performed on a 3T MRI (MR Solutions). Mice were anesthetized with 1-2% isoflurane and then tail cannulation was performed for injection of the gadobutrol contrast agent. Single slice positioning was performed in the axial plane, between the bregma 3.56mm and -4.36mm. The following parameters were used: Slices: 7; Slice thickness: 1.0 mm; FOV: 40; Slice gap: 0.1; FOV ratio: 1.000. After setting the positioning parameters, and performing a Scout image, a series of serial T1-weighted images were obtained pre-contrast, during contrast, and post-contrast injection with gadobutrol (0.1 mmol kg-1; GadavistTM, Bayer). T1-weighted images were obtained using a Rapid Imaging with Refocused Echoes (RARE) pulse sequence with varying TIs (Pre-contrast: 280, 500, 900, 1200, 1500, 4650, 1200ms; During contrast: 1200ms x 10; Post-contrast: 280, 500, 900, 1200, 1500, 4650ms). The following imaging acquisition parameters were used: Echo spacing: 16; TE: 16; Echo train: 8; Views: 240.

Analysis of the scans was performed using the VivoQuant software. Four Regions of Interest (ROIs) were drawn using the 3D ROI Tool on 6 slices of each of the scans. Note, the first slice for each scan was not included in analysis due to the presence of the skull, which limited image resolution and clarity. The four ROIs included the brain, the ventricles, the meninges and the middle cerebral artery, which was referred to as blood. The mean voxel intensity in each of the ROIs across all six slices was generated for the scan immediately before gadobutrol injection (TI of 1200 ms) and then for the 10 consecutive scans taken at 3-minute intervals post gadobutrol injection (TI of 1200 ms). The data was then plotted for each of the ROI as the percentage change in voxel intensity, which was calculated by dividing the mean voxel intensity in each of the 10 consecutive scans taken post gadobutrol injection by the single scan taken immediately before gadobutrol injection. This procedure was performed for each of the timepoints: 5 days pre-impact

(baseline), 6 hours post-impact, 30 hours post-impact, 54 hours post-impact. A generalized linear model (GLM), repeated measures was used to determine whether there were significant differences in the percentage change in voxel intensities in each of the ROIs before and after impact.

5.8.6.2. CEST-MRI

All CEST-MRI acquisitions were performed on a 3T pre-clinical MRI (MR Solutions, Ltd.). A single slice Single Shot Rapid Imaging with Refocused Echoes (RARE) pulse sequence was implemented with the following parameters: Average=1, Matrix size=96x96, TE=7 ms, Echo Spacing=7 ms, TR=6000 ms, CEST Length=5000 ms.. Prior to imaging, tail veins were cannulated with an ~1m long cannula (~100 µL dead volume), permitting *intravenous* injection in the MRI. Mice were warmed and respiration rate was monitored through the duration of the imaging experiment. Heads were centered in the FOV using standard localizer sequences. In order to correct for B_o inhomogeneity, a Water Saturation Shift Referencing (WASSR) sequence was implemented prior to any Z-spectra acquisitions. For WASSR, Z-spectra were acquired from +200 to -200 Hz at 25 Hz steps, and a pre-saturation pulse B_1 amplitude B_1 = 0.65 µT . The total acquisition time for WASSR was 1 min 42 seconds. CEST MRI prior to contrast agent administration (single slice, slice thickness = 2.0 mm FOV = 35 x 35 mm, CEST frequency range from +1500 to -1500 Hz centered on the water resonance, sampled in steps of 100 Hz, a pre-saturation pulse B_1 amplitude B_1 = 2.61 µT, and acquisition time 3 minutes 6 seconds). After the completion of the initial Z-spectrum, each mouse received a bolus injection of 100 µL of 40 mM of PHBA dissolved in saline, and the line was flushed with 100 µL saline. No adverse events were noted in any of the mice receiving PHBA injections. Post-contrast Z-spectra were acquired sequentially for 45 min post-injection. An anatomical reference image was acquired using a T_2-weighted RARE sequence (Average=2, Matrix size=256x256, TE=68 ms, Echo Spacing=17 ms, TR=4800 ms) with the same FOV as the Z-spectra acquisitions.

Images were post-processed and analyzed using the Matlab routine provided by Guanshu Liu *et al*., available for download here: http://godzilla.kennedykrieger.org/CEST/ [107]. Code modifications were necessary to read the vendor specific imaging files and to reorder the image data. Image maps were

generated to plot %MTRasym at Dw = 6.5 ppm over the entire slice, and a final map of the ratio of 45 min post-PHBA injection divided by pre-PHBA injection images was plotted using Image J. This map was colour coded using a custom lookup table and overlaid onto the corresponding anatomical image. Brain regions of interest (ROI) of the ratio map were quantified by histogram analysis using ImageJ.

5.8.7. Histology

Mice were anesthetized with isoflurane and perfused with 4% PFA. The brain was delicately removed from the skull and placed in a 50mL tube containing 4% PFA, at 4°C for 24 hours. The brains were then cryoprotected in sequential 15% and 30% sucrose solutions at 4°C. They were then embedded in OCT (Tissue-Trek) over dry ice and moved to -80°C for storage.

5.8.7.1. Tissue sectioning and free-floating immunofluorescence staining

Serial 40µm sections were taken using a cryostat (Leica CM1850) starting at the initial appearance of the lateral ventricles and placed into a 24 well plate containing PBS with 0.01% sodium azide solution and stored at 4°C. 12 sections were taken per brain.

12 brains were excised from mice from each group (naïve, 2 days post-injury, 7 days post-injury) for immunofluorescence staining. One brain was excluded from the 7-day group due to damage during excision. Therefore, 35 mice were used for histological assessment.

Brain sections were removed from sodium azide-containing solution and washed in PBS 3x 5min on a rocker. They were then blocked with a solution containing 5% goat serum, 0.1% Triton X-100 and 0.1% Tween-20 for 1 hour at room temperature. The sections were then incubated with primary antibodies (α-GFAP or α-Iba1) diluted in blocking solution overnight at 4°C on a rocker. After washing with PBS 3x 5min, secondary antibodies were added in blocking buffer for 1 hour at room temperature on a rocker. Secondary antibody solution was removed, and the sections were washed again and then transferred into a petri dish filled with 1X PBS and mounted onto a charged microscope slide using a fine paintbrush. A

coverslip was placed onto the slide using Fluoromount-G mounting medium with DAPI (Invitrogen), and the slide was stored in the dark until imaging.

Imaging was performed on a Zeiss axioscan microscope slide scanner. Images were tiled, z-stacks were taken to ensure total depth was imaged, and at 10X resolution. Post-processing in Zen Blue included tile stitching, shading correction, background subtraction, and maximum intensity projection. For quantification, a 1500x1300pixel rectangular region of interest was drawn on approximately the same region of hippocampus of each image and quantified in Fiji (total GFAP intensity divided by total Hoechst intensity).

5.8.7.2. Western Blotting:

Mice were euthanized *via* CO_2 asphyxiation. Brains and livers were removed and immediately snap-frozen in liquid nitrogen and stored at -80°C until use. Tissues were then homogenized in 1X RIPA buffer with protease inhibitor tablet (Roche) in a bead beater for 5 minutes at 4°C. The protein in the supernatant was then quantified using Pierce BCA protein quantification kit with BSA in lysis buffer for standard curve. 30µg of protein was added per well and run on a 4-20% pre-cast gel (Biorad). Membranes were probed with α-ALDH2 (Proteintech 15310-1-AP) and α-Vinculin (Abcam ab130007).

5.9. Conflicts of interest

The authors have filed a patent (U.S. 11,696,960) regarding the use of *N*-aminoanthranilic acids for aldehyde imaging.

5.10. Acknowledgements

General: The authors would like to thank Dr. Emilio Alarcon for his advice on preparation of 3D scaffolds, and Vivian Franklin for her assistance in mouse colony breeding and maintenance.

Funding: A.J.S. acknowledges funding support from Canada Research Chairs (950-230754), CIHR (PJT-376892), NSERC Discovery Grant (RGPIN- 2021-03387), Government of Ontario Early Researcher Award (ER18-14-102), and the Concussion Injury Group of the uO Brain and Mind Research Institute.

5.11. Author Contributions

A.K., R.D., and A.S. developed *in vivo* mouse model of mTBI. A.K., C.W., A.S. and N.D.C. contributed to corticomimetic scaffold development. J.W. and J.L. performed primary cortical precursor cell dissections. M.S. and N.C. performed all chemistry for probe preparation. A.K., R.D., C.D., and E.S. conducted UTM experiments. A.K. performed histology, microscopy, and molecular biology procedures. A.K. and A.J.S. conducted MR imaging, performed statistical analysis, data interpretation, and drafting of manuscript.

5.12. References

1 Cassidy, J. D. *et al.* Incidence, risk factors and prevention of mild traumatic brain injury: results of the WHO Collaborating Centre Task Force on Mild Traumatic Brain Injury. *Journal of rehabilitation medicine* **36**, 28-60, (2004).

2 Baldwin, G. T., Breiding, M. J. & Comstock, R. D. Epidemiology of sports concussion in the United States. *Handbook of clinical neurology* **158**, 63-74, (2018).

3 Stephenson, S., Langley, J. & Cryer, C. Effects of service delivery versus changes in incidence on trends in injury: a demonstration using hospitalised traumatic brain injury. *Accident Analysis & Prevention* **37**, 825-832, (2005).

4 Montenigro, P. H. *et al.* Cumulative head impact exposure predicts later-life depression, apathy, executive dysfunction, and cognitive impairment in former high school and college football players. *Journal of neurotrauma* **34**, 328-340, (2017).

5 Buki, A. *et al.* Minor and repetitive head injury. *Advances and Technical Standards in Neurosurgery: Volume 42*, 147-192, (2015).

6 Lingsma, H. F. & Cnossen, M. C. Identification of patients at risk for poor outcome after mTBI. *The Lancet Neurology* **16**, 494-495, (2017).

7 Haydel, M. J. *et al.* Indications for computed tomography in patients with minor head injury. *New England Journal of Medicine* **343**, 100-105, (2000).

8 Homer, C. J. & Kleinman, L. Technical report: minor head injury in children. *Pediatrics* **104**, e78-e78, (1999).

9 Olson, A., Ellis, M. J., Selci, E. & Russell, K. Delayed symptom onset following pediatric sport-related concussion. *Frontiers in neurology* **11**, 220, (2020).

10 Giza, C. C. *et al.* Summary of evidence-based guideline update: evaluation and management of concussion in sports: report of the Guideline Development Subcommittee of the American Academy of Neurology. *Neurology* **80**, 2250-2257, (2013).

11 Giza, C. C. & Hovda, D. A. The new neurometabolic cascade of concussion. *Neurosurgery* **75**, S24, (2014).

12 Yu, Z., Li, W. & Brunk, U. T. 3-Aminopropanal is a lysosomotropic aldehyde that causes oxidative stress and apoptosis by rupturing lysosomes. *Apmis* **111**, 643-652, (2003).

13 Petronilho, F. *et al.* Oxidative stress in brain according to traumatic brain injury intensity. *Journal of Surgical Research* **164**, 316-320, (2010).

14 Halstrom, A. *et al.* Elevation of oxidative stress indicators in a pilot study of plasma following traumatic brain injury. *Journal of Clinical Neuroscience* **35**, 104-108, (2017).

15 Cristofori, L. *et al.* Biochemical analysis of the cerebrospinal fluid: evidence for catastrophic energy failure and oxidative damage preceding brain death in severe head injury: a case report. *Clinical biochemistry* **38**, 97-100, (2005).

16 Zahedi, K. *et al.* Polyamine catabolism is enhanced after traumatic brain injury. *Journal of neurotrauma* **27**, 515-525, (2010).

17 Yates, N. J. *et al.* Repeated mild traumatic brain injury in female rats increases lipid peroxidation in neurons. *Experimental brain research* **235**, 2133-2149, (2017).

18 Singh, I. N. *et al.* Phenelzine mitochondrial functional preservation and neuroprotection after traumatic brain injury related to scavenging of the lipid peroxidation-derived aldehyde 4-hydroxy-2-nonenal. *Journal of cerebral blood flow & metabolism* **33**, 593-599, (2013).

19 Cebak, J. E., Singh, I. N., Hill, R. L., Wang, J. A. & Hall, E. D. Phenelzine protects brain mitochondrial function in vitro and in vivo following traumatic brain injury by scavenging the reactive carbonyls 4-hydroxynonenal and acrolein leading to cortical histological neuroprotection. *Journal of neurotrauma* **34**, 1302-1317, (2017).

20 Hall, E. D., Vaishnav, R. A. & Mustafa, A. G. Antioxidant therapies for traumatic brain injury. *Neurotherapeutics* **7**, 51-61, (2010).

21 Shao, C., Roberts, K. N., Markesbery, W. R., Scheff, S. W. & Lovell, M. A. Oxidative stress in head trauma in aging. *Free Radical Biology and Medicine* **41**, 77-85, (2006).
22 Isokuortti, H. *et al.* Who gets head trauma or recruited in mild traumatic brain injury research? *Journal of neurotrauma* **33**, 232-241, (2016).
23 Sohal, R. S. & Orr, W. C. The redox stress hypothesis of aging. *Free Radical Biology and Medicine* **52**, 539-555, (2012).
24 Esterbauer, H., Schaur, R. J. & Zollner, H. Chemistry and biochemistry of 4-hydroxynonenal, malonaldehyde and related aldehydes. *Free radical Biology and medicine* **11**, 81-128, (1991).
25 Ayala, A., Muñoz, M. F. & Argüelles, S. Lipid peroxidation: production, metabolism, and signaling mechanisms of malondialdehyde and 4-hydroxy-2-nonenal. *Oxidative medicine and cellular longevity* **2014**, (2014).
26 Roozenbeek, B., Maas, A. I. & Menon, D. K. Changing patterns in the epidemiology of traumatic brain injury. *Nature Reviews Neurology* **9**, 231-236, (2013).
27 Hume, C. H., Wright, B. J. & Kinsella, G. J. Systematic Review and Meta-analysis of Outcome after Mild Traumatic Brain Injury in Older People. *Journal of the International Neuropsychological Society* **28**, 736-755, (2022).
28 Chen, J. & Yu, B. Detoxification of reactive aldehydes in mitochondria: effects of age and dietary restriction. *Aging Clinical and Experimental Research* **8**, 334-340, (1996).
29 Anderson, E. J., Katunga, L. A. & Willis, M. S. Mitochondria as a source and target of lipid peroxidation products in healthy and diseased heart. *Clinical and Experimental Pharmacology and Physiology* **39**, 179-193, (2012).
30 Yoval-Sánchez, B. & Rodríguez-Zavala, J. S. Differences in susceptibility to inactivation of human aldehyde dehydrogenases by lipid peroxidation byproducts. *Chemical research in toxicology* **25**, 722-729, (2012).
31 Er, J. C. *et al.* NeuO: a fluorescent chemical probe for live neuron labeling. *Angewandte Chemie International Edition* **54**, 2442-2446, (2015).
32 Scimone, M. T., Cramer III, H. C., Hopkins, P., Estrada, J. B. & Franck, C. Application of mild hypothermia successfully mitigates neural injury in a 3D in-vitro model of traumatic brain injury. *Plos one* **15**, e0229520, (2020).
33 Suchý, M. *et al.* Methyl 5-MeO-N-aminoanthranilate, a minimalist fluorogenic probe for sensing cellular aldehydic load. *Org Biomol Chem* **17**, 1843-1853, (2019).
34 Xiong, Y., Mahmood, A. & Chopp, M. Animal models of traumatic brain injury. *Nature Reviews Neuroscience* **14**, 128-142, (2013).
35 Petraglia, A. L., Dashnaw, M. L., Turner, R. C. & Bailes, J. E. Models of mild traumatic brain injury: translation of physiological and anatomic injury. *Neurosurgery* **75**, S34-S49, (2014).
36 Meaney, D. F. & Smith, D. H. Biomechanics of concussion. *Clinics in sports medicine* **30**, 19-31, (2011).
37 Statler, K. D. *et al.* Isoflurane exerts neuroprotective actions at or near the time of severe traumatic brain injury. *Brain research* **1076**, 216-224, (2006).
38 Statler, K. D. *et al.* Comparison of seven anesthetic agents on outcome after experimental traumatic brain injury in adult, male rats. *Journal of neurotrauma* **23**, 97-108, (2006).
39 Makdissi, M. *et al.* Natural history of concussion in sport: markers of severity and implications for management. *The American journal of sports medicine* **38**, 464-471, (2010).
40 McClincy, M. P., Lovell, M. R., Pardini, J., Collins, M. W. & Spore, M. K. Recovery from sports concussion in high school and collegiate athletes. *Brain injury* **20**, 33-39, (2006).
41 Ponsford, J. *et al.* Factors influencing outcome following mild traumatic brain injury in adults. *Journal of the International Neuropsychological Society* **6**, 568-579, (2000).
42 Meconi, A. *et al.* Repeated mild traumatic brain injury can cause acute neurologic impairment without overt structural damage in juvenile rats. *PloS one* **13**, e0197187, (2018).

43 Petraglia, A. L. *et al.* The spectrum of neurobehavioral sequelae after repetitive mild traumatic brain injury: a novel mouse model of chronic traumatic encephalopathy. *Journal of neurotrauma* **31**, 1211-1224, (2014).
44 Brady, R. D. *et al.* Modelling traumatic brain injury and posttraumatic epilepsy in rodents. *Neurobiology of disease* **123**, 8-19, (2019).
45 Baskin, Y. K., Dietrich, W. D. & Green, E. J. Two effective behavioral tasks for evaluating sensorimotor dysfunction following traumatic brain injury in mice. *Journal of neuroscience methods* **129**, 87-93, (2003).
46 Heye, A. K., Culling, R. D., Hernández, M. d. C. V., Thrippleton, M. J. & Wardlaw, J. M. Assessment of blood–brain barrier disruption using dynamic contrast-enhanced MRI. A systematic review. *NeuroImage: Clinical* **6**, 262-274, (2014).
47 Turtzo, L. C. *et al.* Meningeal blood–brain barrier disruption in acute traumatic brain injury. *Brain Communications* **2**, fcaa143, (2020).
48 Patel, N. & Kirmi, O. in *Seminars in Ultrasound, CT and MRI.* 559-564 (Elsevier).
49 Dang, T. *et al.* Hydrazo-CEST: Hydrazone-Dependent Chemical Exchange Saturation Transfer Magnetic Resonance Imaging Contrast Agents. *Chemistry – A European Journal* **24**, 9148-9156, (2018).
50 Brun, E. M. S. P.-T. *et al.* Mapping vitamin B 6 metabolism by hydrazoCEST magnetic resonance imaging. *Chemical Communications* **57**, 10867-10870, (2021).
51 Kirby, A., Suchý, M., Brouwer, A. & Shuhendler, A. Mapping aldehydic load in vivo by positron emission tomography with [18 F] NA 3 BF 3. *Chemical Communications* **55**, 5371-5374, (2019).
52 Kitagawa, K. *et al.* Aldehyde dehydrogenase (ALDH) 2 associates with oxidation of methoxyacetaldehyde; in vitro analysis with liver subcellular fraction derived from human and Aldh2 gene targeting mouse. *FEBS letters* **476**, 306-311, (2000).
53 Guillot, A. *et al.* Targeting liver aldehyde dehydrogenase-2 prevents heavy but not moderate alcohol drinking. *Proceedings of the National Academy of Sciences* **116**, 25974-25981, (2019).
54 Farina, C., Aloisi, F. & Meinl, E. Astrocytes are active players in cerebral innate immunity. *Trends in Immunology* **28**, 138-145, (2007).
55 Walus, K., Beyer, S. & Willerth, S. M. Three-dimensional bioprinting healthy and diseased models of the brain tissue using stem cells. *Current Opinion in Biomedical Engineering* **14**, 25-33, (2020).
56 Tang-Schomer, M. D. *et al.* Bioengineered functional brain-like cortical tissue. *Proceedings of the National Academy of Sciences* **111**, 13811-13816, (2014).
57 Warren, D., Tomaskovic-Crook, E., Wallace, G. G. & Crook, J. M. Engineering in vitro human neural tissue analogs by 3D bioprinting and electrostimulation. *APL bioengineering* **5**, (2021).
58 Lee, W. *et al.* Three-dimensional bioprinting of rat embryonic neural cells. *Neuroreport* **20**, 798-803, (2009).
59 Rockwood, D. N. *et al.* Materials fabrication from Bombyx mori silk fibroin. *Nature protocols* **6**, 1612-1631, (2011).
60 Nazarov, R., Jin, H.-J. & Kaplan, D. L. Porous 3-D scaffolds from regenerated silk fibroin. *Biomacromolecules* **5**, 718-726, (2004).
61 Bouvier, D., Oris, C., Brailova, M., Durif, J. & Sapin, V. Interest of blood biomarkers to predict lesions in medical imaging in the context of mild traumatic brain injury. *Clinical biochemistry* **85**, 5-11, (2020).
62 Bazarian, J. J. *et al.* Serum GFAP and UCH-L1 for prediction of absence of intracranial injuries on head CT (ALERT-TBI): a multicentre observational study. *The Lancet Neurology* **17**, 782-789, (2018).
63 Çevik, S. *et al.* NRGN, S100B and GFAP levels are significantly increased in patients with structural lesions resulting from mild traumatic brain injuries. *Clinical neurology and neurosurgery* **183**, 105380, (2019).

64 Huebschmann, N. A. *et al.* Comparing glial fibrillary acidic protein (GFAP) in serum and plasma following mild traumatic brain injury in older adults. *Frontiers in Neurology* **11**, 1054, (2020).
65 Czeiter, E. *et al.* Blood biomarkers on admission in acute traumatic brain injury: relations to severity, CT findings and care path in the CENTER-TBI study. *EBioMedicine* **56**, (2020).
66 Gill, J. *et al.* Glial fibrillary acidic protein elevations relate to neuroimaging abnormalities after mild TBI. *Neurology* **91**, e1385-e1389, (2018).
67 Mahan, M. Y. *et al.* Glial fibrillary acidic protein (GFAP) outperforms S100 calcium-binding protein B (S100B) and ubiquitin C-terminal hydrolase L1 (UCH-L1) as predictor for positive computed tomography of the head in trauma subjects. *World neurosurgery* **128**, e434-e444, (2019).
68 Nichols, N. R., Day, J. R., Laping, N. J., Johnson, S. A. & Finch, C. E. GFAP mRNA increases with age in rat and human brain. *Neurobiology of aging* **14**, 421-429, (1993).
69 Gardner, R. C. *et al.* Age-related differences in diagnostic accuracy of plasma glial fibrillary acidic protein and tau for identifying acute intracranial trauma on computed tomography: a TRACK-TBI study. *Journal of neurotrauma* **35**, 2341-2350, (2018).
70 Calcagnile, O., Holmén, A., Chew, M. & Undén, J. S100B levels are affected by older age but not by alcohol intoxication following mild traumatic brain injury. *Scandinavian journal of trauma, resuscitation and emergency medicine* **21**, 1-6, (2013).
71 Dash, P. K., Zhao, J., Hergenroeder, G. & Moore, A. N. Biomarkers for the diagnosis, prognosis, and evaluation of treatment efficacy for traumatic brain injury. *Neurotherapeutics* **7**, 100-114, (2010).
72 Chou, S. H., Robertson, C. S. & Monitoring, P. i. t. I. M.-d. C. C. o. t. M. Monitoring biomarkers of cellular injury and death in acute brain injury. *Neurocritical care* **21**, 187-214, (2014).
73 Brooks, P. J., Enoch, M.-A., Goldman, D., Li, T.-K. & Yokoyama, A. The alcohol flushing response: an unrecognized risk factor for esophageal cancer from alcohol consumption. *PLoS medicine* **6**, e1000050, (2009).
74 Wu, B. *et al.* Aldehyde dehydrogenase 2 activation in aged heart improves the autophagy by reducing the carbonyl modification on SIRT1. *Oncotarget* **7**, 2175, (2016).
75 Kasai, A. *et al.* Aldehyde dehydrogenase 2 deficiency promotes skeletal muscle atrophy in aged mice. *American Journal of Physiology-Regulatory, Integrative and Comparative Physiology* **322**, R511-R525, (2022).
76 Comporti, M. Lipid peroxidation and cellular damage in toxic liver injury. *Laboratory investigation; a journal of technical methods and pathology* **53**, 599-623, (1985).
77 Baeuerle, P. A. & Baltimore, D. NF-κB: ten years after. *Cell* **87**, 13-20, (1996).
78 Grossmann, M., Nakamura, Y., Grumont, R. & Gerondakis, S. New insights into the roles of ReL/NF-κB transcription factors in immune function, hemopoiesis and human disease. *The international journal of biochemistry & cell biology* **31**, 1209-1219, (1999).
79 Clark, D. P. *et al.* Inflammation in traumatic brain injury: roles for toxic A1 astrocytes and microglial–astrocytic crosstalk. *Neurochemical research* **44**, 1410-1424, (2019).
80 Wheeler, M. A. & Quintana, F. J. Regulation of astrocyte functions in multiple sclerosis. *Cold Spring Harbor perspectives in medicine* **9**, (2019).
81 Dresselhaus, E. C. & Meffert, M. K. Cellular specificity of NF-κB function in the nervous system. *Frontiers in immunology* **10**, 1043, (2019).
82 Nonaka, M. *et al.* Prolonged activation of NF-κB following traumatic brain injury in rats. *Journal of neurotrauma* **16**, 1023-1034, (1999).
83 Sanz, O., Acarin, L., González, B. & Castellano, B. NF-κB and IκBα expression following traumatic brain injury to the immature rat brain. *Journal of neuroscience research* **67**, 772-780, (2002).
84 Sun, L. *et al.* Inhibition of HMGB1 reduces rat spinal cord astrocytic swelling and AQP4 expression after oxygen-glucose deprivation and reoxygenation via TLR4 and NF-κB signaling in an IL-6-dependent manner. *Journal of neuroinflammation* **14**, 1-18, (2017).

85 Pan, C. *et al.* Aldehyde dehydrogenase 2 inhibits inflammatory response and regulates atherosclerotic plaque. *Oncotarget* **7**, 35562, (2016).
86 Saggu, R. *et al.* Astroglial NF-kB contributes to white matter damage and cognitive impairment in a mouse model of vascular dementia. *Acta neuropathologica communications* **4**, 1-10, (2016).
87 Dwivedi, S., Sharma, A., Patrick, B., Sharma, R. & Awasthi, Y. C. Role of 4-hydroxynonenal and its metabolites in signaling. *Redox Report* **12**, 4-10, (2007).
88 Müller, J. M., Rupec, R. A. & Baeuerle, P. A. Study of gene regulation by NF-κB and AP-1 in response to reactive oxygen intermediates. *Methods* **11**, 301-312, (1997).
89 Meyer, M., Pahl, H. L. & Baeuerle, P. A. Regulation of the transcription factors NF-κB and AP-1 by redox changes. *Chemico-biological interactions* **91**, 91-100, (1994).
90 Yadav, U. C., Ramana, K. V., Awasthi, Y. C. & Srivastava, S. K. Glutathione level regulates HNE-induced genotoxicity in human erythroleukemia cells. *Toxicology and applied pharmacology* **227**, 257-264, (2008).
91 Žarković, N. *et al.* 4-Hydroxynonenal as a second messenger of free radicals and growth modifying factor. *Life Sciences* **65**, 1901-1904, (1999).
92 Thompson, C. A. & Burcham, P. C. Genome-wide transcriptional responses to acrolein. *Chemical Research in Toxicology* **21**, 2245-2256, (2008).
93 Kikuchi, N. *et al.* The ALDH2 rs671 polymorphism is associated with athletic status and muscle strength in a Japanese population. *Biology of Sport* **39**, 429-434, (2022).
94 Kenny, L. M. & Aboagye, E. O. Clinical translation of molecular imaging agents used in PET studies of cancer. *Advances in cancer research* **124**, 329-374, (2014).
95 Shaw, R. C., Tamagnan, G. D. & Tavares, A. A. S. Rapidly (and successfully) translating novel brain radiotracers from animal research into clinical use. *Frontiers in Neuroscience* **14**, 871, (2020).
96 Van de Bittner, G. C., Ricq, E. L. & Hooker, J. M. A philosophy for CNS radiotracer design. *Accounts of chemical research* **47**, 3127-3134, (2014).
97 Isse, T. *et al.* Diminished alcohol preference in transgenic mice lacking aldehyde dehydrogenase activity. *Pharmacogenetics and Genomics* **12**, 621-626, (2002).
98 Loan, A. *et al.* Prenatal low-dose methylmercury exposure causes premature neuronal differentiation and autism-like behaviors in a rodent model. *Iscience* **26**, (2023).
99 Azari, H., Sharififar, S., Rahman, M., Ansari, S. & Reynolds, B. A. Establishing embryonic mouse neural stem cell culture using the neurosphere assay. *J Vis Exp* **47**, (2011).
100 Shohami, E., Novikov, M. & Bass, R. Long-term effect of HU-211, a novel non-competitive NMDA antagonist, on motor and memory functions after closed head injury in the rat. *Brain research* **674**, 55-62, (1995).
101 Beni-Adani, L. *et al.* A peptide derived from activity-dependent neuroprotective protein (ADNP) ameliorates injury response in closed head injury in mice. *Journal of Pharmacology and Experimental Therapeutics* **296**, 57-63, (2001).
102 Flierl, M. A. *et al.* Mouse closed head injury model induced by a weight-drop device. *Nature protocols* **4**, 1328-1337, (2009).
103 Khalin, I. *et al.* A mouse model of weight-drop closed head injury: emphasis on cognitive and neurological deficiency. *Neural regeneration research* **11**, 630, (2016).
104 Chao, O., Pum, M., Li, J.-S. & Huston, J. The grid-walking test: assessment of sensorimotor deficits after moderate or severe dopamine depletion by 6-hydroxydopamine lesions in the dorsal striatum and medial forebrain bundle. *Neuroscience* **202**, 318-325, (2012).
105 McKay, C. S. & Finn, M. Polyvalent catalysts operating on polyvalent substrates: A model for surface-controlled reactivity. *Angewandte Chemie* **128**, 12833-12839, (2016).
106 Blockx, I. *et al.* Monitoring blood-brain barrier integrity following amyloid-β immunotherapy using gadolinium-enhanced MRI in a PDAPP mouse model. *Journal of Alzheimer's Disease* **54**, 723-735, (2016).

107 Liu, G., Song, X., Chan, K. W. & McMahon, M. T. Nuts and bolts of chemical exchange saturation transfer MRI. *NMR in Biomedicine* **26**, 810-828, (2013).

Appendix to Chapter 5

Supplemental material for:

Aldehydic load as an objective imaging biomarker of mild traumatic brain injury

Alexia Kirby, Cian Ward, Nicholas D. Calvert, Ryan Daniel, Joseph Leung, Ashwin Sharma, Mojmír Suchý, Cassandra Donatelli, Jing Wang, Emily Standen, Adam J. Shuhendler

Supplemental figures and table

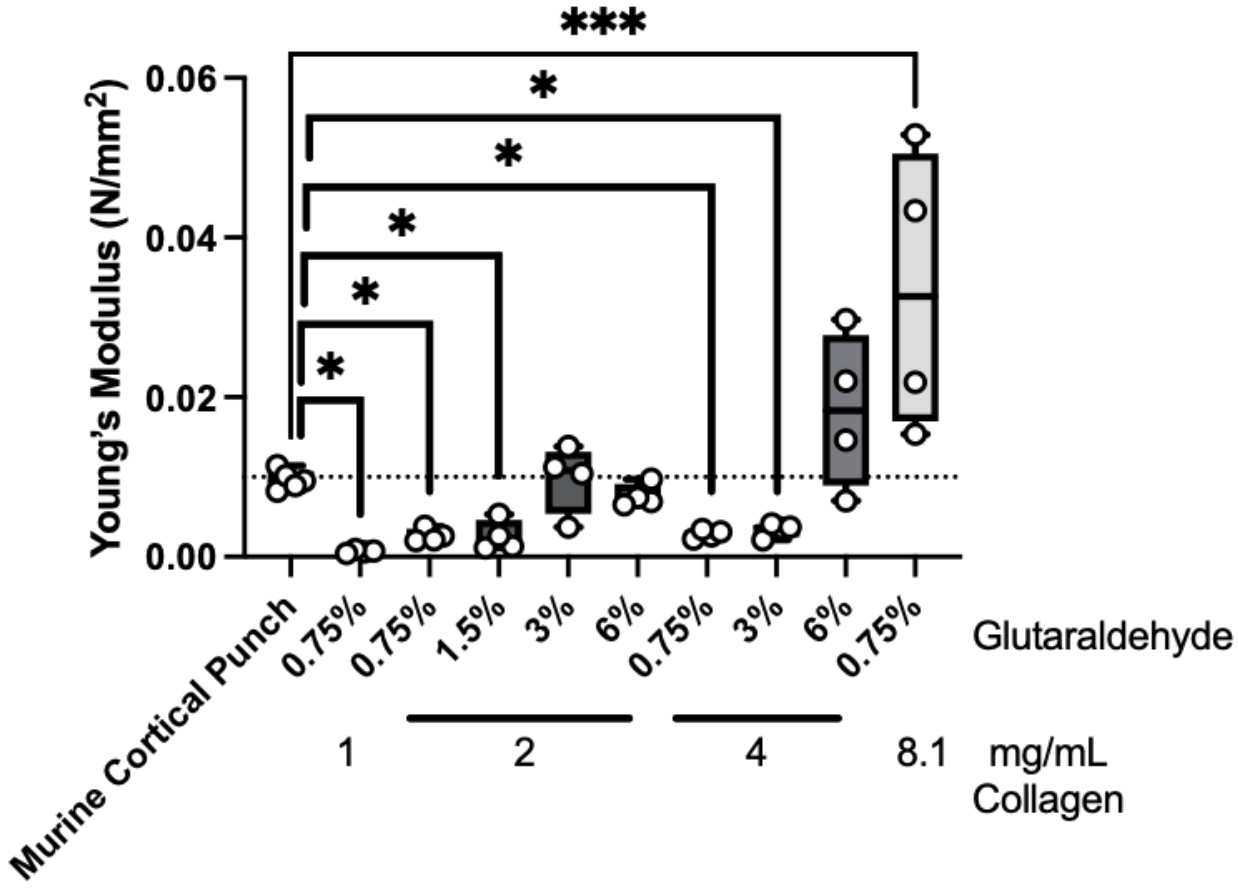

Fig. S5.1. Young's Modulus of different formulations of corticomimetic scaffold exterior in comparison to murine cortical punch. Various concentrations of glutaraldehyde cross-linker and collagen (n=4 per group) were tested and compared to a punch of cortical brain tissue of a mouse (n=5) using a universal testing machine (UTM). Boxplots and individual data points are shown, *$p<0.05$.

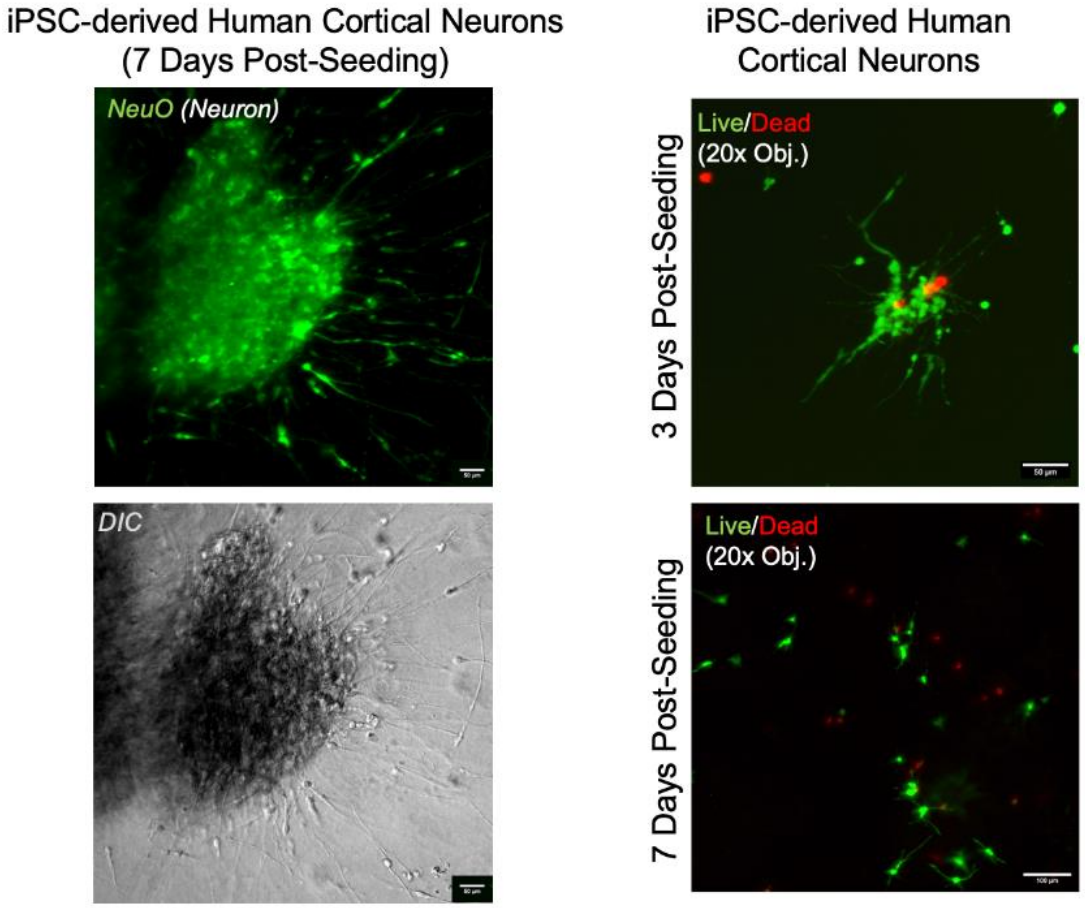

Fig. S5.2. 3D corticomimetic scaffold made for *in vitro* concussion model can support growth of primary human neurons. iPSC-derived human cortical neurons were seeded into the central neural plug of the corticomimetic scaffold. NeuO staining was performed and imaged on a confocal microscope 7 days post-seeding to confirm differentiation of neurons (left; scale bar= 50μM). A majority of cells were alive following live/dead staining with calcein-AM (green; alive) and ethidium homodimer-1 (red/dead) at 3 days- (top) and 7-days (bottom) post-seeding. Scale = 100 μM.

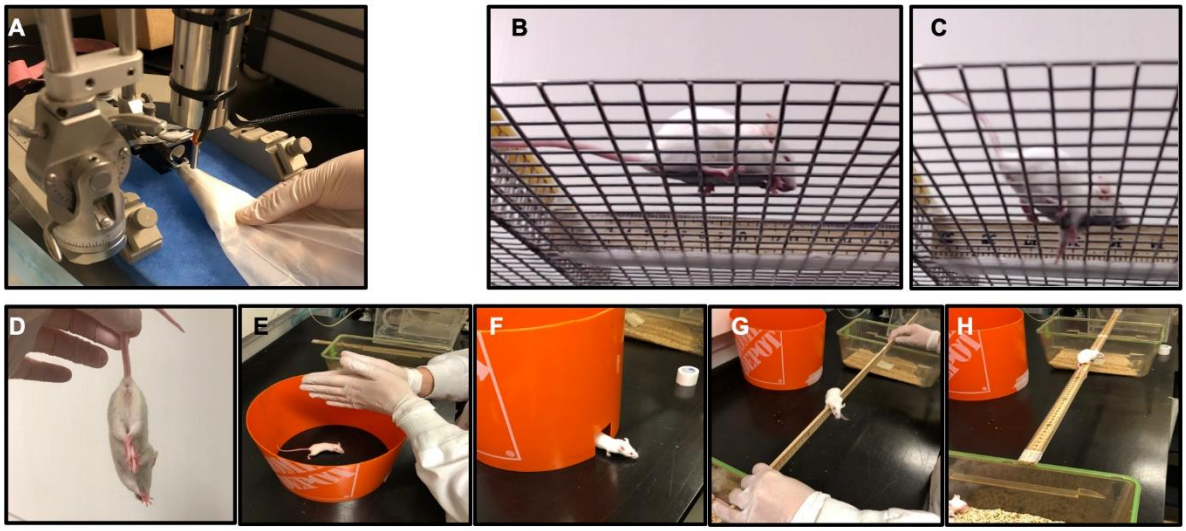

Fig. S5.3. Awake closed head impact (ACHI) setup and behavioural tests for mouse model of mTBI. (**A**) Awake mice are restrained in a conical bag with an opening to allow for breathing. The mouse is then placed under a 5mm impactor tip held by a stereotaxic rig, with filter floss placed underneath to allow free rotation of the head and neck. (**B-C**) Examples of mice performing the grid walk test where they are allowed to walk around a raised grid for three minutes before (B) and after (C) ACHI, where foot faults and activity time are recorded. (**D-H**) Five pass-or-fail tests are conducted before and after ACHI which comprise the neurological severity score (NSS). (D) Mice are hung from the tail and awarded a point (fail) if the hindlimbs cross; (E) startle reflex, where the researcher claps and a point is awarded for any reaction to the sound; (F) escape paradigm, where mice are placed in the middle of a ~25cm diameter cylinder with a door and given 3 minutes to escape; (G) balance test, where mice are hung by the front paws and given 10 seconds to lift themselves into a perched position as in the photo; (H) beam walk test where a mouse is placed on a meter stick 30cm away from a cage (one home cage, one new cage) on either end and given 3 minutes to reach a cage.

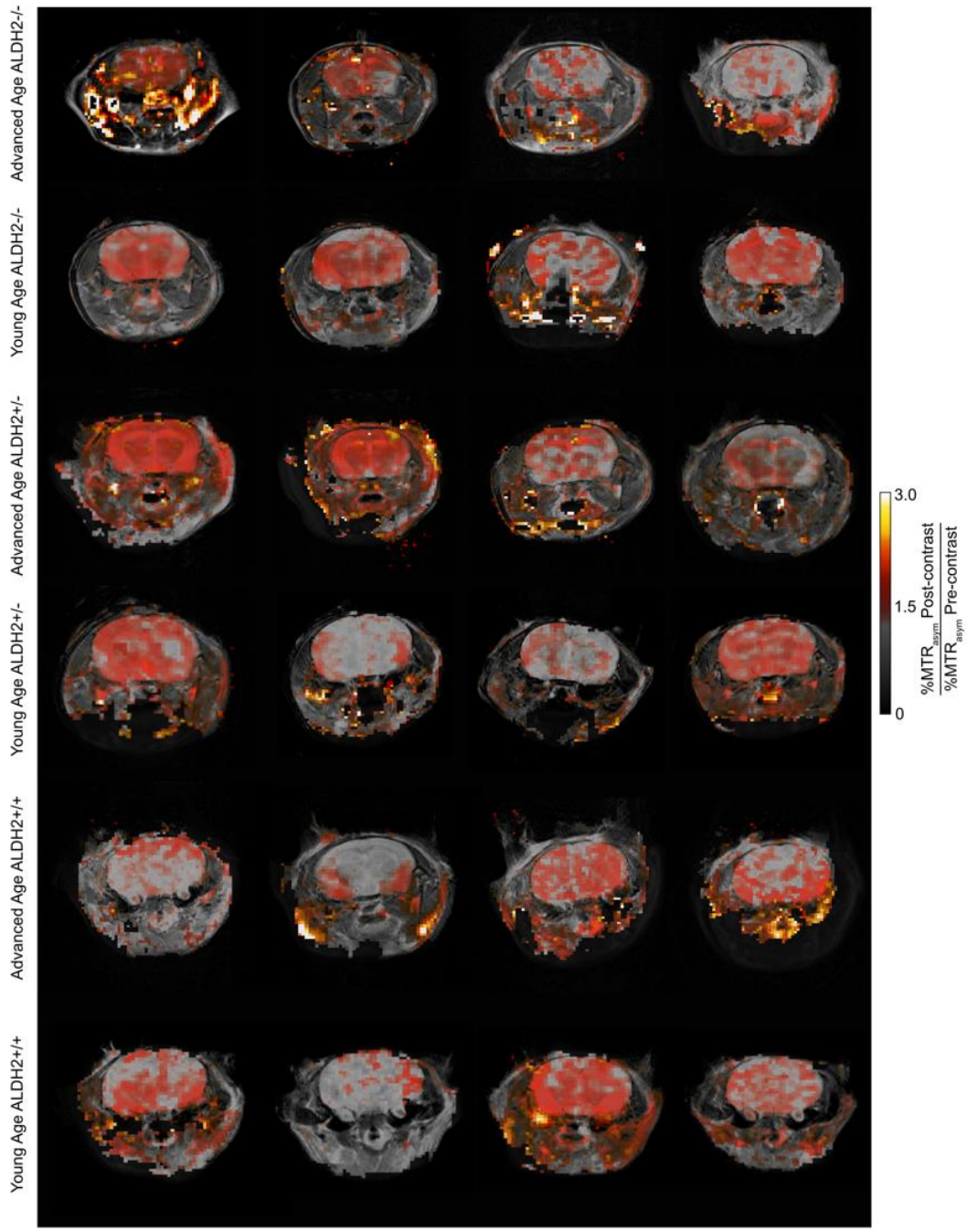

Fig. S5.4. Mapping of brain aldehydes by ProxyNA$_3$ in mice two days post-mTBI. Mice separated into groups by age (young <16 weeks, aged >65 weeks) and genotype (ALDH2 $^{+/+}$, $^{+/-}$, $^{-/-}$) underwent CEST-MRI at two days post-concussive impact. %MTR$_{asym}$ after ProxyNA$_3$ injection normalized to pre-contrast signal is mapped onto coronal T$_2$-weighted image for each mouse. There is sufficient binding of ProxyNA$_3$ to endogenous aldehydes for detection in every mouse two days post-mTBI.

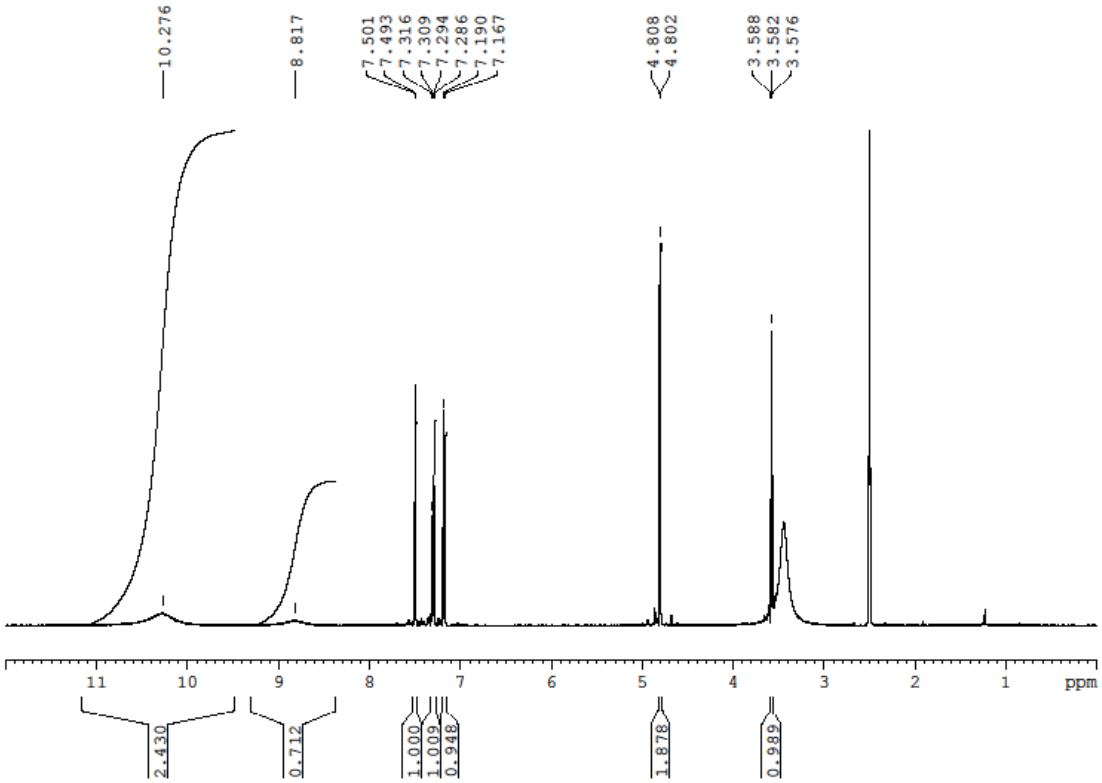

Fig. S5.5 ^{1}H NMR spectrum of ProxyNA$_3$. Signal at δ 3.56 ppm indicates the presence of small amount of dioxane in the sample.

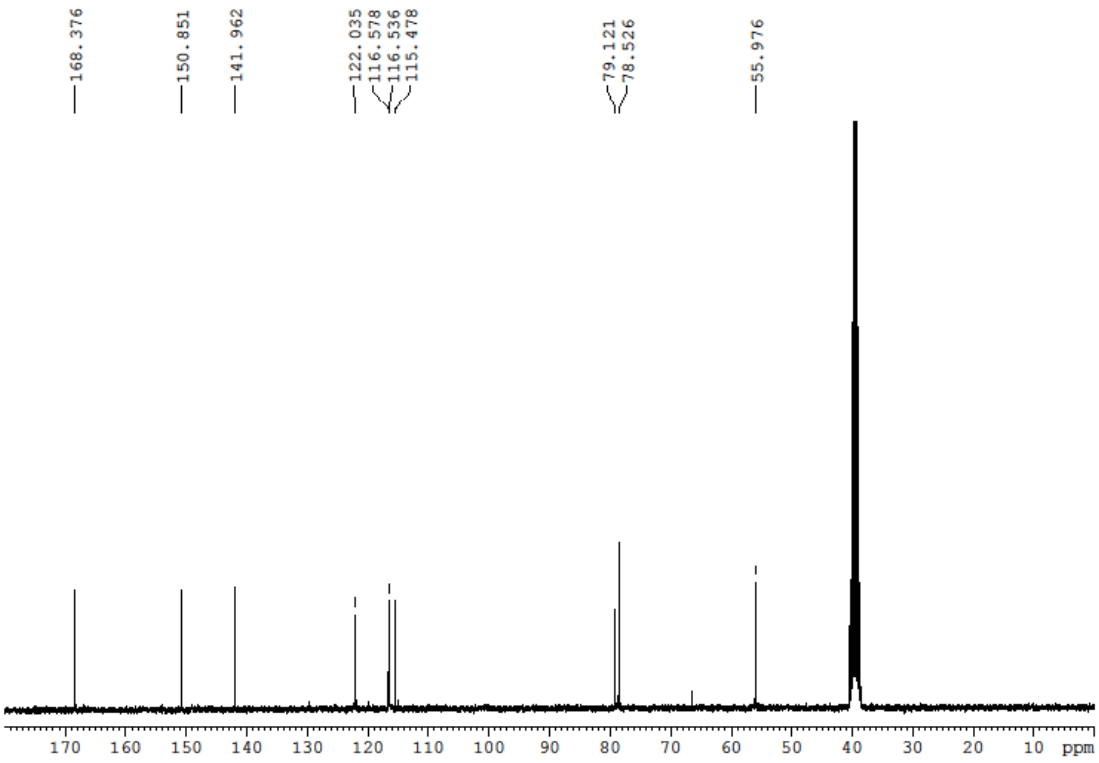

Fig. S5.6 ^{13}C NMR spectrum of ProxyNA$_3$.

Table S5.1. Impact velocities tested for mouse model of mTBI using electromechanical impactor device. Three impact velocities were evaluated using a 5mm tip on an impactor device based on previously reported models of mTBI. Behavioural deficits were only noted for 5 and 6m/s impacts. Less than 5% of mice impacted at 5m/s elicited an unwanted outcome, compared to 100% impacted at 6m/s.

Impact Velocity	Behavioural outcome	Unwanted outcome*	References
2.35m/s	None	None	[1,2]
5m/s	Present	<5%	[3-13]
6m/s	Present	100%	[14]**

*Unwanted outcome= severe TBI (seizure, skull fracture, brain hemorrhaging, death)
**6.8m/s; our impactor device had maximum velocity of 6.0m/s

References

1 Main, B. S., Sloley, S. S., Villapol, S., Zapple, D. N. & Burns, M. P. A mouse model of single and repetitive mild traumatic brain injury. *JoVE (Journal of Visualized Experiments)*, e55713, (2017).

2 Winston, C. N. *et al.* Dendritic spine loss and chronic white matter inflammation in a mouse model of highly repetitive head trauma. *The American journal of pathology* **186**, 552-567, (2016).

3 Bachstetter, A. D. *et al.* Attenuation of traumatic brain injury-induced cognitive impairment in mice by targeting increased cytokine levels with a small molecule experimental therapeutic. *Journal of neuroinflammation* **12**, 1-9, (2015).

4 Creed, J. A., DiLeonardi, A. M., Fox, D. P., Tessler, A. R. & Raghupathi, R. Concussive brain trauma in the mouse results in acute cognitive deficits and sustained impairment of axonal function. *J Neurotrauma* **28**, 547-563, (2011).

5 Goodus, M. T. *et al.* Leukemia inhibitory factor haplodeficiency desynchronizes glial reactivity and exacerbates damage and functional deficits after a concussive brain injury. *Journal of Neurotrauma* **33**, 1522-1534, (2016).

6 Schneider, B. L. *et al.* Increased Cortical Gamma-Aminobutyric Acid Precedes Incomplete Extinction of Conditioned Fear and Increased Hippocampal Excitatory Tone in a Mouse Model of Mild Traumatic Brain Injury. *J Neurotrauma* **33**, 1614-1624, (2016).

7 Webster, S. J., Van Eldik, L. J., Watterson, D. M. & Bachstetter, A. D. Closed head injury in an age-related Alzheimer mouse model leads to an altered neuroinflammatory response and persistent cognitive impairment. *The Journal of neuroscience : the official journal of the Society for Neuroscience* **35**, 6554-6569, (2015).

8 Wendel, K. M. *et al.* Corpus Callosum Vasculature Predicts White Matter Microstructure Abnormalities after Pediatric Mild Traumatic Brain Injury. *J Neurotrauma*, (2018).

9 Emmerich, T. *et al.* Mild TBI Results in a Long-Term Decrease in Circulating Phospholipids in a Mouse Model of Injury. *Neuromolecular medicine* **19**, 122-135, (2017).

10 Han, X. *et al.* In vivo two-photon imaging reveals acute cerebral vascular spasm and microthrombosis after mild traumatic brain injury in mice. *Frontiers in neuroscience* **14**, 210, (2020).

11 Shitaka, Y. *et al.* Repetitive closed-skull traumatic brain injury in mice causes persistent multifocal axonal injury and microglial reactivity. *Journal of Neuropathology & Experimental Neurology* **70**, 551-567, (2011).

12 Velosky, A. G., Tucker, L. B., Fu, A. H., Liu, J. & McCabe, J. T. Cognitive performance of male and female C57BL/6J mice after repetitive concussive brain injuries. *Behavioural brain research* **324**, 115-124, (2017).

13 Mouzon, B. *et al.* Repetitive mild traumatic brain injury in a mouse model produces learning and memory deficits accompanied by histological changes. *Journal of neurotrauma* **29**, 2761-2773, (2012).

14 Lynch, J. R. *et al.* A novel therapeutic derived from apolipoprotein E reduces brain inflammation and improves outcome after closed head injury. *Experimental neurology* **192**, 109-116, (2005).

Chapter 6: It's a Trap! Aldolase-prescribed C_4-deoxyradiofluorination affords intracellular trapping and the tracing of fructose metabolism by PET

Alexia Kirby[1,2], Dominic Graf[2,3], Mojmir Suchy[2,3], Nicholas D. Calvert[2,3], Thomas A. Charlton[2], Robert N. Ben[2], Christina L. Addison[4,5,6], Adam Shuhendler[1,2,3,7]*

[1]Department of Biology, University of Ottawa; Ottawa, ON, Canada. [2]University of Ottawa Heart Institute; Ottawa, ON, Canada. [3]Department of Chemistry and Biomolecular Sciences; University of Ottawa, Ottawa, ON, Canada; [4]Program for Cancer Therapeutics, Ottawa Hospital Research Institute, Ottawa, ON, Canada; [5]Department of Medicine, University of Ottawa, Ottawa, ON, Canada; [6]Department of Biochemsitry, Microbiology and Immunology, University of Ottawa, Ottawa, ON, Canada; [7]Brain and Mind Research Institute, University of Ottawa; Ottawa, ON, Canada.

*Correspondence should be addressed to:

Adam Shuhendler

10 Marie Curie Pvt.

Ottawa, Ontario, Canada

K1N 6N5

adam.shuhendler@uottawa.ca

6.1. Introduction to the Research Article Presented Within this Chapter

While the previous manuscripts have consisted of probe development for aldehydes as biomarkers of inflammation, the paper presented in this chapter takes a different approach to imaging the inflammatory response by targeting the disruption of normal metabolism. Here, a new metabolic radiotracer, [^{18}F]4-FDF, is presented. This radiotracer was developed to complement the current clinical gold standard for cancer imaging, [^{18}F]FDG. [^{18}F]FDG is a radiolabeled glucose analog, that accumulates in tissues with high glycolysis, making it a very useful non-invasive tool for imaging many cancers. However, the signal to noise ratio becomes too large when these cancers are present in organs with high baseline metabolism like the brain and heart, creating a gap in our clinical diagnostic imaging capabilities. Furthermore, the switch to fructose metabolism has been implicated in a wide variety of pathologies, as outlined in chapter 1. Here, we present a radiolabeled fructose analog that accumulates in tissues with high fructolysis. Since baseline levels of fructolysis are low in the brain and heart, [^{18}F]4-FDF may fill the gap that [^{18}F]FDG leaves in clinical metabolic imaging.

6.2. Author Contributions

A.K. conducted all *in vivo* mouse experiments and image analysis. A.K., R.B., C.A., and A.J. conceptualized the study. M.S, D.G., T.C. performed chemical synthesis. N.C. performed cell experiments for metabolomics study. A.K. and A.S. wrote and edited the manuscript.

6.3. Copyright

Reproduced from Ref. ***Journal of Nuclear Medicine*** 65.3 (2024): 475-480.

https://doi.org/10.2967/jnumed.123.266905.

6.4. Abstract

Fructose metabolism has been implicated in various diseases, including metabolic, neurodegenerative, cardiac disorders, and cancer. However, the limited availability of a quantitative imaging radiotracer has hindered its exploration in pathology and diagnostic imaging. In response, we adopted a molecular design strategy based on the catalytic mechanism of aldolase, a key enzyme in fructolysis. We successfully

synthesized a novel radiodeoxyfluorinated fructose analog, [^{18}F]4-fluoro-4-deoxyfructose ([^{18}F]4-FDF), in high molar activity. Through heavy isotope tracing by mass spectrometry, we demonstrated that C_4-deoxyfluorination of fructose led to effective trapping as fluorodeoxysorbitol and fluorodeoxyfructose-1-phosphate *in vitro*, unlike C_1- and C_6-fluorinated analogs that resulted in fluorolactate accumulation. This observation was consistent *in vivo*, where [^{18}F]6-FDF displayed substantial bone uptake due to metabolic processing, while [^{18}F]4-FDF did not. Importantly, [^{18}F]4-FDF exhibited low radiotracer uptake in healthy brain and heart tissues, known for their high glycolytic activity and background levels of [^{18}F]FDG uptake. [^{18}F]4-FDF PET/CT allowed for sensitive mapping of neuro- and cardioinflammatory responses to systemic LPS administration. Our study highlights the significance of aldolase-guided C_4-radiodeoxyfluorination of fructose in enabling effective radiotracer trapping, overcoming limitations of C_1- and C_6-radioanalogs towards a clinically viable tool for imaging fructolysis in highly glycolytic tissues.

Acknowledgments

AJS wishes to acknowledge funding from NSERC (RGPIN- 2021-03387) and the Canada Research Chairs Program (950-230754). CLA and AJS acknowledge funding from the Canadian Cancer Society (grant #707503). Metabolites were analysed at the University of Ottawa Metabolomics Core Facility. This facility is supported by the Terry Fox Foundation and Ottawa University.

Disclosure

No potential conflicts of interest relevant to this article exist.

Key Points

Question: Can fructose metabolism accurately be mapped by PET?

Pertinent Findings: By installing radiofluorine at the C4' position of fructose, fructose metabolism can be accurately mapped due to intracellular trapping of the phosphorylated metabolite. It was found that fructose

utilization was very low in the healthy brain and heart, but elevated in disease, providing an opportunity for imaging neuro- and cardioinflammation.

Implications for Patient Care: The introduction of [^{18}F]-4-fluoro-4-deoxyfructose opens new doors for mapping inflammation in cardiac and neural diseases with a biosimilar radiotracer based on a modified dietary sugar.

6.5. Introduction

The use of fructose as an energy source (i.e. fructolysis) during the onset and progression of a variety of diseases is a continued area of both fundamental and clinical investigation, where inflammation-induced energy crises activate a fructolytic state in the affected tissues. In the heart, the switch from glycolysis to fructolysis has been identified in cardiac hypertrophy[1,2] and myocardial infarction[3], with data supporting a hypoxia-driven activation of this aberrant metabolic program. In the brain, fructolysis is thought to be a putative driver of Alzheimer's disease[4], and has been shown to be pro-inflammatory with negative implications following traumatic injury, stroke injury, and psychological health[5]. The switch from glucose to fructose as energy source may also be a key oncologic driver, promoting the progression of a variety of solid tumors through the concerted transcriptional activation of transport and metabolic machinery[6-10]. Excessive fructose consumption has also been associated with a hepatic-centered metabolic syndrome thought to drive obesity and diabetes[11], and to be a major player in the related cardiovascular[11,12], ocular,[13] and degenerative outcomes[12]. The fundamental importance of fructolysis in a range of diseases has encouraged the development of methods to non-invasively map fructose metabolism, a challenge that is currently an unsolved problem.

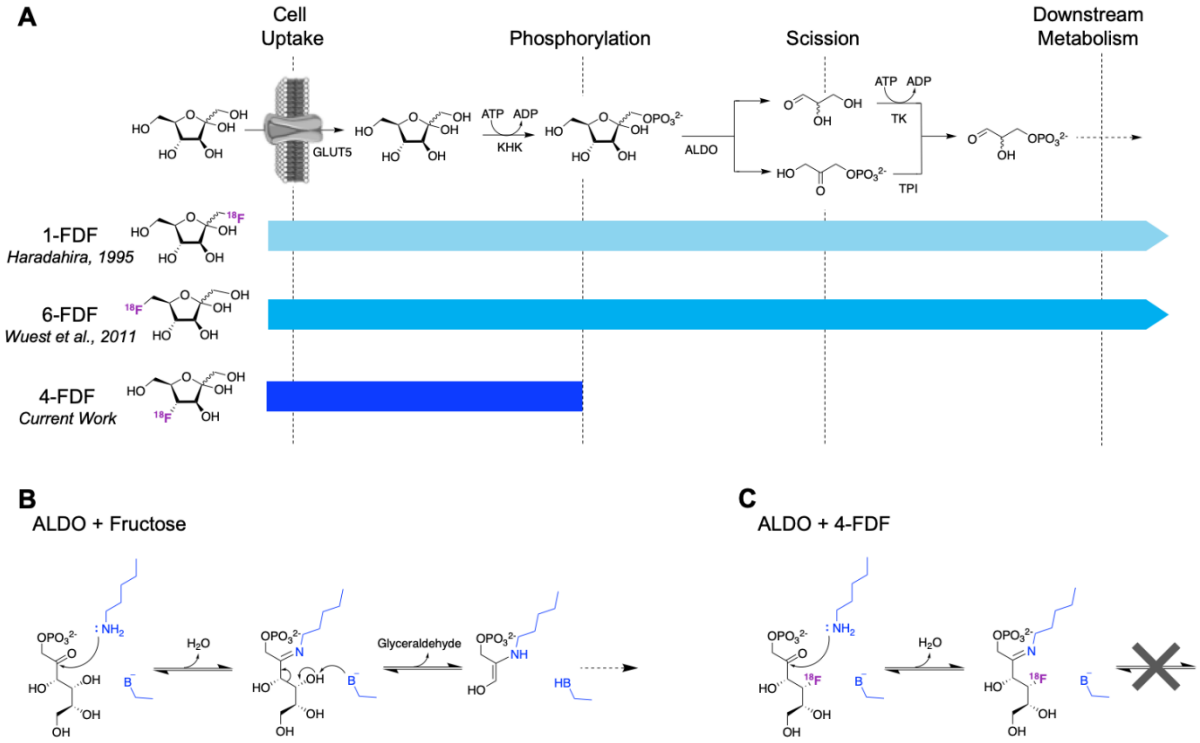

Figure 6.1. Fructose metabolism tracing, then and now. A) The initial metabolism of fructose comprises cell uptake, phosphorylation and scission steps mediated by GLUT5, ketohexokinase (KHK) and aldolase (ALDO), respectively. The proposed progression of existing fructose-derived radiotracers, 1- and 6-FDF, as well as the hypothesized trapping of the proposed 4-FDF are shown. B) The first two steps of the aldolase-mediated scission of fructose is shown. B^-: basic residue; Blue: aldolase active site residue. C) The proposed effect of C_4 deoxyfluorination on the aldolase mechanism. B^-: basic residue; Blue: aldolase active site residue.

Canonical fructose metabolism begins with Glucose Transporter 5 (GLUT5)-mediated transport into the cell and ketohexokinase-mediated trapping of the sugar as fructose-1-phosphate (Fig. 6.1A)[11]. Phosphorylation is followed by carbon chain scission through the activity of aldolase enzymes, and the subsequent formation of glyceraldehyde-3-phosphate that continues to be metabolized downstream. This

metabolic cascade has been followed using non-invasive *in vivo* imaging in preclinical models, taking advantage of the spectroscopic capabilities of deuterium and hyperpolarized magnetic resonance imaging[14,15]. Towards the clinical translational utilization of fructolysis as a quantitative imaging biomarker, previous work has attempted to trace fructose metabolism by positron emission tomography (PET) by installing radiofluorine (^{18}F) at the C_1 or C_6 positions [16-20]. The early metabolic trapping of fructose would lend itself to tracing of aberrant metabolism similarly to [^{18}F]-2-fluoro-2-deoxy-D-glucose ([^{18}F]FDG), the most extensively applied PET nuclear diagnostic used in the clinic. However, the significant bone-derived radioactivity observed by PET from previous radiodeoxyfluorofructose analogs suggest that cellular trapping was not achieved (Fig. 6.1A).

In redesigning a radiofluorinated fructose analog that results in trapping of the phosphorylated metabolite, the catalytic mechanism of aldolase, the enzyme for which fructose-1-phosphate is a substrate, was closely examined (Fig. 6.1B)[21]. Within the aldolase active site, the initial Schiff base formation with the C_2-carbonyl is immediately followed by a base-mediated proton abstraction from the C_4-hydroxyl moiety to induce C-C bond scission. Given the critical role of the C_4-OH in the catalytic mechanism, we hypothesized that the deoxyfluorination of the C_4-position would prevent aldolase-mediated scission (Fig. 6.1C), resulting in the trapping of 4-deoxy-4-fluoro-D-fructose (4-FDF) within the metabolic cell of origin (Fig. 6.1A). Herein we generate 4-FDF, evaluate its metabolic flux *in vitro* relative to 1- and 6-FDF, and compare the PET imaging of [^{18}F]4-FDF to [^{18}F]6-FDF and [^{18}F]FDG in tracing metabolism in mouse models of cancer and systemic inflammation.

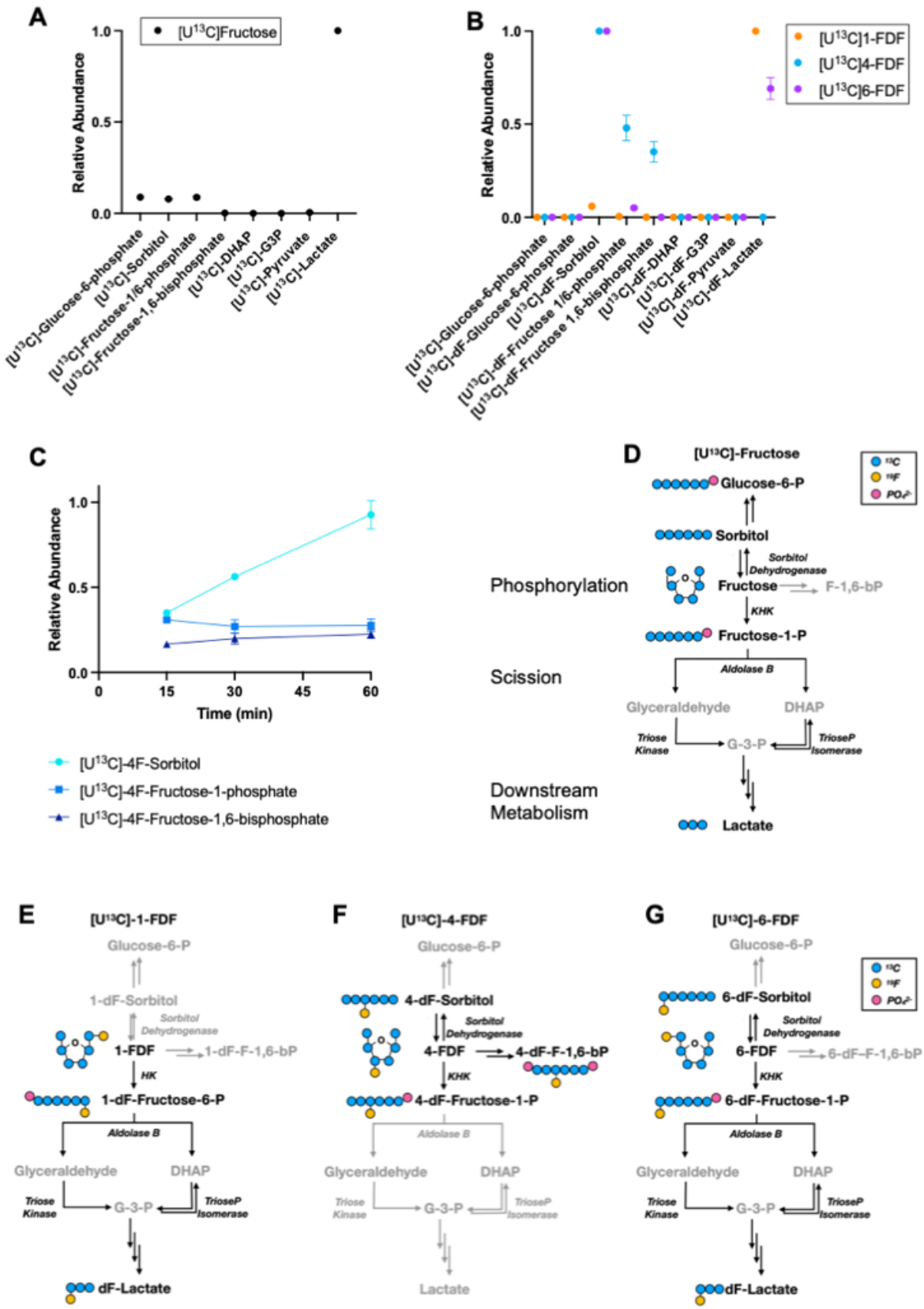
A
[U13C]Fructose
Relative Abundance
1.0
0.5
0.0
[U13C]-Glucose-6-phosphate
[U13C]-Sorbitol
[U13C]-Fructose-1/6-phosphate
[15C]-Fructose-1,6-bisphosphate
[U13C]-DHAP
[U13C]-G3P
[U13C]-Pyruvate
[U13C]-Lactate
B
[U13C]1-FDF
[U13C]4-FDF
[U13C]6-FDF
Relative Abundance
[U13C]-Glucose-6-phosphate
[U13C]-dF-Glucose-6-phosphate
[U13C]-dF-Sorbitol
[U13C]-dF-Fructose 1/6-phosphate
[U13C]-dF-Fructose 1,6-bisphosphate
[U13C]-dF-DHAP
[U13C]-dF-G3P
[U13C]-dF-Pyruvate
[U13C]-dF-Lactate
C
Relative Abundance
1.0
0.5
0.0
0
15
30
45
60
Time (min)
[U13C]-4F-Sorbitol
[U13C]-4F-Fructose-1-phosphate
[U13C]-4F-Fructose-1,6-bisphosphate
D
[U13C]-Fructose
Glucose-6-P
Sorbitol
Sorbitol Dehydrogenase
Fructose
F-1,6-bP
KHK
Fructose-1-P
Aldolase B
Glyceraldehyde
DHAP
Triose Kinase
G-3-P
TrioseP Isomerase
Lactate
Phosphorylation
Scission
Downstream Metabolism
E
[U13C]-1-FDF
Glucose-6-P
1-dF-Sorbitol
Sorbitol Dehydrogenase
1-FDF
1-dF-F-1,6-bP
HK
1-dF-Fructose-6-P
Aldolase B
Glyceraldehyde
DHAP
Triose Kinase
G-3-P
TrioseP Isomerase
dF-Lactate
F
[U13C]-4-FDF
Glucose-6-P
4-dF-Sorbitol
Sorbitol Dehydrogenase
4-FDF
4-dF-F-1,6-bP
KHK
4-dF-Fructose-1-P
Aldolase B
Glyceraldehyde
DHAP
Triose Kinase
G-3-P
TrioseP Isomerase
Lactate
G
[U13C]-6-FDF
Glucose-6-P
6-dF-Sorbitol
Sorbitol Dehydrogenase
6-FDF
6-dF-F-1,6-bP
KHK
6-dF-Fructose-1-P
Aldolase B
Glyceraldehyde
DHAP
Triose Kinase
G-3-P
TrioseP Isomerase
dF-Lactate

Figure 6.2. Decoding the positional effects of fructose deoxyfluorination on its metabolism *in vitro* in HepG2 cells by mass spectrometry. The relative abundance of metabolites from isotopically labelled [U^{13}C]-fructose (A) and [U^{13}C]-1- (orange), [U^{13}C]-4- (blue), and [U^{13}C]-6-FDF (purple). C) Time course of metabolite generation from [U^{13}C]-4-FDF. Metabolism schemes based on mass spectrometry results for [U^{13}C]-fructose (D), [U^{13}C]-1- (E), [U^{13}C]-4- (F), and [U^{13}C]-6-FDF (G). Light grey: undetected metabolite or pathway; Black: detected metabolite or pathway; Blue circle: ^{13}C, Yellow circle: ^{19}F, Pink circle: PO_4^{2-}.

6.6. Materials & Methods

5.6.1. Synthesis.

All synthetic procedures are described in detail in the Supplemental Information.

6.6.2. *In vitro* Metabolic Tracing.

All procedures for metabolic tracing of [U^{13}C]-fructose analogs are provided in the Supplementary Information

6.6.3. Animal Models.

All animal research was approved by the IACUC of uOttawa under AUP SCe-3254-R3 (tumor study) and SCe-4019-A1 (inflammation study). Mice were housed in standard cages, kept on a 12-hr light/dark cycle and provided standard rodent chow and water *ad libitum*.

Eight week-old female nu/nu mice were inoculated with 10x10^6 HepG2 cells suspended in 50% Matrigel:DMEM *subcutaneously* under the left shoulder. Within 3-weeks of implantation, mice were imaged by PET/CT.

Eight week old male C57Bl6 mice received 5 mg/kg LPS through *intraperitoneal* injection 24-hr prior to planned PET/CT imaging. Mice were supported by being warmed, and by being given fluids *subcutaneously* 12 hr after LPS injection. The mice were monitored and scored for severity of response to LPS as published previously[22]

6.6.4. PET/CT Imaging.

PET/CT imaging was carried out on a Bruker Si78PET/CT scanner with a 4-position hotel having adjustable isoflurane and respiratory monitoring for each position (Bruker USA). Tail veins were catheterized, and an anatomical CT was acquired over the whole of the mouse bodies using the “rat” settings. PET acquisition was started just prior to a bolus *i.v.* injection of approximately 7.4 MBq of radiotracer. Dynamic scans were acquired in list mode format over 45 min, and sorted into 16 × 0.5-mm sinogram bins for image reconstruction (4 × 15 s, 4 × 60 s and 8 × 300 s). Iterative reconstruction was performed using 3D ordered-

subsets expectation maximization (3D-OSEM) followed by fast maximum *a posteriori* (fastMAP) using Paravision 360 software v.3.4 (Bruker, USA). Four-mouse images were split into individual mice, and the bed was removed using PMOD v (Bruker, USA). VivoQuant v.2022 (InviCRO) was used for visualization of radioradiotracer uptake in tissues, to define the three-dimensional (3D) volumes of interest (VOI) and for 3D-visualisation to create volume rendering technique images. The count densities were averaged for all volumes of interest at each time point to obtain a time versus activity curve (TAC). Tumor and tissue TACs were normalized to injected dose, measured by a CRC-15 PET dose calibrator (Capintec, Inc., NJ, USA), and expressed as percentage injected dose per cubic centimeter of tissue (%ID/cc).

6.6.5. Statistical Analyses.

Statistical analyses were performed using Prism (v. 9.5.0, GraphPad, Inc.). Comparisons across more than two groups was performed by one-way ANOVA followed by Tukey's test for honestly significant differences. Normality was assumed where appropriate for all data sets. Prior to ANOVA, Levene's test was used to confirm equal variance, and visual quantile-quantile plot analysis was used to confirm homoscedasticity.

6.7. Results

In order to characterize the structure-activity effect of fructose deoxyfluorination on metabolic flux, we evaluated the metabolism of isotopically labelled [U^{13}C]-fructose, and [U^{13}C]-1-, [U^{13}C]-6-, and [U^{13}C]-4-FDF deoxyfluorinated fructose analogs *in vitro* in HepG2 human hepatocarcinoma cells by mass spectrometry (Fig. 6.2). HepG2 were chosen as a model cell line due to a recent report by Tee *et al*. outlining their propensity for fructolysis[23]. [U^{13}C]-1- and [U^{13}C]-6-FDF were synthesized according to previously published methods[16,17], and [U^{13}C]-4-FDF was synthesized as described in the supporting information. After confirming that [U^{13}C]-fructose was metabolized as expected through both fructolytic and polyol pathways to establish a baseline for tracing fructose metabolism (Fig. 6.2A), we next examined the relative flux of the deoxyfluorinated analogs (Fig. 6.2B). [U^{13}C]-1-FDF showed limited metabolism through the polyol pathway, with the majority of the ^{13}C-labelled cellular product being [U^{13}C]-deoxyfluorolactate (Fig.

6.2B, orange). Of critical importance, however, is that while [U^{13}C]-6-FDF metabolism resulted in a substantial amount of [U^{13}C]-deoxyfluorolactate production as a result of proceeding through scission and downstream metabolism (Fig.6.2B, purple), [U^{13}C]-4-FDF metabolism halted at [U^{13}C]-4-fluorodeoxy-1-phosphate, the fructolytic metabolite that is the substrate for aldolase-mediated scission (Fig. 6.2B, blue). Uniquely, [U^{13}C]-4-FDF metabolism also resulted in the accumulation of [U^{13}C]-4-fluorodeoxyfructose-1,6-bisphophate. A key outcome of this experiment was the confirmation that all deoxyfluorinated analogs of fructose entered the cells rapidly (within 30 min). To validate the observed metabolite trapping, a time course evaluation of [U^{13}C]-4-FDF metabolism was performed over 60 min, demonstrating the steady-state accumulation of [U^{13}C]-4-fluorodeoxyfructose-1-phosphate and [U^{13}C]-4-fluorodeoxyfructose-1,6-bisphosphate, and increase in [U^{13}C]-4-fluorodeoxysorbitol throughout the 60 min of incubation (Fig. 6.2C). The results of this study support our hypothesis that, like native fructose (Fig. 6.2D) neither [U^{13}C]-1- (Fig. 6.2E) nor [U^{13}C]-6-FDF are metabolically trapped (Fig. 6.2G), but that the deoxyfluorination of fructose at C_4 prevents aldolase-mediated hexose scission and traps the deoxyfluorinated fructose analog in the cell (Fig. 6.2F). By rethinking the site of deoxyfluorination to afford metabolic trapping as informed by the catalytic mechanism of the enzyme immediately ensuing to the intended trapped metabolite, the chemical requirements for mapping fructolysis were uncovered.

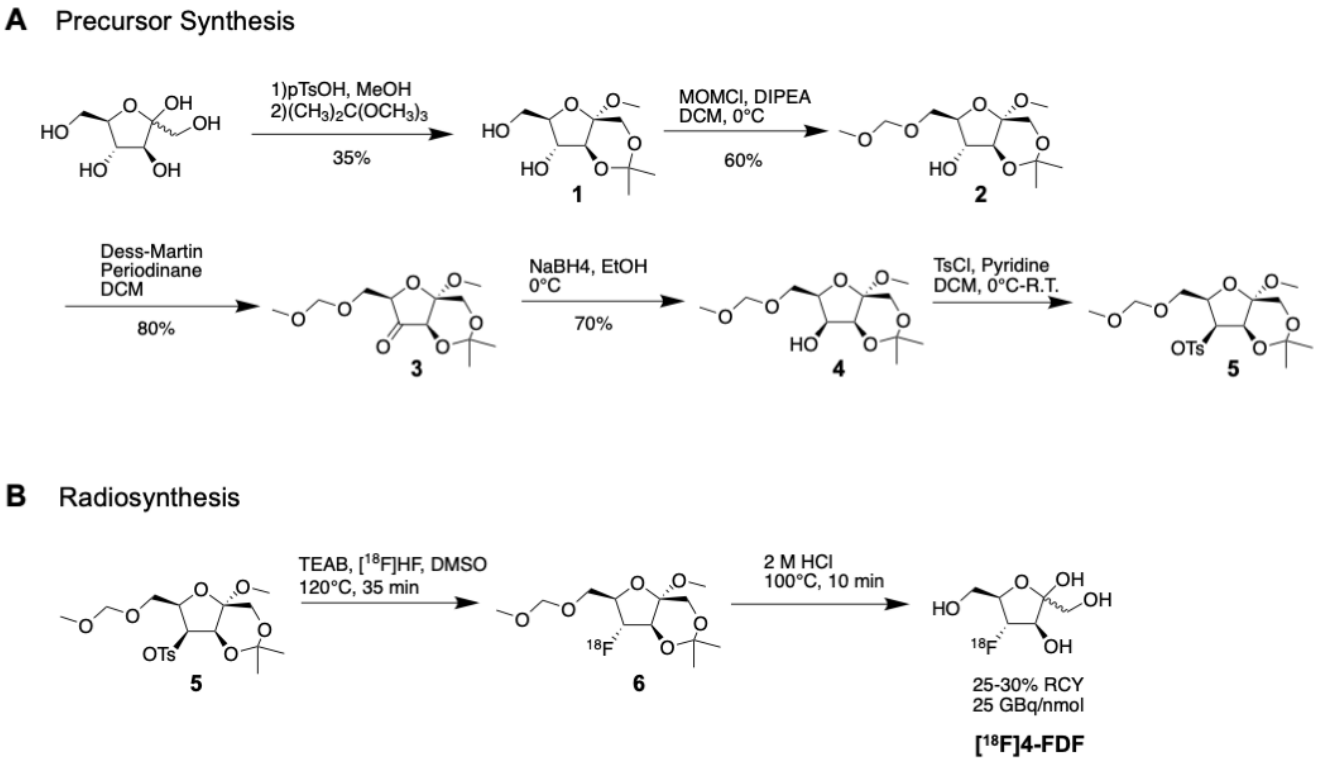

Figure 6.3. Synthesis of (A) the radiochemical precursor and (B) the final radiofluorinated [^{18}F]4-FDF.

In order to proceed towards fructolysis mapping *in vivo* by PET, a radiodeoxyfluorination approach was designed to afford nucleophilic substitution at the C_4 position using standard radiochemical techniques somewhat related to the routine production of [^{18}F]FDG. Details of the synthesis of compounds **1**-**4** have been reported previously[24], and further synthetic steps and chemical characterization for compounds **5**, **6**, and [^{18}F]4-FDF are provided in the supporting information (Supplemental schemes 1-5 and Supplemental Figures. 3-232). The precursor synthesis began with C_1-OH methylation and dimethyl ketalation of C_2-OH and C_3-OH, followed by the protection of C_6-OH with chloromethyl methyl ether (MOM Cl) in order to isolate the C_4-OH (Fig. 6.1A). The stereochemistry at C_4 was then inverted in two steps, and was converted to the tosylated precursor **5** (Fig. 6.1A). The C_4-stereoinversion was necessary to allow the subsequent radiodeoxyfluorination step to restore the C_4-D-enantiomer after the [^{18}F]TEAF-mediated nucleophilic

attack (Fig. 6.1B, **6**). Rapid on-module deprotection resulted in [^{18}F]4-FDF in good radiochemical yield (25-30%) and molar activity (25.3±0.6 GBq/nmol) comparable to that resulting from the routine production of [^{18}F]FDG[25].

With the confirmation of cell uptake and intracellular trapping of [U^{13}C]4-FDF, and the successful production of the radiofluorinated analog, the biodistribution of [^{18}F]4-FDF was evaluated in a heterotopic HepG2 xenograft mouse model and compared to the biodistribution of [^{18}F]6-FDF and [^{18}F]FDG (Fig. 6.4). [^{18}F]1-FDF was not evaluated *in vivo* since it was already demonstrated to be poorly retained in cells *in vitro* and *in vivo*[18]. Following *intravenous* injection, [^{18}F]4-FDF was found to accumulate in the tumor, with renal exceeding hepatobiliary excretion (Fig. 6.4A). This pattern of radiotracer retention was similarly observed for [^{18}F]6-FDF, with a key difference, however, being bone uptake (Fig. 6.4B). While any bone uptake was limited to <2 %ID/g for [^{18}F]4-FDF (Fig. 6.4A and Supplementary Figure 2), bone uptake was 3.69-fold higher (>7 %ID/g) following [^{18}F]6-FDF imaging (Fig. 6.4B and D). This extensive bone uptake, which continues to increase over time (Fig. S6.1), was reported previously for [^{18}F]6-FDF[17], and is supported by the metabolic flux outcomes of [U^{13}C]6-FDF demonstrating the production of [U^{13}C]fluorodeoxylactate (Fig. 6.2B and G).

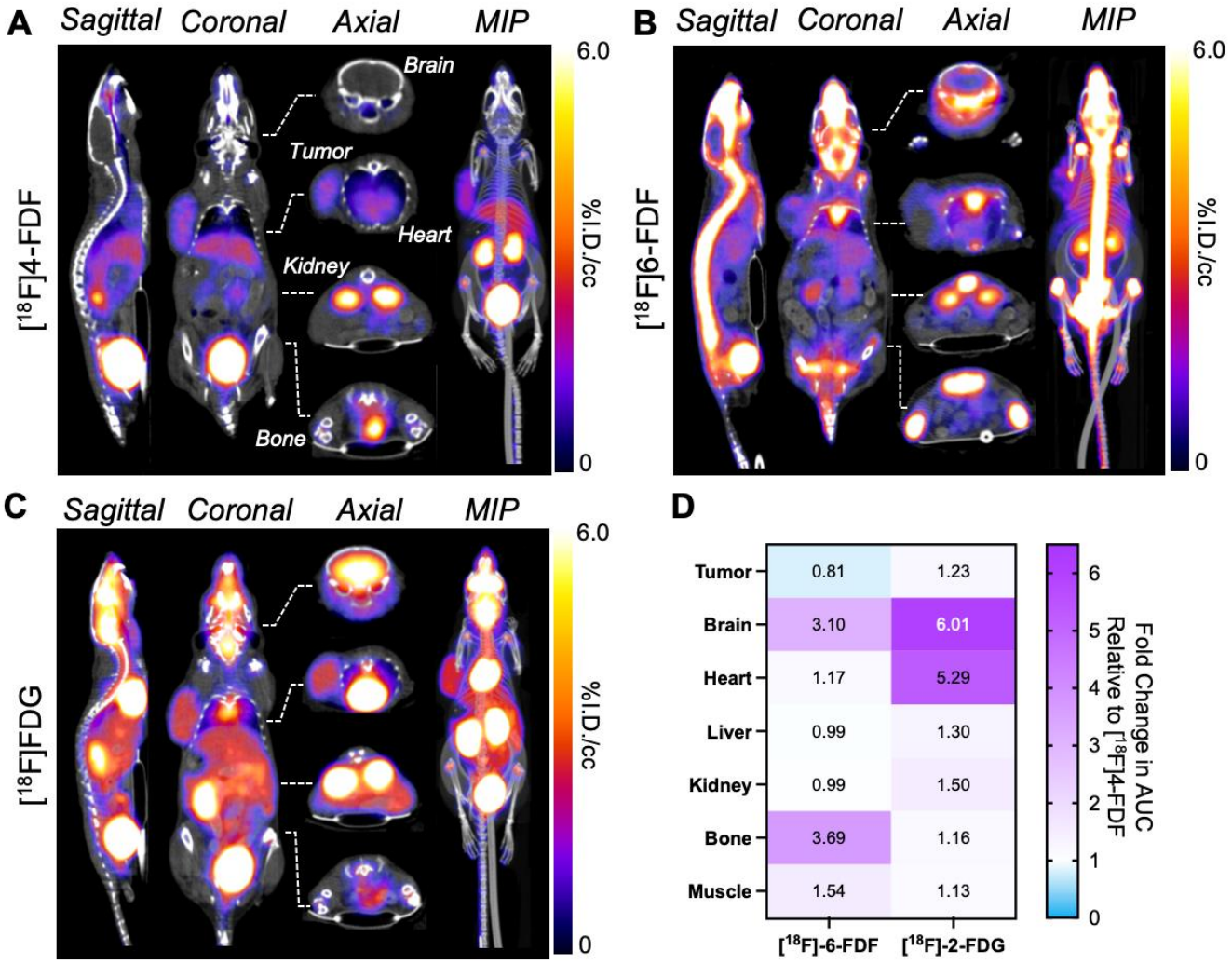

Figure 6.4. Comparative PET/CT imaging in a heterotopic HepG2 xenograft mouse model. PET/CT images shown are the summed images from 20-45 min after intravenous injection of (A) [^{18}F]4-FDF, (B) [^{18}F]6-FDF, or (C) [^{18}F]FDG. Sagittal, coronal, and maximum intensity projection (MIP) are show, in addition to axial sections at the level of the brain, heart, liver/kidneys, and hips. D) The fold change in area under the curve (AUC) for the entire time-activity curve in Fig. S5.2 are shown for [^{18}F]6-FDF and [^{18}F] FDG normalized to the values for [^{18}F]4-FDF. Purple represents an increase in AUC and blue represents a decrease in AUC. The values are normalized fold-change in AUC.

Overall, the accumulation of [^{18}F]4-FDF in normal mouse tissues was lower than that observed with [^{18}F]FDG (Fig. 6.4A *vs. 6*.4C). Notably, the area under the time activity curve (AUC) for [^{18}F]FDG in the brain and heart was 6.01- and 5.29-fold greater, respectively, than for [^{18}F]4-FDF (Fig. 6.3D), suggesting that healthy brain and heart have a limited dependence on fructolysis for energy production. In order to further investigate whether a fructolytic switch occurs in inflammatory neural and cardiac tissues, as previously proposed[1-5,12], a mouse model of systemic inflammation was examined (Fig. 6.5). Mice receiving saline vehicle (Fig. 6.5A) or *intraperitoneal* bacterial cell wall lipopolysaccharide (LPS), as previously described (Fig. 6.5B)[22], were imaged by [^{18}F]4-FDF PET/CT 24 hr after injection. A significant increase in cardiac (Fig. 6.5D and F) and brain (Fig. 6.5C and F) uptake of [^{18}F]4-FDF was observed following LPS treatment in all mice evaluated. Both the brain and heart demonstrate inflammatory responses to LPS stimulation within 24 hr of its systemic introduction, mediated through toll-like receptor engagement on microglia or cardiac adrenergic cells[26,27]. The low uptake of [^{18}F]4-FDF in healthy brain and heart contributed to an increased signal-to-noise ratio for the mapping of cardio- and neuroinflammation (Fig. 6.5C and D).

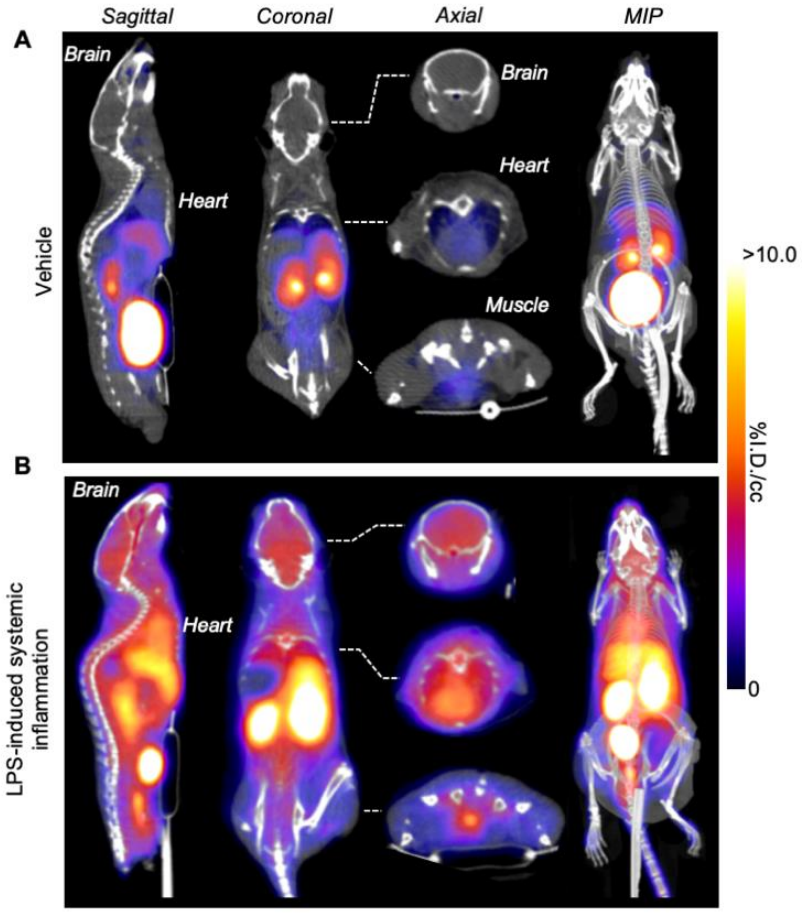
Sagittal
Coronal
Axial
MIP
A
Brain
Heart
Vehicle
Brain
Heart
Muscle
>10.0
%I.D./cc
0
B
Brain
Heart
LPS-induced systemic inflammation

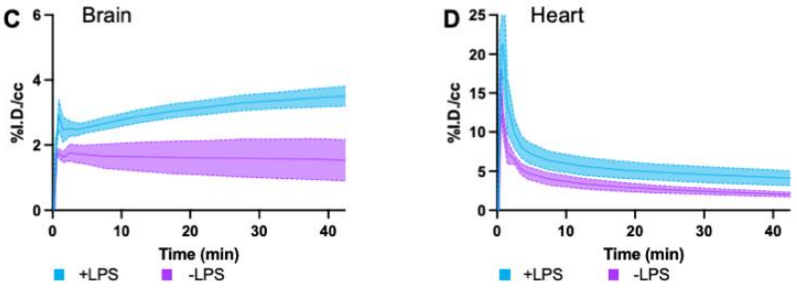
C
Brain
%I.D./cc
Time (min)
+LPS
-LPS
D
Heart
%I.D./cc
Time (min)
+LPS
-LPS

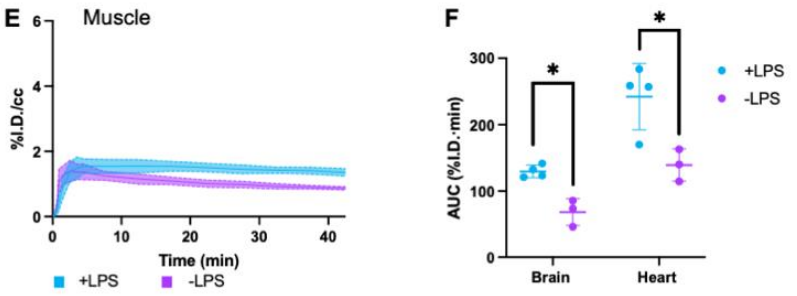
E
Muscle
%I.D./cc
Time (min)
+LPS
-LPS
F
AUC (%I.D.·min)
Brain
Heart
+LPS
-LPS

Figure 6.5. Imaging inflammation in the brain and heart. [^{18}F]4-FDF PET/CT was performed on mice receiving vehicle (A) or bacterial cell wall LPS (B) 24 hr after injection. Sagittal, coronal, MIP, and axial sections of the brain, heart and muscle are shown. Time-activity curves (TAC) for brain (C), heart (D), and muscle (E) are shown for mice receiving vehicle (-LPS, purple) or LPS (+LPS, blue). Solid lines are the means and shaded region are standard deviation. F) Comparison of TAC AUC values for brain and heart ROIs for mice receiving vehicle (-LPS, purple) or LPS (+LPS, blue. Plots shows individual data points (circles), mean (long line) and s.d. (vertical line). * $p<0.05$ by ANOVA followed by Tukey's test.

6.8. Discussion

While the pathological switch to fructose metabolism has been implicated in a variety of metabolic, neurodegenerative and cardiac diseases, as well as a driver and/or consequence of malignancy, the evaluation of fructolysis in fundamental mechanisms of pathology and its implementation as a diagnostic imaging biomarker has been limited by the lack of a quantitative radiotracer for imaging-based analysis. Taking a molecular design approach informed by the catalytic mechanism of aldolase, the fructolytic enzyme whose activity must be blocked in order to afford metabolic trapping, we synthesized a novel radiodeoxyfluorinated analog of fructose: [^{18}F]4-FDF. Radiosynthesis was realised on a standard radiofluorination module in good yield and molar activity, mimicking the nucleophilic radiofluorination and acid-catalyzed deprotection used for the preparation of [^{18}F]FDG (Fg. 6.3).

As compared to previously reported C_1- and C_6-radioanalogs of fructose, using heavy isotope tracing by mass spectrometry we demonstrated that the C_4-deoxyfluorination of fructose led to trapping as fluorodeoxysorbitol and fluorodeoxyfructose-1-phosphate *in vitro* (Fig. 6.2). Key differences in polyol pathway flux was also observed between the different fluorinated positional isomers. The limited polyol flux observed for C_1-fluorodeoxyfructose is likely the result of improper substrate positioning in the sorbitol dehydrogenase active site by the deoxyfluorination of C_1, which prevents a critical C_1-OH-to-Zn interaction[28]. In contrast, both [U^{13}C]-6- and [U^{13}C]-4-FDF were capable of proceeding through the polyol

pathway, but did not form detectable amounts of glucose-6-phosphate (Fig. 6.2B, purple and blue, respectively). The arrest at [U^{13}C]-4/6-fluorodeoxysorbitol could be the result of the reduction of aldose reductase activity either through active site water displacement or catalytically detrimental interactions with the active site-adjacent specificity pocket[29,30]. Notably, neither the C_1- nor C_6-fluorinated analogs led to trapping, but rather proceeded through fructolysis to produce fluorolactate. This result was recapitulated *in vivo*, where [^{18}F]6-FDF showed significant bone uptake that was a result of metabolic processing, but which was not observed using [^{18}F]4-FDF (Fig. 6.4).

Our metabolic tracing studies suggest that the bone uptake observed with [^{18}F]6-FDF imaging *in vivo* (Fig. 6.4) may not be the result of tumor cell-induced defluorination, but rather the formation of lactate (Fig. 6.2). Lactate is actively pumped out of tumor cells by influx/efflux monocarboxylate transporters MCT1 and MCT4, which contributes to the acidic tumor microenvironment that is a hallmark of solid tumors[31,32]. The direct mechanism of radiofluorinated metabolite uptake by bone remains to be uncovered, however it is known that osteoblasts express MCT1 and actively take up lactate[33-35]. Additionally, extra-tumoral metabolism may also contribute to radioactivity uptake in the bone, as hepatic lactate metabolism through lactate dehydrogenase can result in the production of pyruvate with a potential for defluorination[36]. By any mechanism, both *in vitro* and *in vivo* data demonstrate that radiodeoxyfluorination of fructose at C_4, but not C_6, can subvert cellular radiometabolite loss and bone accumulation.

An important outcome of the stable tracing of fructolysis afforded by [^{18}F]4-FDF was the observation of very low radiotracer uptake in healthy brain and heart (Fig. 6.5), tissues that are highly glycolytic and associated with high background levels of [^{18}F]FDG uptake (Fig. 6.4). The low fructolytic background rates in these tissues afforded the sensitive mapping of the neuro- and cardioinflammatory response to systemic LPS administration by [^{18}F]4-FDF (Fig. 6.5). Therefore, the aldolase-prescribed C_4-radiodeoxyfluorination of fructose resulted in radiotracer trapping upon intracellular uptake and phosphorylation (Fig. 6.1), overcoming limitations to fructolysis tracing by C_1- and C_6-radioanalogs.

While [^{18}F]FDG is used clinically to map glucose uptake for diagnostic imaging of traumatic brain injury[37], dementia[38], and Alzheimer's Disease[39], the estimation of neuroinflammation by [^{18}F]FDG PET is difficult as physiological glucose uptake may obscure inflammation-specific signal. The presence of inflammatory cells can mask metabolic deficits in neurodegenerative diseases, hindering the use of glucose consumption as a biomarker in these cases[40]. Neuronal [^{18}F]FDG uptake in an LPS-treated mouse therefore does not necessarily reflect metabolic state or neuronal damage, as microglial activation and immune cell infiltration confound uptake[41]. [^{18}F]FDG-PET may also be used for diagnostic imaging of cardiopulmonary inflammation[42] and infection[43], and atherosclerosis, however, efforts must be made to minimize myocardial glucose metabolism prior to imaging to reduce false-positive rate due to low signal-to-noise ratio[44,45]. These efforts rely on a diet-based metabolic switch from glucose to free fatty acids, relying heavily on patient-compliance. The low brain and heart uptake in healthy, unfasted mice described herein make fructose metabolism an attractive biomarker in tissues that are otherwise highly glycolytic, and have high [^{18}F]FDG uptake in the absence of disease.

6.9. Conclusion

The metabolic flux of deoxyfluorofructose was characterized heavy isotope labelling. [U^{13}C]-1-FDF exhibited limited polyol metabolism, while both [U^{13}C]-6-FDF and [U^{13}C]-4-FDF showed polyol pathway involvement. Only [U^{13}C]-4-FDF metabolism halted at [U^{13}C]-4-fluorodeoxyfructose-1-phosphate, supporting its unique ability to be trapped within cells. [^{18}F]4-FDF was synthesized with good molar activity and radiochemical yield. In a HepG2 xenograft mouse model, [^{18}F]4-FDF exhibited tumor accumulation with minimal bone uptake, whereas [^{18}F]6-FDF displayed substantial bone retention. [^{18}F]4-FDF displayed lower accumulation in normal mouse tissues than [^{18}F]FDG, notably in the brain and heart. As a result, a significant increase in [^{18}F]4-FDF uptake in cardiac and brain tissues was observed after LPS treatment, highlighting the potential of [^{18}F]4-FDF PET/CT for sensitive mapping of cardio- and neuroinflammation in highly glycolytic tissues. Overall, this research provides critical insights into the metabolic fate of deoxyfluorinated fructose analogs and demonstrates the potential of [^{18}F]4-FDF for mapping disease and/or

injury involving cardio- and neuroinflammation. With the ability to safely and effectively map fructolysis in mice, and low uptake in healthy tissues compared to [^{18}F]FDG, [^{18}F]4-FDF offers a clinically viable tool for diagnostic imaging of tissues with a high baseline glycolytic index. As dosimetry is not expected to be limiting, the clinical translation of this biosimilar radiotracer is feasible.

6.9. References

1 Mirtschink, P. *et al.* HIF-driven SF3B1 induces KHK-C to enforce fructolysis and heart disease. *Nature* **522**, 444-449, (2015).

2 Mirtschink, P., Jang, C., Arany, Z. & Krek, W. Fructose metabolism, cardiometabolic risk, and the epidemic of coronary artery disease. *European heart journal* **39**, 2497-2505, (2018).

3 Williams, A. L. *et al.* HIF1 mediates a switch in pyruvate kinase isoforms after myocardial infarction. *Physiological genomics* **50**, 479-494, (2018).

4 Johnson, R. J. *et al.* Cerebral fructose metabolism as a potential mechanism driving Alzheimer's disease. *Frontiers in aging neuroscience* **12**, 299, (2020).

5 Spagnuolo, M. S., Iossa, S. & Cigliano, L. Sweet but bitter: Focus on fructose impact on brain function in rodent models. *Nutrients* **13**, 1, (2020).

6 Chen, C. *et al.* ATF4-dependent fructolysis fuels growth of glioblastoma multiforme. *Nature Communications* **13**, 6108, (2022).

7 Liu, H. *et al.* Fructose induces transketolase flux to promote pancreatic cancer growth. *Cancer research* **70**, 6368-6376, (2010).

8 Helsley, R. N. *et al.* Ketohexokinase-C regulates global protein acetylation to decrease carnitine palmitoyltransferase 1a-mediated fatty acid oxidation. *Journal of Hepatology* **79**, 25-42, (2023).

9 Ward, P. S. & Thompson, C. B. Metabolic reprogramming: a cancer hallmark even warburg did not anticipate. *Cancer cell* **21**, 297-308, (2012).

10 Song, A., Mao, Y. & Wei, H. GLUT5: structure, functions, diseases and potential applications. *Acta Biochimica et Biophysica Sinica* **55**, 1519, (2023).

11 Hannou, S. A., Haslam, D. E., McKeown, N. M. & Herman, M. A. Fructose metabolism and metabolic disease. *The Journal of clinical investigation* **128**, 545-555, (2018).

12 Kolderup, A. & Svihus, B. Fructose metabolism and relation to atherosclerosis, type 2 diabetes, and obesity. *Journal of nutrition and metabolism* **2015**, (2015).

13 Harder, J. M. *et al.* Disturbed glucose and pyruvate metabolism in glaucoma with neuroprotection by pyruvate or rapamycin. *Proceedings of the National Academy of Sciences* **117**, 33619-33627, (2020).

14 Keshari, K. R. *et al.* Hyperpolarized [2-13C]-fructose: a hemiketal DNP substrate for in vivo metabolic imaging. *Journal of the American Chemical Society* **131**, 17591-17596, (2009).

15 Zhang, G. *et al.* [6, 6′-2H2] fructose as a deuterium metabolic imaging probe in liver cancer. *NMR in Biomedicine*, e4989, (2023).

16 Haradahira, T. *et al.* Radiosynthesis, rodent biodistribution, and metabolism of 1-deoxy-1-[18F] fluoro-D-fructose. *Nuclear medicine and biology* **22**, 719-725, (1995).

17 Wuest, M. *et al.* Radiopharmacological evaluation of 6-deoxy-6-[18F] fluoro-D-fructose as a radiotracer for PET imaging of GLUT5 in breast cancer. *Nuclear medicine and biology* **38**, 461-475, (2011).

18 Wuest, M. *et al.* Molecular imaging of GLUT1 and GLUT5 in breast cancer: a multitracer positron emission tomography imaging study in mice. *Molecular pharmacology* **93**, 79-89, (2018).

19 Bouvet, V. *et al.* Automated synthesis and dosimetry of 6-deoxy-6-[18F] fluoro-D-fructose (6-[18F] FDF): A radiotracer for imaging of GLUT5 in breast cancer. *American Journal of Nuclear Medicine and Molecular Imaging* **4**, 248, (2014).

20 Boyle, A. J. *et al.* PET Imaging of Fructose Metabolism in a Rodent Model of Neuroinflammation with 6-[18F] fluoro-6-deoxy-D-fructose. *Molecules* **27**, 8529, (2022).

21 Fushinobu, S., Nishimasu, H., Hattori, D., Song, H.-J. & Wakagi, T. Structural basis for the bifunctionality of fructose-1, 6-bisphosphate aldolase/phosphatase. *Nature* **478**, 538-541, (2011).

22 Shrum, B. *et al.* A robust scoring system to evaluate sepsis severity in an animal model. *BMC research notes* **7**, 1-11, (2014).

23 Tee, S. S. *et al.* Ketohexokinase-mediated fructose metabolism is lost in hepatocellular carcinoma and can be leveraged for metabolic imaging. *Science Advances* **8**, eabm7985, (2022).
24 Suchý, M., Charlton, T. A., Ben, R. N. & Shuhendler, A. J. Synthesis of natural/13C-enriched d-tagatose from natural/13C-enriched d-fructose. *Carbohydrate Research* **507**, 108377, (2021).
25 Luurtsema, G. *et al.* EANM guideline for harmonisation on molar activity or specific activity of radiopharmaceuticals: impact on safety and imaging quality. *EJNMMI Radiopharmacy and Chemistry* **6**, 1-16, (2021).
26 Yang, D. *et al.* Intrinsic cardiac adrenergic cells contribute to LPS-induced myocardial dysfunction. *Communications Biology* **5**, 96, (2022).
27 Batista, C. R. A., Gomes, G. F., Candelario-Jalil, E., Fiebich, B. L. & De Oliveira, A. C. P. Lipopolysaccharide-induced neuroinflammation as a bridge to understand neurodegeneration. *International journal of molecular sciences* **20**, 2293, (2019).
28 Pauly, T. A. *et al.* X-ray crystallographic and kinetic studies of human sorbitol dehydrogenase. *Structure* **11**, 1071-1085, (2003).
29 Rechlin, C. *et al.* Price for opening the transient specificity pocket in human aldose reductase upon ligand binding: structural, thermodynamic, kinetic, and computational analysis. *ACS Chemical Biology* **12**, 1397-1415, (2017).
30 Sandner, A. *et al.* Which Properties Allow Ligands to Open and Bind to the Transient Binding Pocket of Human Aldose Reductase? *Biomolecules* **11**, 1837, (2021).
31 Pérez-Tomás, R. & Pérez-Guillén, I. Lactate in the tumor microenvironment: An essential molecule in cancer progression and treatment. *Cancers* **12**, 3244, (2020).
32 Wang, Z.-H., Peng, W.-B., Zhang, P., Yang, X.-P. & Zhou, Q. Lactate in the tumour microenvironment: From immune modulation to therapy. *EBioMedicine* **73**, (2021).
33 Sasa, K. *et al.* Monocarboxylate transporter-1 promotes osteoblast differentiation via suppression of p53, a negative regulator of osteoblast differentiation. *Scientific Reports* **8**, 10579, (2018).
34 Luo, Y. *et al.* Lactate inhibits osteogenic differentiation of human periodontal ligament stem cells via autophagy through the MCT1-mTOR signaling pathway. *Bone* **162**, 116444, (2022).
35 Zhu, Z. *et al.* Lactate Mediates the Bone Anabolic Effect of High-Intensity Interval Training by Inducing Osteoblast Differentiation. *JBJS* **105**, 369-379, (2023).
36 Rabinowitz, J. D. & Enerbäck, S. Lactate: the ugly duckling of energy metabolism. *Nature metabolism* **2**, 566-571, (2020).
37 Jassam, Y. N., Izzy, S., Whalen, M., McGavern, D. B. & El Khoury, J. Neuroimmunology of traumatic brain injury: time for a paradigm shift. *Neuron* **95**, 1246-1265, (2017).
38 Kato, T., Inui, Y., Nakamura, A. & Ito, K. Brain fluorodeoxyglucose (FDG) PET in dementia. *Ageing research reviews* **30**, 73-84, (2016).
39 Marcus, C., Mena, E. & Subramaniam, R. M. Brain PET in the diagnosis of Alzheimer's disease. *Clinical nuclear medicine* **39**, e413, (2014).
40 Backes, H. *et al.* Glucose consumption of inflammatory cells masks metabolic deficits in the brain. *Neuroimage* **128**, 54-62, (2016).
41 Szöllősi, D. *et al.* Evaluation of brain nuclear medicine imaging tracers in a murine model of sepsis-associated encephalopathy. *Molecular imaging and biology* **20**, 952-962, (2018).
42 Bertagna, F. *et al.* Possible role of F18-FDG-PET/CT in the diagnosis of endocarditis: preliminary evidence from a review of the literature. *The International Journal of Cardiovascular Imaging* **28**, 1417-1425, (2012).
43 Eibschutz, L. S. *et al.* in *Seminars in nuclear medicine.* 61-70 (Elsevier).
44 Cusso, L., Vaquero, J. J., Bacharach, S. & Desco, M. Comparison of methods to reduce myocardial 18F-FDG uptake in mice: calcium channel blockers versus high-fat diets. *PLoS One* **9**, e107999, (2014).
45 Wykrzykowska, J. *et al.* Imaging of inflamed and vulnerable plaque in coronary arteries with 18F-FDG PET/CT in patients with suppression of myocardial uptake using a low-carbohydrate, high-fat preparation. *Journal of nuclear medicine* **50**, 563-568, (2009).

Appendix to Chapter 6

Supporting Information for:

It's a Trap! Aldolase-prescribed C_4-deoxyradiofluorination affords intracellular metabolite trapping and the tracing of fructose metabolism by PET

Alexia Kirby[1,2], Dominic Graf[2,3], Mojmír Suchý[2,3], Nicholas D. Calvert[2,3], Thomas A. Charlton[2], Robert N. Ben[2], Christina L. Addison[4,5,6], Adam Shuhendler[1,2,3,7]*

[1]Department of Biology, University of Ottawa; Ottawa, ON, Canada. [2]University of Ottawa Heart Institute; Ottawa, ON, Canada. [3]Department of Chemistry and Biomolecular Sciences; University of Ottawa, Ottawa, ON, Canada; [4]Program for Cancer Therapeutics, Ottawa Hospital Research Institute, Ottawa, ON, Canada; [5]Department of Medicine and Biochemistry, University of Ottawa, Ottawa, ON, Canada; [6]Department of Microbiology and Immunology, University of Ottawa, Ottawa, ON, Canada; [7]Brain and Mind Research Institute, University of Ottawa; Ottawa, ON, Canada.

Note: only sections of supporting information relevant to this thesis are copied here. For full SI, see online version of this manuscript (https://doi.org/10.2967/jnumed.123.266905).

Tracing of [U^{13}C]-fructose metabolism *in vitro*.

Human hepatocellular carcinoma cells (HepG2) were grown in Dulbecco's modified Eagle medium (DMEM) supplemented with 10% heat-inactivated fetal bovine serum (FBS) and 1% penicillin-streptomycin (P/S) until 80% confluent under cell culture conditions (37°C, 5% CO_2, humidified), at which point they were passaged. Cells were passaged three times before being seeded in to a 6-well plate and grown until 80% confluent. Supplemented media was aspirated and replaced with lactated Ringer's buffer (LRB) alone or containing 25 mM [U^{13}C]-1-FDF, [U^{13}C]-4-FDF, or [U^{13}C]-6-FDF. Cells were incubated under cell culture conditions for 0, 15, 30, or 60 min. Following incubation, the plates were placed on ice and wells were aspirated. Wells were washed three times with ice-cold ammonium formate buffer (150 mM, pH 7.4) to remove unbound probe. A chilled (-20°C) solution of 1:1 methanol:water was added to the wells

and cells were scraped off of the wells into the solution. This solution was collected into bead-beater tubes containing 6 beads and stored at -80ºC until further analysis was performed.

Levels of fructose metabolites were assessed by liquid chromatography mass spectrometry (LC-MS). Sample temperature was maintained on ice or dry ice where possible, and all solvents were MS grade and pre-equilibrated to -20°C.

Metabolite extraction. Cell pellets were collected to a pre-chilled 2 mL tube containing 6 washed ceramic beads (1.4 mm). 380 µl of methanol:water (1:1) added in the tube and kept in -80 °C until the day of metabolite extraction. On the day of extraction, samples were vortexed for 10 s and cell lysis was done by beating for 60 s at 2000 rpm (bead beating was done twice) after adding 220 µL of acetonitrile. Samples were then incubated with a 2:1 dichloromethane:water solution on ice for 10 minutes. The polar and non-polar phases were separated by centrifugation at 4000 g for 10 minutes at 1 °C. The resulting upper phase, consisting of polar metabolites was dried with a refrigerated (-4 °C) centrivap concentrator (Labconco) and stored at -80 °C before LC-MS analyses.

LC-MS metabolite quantification. Samples to be injected in -ESI were re-suspended with 75% acetonitrile, cleared by centrifugation and run on an Agilent 6545B Q-TOF mass spectrometer equipped with a 1290 Infinity II ultra-high performance LC (Agilent Technologies). Continuous internal mass calibration was executed using signals from purine [12,000 full width at half maximum (FWHM) resolution] and hexakis (1H, 1H, 3H-tetrafluoropropoxy) phosphazine (24,000 FWHM resolution). All study samples were randomized before analysis and run using both high and low pH hydrophilic interaction chromatography (HILIC-Z) in negative ionization mode. HILIC separation was obtained using the Poroshell 120 HILIC-Z column (2.1 100 mm, 2.7 mm; Agilent) and corresponding guard column. The chromatographic conditions and mass spectrometry acquisition parameters are described elsewhere (see 10.1523/ENEURO.0292-20.2021). Metabolite identification was confirmed by exact mass, retention time and subsequent MS/MS

fragmentation for where standards are available. For the fluoro-fructose labelled metabolites, exact mass and MS/MS was considered for metabolites confirmation.

Supporting Data

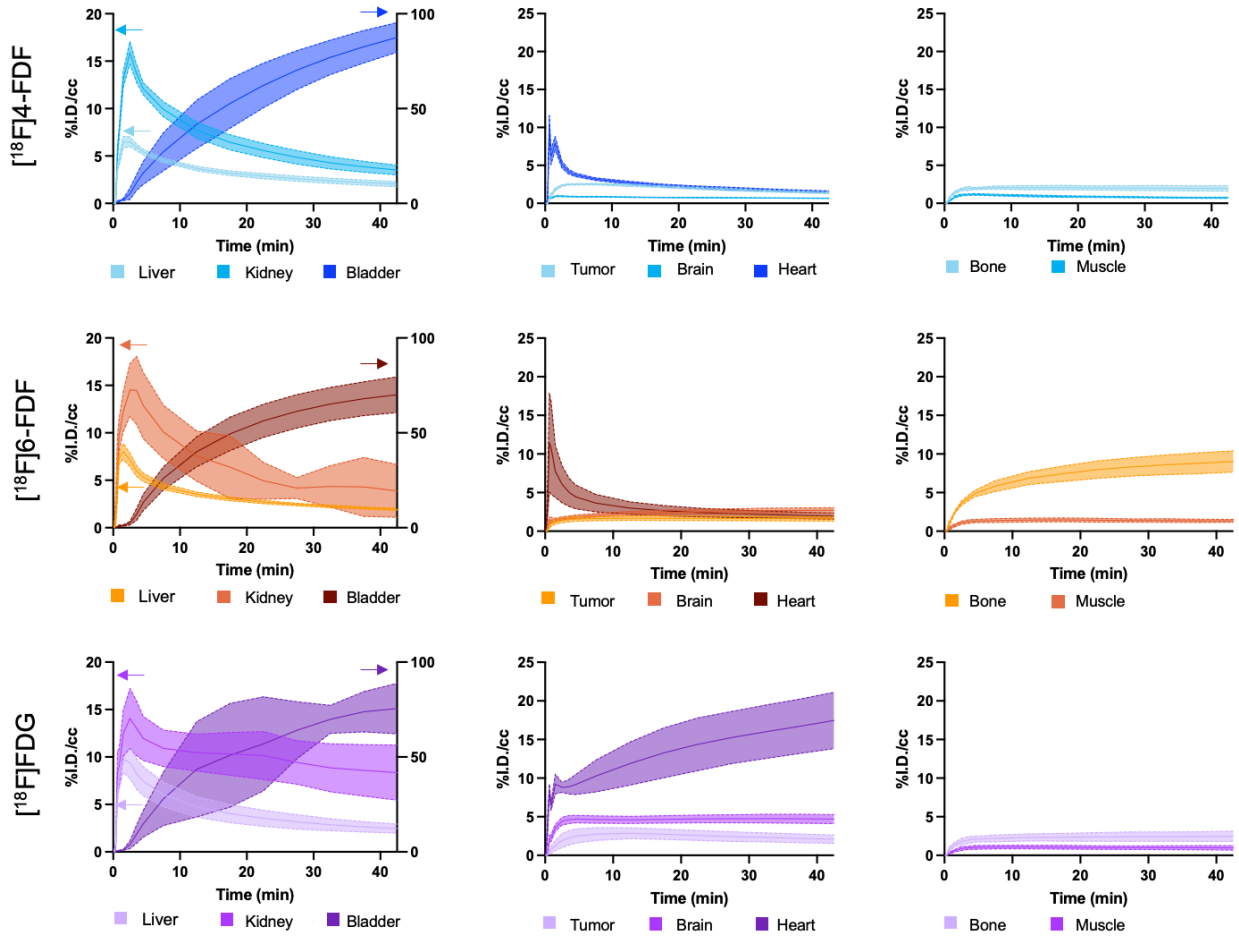

Figure S6.1. TACs for PET/CT of HepG2 xenograft-baring mice after [^{18}F]4-FDF (top), [^{18}F]6-FDF (middle), [^{18}F]FDG (bottom) PET/CT imaging. Solid line = mean; Shaded region = standard deviation.

Chapter 7: Small animal multisubject PET/CT workflow

Alexia Kirby[a,b] and Adam Shuhendler[a,b,c]

[a]Department of Biology, University of Ottawa, Ottawa, Canada

[b]University of Ottawa Heart Institute, Ottawa, Canada

[c]Department of Chemistry and Biomolecular Sciences, University of Ottawa, Ottawa, Canada

7.1. Introduction to the Methods Article Presented Within this Chapter

In this chapter, I present the methodology for the simultaneous imaging of multiple mice by PET/CT. The combination of PET/CT allows for sensitive molecular imaging with anatomical reference in an efficient manner. Included is an example of PET imaging of a mouse model of liver toxicity from acetaminophen overdose using our aldehyde-binding PET probe described in Chapter 4 of this thesis.

7.2. Author Contributions

AK and AS developed the method described in this article. AK conceptualized and performed experiments and wrote the manuscript.

7.3. Copyright

7.4. Abstract

Positron emission tomography (PET) is a highly sensitive molecular imaging technique that uses radioactive tracers to map molecular and metabolic processes in living animals. PET can be performed as a stand-alone modality, but is often combined with CT to provide for objective anatomical localization of PET signals in a multimodality approach. In order to outline the general approach to evaluating four mice simultaneously by dynamic PET imaging, the use of the aldehyde-targeted radiotracer [18F]NA3BF3 in mouse models of hepatotoxicity will be described. Indeed the production of aldehydes is upregulated in a wide range of disease and injury, making them a suitable biomarker for PET imaging of numerous pathologies.

7.5. Introduction

PET is an important preclinical molecular imaging technique that uses radionuclide-labelled molecules to non-invasively map biological processes of interest with high sensitivity and in three-dimensions. While

PET imaging is an important clinical tool, it is also a powerful pre-clinical technique that not only leads to the development of clinical tracers, but is also used for longitudinal studies in animal models to better understand certain biological processes. While PET provides high sensitivity information about the localization of radiotracers, it does not provide anatomical information about the subject under study. As a result, PET is often combined with computed tomography (CT), an X-ray-based imaging technique that can generate high resolution images of subject anatomy. This multimodality approach is invaluable for the objective quantitation of radiotracer uptake in tissues and pathologies with a high degree of spatial certainty and accuracy.

In vivo aldehydes are produced and maintained by tightly regulated mechanisms [1]. Disruption of these mechanisms often results in an increase of aldehyde production, creating a tissue environment with high aldehydic load [2]. This increase in aldehydic load often underlies the early stages of many pathologies including cancer, cardiovascular disease, and acutely following injury [3-6]. These aldehydes are highly reactive and quickly form adducts with DNA and proteins, which may contribute to the propagation of injury and disease. The diversity of aldehydes with pathogenic potential supports the need for *in vivo* imaging of aldehydes.

A radiotracer designed to measure aldehydic load is unlike the most common radiotracer, 2-deoxy-2-[^{18}F]fluoro D-glucose (FDG), in that it does not act as a metabolic surrogate. FDG is taken up by glucose transporters, phosphorylated, and subsequently trapped intracellularly, and therefore maps aerobic metabolism. Imaging *in vivo* aldehydes, however, is more efficient through a substrate-binding mechanism rather than a surrogate mechanism. For a PET radiotracer to work effectively to map aldehydes, the reaction must occur rapidly, without a catalyst, under physiological conditions, and stick to the location where the substrate was bound.

Two radiotracers have been developed for this technique: ^{68}Ga-NODAGA-Indole [7]; and ^{18}F-NA_3BF_3 [8]. The former is an allysine-reactive probe that binds to converted lysine residues of oxidized collagen in fibrotic lung tissue. ^{18}F-NA_3BF_3 is an anthranilic acid-based probe that reacts with both intra- and extracellular

aldehydes to form hydrazones. This tracer represents a first-generation aldehyde PET tracer that can be used to map whole-body *in vivo* aldehydic load.

Here, aldehyde PET imaging with ^{18}F-NA_3BF_3 is described in a mouse model of acetaminophen overdose-induced hepatotoxicity. The model involves a single, same-day injection of acetaminophen, which induces lipid peroxidation and aldehyde production especially in the liver, and has been shown to cause an increase in aldehydic load. The goal of the method is to quantitatively map the *in vivo* aldehydic load in mice over time and across acetaminophen doses using [^{18}F]-NA_3BF_3-PET.

7.6. Materials

7.6.1. PET/CT scanner preparation

1. Small animal PET/CT scanner with heater, and integrated animal monitoring system for respiration and temperature
2. Computer station with associated software
3. Multi-mouse imaging bed (See *Note 1*)

7.6.2. Animal Preparation

1. Personal protective equipment (PPE, including but not limited to gloves and lab coat)
2. Acetaminophen-injected or sham injected mice
3. Absorbent pads
4. Heat lamp
5. Water pump heating mat
6. Isoflurane system directed to either induction box or nose cone
7. Isoflurane scavenging system
8. Oxygen tank
9. Small animal anesthesia induction box
10. Preparation table with nose cone
11. 27G or 30G 13mm needles

12. Polyethylene tubing
13. 0.9% saline solution
14. Isopropyl alcohol swabs
15. 1ml syringes
16. Needle forceps
17. Paper tape (3M micropore)
18. Surgical plastic tape (3M transpore)
19. Topical skin adhesive (vetbond)
20. Eye gel

7.6.3. Radiotracer preparation and animal injection

1. $[^{18}F]NA_3BF_3$ or other non-metabolic PET radiotracer
2. Lead-lined radioisotope workstation with plexiglass shield (see *Note 2*)
3. Contamination monitor (Geiger counter)
4. 0.9% saline solution
5. 1ml syringes
6. 27G needles
7. Dose calibrator (Capintec)

7.6.4. Image analysis

1. Image analysis software (Vivoquant)

7.7. Methods

7.7.1. PET/CT scanner preparation

1. PET/CT calibration should be performed on a regular schedule based on manufacturer's instructions prior to beginning an imaging study
2. If CT is to be used, X-ray tube conditioning of the CT scanner should be performed at least 30 minutes prior to receiving radiotracer

3. Heat imaging bed to 37°C
4. Prepare respiration monitor and rectal temperature probe on PET bed

7.7.2. Animal Preparation

1. Create a sterile environment by wiping area with disinfecting spray and placing absorbent padding on bench. Lay out all materials needed to prepare the animals for cannulation
2. Prepare one tail vain cannula per mouse (Figure 7.1). Cut a length of polyethylene tubing long enough to allow access when animals are centered in PET scanner (approx. 10-15cm for most scanners). Remove a 27G or 30G needle from its hub by breaking the plastic with needle forceps, and secure the blunt end into one end of the tubing. Draw 500 μL saline with a needle attached to a 1mL syringe, and secure onto the other end of the tube. Push the syringe until the saline exits from the needle end of the cannula, and take note of the volume pushed through. Ensure there are no air bubbles anywhere in the line.
3. Place mouse in induction box on heating pad with 3% isoflurane at 1.5-2 L/min
4. When mouse anesthetized (unresponsive to touch), remove from box and place head in nose cone on prep table on heating pad.
5. Apply eye gel to the eyes.
6. Place mouse on its side to expose lateral tail vein. The vein will be more difficult to see in strains with darker pigmented tails (e.g. C57bl/6)
7. Warm tail with heat lamp, taking care not to burn the tail (see *Note 3*)
8. Wipe the tail with an alcohol swab.
9. Cannula insertion should be attempted toward the distal end of the tail, with following attempts moving more proximal. In the non-dominant hand, either hold the tail between the thumb and index finger, or weave the tail under the forefinger, under the third and fourth, and over the fifth finger (Figure 7.1A). Bend the tail slightly to expose an area for cannulation. Insert the

needle of the cannula into the lateral tail vein at a ~5° angle to the tail, ensuring at least half (>6.5mm) of the needle is in the vein (Figure 7.1B, C).

10. Verify the cannula is in the vein by pushing on the syringe. The vein will visibly flush with saline, and the plunger will have no resistance. If the needle is not in place, the syringe will be difficult to push, and the tail will blanche at needle insertion site.
11. Add one drop of skin adhesive where the needle meets the tail and allow to dry for 30 seconds.
12. Secure the cannula with paper tape (Figure 7.1D).
13. Turn on isoflurane to PET/CT bed to 2%.
14. Move the mouse over to the PET/CT bed, with the mouse in one hand and syringe in the other to avoid displacing the cannula. Place the mouse in a prone position.
15. Secure the body of the mouse, tail, and cannula with tape, and ensure the cannula is in place by pushing the plunger of the syringe. This will ensure proper injection of the radiotracer. Insert rectal temperature probe and secure with tape.
16. Verify that temperature and respiration monitors are working and within range. Respiration rate should be maintained at 60-100 breaths per minute, which can be adjusted by increasing or decreasing isoflurane. Body temperature should be maintained at 35-37°C.
17. Note the position of each mouse in the imaging bed, and ensure the bed is aligned with the imaging field of view (FOV) of the scanner. The specific method for FOV centering will change depending on the vendor. Ensure both PET and CT FOVs are adequate for region of interest of imaging (i.e. whole mouse, head only, abdomen only).

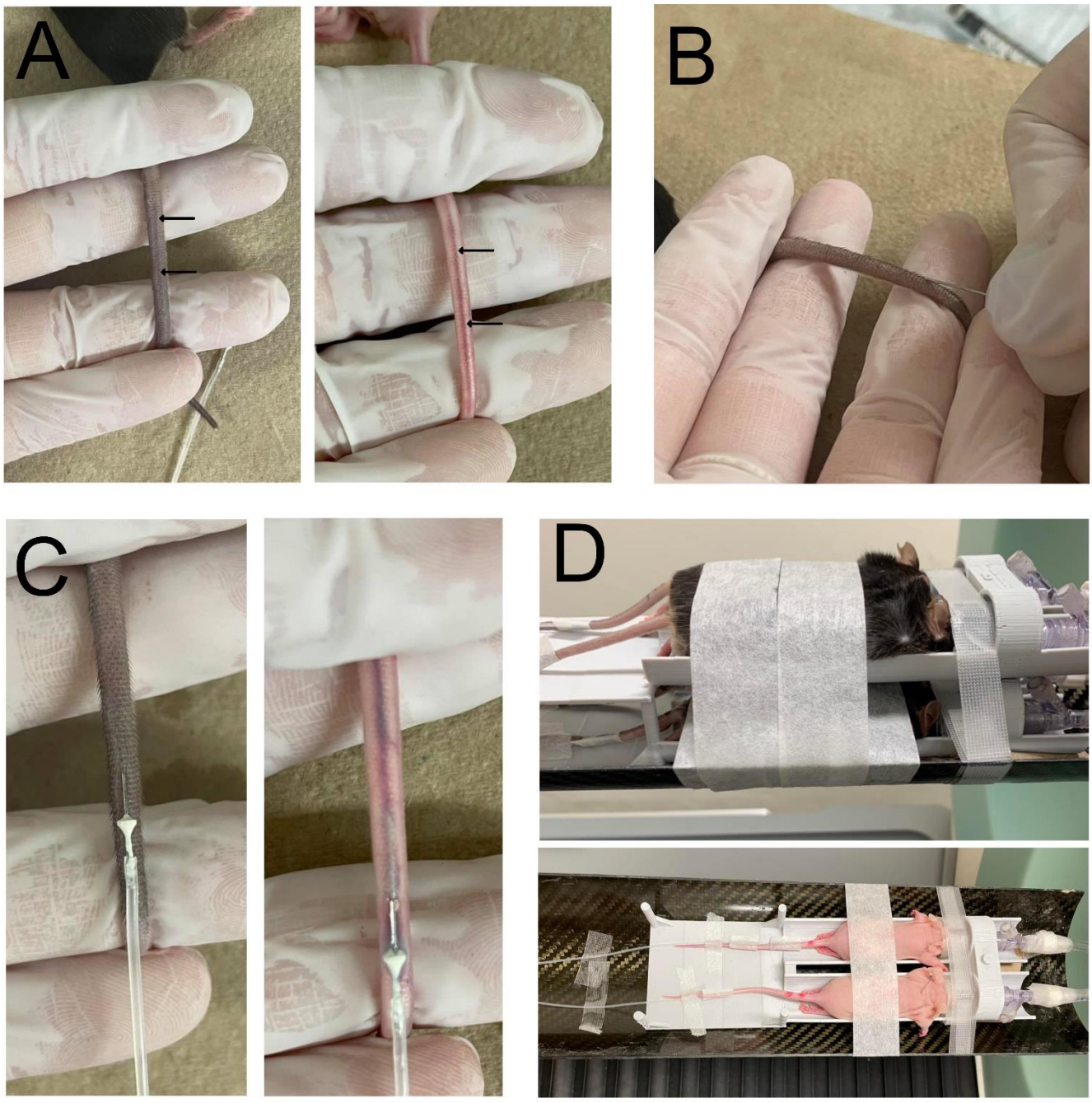

Fig 7.1. Animal preparation for PET scan. Before the radiotracer is received, mice are prepared for injection. (A) The lateral tail vein is located and dilated with a heat lamp in a C56Bl/6 mouse (left) and nu/nu mouse (right). (B) Successful placement of the needle of the cannula is shown in both mice, after insertion at a ~5° angle to the tail (C). (D) The animals are moved to the PET bed and tape is placed to secure the bodies of the mice, the tails, and the cannulas.

7.7.3. Radiotracer preparation

1. Synthesize radiotracer as previously described. Due to the short half-life of ^{18}F, the subsequent steps need to be done quickly.
2. Radiotracer dose preparation is performed behind lead shield, with one dose prepared for each animal in the immediately following scan.
3. Measure the total radioactivity obtained in the dose calibrator. Note the time of this measurement to account for decay.
4. Dilute stock radiotracer to ~200 μCi/100 μL. If more than one round of imaging will be done with the same stock, only dilute a portion of the stock.
5. Draw up 150-200 μCi of activity per mouse with 27G insulin syringes, ensuring the volume is a maximum of 10 mL/kg per mouse. If multiple mice are being scanned, mark each syringe with a number corresponding to each mouse ID. Measure each syringe in the dose calibrator and note the activity and time for each syringe.
6. When all doses have been prepared, place in a lead carrier and bring to PET/CT animal bed or cradle.

7.7.4. Injection and scanning

1. Attach the radiotracer dose to the tail vein cannula. With a pair of forceps, grasp the end of the cannula and remove the syringe and needle containing saline and place to the side. Carefully insert the needle of the tracer-containing syringe into the cannula. Repeat for all mice.
2. The scan types should be selected and placed in queue. For PET/CT, select the PET scan program desired (e.g. static scan of a given time frame, dynamic scan with pre-set imaging bins) as well as the CT program necessary (see *Note 4*). Importantly, for dynamic scans, an initial 15-30 sec bin should be included to allow delay between scan program initiation and radiotracer injection. This is key for accurate kinetic analyses.

3. On the instrument control station, start the scan and timer simultaneously
4. After the delay set in the first bin of a dynamic scan has passed (15 or 30 seconds), inject the radiotracer over a period of 3-5 seconds.
5. Replace the empty radiotracer syringes with the saline-filled syringes and inject enough volume to simultaneously flush all of the cannulae (~50-100 μL) with saline.
6. Measure the residual radioactivity in each radiotracer syringe and note the time.
7. Monitor respiration rate carefully during the scan, and adjust isoflurane if necessary.
8. If another PET/CT scan is to be performed afterwards, use this time to set up for the next scan. Mice can be cannulated and doses can be drawn toward the end of the first scan.
9. When imaging is complete, remove all tape securing the cannula to the bed and the tail. Pinch the injection site on the with gauze while removing the needle to stop bleeding. Place mouse back in cage on heating pad to recover. The mice should be held in a designated area behind a lead shield overnight or until ready to replace back in housing room, depending on the facility.

7.7.5. Image reconstruction

1. Depending on the vendor there will be a variety of image reconstruction algorithms to choose from. Reconstruction algorithm choice will depend on a balance of resolution, time, and quantitative accuracy required, and should be evaluated in a pilot fashion.
2. Reconstruction will necessarily involve data about photon attenuation derived from the CT or an attenuation scan if PET-only imaging is performed.

7.7.6. Image analysis

1. The specific workflow for image analysis will depend on the tissue/organ of interest and the disease model utilized, as well as the software package chosen for analysis.
2. For multi-animal scans, each animal should be cropped from the image and analyzed separately so that precise injected dose can be input into time-activity curves, or use for radiotracer uptake (either as % injected dose per gram or summed uptake value).

3. Output images should include a standardized scale range and scale unit (either as % injected dose per gram or summed uptake value) to afford comparison across individuals between treatment groups (Figure 7.2).

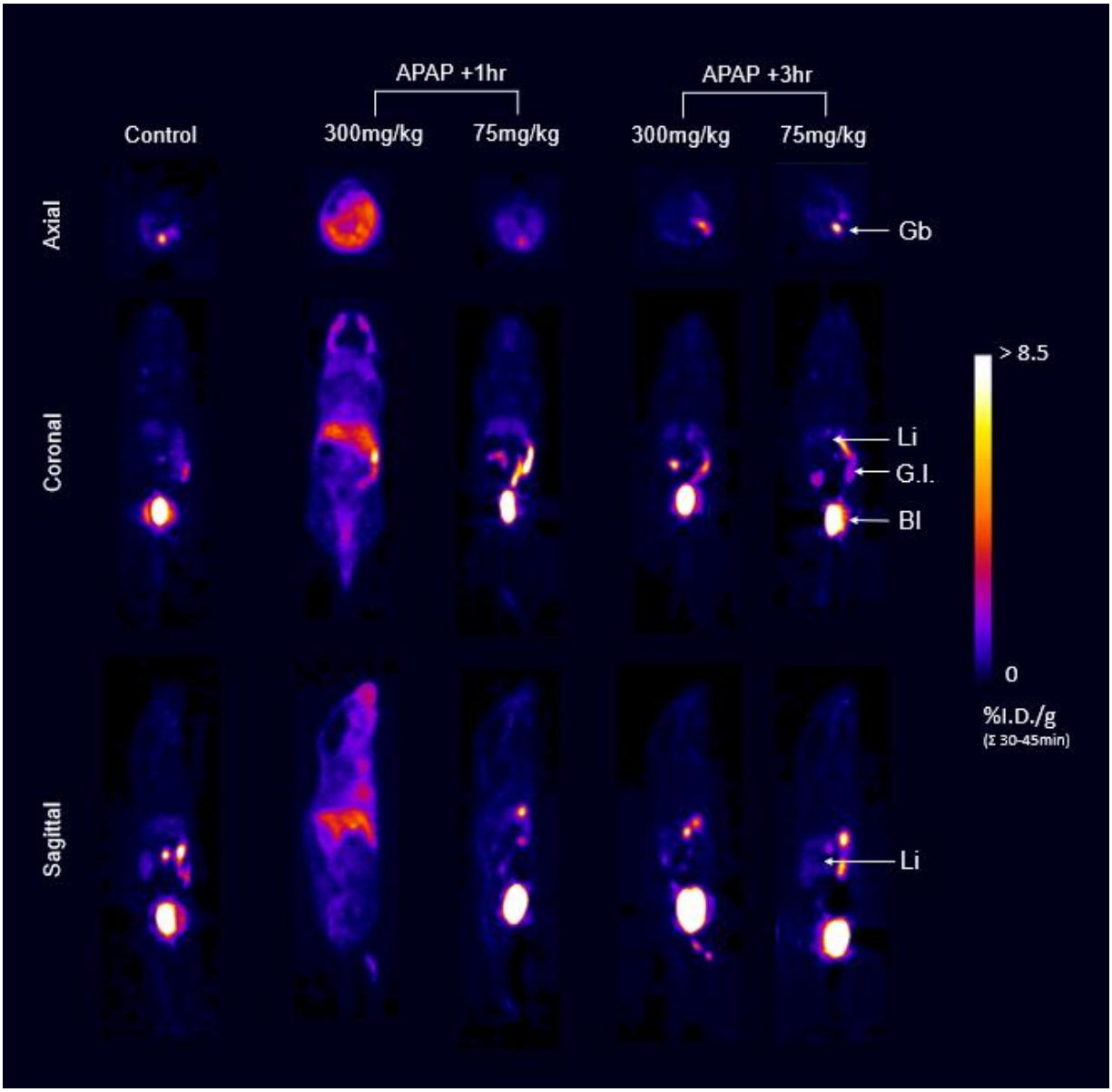

Fig 7.2. Distribution of [^{18}F]-NA_3BF_3 in mice following acetaminophen dosing by PET imaging. Mice were untreated (left-most), or given an overdose (300 mg/kg) or therapeutic dose (75 mg/kg) acetaminophen i.p., and imaged 1 or 3 hr after administration. Images are summed from the time activity curves from 30-45 min after PET scan initiation.

7.8. Notes

1. Multi-mouse beds are commonly provided by the PET/CT instrument manufacturers and are supplied with anesthesia and heating with proprietary adaptors. If this is not the case, a multi-mouse bed can be 3-D printed, however heating and the equal distribution of anesthesia to all positions must be tested prior to implementation on live animals.
2. Use of radioisotopes and radiotracers should comply with institutional and Federal policies for the safe use of radioactivity.
3. Keeping one hand next to mouse under heat lamp will ensure heating does not result in burn.
4. CT program for single mouse and multimouse will be different with different total deposited dose. These programs can be found pre-programmed on most scanners and should be evaluated prior to use.
5. Unlike in metabolism-based imaging (eg FDG), animals do not need to be fasted overnight to image aldehydes.
6. ^{18}F-NA_3BF_3 does not cross the blood brain barrier and therefore cannot be used for aldehydes imaging in brain tissue.
7. Animals should always be warmed while under general anaesthesia, as they cannot regulate their body temperature. The effect of body temperature on ^{18}F-NA_3BF_3 distribution is unknown, but animals should be kept at 37°C for animal welfare.
8. F18-labelled radiotracers have a half-life of 109.7 minutes, which makes it possible to perform multiple scans in a day if the production yield is good.
9. Always be sure to choose an appropriate mouse model for the pathology of interest.
10. Dynamic scans are recommended for novel radiotracers as the optimal time with peak uptake will be unknown. A dynamic scan will capture the tracer's entry into the blood stream and biodistribution, as well as clearance (hepatic or urinary).
11. Position the area of interest (e.g. tumour, organ) to the centre of the PET camera where the sensitivity and resolution are highest.

7.9. Conflicts of interest

N/A

7.10. References

1 O'Brien, P. J., Siraki, A. G. & Shangari, N. Aldehyde Sources, Metabolism, Molecular Toxicity Mechanisms, and Possible Effects on Human Health. *Critical Reviews in Toxicology* **35**, 609-662, (2005).

2 Wood, P. L., Khan, M. A. & Moskal, J. R. The concept of "aldehyde load" in neurodegenerative mechanisms: cytotoxicity of the polyamine degradation products hydrogen peroxide, acrolein, 3-aminopropanal, 3-acetamidopropanal and 4-aminobutanal in a retinal ganglion cell line. *Brain research* **1145**, 150-156, (2007).

3 Antoniak, D. T., Duryee, M. J., Mikuls, T. R., Thiele, G. M. & Anderson, D. R. Aldehyde-modified proteins as mediators of early inflammation in atherosclerotic disease. *Free radical biology & medicine* **89**, 409-418, (2015).

4 Burke, W. J. *et al.* Neurotoxicity of MAO metabolites of catecholamine neurotransmitters: role in neurodegenerative diseases. *Neurotoxicology* **25**, 101-115, (2004).

5 Burke, W. J. *et al.* Aggregation of α-synuclein by DOPAL, the monoamine oxidase metabolite of dopamine. *Acta neuropathologica* **115**, 193-203, (2008).

6 Cristofori, L. *et al.* Biochemical analysis of the cerebrospinal fluid: evidence for catastrophic energy failure and oxidative damage preceding brain death in severe head injury: a case report. *Clinical biochemistry* **38**, 97-100, (2005).

7 Chen, H. H. *et al.* Molecular imaging of oxidized collagen quantifies pulmonary and hepatic fibrogenesis. *JCI Insight* **2**, e91506, (2017).

8 Kirby, A., Suchý, M., Brouwer, A. & Shuhendler, A. Mapping aldehydic load in vivo by positron emission tomography with [18 F] NA 3 BF 3. *Chemical Communications* **55**, 5371-5374, (2019).

Chapter 8: Tracking the fate of bacteria-derived site-specific immunomodulators by Positron Emission Tomography

Alexia Kirby[a,b], Mojmir Suchy[b,c], Daniel Duan[b], Mark Bazett[d], Shirin Kalyan[d,e], Adam J Shuhendler[a,b,c*]

[a]Department of Biology, University of Ottawa, Ottawa, ON, Canada

[b]University of Ottawa Heart Institute, Ottawa, ON, Canada

[c]Department of Chemistry and Biomolecular Sciences, Ottawa, ON, Canada

[d]Qu Biologics Inc., Vancouver, BC, Canada

[e]Department of Medicine, Division of Endocrinology, University of British Columbia, Vancouver, BC, Canada

*Corresponding author: 10 Marie Curie Pvt. Ottawa, Ontario, Canada K1N 6N5
Email address: adam.shuhendler@uottawa.ca

8.1. Introduction to the Research Article Presented Within this Chapter

The experiments conducted in this chapter were a collaboration with a pharmaceutical company, Qu Biologics (Vancouver, BC, Canada). Qu Biologics develops biological therapeutics designed to restore the innate immune response of patients with autoimmune disorders or cancer. The therapeutics are termed Site Specific Immunomodulators (SSIs), which contain all the macromolecules of inactivated bacteria. The bacteria from which the SSIs are produced are most commonly found in the target organ of disease. For example, the SSI designed for lung cancer and asthma is derived from *Klebsiella Pneumoniae* (*k. pneumoniea*), the bacteria that commonly causes pneumonia. The SSI designed for ulcerative colitis and inflammatory bowel disease is *Escherichia Coli* (*E. coli*), an enteropathic bacteria of the gut. While these therapies were in Phase I/II clinical trials when this project was initiated, the full mechanism of action of SSIs was mostly unknown. Our approach was to radiolabel these compounds with a long half-life isotope, administer them to healthy mice, and track the biodistribution non-invasively by PET.

8.2. Author Contributions

A.K., M.S., M.B., S.K. and A.J.S. conceptualized the study. M.S., D.D., and A.J.S. performed chemistry experiments. A.K. and A.J.S. performed all animal experiments, data analysis, and wrote the manuscript. All authors reviewed and approved the final version of the manuscript.

8.3. Copyright

Reproduced from Ref. ***Nuclear Medicine and Biology*** (2024): 108908.

https://doi.org/10.1016/j.nucmedbio.2024.108908

8.4. Abstract

Introduction: Site-specific immunomodulators (SSIs) are a novel class of therapeutics made from inactivated bacterial species designed to regulate the innate immune system in targeted organs. QBECO is a gut-targeted SSI that is being advanced clinically to treat and/or prevent inflammatory bowel disease, cancer, and serious infections of the gastrointestinal (GI) tract and proximal organs, and QBKPN is a lung-targeted SSI that is in clinical development for the treatment and/or prevention of chronic inflammatory

lung disease, lung cancers and respiratory tract infections. While these SSIs have demonstrated both safety and proof-of-concept in preclinical and clinical studies, detailed understanding of their trafficking and biodistribution is yet to be fully characterized.

Methods: QBECO and QBKPN were radiolabeled with [^{89}Zr] and injected subcutaneously into healthy mice. The mice underwent Positron Emission Tomography (PET) imaging every day for eight days to track biodistribution of the SSIs. Tissue from the site of injection was collected and immunohistologically probed for immune cell infiltration.

Results: Differential biodistribution of the two SSIs was seen, adhering to their site-specific targeting. QBKPN appeared to migrate from the site of injection (abdomen) to the cervical lymph nodes which are nearer to the respiratory tract and lungs. QBECO remained in the abdominal region, with lymphatic trafficking to the inguinal lymph nodes, which are nearer to GI-proximal tissues/organs. Immune infiltration at the site of injection comprised of neutrophils for both SSIs, and macrophages for only QBKPN.

Conclusion: Radiolabeling of SSIs allows for longitudinal *in vivo* imaging of biodistribution and trafficking. PET imaging revealed differential biodistribution of the SSIs based on the organotropism of the bacteria from which the SSI is derived. Trafficking from the site of injection to the targeted site is in part mediated *via* the lymphatics and involves macrophages and neutrophils.

Key words: PET imaging, ^{89}Zr, biodistribution, immunomodulation

Abbreviations: SSI= Site Specific Immunomodulator; GI= gastrointestinal; CLN= cervical lymph node; ILN= inguinal lymph node

8.5. Introduction

Since the 1800s, spontaneous tumor remission has been observed in some patients experiencing acute microbial infections[1-4]. Recent studies have also demonstrated successful bacteria-induced immune stimulation for anti-cancer therapy and reduction of post-operative infection[5-11]. While these results are intriguing as alternatives to drug-based therapeutics, these treatments rely on intra-tumoral administration of live bacteria, limiting the clinical applications to those with accessible and/or susceptible tumors, and posing significant potential risks[12]. While these studies establish the immune-stimulatory effects of bacteria, limited disease accessibility, poor ability to control and target the treatment, and the potential safety risks of using live opportunistic pathogens, have prevented broad clinical adoption of such immunotherapies.

To harness the broad curative potential of innate immunomodulation while overcoming the limitations of introducing live bacteria into patients, Site-Specific Immunomodulators (SSIs) have been developed. SSIs are a first-in-class immunotherapy derived from specific species of bacteria designed to mobilize, train and target the innate immune system in an organ-specific manner. These immunomodulators work by reestablishing a balanced immune response through immune restoration by enhancing immune resiliency in specific sites in the body affected by disease, ultimately regulating the immune response to reduce unproductive inflammation and tissue damage. In this manner, SSIs are distinct from other immunosuppressive therapies, which broadly suppress immune function by blocking specific immune pathways. Instead, the SSIs offer the advantage of targeting the immune response to active disease sites, restore immune and barrier function, and avoid the associated side effects of immunotherapies that force activation or suppression of important immune signaling pathways.

Investigations [13,14] of humoral and tissue immune components and associated signaling regimes has led to the identification of the putative mechanism of SSI function (**Fig. 8.1A**)[15]. The administration of SSIs induces a broad production of immune cell expansion, a process known as emergency hematopoesis, dominated by bone marrow myelopoiesis through the expansion of lineage-negative hematopoietic stem

cells (c-kit^{+}Sca^{+}), ultimately increasing organ-specific trained monocyte and neutrophil populations. The organ specificity is governed by organ-specific chemokine release from the organ-site where the bacteria from which the SSI is formulated is endogenous and a common potential cause of infection. The enriched monocyte population exhibit a "trained" phenotype (Ly6C^{HI}) due to transcriptional reprogramming within the bone marrow matching that seen following microbial stimulation[16], and showing enhanced functional response upon immune challenge. These "trained" monocytes are then recruited to SSI-directed tissues through treatment induced CCL2/CCL5 chemokine gradients, ultimately increasing M1 macrophage and activated natural killer (NK) cell recruitment. In lung cancer models, the reduction of lung tumor burden was shown to be dependent on NKG2D receptor mediated through the upregulation of Rae-1, the ligand of the NKG2D receptor, on cancer cells, which resulted in making them more visible to immune surveillance[14].

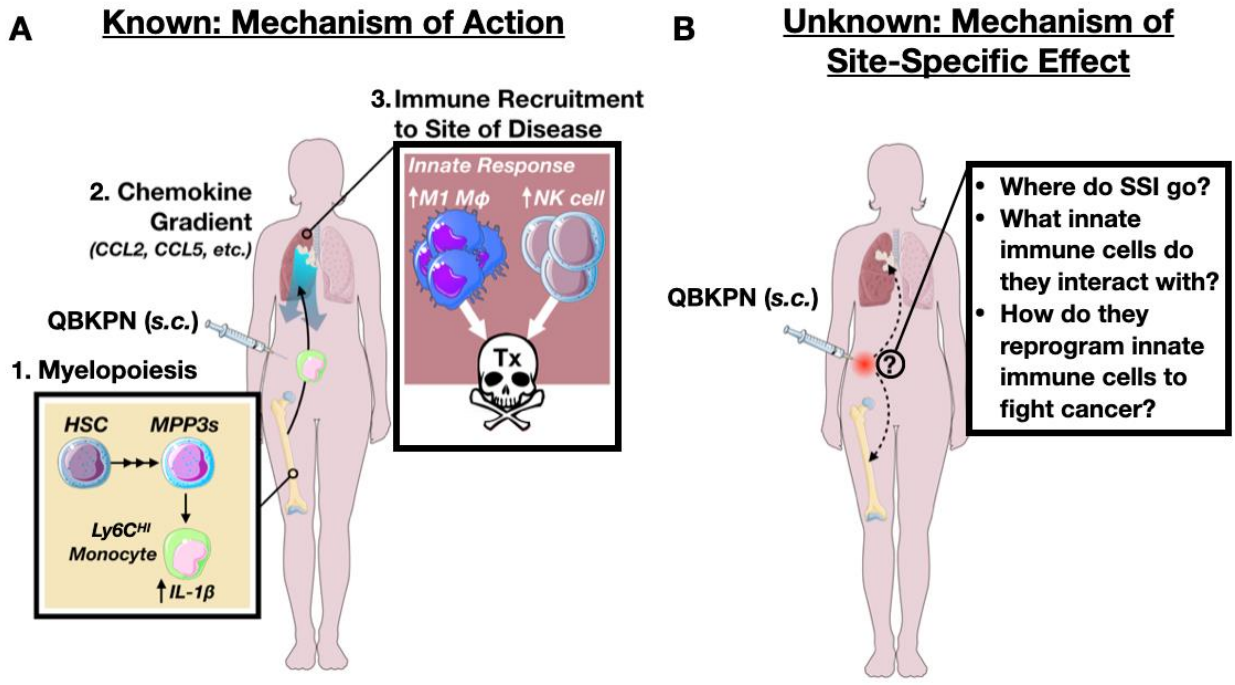

Figure 8.1. The current state of what is known (A) and unknown (B) about the mechanism of action of SSIs. (A) Myelopoiesis in the bone is stimulated by SSIs, and monocytes are recruited to target tissue by

chemokines, increasing macrophage (Mf) and NK cell numbers. (B) The fate of SSIs post-injection remains unknown.

SSIs are a first-in-class immunotherapy platform being developed by Qu Biologics that uses inactivated derivatives of a single species of bacteria that retain all of the major macromolecular components of the organism that allows its recognition by the immune system (**Fig. 8.2A**). The site of immunomodulation can be tuned by deriving the SSI from bacteria that are a common cause of infection in the organ targeted for therapeutic intervention[15]. Therefore, SSIs do not need to be introduced at the disease site, but rather it has been demonstrated that they can be administered subcutaneously to activate an immune response in an organ-specific manner[13,17-19].

QBECO is an SSI derived from components of inactivated enteropathogenic *Escherichia coli* (*E. coli*), which targets the gastrointestinal tract and colon. QBECO has been shown to improve histological score, reduce T-cell infiltration, and decrease neutrophil numbers in the colon of mouse models of ulcerative colitis (UC)[20]. UC is characterized by mucosal inflammation of the colon, which, without treatment, can develop into inflammation of the entire large bowel and lead to an increased risk of colon cancer[21,22]. All current treatment strategies involve immunosuppression, however 65-80% of patients do not experience a full remission, and 40-55% of patients have no response to therapy[23]. With this current lack of safe and effective treatments for UC, there is a recognized clinical need for new treatment strategies.

QBKPN is an SSI derived from inactivated *Klebsiella pneumoniae* (*K. pneumoniae*) related species, targeting immune stimulation to the lungs. QBKPN has shown promising anti-cancer effects in pre-clinical models of lung cancer, resulting from an increase in activated NK cells and polarized macrophages in the lungs[14] (**Fig. 8.1A**). Significant heterogeneity with regards to drug resistance in lung cancer complicates the selection of therapy, and necessitates the development of strategies that can overcome the diversity of multidrug resistance phenotypes associated with lung cancer[24]. While there has been a reduction in lung cancer mortality over the last decade due to advances in clinical detection and therapeutic strategies[25], the persistence of high treatment failure rates and high mortality rates associated with lung cancer today clearly

identifies a clinical need for alternative treatment strategies to increase cure rates. QBKPN has also shown proof-of-principle for the treatment of inflammatory lung diseases and respiratory infections[15,17,18].

As summarized above, the immune modulatory effects of QBECO and QBKPN have been characterized and have shown broad pre-clinical and clinical efficacy in cancer, chronic inflammatory diseases, and infection. However, the biodistribution and trafficking governing the SSI's signal relay from the site of injection to the sites of immunostimulation still require elucidation (**Fig. 8.1B**). In this study, the biodistribution and associated trafficking mechanisms of two SSIs, QBECO and QBKPN were investigated.

8.6. Methods

8.6.1. SSI radiolabeling and evaluation

SSI products comprising QBECO and QBKPN (obtained from Qu Biologics, BC, Canada) were radiolabeled with ^{89}Zr using a standard protocol[26]. Briefly, isothiocyanate-functionalized desferrioxamine (DFO-Bn-NCS) was conjugated to the particles forming a thiourea linkage with lysine residues exposed on the surface (**Fig. 8.2B**). A volume of 300 uL of QBECO or QBKPN (O.D.600= 5 absorbance units) were centrifuged and the supernatant discarded. Pellets were resuspended in 200 uL of 0.2M Borate buffer (pH 8.5), and 0.4 µmol of DFO-Bn-NCS was added while stirring and incubated for 90 min at room temperature for the reaction to occur. Particles were washed three-times with PBS and suspended to a final volume of 300 uL. Once conjugated, approximately 37 MBq of Na_2CO_3-neutralized [^{89}Zr]Zr oxalate was added to the SSI suspension and stirred for 60 min at room temperature. The SSIs were washed twice in PBS and resuspended in 300 uL PBS. The obtained radiochemical yields of [^{89}Zr]Zr-DFO-labelled SSI were 92±2% for QBECO and 89±5% for QBKPN (n=3 preparations each). Radiochemical purity was evaluated by thin layer chromatography using standard aluminum-backed silica plates and 0.1 M citrate (pH 6.0) as mobile phase [27]. Radio-TLC plates were scanned and quantified using an AR-2000 Imaging Scanner (Bioscan Inc.).

8.6.2. Animals

All procedures for animal experimentation were conducted under Animal Use Protocol SCe-4019 approved by the IACUC at the University of Ottawa. Mice were housed under 12 hr light/dark cycle, and ambient temperature of 20-24°C and 45 to 65% humidity. All mice were provided access to food (Rodent Laboratory Chow) and water *ad libitum*.

8.6.3. Short-term biodistribution studies

Balb/c mice received a single subcutaneous (s.c.) injection of [^{89}Zr]Zr-QBECO or [^{89}Zr]Zr-QBKPN (~1.85MBq) in the left abdominal region (n = 5 per SSI). Mice were secured into a plastic sled to prevent body movement when transferring between PET and MRI. The mice underwent PET imaging (Inveon DPET, Siemens) at 45 min, 2 h, and 3 h post-injection, followed by a T_1-weighted RARE image with parameters of slice thickness of 5 mm, FOV of 40 ´ 40 mm, averages = 3, matrix size = 96 ´ 96, TE_{eff}= 11 ms, echo spacing = 7 ms, TR = 720 ms at 3.0 T on a small animal MRI (MR solutions) for anatomical reference. Mice were then euthanized by cervical dislocation and thoracotomy under anesthesia (isoflurane, 5%), and organs were collected and weighed. Radioactivity of organs was measured using a gamma spectrometer (Wallac 2480 Wizard, Perkin Elmer). Tissue uptake values were calculated as percentage-injected dose per gram tissue (%ID/g).

8.6.4. Long-term biodistribution studies

Healthy Balb/c mice (n = 4 per SSI) received a s.c. injection (1.85MBq) of either [^{89}Zr]QBECO (upper abdomen), or [^{89}Zr]QBKPN (lower abdomen). The mice were imaged by PET at 4 h post-injection, and every 24 h for 8 days. Mice in the two-dose study received a dose of unlabeled SSI 48 h before s.c. injection of the radiolabeled SSI, followed by PET imaging at the same time points (n = 4 per SSI).

Data analysis was performed on Vivoquant (Invicro). PET data are collected by 10 min static scan and are attenuation correction. Volumes of interest were drawn on kidneys and lymph nodes, and data are presented as %ID/g.

8.6.5. Histology

Upon completion of the imaging studies at day eight post-injection, a small area of tissue (~2 cm x 2 cm) around the injection site was collected. In all cases, a small nodule (~0.5 cm) was present within the injection site. The tissue was placed in formalin overnight for fixation, embedded in paraffin and sliced on a microtome. The sections were stained with either hematoxylin and eosin (H&E), picrosirius red (PSR), or immunohistologically probed with anti-NMP-R14 (Abcam ab2557), or anti-CD68 (BioRad MCA1957) for identification of neutrophils and macrophages/monocytes, respectively.

8.6.6. Statistical analyses

Tissue distribution data were analyzed by 2-way ANOVA with repeated measures analysis using Prism (GraphPad Inc.), and time-course data were analyzed by generalized linear model repeated measures analysis using SPSS (IBM).

8.7. Results

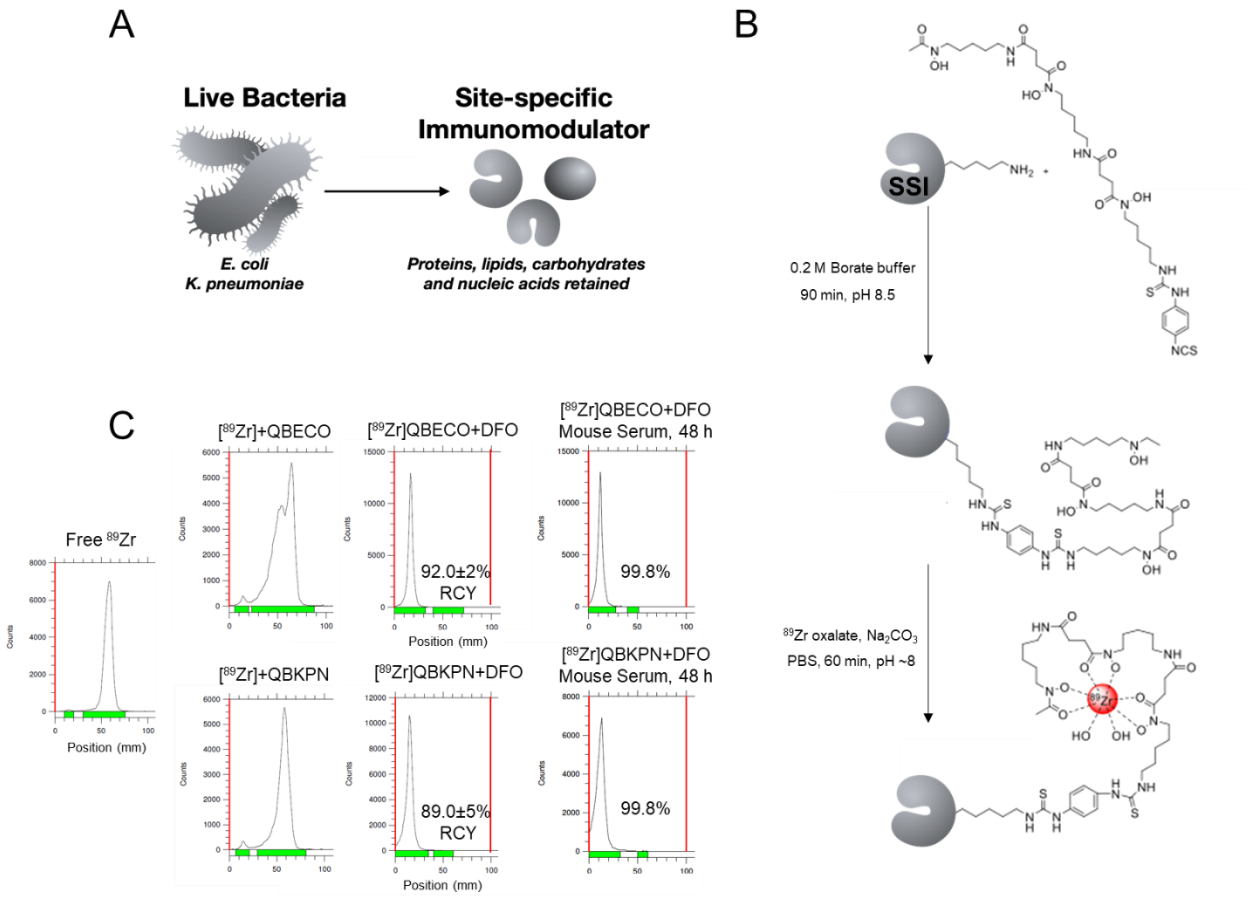

Figure 8.2. Synthesis and characterization of radiolabeled site specific immunomodulators with [^{89}Zr]. (A) SSIs are formulated from bacteria that are common endogenous causes of infection in a targeted organ (gut or lungs). (B) SSIs conjugated to isothiocyanate-functionalized desferrioxamine (DFO) forming a thiourea linkage and radiolabeled with [^{89}Zr]Zr oxalate. (C) RadioTLCs of unchelated [^{89}Zr]Zr oxalate and SSIs +/- DFO revealed successful radiolabeling of DFO-SSIs with good radiochemical yield (RCY) and stability of the radiolabeled SSIs was demonstrated after incubation with mouse serum for 48 h.

The radiolabeling of DFO-labelled SSIs by [^{89}Zr]Zr oxalate was accomplished through standard thiourea formation chemistry (**Fig. 8.2B**), and the chelation of neutralized radiometal. RadioTLC results supports successful radiolabeling, where native SSI (i.e. not bound to DFO) resulted in the majority of [^{89}Zr]Zr remaining unbound (rf @ 0.6 cm), but DFO-bound SSI trapped [^{89}Zr]Zr near the baseline (rf @ 0.1 cm) for

both QBECO and QBKPN (**Fig. 8.2C**). Total radiochemical yields were acceptable at 92±2% and 89±5% for QBECO and QBKPN, respectively. Importantly, both formulations of radiolabeled SSIs were found to be stable over 48 h in mouse serum, where both QBECO and QBKPN retained their radiolabel (>99% radiochemical purity, **Fig. 8.2C**). The stability of radiolabeled SSIs in mouse serum suggests that the biodistribution of radiolabeled SSI can be tracked with high confidence *in vivo* for an extended period of time.

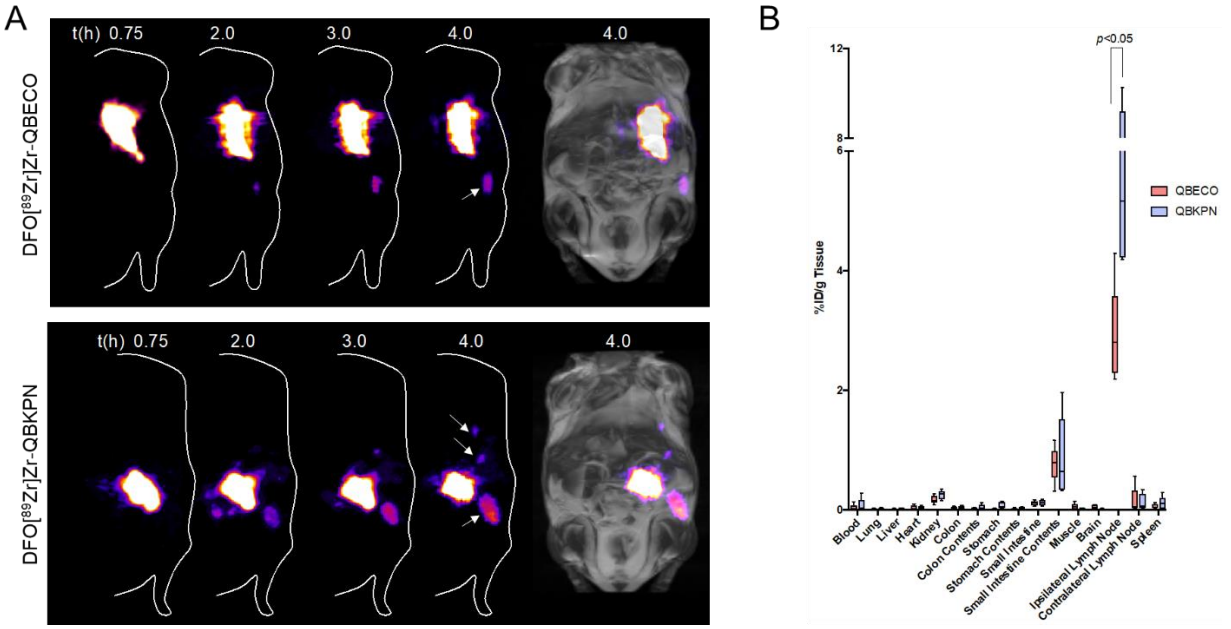

Figure 8.3 High lymph node uptake of [^{89}Zr]Zr-QBECO and [^{89}Zr]Zr-QBKPN suggests early immune modulation. (A) Mice were injected subcutaneously with either [^{89}Zr]Zr-QBECO or [^{89}Zr]Zr-QBKPN, followed by PET imaging at indicated times post-injection. At 4 h post-injection, sequential T_1-weighted MRI was also performed for anatomical reference. White arrows indicate signal accumulation due to SSI migration from injection site. **(B)** Tissues were collected, and radioactivity was quantified as injected dose per tissue using a gamma counter. Data are shown as mean±s.d. of n = 5 mice.

With the experimental support for stable SSI radiolabeling, the short-term (<4 h) *in vivo* biodistribution of QBECO and QBKPN in healthy animals was evaluated (**Fig. 8.3A)**. Mice were injected s.c. with either [^{89}Zr]Zr-QBECO or [^{89}Zr]Zr-QBKPN, and the SSIs were tracked by PET imaging followed by the resection of tissues at 4 h post-injection. PET/MRI reveals the differential migration of radiolabelled SSI from the site of injection to lymph nodes from 2-4 h post-injection, with QBECO migrating to the inguinal lymph node only while QBKPN exhibits inguinal lymph node as well as rostral migration **(Fig. 8.3A).** The site-specific and differential migration of QBECO and QBKPN match the site-specificity of their demonstrated therapeutic effects, with QBECO treating disease of the gut[13] and QBKPN treating lung disease[14]. The biodistribution at 4 h post-injection was confirmed with gamma counting of resected tissues, which supported the imaging-based uptake in the ipsilateral inguinal lymph node (**Fig. 8.3B**). Importantly, the lack of bone uptake further supported the stability of the [^{89}Zr]Zr-SSI chelates *in vivo*.

We next set out to evaluate the long-term distribution of SSI after single s.c. administration, which was afforded by the long half-life of ^{89}Zr (3.3 days; **Fig. 8.4**). Following an s.c. injection of 1.85MBq of [^{89}Zr]Zr-QBECO or [^{89}Zr]Zr-QBKPN, mice were imaged by PET at time points of 30 min, 4 h, 24 h, and every subsequent 24 h for 8 days following injection. Just as observed in the short-term biodistribution study (**Fig. 8.3A**), a differential biodistribution between QBECO and QBKPN was noted up to 8 days post-injection (**Fig. 8.4**). QBKPN, the lung-targeted treatment, was observed to travel from the site of injection to the kidneys, thoracic cavity, and cervical lymph nodes by 24 h post-injection. Conversely, QBECO, the G.I.-targeted treatment, remained largely in the abdominal region for the duration of the study, appearing briefly in the cervical lymph nodes 4-5 days post-injection. In order to evaluate possible trafficking routes, animals were exsanguinated at 4 h, 48 h, 120 h, and 192 h after injection of radiolabelled SSIs, and radioactivity was quantified using a gamma counter. Negligible radioactivity was found in the blood (data not shown), suggesting a trafficking mechanism primarily outside of the blood circulation.

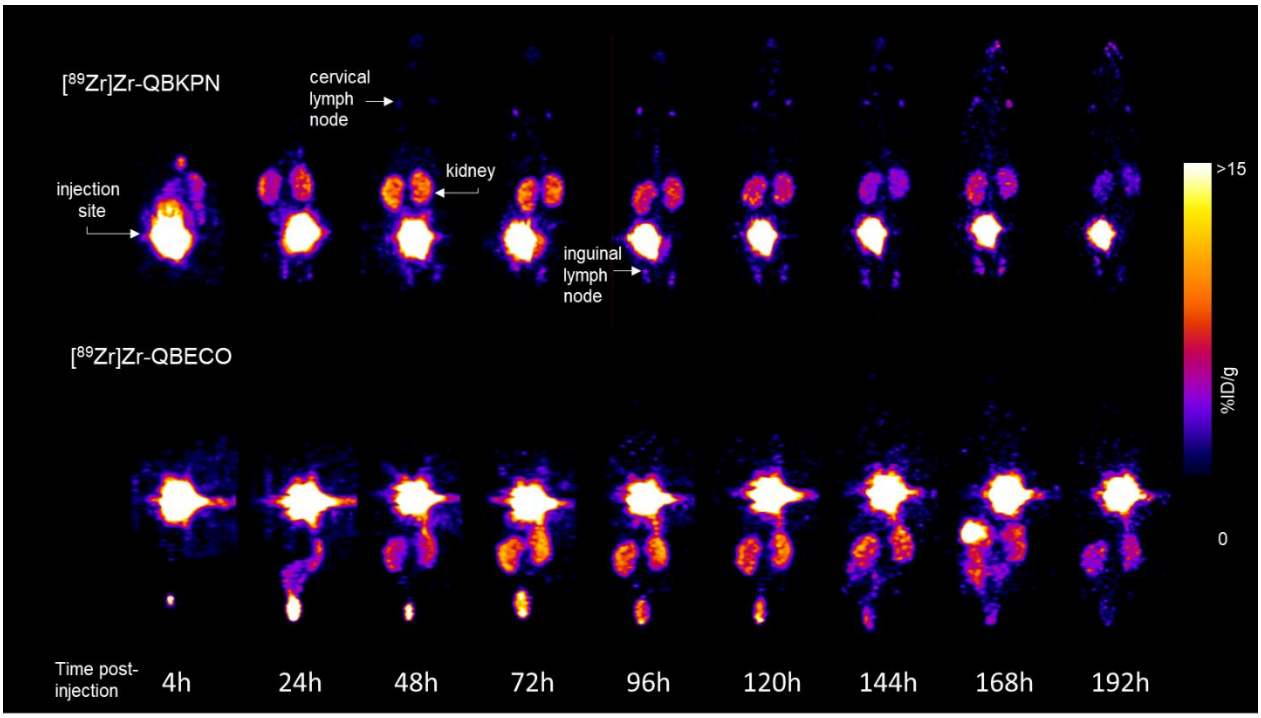

Figure 8.4. Long-term PET imaging after single dose of [^{89}Zr]Zr-SSI reveals differential biodistribution. Healthy mice were given a subcutaneous injection of 1.85MBq of radiolabeled SSIs. Representative PET images of two mice over time after single subcutaneous with (top) [^{89}Zr]Zr-QBKPN, a lung-targeted SSI, or (bottom) [^{89}Zr]Zr-QBECO, a gut-targeted SSI. Injection sites were chosen to minimize area of injection signal on targeted tissues. Mice underwent 10min static PET scans at indicated time points post-injection. Maximum intensity projections are shown as %ID/g.

A second long-term *in vivo* study was conducted in mice to evaluate the effect of repeated SSI injections on biodistribution, where mice received a primary, unlabeled dose of SSI prior to inoculation with a radiolabeled dose (**Fig. 8.5**). In clinical and pre-clinical trials, QBKPN and QBECO are administered subcutaneously every other day for the treatment of cancer and chronic diseases [13,14], justifying the need to evaluate repeated administration on SSI disposition. It is important to note, the SSIs are not administered at or near the previous injection site, and test subjects are instructed to rotate the site of injection to different areas of the body. PET imaging over 8 days revealed a marked decrease in SSI migration away from the injection site for both QBECO and QBKPN in mice that received two doses compared to those receiving a single dose (**Fig. 8.5A)**. With a single injection, the labelled QBKPN travelled upward toward the thoracic cavity of the mice with the peak activity in the cervical lymph nodes appearing at 144 h post-injection. In comparison, the second injection of QBKPN appeared to have a delayed onset of distribution, with peak cervical lymph node uptake at 192 h post-injection. Furthermore, there was significantly more [^{89}Zr]QBKPN in the kidneys, the primary organ of excretion, from 24 h to 144 h post-injection in the first dose compared to the second, indicating a delayed clearance of the therapeutic from the injection site (**Fig. 8.5B)**. A similar distribution pattern was observed in the QBECO groups, where the labeled SSI was moved from the site of injection to lymph nodes and kidneys faster in with first injection of SSI as compared to the second.

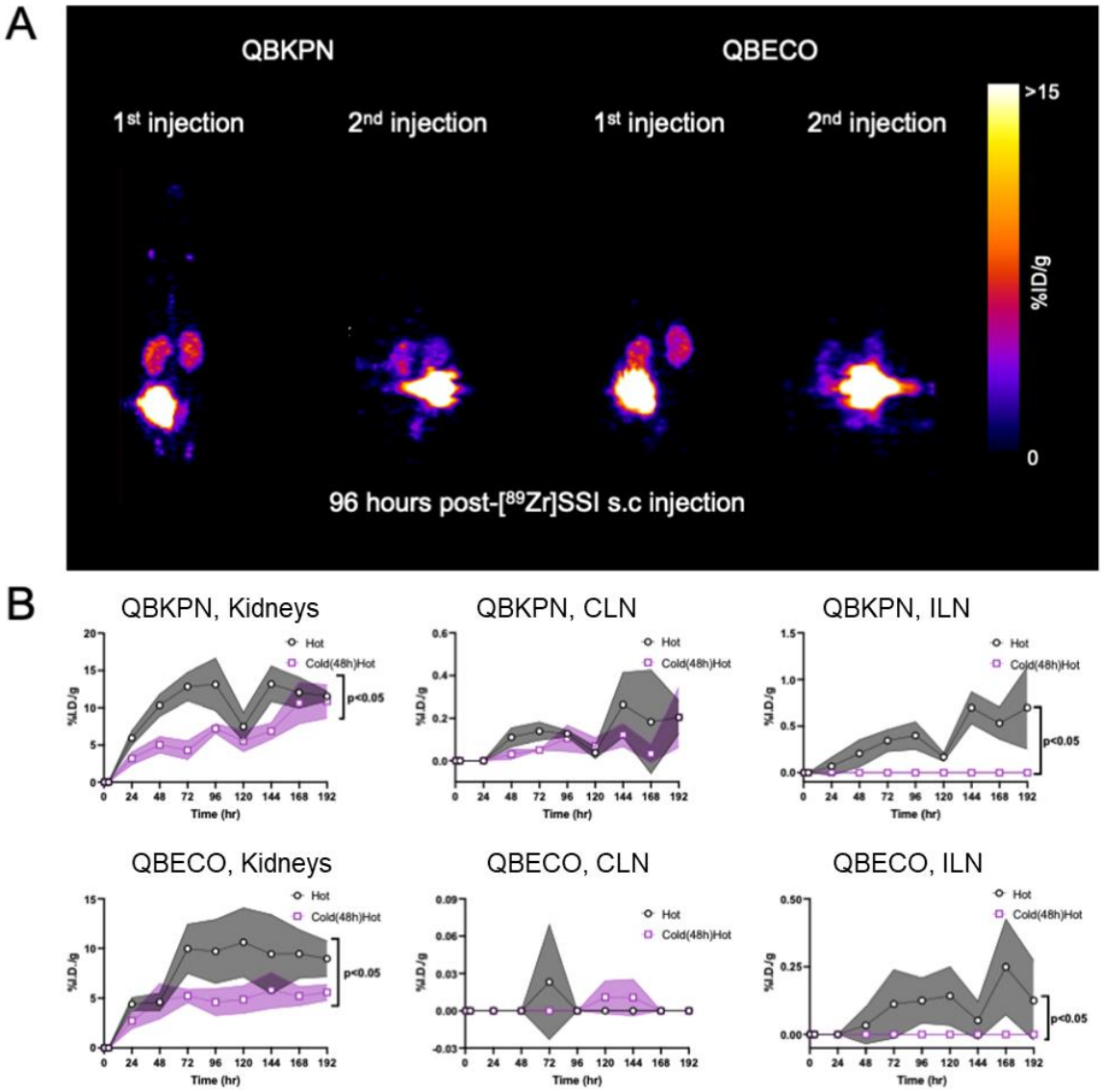

Figure 8.5. Biodistribution of SSIs after one *vs* two injections. (A) PET images of mice 96 h post-[^{89}Zr]Zr-SSI injection. Mice either received one 1.85MBq dose of labelled QBKPN or QBECO, or one unlabeled dose 48 h prior to a second, labeled dose of either SSI. Mice were imaged at time points of 30 min, 4 h, 24 h, and every 24 h for 8 days. Representative images are shown of mice 96 h post-labeled injection. (B) Uptake of [^{89}Zr]Zr-QBKPN (top) and [^{89}Zr]QBECO (bottom) in kidneys and inguinal (ILN) and cervical (CLN) lymph nodes of mice after first (black) vs second (purple) injection. Data are shown as means + standard deviation at time points indicated after labeled SSI injection, n=4 per group. Statistical significance is denoted as $p<0.05$ by Generalized Linear Model Repeated Measures analysis.

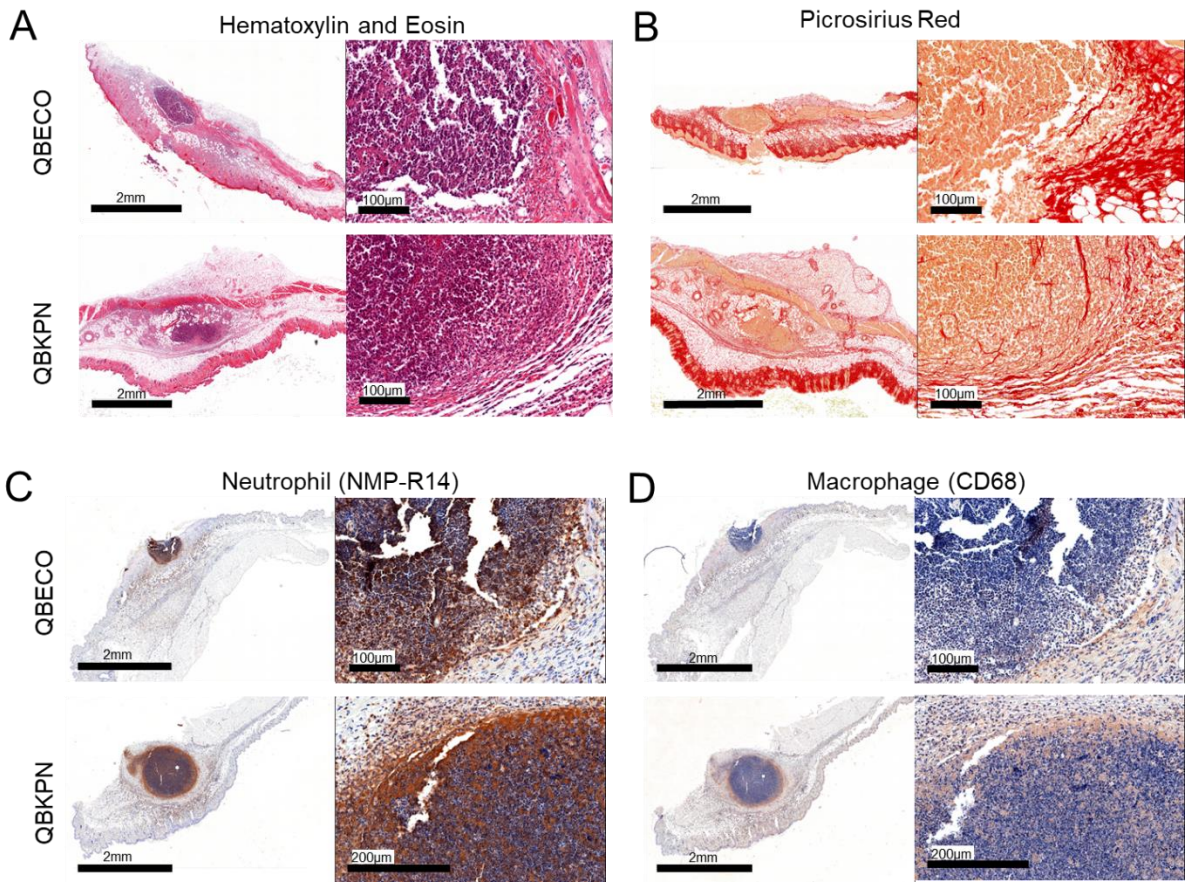

Figure 8.6. Histology of nodule formed at site of injection shows invading immune cells. Representative sections are shown for lesions removed from mice 192 h after [^{89}Zr]Zr-SSI injection. A zoomed region is displayed to the right of each section. (A) Hemotoxylin and Eosin were used to identify cell composition, and (B) Picrosirius red was used to identify collagen (red). α-NMP-R14 and α-CD68 antibodies were used to visualize infiltration of neutrophils (C) and macrophages (D), respectively, to the injection site.

In order to investigate the cellular response to SSI injection that may contribute to SSI trafficking, we resected small nodules at the site of SSI injection, which we hypothesized was a local innate response observed in all mice following administration of either [^{89}Zr]Zr-SSI or unlabeled SSI (**Fig. 8.6**). Hematoxylin and Eosin (H&E) staining revealed an infiltration of cells at the site of injection (**Fig. 8.6A**). Picrosirius red (PSR) was used to determine whether the nodule was composed of scar tissue, but a lack of red stain within the nodule revealed collagen was not present in the injection site (**Fig. 8.6B**). The samples

were then probed with anti-NMP-R14[28] (a neutrophil marker; **Fig. 8.6C**) and anti-CD68[29] (a macrophage marker; **Fig. 8.6D**) antibodies to determine whether this increase in cell population was composed of innate immune cells. Neutrophil accumulation at, and infiltration into, the site of injection was noted for both QBECO and QBKPN. However, the macrophage accumulation and infiltration appeared greater for QBKPN than was observed for QBECO.

8.8. Discussion

When pathogens enter the body, innate immune cells are recruited to stop the systemic spread of the pathogens through the circulatory system, such that bacterial dissemination from the afflicted site to systemic circulation is rare in healthy individuals[30]. Depending on the context of infection, the task of innate immunity is to determine where the source of infection is arising to ensure that it is retained therein and prevented from spreading. This need initiates rapid immune mobilization to source where in the body the infective organism detected is most abundantly located and has been seen before. This is critical resource management by the innate immune system, as it would be ineffective to send the new army of immune cells being generated in response to infection everywhere. In the case of bacterial dissemination through the lymphatic system, the lymph nodes serve as a crucial barrier. Pathogens leave the site of injection and are transported to lymph nodes *via* the lymphatics. Once at the lymph node, resident macrophages begin to phagocytose the invading pathogens[31]. Neutrophils, present both in the parenchyma of lymph nodes and in circulation, are also recruited *via* chemoattractants[32] or cytokines[31] to capture the pathogens. Together, the macrophages and neutrophils provide critical protection against these bacterial pathogens reaching systemic circulation. Subcutaneously injected bacteria reach the lymph node within a few minutes of injection[33], and are quickly captured by resident macrophages[34]. Several studies have noted neutrophils swarming pathogens following administration of mycobacterium[35], *Toxoplasma gondii*[36], *Pseudomonas aeruginosa*[31], and *Staphylococcus aureus*[37], likely to clear both the pathogens themselves and infected macrophages. One study showed *S. aureus,* once past the skin barrier, migrates to the draining lymph node only, where is it

quickly phagocytosed by subcapsular sinus macrophages and neutrophils *via* high endothelial venules (HEVs)[32].

Based on the data in the current study, the SSIs QBKPN and QBECO behave like bacterial pathogens in the first 4 hours of subcutaneous administration in healthy individuals, as they were observed to travel to the draining lymph node *via* the lymphatics (**Fig. 8.3**). Negligible amounts of radiolabeled SSI were found in the blood at multiple timepoints from 4 hours to 192 hours post-administration, however immune cell infiltration is seen at the site of injection (**Fig. 8.6**). Interestingly, neutrophils seem to play a major role at the site of injection for both QBKPN and QBECO (**Fig. 8.6C**). Whereas macrophages appeared greater in abundance following QBKPN administration relative to QBECO (**Fig. 8.6D**). During acute inflammation, activated macrophages are recruited and release pro-inflammatory mediators to promote efficient elimination of the insulting agent[38].

Our data support the organ site-specific systemic biodistribution of the SSI previously demonstrated in preclinical and clinical studies[14,15,20], which is dependent on the bacteria from which the SSI is derived (**Fig. 8.4**). The *E. coli*-derived gut-targeted SSI, QBECO, is seen in the injection site, inguinal lymph nodes, and kidneys over 8 days following s.c. injection. In all *in vivo* biodistribution studies (**Figs. 3-5**), overall migration of the SSI to regions of interest was higher in QBKPN compared to QBECO groups. This increased trafficking is likely due to the activity of macrophages on QBKPN (**Fig. 6**). In contrast, the *K. pneumoniae*-derived SSI, QBKPN, travels to the cervical lymph nodes, closer to the target organ of the lungs. In both clinical and preclinical investigations of these therapies, the SSIs are administered subcutaneously every 48 hours[13,14]. An injection of unlabeled SSI 48 hours before [^{89}Zr]Zr-SSI administration resulted in decreased kidney and lymphatic uptake in both QBECO and QBKPN groups (**Fig. 8.5**). While further investigations are necessary to determine the cause of this decreased trafficking, we hypothesize that in healthy mice, the first dose of SSI induces an innate immune response, recruiting macrophages and neutrophils to the site of injection. The increased presence of activated immune cells

remain at the injection site for at least 8 days as demonstrated by histological evaluation of the site of injection (**Fig. 8.6**), and are likely primed for the next insult, increasing their efficacy of pathogen clearance.

In a mouse model of lung cancer, the administration of QBKPN resulted in an acute infection-like response in the lungs[14], which is not seen in mice bearing lung tumors upon administration of QBECO[15], indicating these therapies are not disease-specific, but specific to the organ from which the microbial-based SSI are endogenous. Likewise, in a mouse model of spontaneous ulcerative colitis, QBECO decreases immune cell infiltration to the colon, ameliorating the mouse's condition[13]. This suggests that SSIs work by modulating the immune response to affected organs, dependent on whether increased or decreased immune activity is needed. The current study confirms the site-specificity of these therapies in healthy individuals. The biodistribution of SSI is dependent on the organotropism of the bacteria from which the SSI is derived, regardless of presence of disease.

There are known limitations to this study. The method of analysis does not reveal in what form the SSIs are trafficking. It would be assumed that microbial products would be quickly phagocytosed and degraded at the site of injection, and it is still unknown how the SSIs are carried through the body. However, our results suggest that there is an important role for phagocytic cells in this process. It is also important to note that the amount of SSI being delivered in these experiments are significantly greater, based on body size, to what would be administered to a human, so the trafficking and abundance of these immunotherapy products may be different between mice and humans.

8.9. Conclusion

In conclusion, the stable radiolabeling of these unique SSI immunotherapy products provides a useful tool to map their long-term disposition in a live animal over time. PET imaging revealed differential biodistribution of [^{89}Zr]Zr-QBECO and [^{89}Zr]Zr-QBKPN, supporting their tissue-targeted design. The current investigation points to macrophages and/or neutrophils as the putative traffickers of the SSI from the site of injection to the organ-specific site of bacterial colonization, however, further investigations will

be required to determine the precise role for these cells, and whether SSI are processed prior to, during, or after trafficking.

8.9. Funding

The authors wish to acknowledge funding from NSERC ENGAGE (507652-16), which leveraged in-kind provision of QBECO and QBKPN by Qu Biologics, Inc., to carry out this study.

8.10. Authors' contributions

A.K., M.S., M.B., S.K. and A.J.S. conceptualized the study. M.S., D.D., and A.J.S. performed chemistry experiments. A.K. and A.J.S. performed all animal experiments, data analysis, and wrote the manuscript. All authors reviewed and approved the final version of the manuscript.

8.11. Declaration of Competing Interests

S.K. is an employee of Qu Biologics.

8.12. Acknowledgements

The authors wish to acknowledge Dr. XiaoLing Zhao from the High Resolution Cell Imaging Core Facility at UOHI for histological processing and imaging.

8.11. References

1 Coley, W. B. The therapeutic value of mixed toxins of the streptococcus of erysipelas and bacillus prodigiosus in the treatment of inoperable malignant tumors. *Am J Med Sci* **112**, 251-280, (1896).

2 Karbach, J. *et al.* Phase I clinical trial of mixed bacterial vaccine (Coley's toxins) in patients with NY-ESO-1 expressing cancers: immunological effects and clinical activity. *Clinical Cancer Research* **18**, 5449-5459, (2012).

3 Kucerova, P. & Cervinkova, M. Spontaneous regression of tumour and the role of microbial infection–possibilities for cancer treatment. *Anti-Cancer Drugs* **27**, 269, (2016).

4 Redelman-Sidi, G., Glickman, M. S. & Bochner, B. H. The mechanism of action of BCG therapy for bladder cancer—a current perspective. *Nature Reviews Urology* **11**, 153, (2014).

5 Lizotte, P. H. *et al.* Attenuated Listeria monocytogenes reprograms M2-polarized tumor-associated macrophages in ovarian cancer leading to iNOS-mediated tumor cell lysis. *Oncoimmunology* **3**, e28926, (2014).

6 Pan, Z.-K., Weiskirch, L. M. & Paterson, Y. Regression of established B16F10 melanoma with a recombinant Listeria monocytogenes vaccine. *Cancer research* **59**, 5264-5269, (1999).

7 Baird, J. R. *et al.* Immune-mediated regression of established B16F10 melanoma by intratumoral injection of attenuated Toxoplasma gondii protects against rechallenge. *The Journal of Immunology* **190**, 469-478, (2013).

8 Sanders, K. L., Fox, B. A. & Bzik, D. J. Attenuated Toxoplasma gondii stimulates immunity to pancreatic cancer by manipulation of myeloid cell populations. *Cancer immunology research* **3**, 891-901, (2015).

9 Sottnik, J. L., U'Ren, L. W., Thamm, D. H., Withrow, S. J. & Dow, S. W. Chronic bacterial osteomyelitis suppression of tumor growth requires innate immune responses. *Cancer immunology, immunotherapy* **59**, 367-378, (2010).

10 Lascelles, B. D. X. *et al.* Improved survival associated with postoperative wound infection in dogs treated with limb-salvage surgery for osteosarcoma. *Annals of Surgical Oncology* **12**, 1073-1083, (2005).

11 Baird, J. R. *et al.* Avirulent Toxoplasma gondii generates therapeutic antitumor immunity by reversing immunosuppression in the ovarian cancer microenvironment. *Cancer research* **73**, 3842-3851, (2013).

12 Felgner, S., Kocijancic, D., Frahm, M. & Weiss, S. Bacteria in cancer therapy: renaissance of an old concept. *International journal of microbiology* **2016**, (2016).

13 Sham, H. P. *et al.* Immune stimulation using a gut microbe-based immunotherapy reduces disease pathology and improves barrier function in ulcerative colitis. *Frontiers in immunology* **9**, 2211, (2018).

14 Bazett, M. *et al.* Harnessing innate lung anti-cancer effector functions with a novel bacterial-derived immunotherapy. *Oncoimmunology* **7**, e1398875, (2018).

15 Kalyan, S. *et al.* Distinct inactivated bacterial-based immune modulators vary in their therapeutic efficacies for treating disease based on the organ site of pathology. *Scientific Reports* **10**, 5901, (2020).

16 Askenase, M. H. *et al.* Bone-marrow-resident NK cells prime monocytes for regulatory function during infection. *Immunity* **42**, 1130-1142, (2015).

17 Bazett, M. *et al.* Attenuating immune pathology using a microbial-based intervention in a mouse model of cigarette smoke-induced lung inflammation. *Respiratory research* **18**, 92, (2017).

18 Bazett, M. *et al.* A novel microbe-based treatment that attenuates the inflammatory profile in a mouse model of allergic airway disease. *Scientific reports* **6**, 35338, (2016).

19 Wenzel, U. A. *et al.* Spontaneous colitis in Muc2-deficient mice reflects clinical and cellular features of active ulcerative colitis. *PloS one* **9**, (2014).

20 Sham, H. P. *et al.* Immune Stimulation Using a Gut Microbe-Based Immunotherapy Reduces Disease Pathology and Improves Barrier Function in Ulcerative Colitis. *Frontiers in Immunology* **9**, (2018).
21 Kaplan, G. G. *et al.* The Impact of Inflammatory Bowel Disease in Canada 2018: Epidemiology. *Journal of the Canadian Association of Gastroenterology* **2**, S6-S16, (2018).
22 Olén, O. *et al.* Colorectal cancer in ulcerative colitis: a Scandinavian population-based cohort study. *The Lancet* **395**, 123-131, (2020).
23 Sandborn, W. J. The present and future of inflammatory bowel disease treatment. *Gastroenterology & hepatology* **12**, 438, (2016).
24 Dagogo-Jack, I. & Shaw, A. T. Tumour heterogeneity and resistance to cancer therapies. *Nature reviews Clinical oncology* **15**, 81, (2018).
25 Jones, G. S. & Baldwin, D. R. Recent advances in the management of lung cancer. *Clinical Medicine* **18**, s41, (2018).
26 Price, E. W. & Orvig, C. Matching chelators to radiometals for radiopharmaceuticals. *Chemical Society Reviews* **43**, 260-290, (2014).
27 Dijkers, E. C. *et al.* Development and characterization of clinical-grade 89Zr-trastuzumab for HER2/neu immunoPET imaging. *Journal of nuclear medicine* **50**, 974-981, (2009).
28 Rajesh, Y. *et al.* Dissecting the Balance Between Metabolic and Oncogenic Functions of Astrocyte-Elevated Gene-1/Metadherin. *Hepatology Communications* **6**, 561-575, (2022).
29 Menzies, R. I. *et al.* Hyperglycemia-induced renal P2X7 receptor activation enhances diabetes-related injury. *EBioMedicine* **19**, 73-83, (2017).
30 Jin, S., Wetzel, D. & Schirmer, M. Deciphering mechanisms and implications of bacterial translocation in human health and disease. *Current Opinion in Microbiology* **67**, 102147, (2022).
31 Kastenmüller, W., Torabi-Parizi, P., Subramanian, N., Lämmermann, T. & Germain, R. N. A spatially-organized multicellular innate immune response in lymph nodes limits systemic pathogen spread. *Cell* **150**, 1235-1248, (2012).
32 Bogoslowski, A., Butcher, E. C. & Kubes, P. Neutrophils recruited through high endothelial venules of the lymph nodes via PNAd intercept disseminating Staphylococcus aureus. *Proceedings of the National Academy of Sciences* **115**, 2449-2454, (2018).
33 Nossal, G., Abbot, A. & Mitchell, J. Antigens in immunity: XIV. Electron microscopic radioautographic studies of antigen capture in the lymph node medulla. *The Journal of experimental medicine* **127**, 263-276, (1968).
34 Junt, T. *et al.* Subcapsular sinus macrophages in lymph nodes clear lymph-borne viruses and present them to antiviral B cells. *Nature* **450**, 110-114, (2007).
35 Abadie, V. *et al.* Neutrophils rapidly migrate via lymphatics after Mycobacterium bovis BCG intradermal vaccination and shuttle live bacilli to the draining lymph nodes. *Blood* **106**, 1843-1850, (2005).
36 Chtanova, T. *et al.* Dynamics of neutrophil migration in lymph nodes during infection. *Immunity* **29**, 487-496, (2008).
37 Hampton, H. R., Bailey, J., Tomura, M., Brink, R. & Chtanova, T. Microbe-dependent lymphatic migration of neutrophils modulates lymphocyte proliferation in lymph nodes. *Nature communications* **6**, 7139, (2015).
38 Watanabe, S., Alexander, M., Misharin, A. V. & Budinger, G. S. The role of macrophages in the resolution of inflammation. *The Journal of clinical investigation* **129**, 2619-2628, (2019).

Chapter 9: Conclusions and Future Perspectives

9.1. Chapter 2: MRI Probes for *In vivo* Aldehyde Sensing

9.1.1. Conclusions to Chapter 2

The production and clearance of endogenous aldehydes is tightly controlled during normal metabolic processes. When production outpaces their clearance by aldehyde dehydrogenases, a build-up of aldehydes in tissues occurs. These highly electrophilic aldehydes bind rapidly with DNA, protein, and amino acids to form adducts, causing catastrophic damage. The over-production of aldehydes is associated with many pathologies including fibrotic diseases, cancer, brain injury, neurodegenerative, and cardiovascular diseases. While the need for non-invasive molecular imaging of aldehydes is widely discussed in the literature, the development of *in vivo* aldehyde-trapping probes presents many challenges due to their transient and highly reactive nature. These challenges, and the requirements for developing such probes are described in this review. Also presented is a comprehensive summary of all current aldehyde-trapping MRI probes, classified into two groups. The first group are macrocyclic metal-based compounds for extracellular aldehyde sensing developed by Dr. Caravan and his group. These probes were designed to bind to allysine residues which are characteristic of active fibrogenesis. We reviewed the development of probes, the importance of aldehyde-binding warheads, their kinetics, and *in vivo* mouse models of fibrosis that were used to test the probes. Secondly, three CEST-MRI probes (Hydrazo-CEST) designed by Dr. Shuhendler and his group were discussed. These small molecule metal-free compounds are designed for intracellular trapping of either aliphatic or aromatic aldehydes, affording the *in vivo* imaging of total aldehydic load. The development of these probes and their characterization in mouse models of lung cancer and traumatic brain injury were discussed.

Overall, the development of these whole-body *in vivo* aldehyde-binding probes allow for the pre-clinical visualization of both extracellular and intracellular endogenous aldehyde production using MRI. Using these tools, researchers may begin to close the knowledge gap of the pathophysiology of aldehydes in disease and injury.

9.1.2. Future Perspectives to Chapter 2

In this chapter, we highlight the need for further development in the field of molecular imaging of aldehydes, both at the pre-clinical and clinical stage. Clinical translation of these non-invasive diagnostic probes is essential for earlier detection of a wide array of diseases. Continuing efforts must be made to identify and fully characterize the role of aldehydes in disease so as to broaden the clinical use of this toolkit. Aldehydes have been implicated in many diseases, however, their utility as biomarkers for early detection of these diseases must be investigated. Furthermore, as we believe aldehydes are propagators of disease, the aldehyde-trapping MRI probes discussed in this chapter may be interrogated as aldehyde-sequestering agents, identifying a potential therapeutic avenue for this class of probes.

9.2. Chapter 3: Methyl 5-MeO-N-aminoanthranilate

9.2.1. Conclusion to Chapter 3

A novel aldehyde-binding fluorophore, methyl 5-MeO-*N*-amintoanthranilate was described in this chapter. This represents the first fluorophore capable of detecting total intracellular aldehydic load, as it quickly binds and elicits a turn-on fluorescence upon complexation with aliphatic aldehydes. This probe was tested in a cell model of oxidative stress, showing an increase in total aldehydes following incubation with diethyl maleate, and an attenuation of aldehyde production with pre-treatment of an antioxidant, α-tocopherol. Overall, the outcomes of this research will facilitate our understanding of the biochemical processes involving endogenous aldehydes, including where they are produced in the cell, why they are produced, if they are trafficked, their role in pathology, and their role in diagnostic and therapeutic medicine.

9.2.2. Future Perspectives to Chapter 3

Future work on this probe involves chemical modification to prevent spontaneous cyclization in aqueous conditions to extend imaging time. This could allow for the tracking of intracellular aldehydes, including where they are produced, and where they migrate, informing on whether they act as signaling molecules of

stress, propagating disease. Furthermore, a modification toward longer emission wavelengths would greatly improve the risk of photobleaching while imaging this probe. Finally, a modification to withstand fixation would vastly increase the interrogation of endogenous aldehydes in cell models, as co-staining with antibodies could be performed.

Following optimization, it may be possible to integrate this probe into an affordable, rapid, and easily implemented point-of-care diagnostic tool for disease or injury resulting in an increase in aldehydic load in bodily fluid (e.g., blood, saliva, urine). For example, at-home kit could be used to monitor brain injury following an impact at a football game or following a motor vehicle accident, providing the patient with a guideline on when to seek further diagnostic imaging or treatment at a hospital.

9.3. Chapter 4: Mapping Aldehydic Load *In vivo* by Positron Emission Tomography with $[^{18}F]NA_3BF_3$

9.3.1. Conclusion to Chapter 4

A new aldehyde-binding radiotracer $[^{18}F]NA_3BF_3$ capable of mapping total endogenous aldehydes in living subjects by PET was introduced in this chapter. Using the same *N*-amino anthranilic acid-based backbone as the fluorophore described in chapter 3, an organotrifluoroborate isotope exchange mechanism was used to radiofluorinate the compound in good yield. The viability of this radiotracer was first assessed in mice with exogenously induced aldehyde-rich tissue. The radiotracer was able to detect the increase in aldehydes compared to control tissue. The use of a non-aldehyde binding control analog and successful blocking study confirmed the specificity of the probe. $[^{18}F]NA_3BF_3$ was then used in an LPS mouse model of inflammation to map whole body endogenous aldehyde production. Increase of aldehydes was seen in the kidneys, liver, and lymph nodes, which coincided with areas of pro-inflammatory signals identified in the literature. With this new radiotracer, aldehyde biomarkers of inflammation including lipid peroxidation and oxidative stress comprising endogenous aldehydic load may now be imaged *in vivo* with the high sensitivity and quantitative nature of PET.

9.3.2. Future Perspectives to Chapter 4

With the new capability of whole-body aldehyde imaging, this radiotracer can be applied to a variety of disease models to better understand the implications of endogenous aldehyde production in pathology. For example, any diseases that are currently known to be propagated by oxidative stress or inflammation can be mapped *in vivo* with this probe. If aldehydes are produced in the early stages of disease, importantly in diseases where early detection is crucial for treatment, this imaging tool may be used for earlier diagnosis. Furthermore, this probe may be used for drug development or treatment monitoring for these diseases.

A major disadvantage of this radiotracer is its inability to cross the intact blood-brain barrier. The inability to image the brain with this probe limits its use cases for the many neurological diseases in which aldehydes may be involved. To overcome this issue, we have designed a second iteration of this aldehyde-trapping PET radiotracer that is more likely to pass the blood-brain barrier (structure shown below). Once synthesized, this new radiotracer will need to be evaluated in the same manner as the current radiotracer, using a mouse model of neuroinflammation.

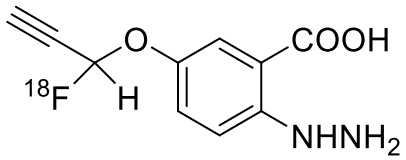

Figure 9.1. Future iteration of an aldehyde-mapping radiotracer designed to cross the blood-brain barrier.

9.4. Chapter 5: Aldehydic Load as an objective biomarker of mild traumatic brain injury by CEST-MRI

9.4.1. Conclusion to Chapter 5

mTBIs present a complex diagnostic challenge due to their often latent and non-specific symptoms, and current evaluations that are prone to diagnostic and selection biases. There is no single objective diagnostic

tool for concussions, but instead diagnosis relies on a combination of medical history, physical examination, symptom evaluation, and, in some cases, anatomical neuroimaging to rule out more severe traumatic brain injury. Our study addresses this critical gap in current diagnostic methods by introducing aldehydic load as an objective biomarker for mTBI. Our research provides a paradigm shift away from traditional approaches reliant on cognitive testing and patient interviews. Instead, we utilize clinically relevant molecular imaging technology to map brain aldehyde content as a novel imaging biomarker we show to be associated with mTBI.

Our work details the stepwise development of total brain aldehyde levels (a.k.a. aldehydic load) as a translational imaging biomarker for the objective diagnosis and characterization of concussion injury. We first detail the generation of an *in vitro* corticomimetic scaffold that supports the culture of primary and iPSC-derived mouse and human neurons in a matrix recapitulating the rheological properties of cortical brain tissues. The scaffold was specifically engineered so that it is easy to generate using standard laboratory cell culture infrastructure. Using this "brain-in-a-dish", we were able to apply a concussive force and map aldehydic load changes using live cell confocal microscopy. With this data supporting neuronal aldehyde generation after concussive impact, we then evaluated a novel MRI contrast agent capable of mapping aldehydes in a novel awake, closed head mouse model of concussion. The mouse model described avoids negative effects of head restraint, surgery, and anesthesia on concussion pathogenesis. We show that the concussive injury sustained in our model is absent from brain bleeding and blood brain barrier permeability changes, but sufficient to induce transient neurological deficits manifesting as sensorimotor disruptions. Using this mouse model, we apply a novel MRI contrast agent we call ProxyNA$_3$, which is based on years of chemistry and probe development by our research group, to map aldehydic load *in vivo.* We show that brain aldehydic load increases 2 days after concussion, preceding the elevation of a classical marker of neuroinflammation, glial fibrillary acid protein. We also show the first direct evidence that post-concussion aldehydic load increases in aged mice, and in mice deficient for aldehyde dehydrogenase enzymes, potentially identifying groups of individuals more susceptible to post-concussive injuries. Overall, the work

supports aldehydic load as an early, and potentially causative, imaging biomarker of concussion accessible by MRI.

9.4.2. Future Perspectives to Chapter 5

Further pre-clinical work needs to be done on this project before progressing to the clinic. First, a new animal model should be developed with brain anatomy more similar to humans, possessing gyri and sulci in order to better replicate concussive injury. With this new model, sex differences should be investigated, as well as more imaging timepoints to determine the ideal window for imaging following the potential concussive blow.

Furthermore, the CEST-MRI pulse sequence used in this study limited our images to a single slice of brain. Modifying this pulse sequence to include the full three-dimensional brain will be instrumental in fully mapping the location of injury. Expanding the field of view in this imaging protocol will also allow investigation into peripheral the effects of concussion, for example, whether aldehydic load is increased in other areas of the body following impact.

Through these studies, our major findings will be instructive for the further evaluation of neuropathology using an *in vitro* corticomimetic scaffold, will provide a translational tool for unprecedented objective diagnosis of concussion and mapping of concussion injury, and provide a validated mouse model with histological and behavioural outcomes recapitulating clinical presentation of concussion. Additionally, the novel MRI contrast agent presented in this work will create new avenues for the mapping of aldehydic load in other neurological and non-neurological injury and disease involving inflammatory pathology. Overall, ProxyNA$_3$ forges a new pathway for improving concussion diagnosis and interventions with immense translational potential.

9.5. Chapter 6: It's a Trap! Aldolase-prescribed C4-deoxyradiofluorination affords intracellular trapping and the tracing of fructose metabolism by PET

9.5.1. Conclusions to Chapter 6

Fructose metabolism has been implicated in many pathologies including metabolic disorders, neurodegenerative conditions, cardiac disorders, and cancer. In particular, a switch from glycolysis to fructolysis has been identified in cardiac hypertrophy and myocardial infarction, is considered a driver of Alzheimer's disease, and promotes inflammation following brain injury and stroke. Despite its clinical importance, the lack of a quantitative imaging tool has impeded our ability to explore fructolysis in pathology and diagnostic imaging. Our study addresses this critical gap by introducing a novel radiodeoxyfluoronated fructose analog, [^{18}F]4-fluoro-4-deoxyfructose ([^{18}F]4-FDF), which can be used to quantitively image fructose metabolism by PET.

The work presented in this chapter details the stepwise development and implementation of [^{18}F]4-FDF in *in vitro* and *in vivo* experiments. Our approach was informed by the catalytic mechanism of aldolase, a key enzyme in fructolysis. We confirmed cell uptake and intracellular trapping of heavy-labelled [U^{13}C]4-FDF in a HEPG2 cells, compared to previously-reported C_1- and C_6-fluorinated analogs which proceed through the fructolytic metabolic pathway. We propose that the deoxyfluorination of the C_4-position prevents aldolase-mediated scission, trapping the deoxyfluorinated fructose analog in the cell.

We synthesized [^{18}F]4-FDF with good radiochemical yield and molar activity, and evaluated its distribution in mice with HepG2 xenograft tumours, and compared its biodistribution to [^{18}F]6-FDF and [^{18}F]-2-fluoro-2-deoxy-D-glucose ([^{18}F]FDG). We found that [^{18}F]4-FDF has a better signal to noise ratio in highly glycolytic tissues including the brain and heart compared to [^{18}F]FDG, and avoids the extensive bone uptake seen with [^{18}F]6-FDF. To further investigate its potential as an inflammatory marker in brain and heart tissue, we evaluated its use in an LPS-induced mouse model of systemic inflammation. Here, we saw a significant increase in brain and heart update of [^{18}F]4-FDF in diseased mice compared to healthy mice,

suggesting this radiotracer may be used to map the pathological switch to fructose metabolism in brain and heart tissues.

9.5.2. Future Perspectives to Chapter 6

The potential impact of our research on clinical imaging and diagnosis of fructolysis-dependent pathologies is immense. Our new radiotracer, [^{18}F]4-FDF, allows for the sensitive mapping of fructose metabolism in highly glycolytic tissues, offering researchers and clinicians a powerful tool to study and diagnose diseases where fructolysis plays a pivotal role. The future perspectives of this work are toward clinical development. As this diagnostic imaging agent is a modified dietary sugar, and safety has been shown in numerous mice, clinical translation is the next step. Once baseline fructolysis is established in cohorts of healthy patients, this radiotracer may be tested for efficacy in a wide range of neurological and cardiovascular diseases, complimenting the current gold standard for PET imaging, [^{18}F]FDG.

As fructose metabolism has been shown to occur in numerous cardiovascular/cardiometabolic, and neurological disorders, as well as in many types of cancer, the molecular imaging of fructolysis may provide clinicians with a diagnostic tool capable of non-invasive detection of numerous diseases at early phases. Furthermore, this probe may be used in drug development and therapy monitoring for pathologies in which fructose metabolism occurs.

9.6. Chapter 7: Small Animal Multisubject PET/CT Workflow

9.6.1. Conclusions to Chapter 7

In this chapter, the methodology for simultaneously imaging multiple mice by PET/CT is described, using [^{18}F]NA_3BF_3-PET as an example. This methodology will help pre-clinical researchers perform PET/CT on animals with greater efficiency, ultimately reducing costs of research and time needed to complete projects.

Along with the methodology, described is a mouse model of APAP overdose, which I developed to map aldehyde production in the liver. It is well known that APAP overdose causes mitochondrial respiration dysfunction and a subsequent inflammatory response. However, the role of aldehydes in APAP metabolism

is poorly understood. For the first time, the aldehyde response to APAP overdose was characterized in a mouse model of drug toxicity.

9.6.2. Future perspectives to Chapter 7

While this methodology chapter was written to increase small animal PET/CT research efficiency, the future research from this paper should focus on the newly developed APAP toxicity model. As previously mentioned, the only clinical antidote for APAP overdose is N-aceytl cysteine, which needs to be administered within a narrow time frame to be effective. The lack of antidotes for this drug toxicity is due in part to the poor understanding of the full mechanism of the drug's metabolism.

If aldehydes play a role in the initiation or propagation of toxicity following APAP overdose, it is possible that mediating the aldehyde response may lead to the development of new treatments. This new therapy development could be performed on the mouse model described in this chapter, using [^{18}F]-NA_3BF_3-PET to monitor endogenous aldehyde production. Possibilities for treatment could be an aldehyde-scavenging agent to decrease the formation of aldehyde-adducts, or by upregulating aldehyde-detoxifying systems.

9.7. Chapter 8: Tracking the fate of bacteria-derived site-specific immunomodulators by Positron Emission Tomography

9.7.1. Conclusions to Chapter 8

SSIs are a novel class of biologic therapy made from different species of inactivated bacteria. These SSIs are designed to modulate the immune system in specific organs, based on the bacteria from which the therapy is derived. QBKPN is a lung-targeted SSI made from inactivated K*lebsiella pneumoniae*, and is currently in clinical development for the treatment of inflammatory lung diseases and respiratory infections. QBECO is a gut-targeted SSI derived from *Escherichia coli*, which is undergoing clinical investigation for treatment of UC. As all the macromolecular components of the organ-specific bacteria are retained, the therapy does not need to be administered directly to the site of disease, rather, it can be introduced subcutaneously to induce an immune response in an organ-specific manner. While these SSIs have shown immunomodulatory effects for pre-clinical and clinical efficacy in a broad range of conditions including

cancer, chronic inflammatory diseases, and infection, their biodistribution and trafficking mechanisms remain unknown.

Our work details the radiolabeling of QBKPN and QBECO with [^{89}Zr] for long-term biodistribution investigations in mice to map the movement of the particles from the site of injection. Isothiocyanate-functionalized desferrioxamine was conjugated to the SSI particles forming a thiourea linkage with exposed lysine residues on the surface. These were then incubated with [^{89}Zr]Zr-oxalate, effectively radiolabeling the SSIs in good radiochemical yield. Given the long half-life of the chosen radionuclide, we were able to map the biodistribution of the SSIs in mice longitudinally over 8 days *via* PET. This study showed differential distribution of the two SSIs in healthy mice. QBKPN, the lung-targeted SSI, traveled from the site of injection (abdomen) toward the thoracic cavity and nearby cervical lymph nodes. In contrast, the gut-targeted SSI, QBECO, remained in the abdominal region over the entire time course. A second biodistribution study revealed a "priming" of the innate immune system after the first dose, resulting in less trafficking of a secondary dose of the SSIs. Immunohistological investigation of tissue from the injection site showed an infiltration of innate immune cells. Interestingly, QBKPN induces the recruitment of both macrophages and neutrophils to the site of administration, whereas QBECO recruits mostly neutrophils. The differential recruitment of immune cells may play a role in the site-specific trafficking of SSIs.

9.7.2. Future Perspectives to Chapter

Through these studies, our major findings will be instructive for the further evaluation and characterization of the mechanism of action of SSIs. Considering the ongoing clinical investigation of this first-in-class immunotherapy program, a detailed understanding of trafficking and distribution is essential for further development of these therapies.

In order to fully understand the mechanisms of action of these SSIs, evaluation of the trafficking of QBKPN and QBECO in immunocompetent mouse models of lung cancer and UC should be performed. A syngeneic model of lung cancer (Lewis lung carcinoma model) can be used for the tracking of QBKPN in a clinically relevant mouse model. Tumour burden can be evaluated non-invasively by MRI, and radiolabeled [^{89}Zr]-

SSI can be tracked by PET/CT using the protocol established in Chapter 8. For the evaluation of QBECO in UC, a well-established immunocompetent mouse model for spontaneous UC with a defective mucus barrier ($Muc2^{-/-}$) can be used.

Immune cell components (macrophages, NK cells, neutrophils, T-cells, B-cells) participating in SSI trafficking (at the site of injection, lymph nodes, and disease) can be analyzed *ex vivo* by comparing diseased mice to disease-free controls. The tissues of interest can be used for autoradiography (for radiolabeled SSI location) and immunofluorescence (for immune cells) to correlate SSI location with innate and adaptive immune cell populations. The outcome of these studies would provide quantitative evaluation of the site-specific tracking of QBKPN and QBECO in mouse models of lung cancer and UC, along with immune cell response, which will contribute to a more complete understanding of the mechanism of SSI-mediate immunomodulation in disease. This data would directly inform the ongoing clinical translation by Qu Biologics.

Appendix 1: Copyright information

Chapter 2: The article titled "MRI Probes for In vivo Aldehyde Sensing" is published Open Access at *Analysis and Sensing*. Alexia Kirby, Mojmír Suchý, Adam Shuhendler, *Anal. Sens.* 2024, e202300087. DOI:10.1002/anse.202300087.

"Analysis & Sensing articles that publish Open Access are published under the terms of the Creative Commons Attribution License. The CC BY license permits commercial and non-commercial re-use of an open access article as long as the author is properly attributed."

Chapter 3: As per Royal Society of Chemistry guidelines, the use of my own material in a thesis or dissertation does not require a permissions request. The correct acknowledgement is included in section 3.3 and below:

Reproduced from Ref. ***Org. Biomol. Chem.***, 2019,**17**, 1843-1853 with permission from the Royal Society of Chemistry. DOI: 10.1039/C8OB02255K.

Chapter 4: The correct acknowledgement for copyright permission from the Royal Society of Chemistry is included section 4.3 and below:

Reproduced from Ref. **Chem. Commun.**, 2019,**55**, 5371-5374 with permission from the Royal Society of Chemistry. DOI: 10.1039/C9CC01831J.

Chapter 5: This manuscript titled "Aldehydic load as an objective imaging biomarker of mild traumatic brain injury by CEST-MRI" is available on the preprint server bioRxiv.

DOI: https://doi.org/10.1101/2024.04.16.589820

Chapter 6: Reproduced from Ref. Journal of Nuclear Medicine 65.3 (2024): 475-480. DOI: https://doi.org/10.2967/jnumed.123.266905.

Chapter 7: Copyright permissions were obtained for this book chapter from Spinger Nature:

Reproduced with permission from Springer Nature: Kirby, Alexia, and Adam J. Shuhendler. "Small Animal Multisubject PET/CT Workflow." *Positron Emission Tomography: Methods and Protocols*. New York, NY: Springer US, 2023. 185-193. https://doi.org/10.1007/978-1-0716-3499-8_11

SPRINGER NATURE LICENSE TERMS AND CONDITIONS
Jan 17, 2024
This Agreement between University of Ottawa -- Alexia Kirby ("You") and Springer Nature ("Springer Nature") consists of your license details and the terms and conditions provided by Springer Nature and Copyright Clearance Center.

License Number	5687690342234
License date	Dec 14, 2023
Licensed Content Publisher	Springer Nature
Licensed Content Publication	Springer eBook
Licensed Content Title	Small Animal Multisubject PET/CT Workflow
Licensed Content Author	Alexia Kirby, Adam J. Shuhendler
Licensed Content Date	Jan 1, 2024
Type of Use	Thesis/Dissertation
Requestor type	academic/university or research institute
Format	electronic
Portion	full article/chapter
Will you be translating?	no
Circulation/distribution	1 - 29
Author of this Springer Nature content	yes
Title of new work	Mapping the fundamental metabolic drivers of inflammation with molecular imaging
Institution name	University of Ottawa
Expected presentation date	Feb 2024
Requestor Location	University of Ottawa, 30 Marie Curie, Ottawa, ON K1N6N5 Attn: University of Ottawa
Billing Type	Invoice
Billing Address	University of Ottawa, 30 Marie Curie, Ottawa, ON K1N6N5 Attn: University of Ottawa
Total	0.00 CAD

Chapter 8: The manuscript titled “Tracking the fate of bacteria-derived site-specific immunomodulators by Positron Emission Tomography” is published in the journal *Nuclear Medicine and Biology* under a creative commons license. https://doi.org/10.1016/j.nucmedbio.2024.108908.